Clay Neomineralization and the Timing, Thermal Conditions and Geofluid History of Upper Crustal Deformation Zones

by

Austin Harold Boles

A dissertation submitted in partial fulfillment
of the requirements for the degree of
Doctor of Philosophy
(Earth and Environmental Sciences)
in The University of Michigan
2017

Doctoral Committee:
- Professor Ben van der Pluijm, Chair
- Professor Jeffrey C. Alt
- Professor Richard B. Rood
- Emeritus Professor Rob Van Der Voo

Corrigendum

4/20/2018

After publication of this dissertation, an equipment malfunction was discovered that affects the dataset included in Chapter VI, “Triassic, Surface-Fluid Derived Clay Diagenesis in the Appalachian Plateau, Northern U.S. Midcontinent.” Reanalysis and corrections are currently being applied, but until that dataset has been published in peer-reviewed literature, the $^{40}Ar/^{39}Ar$ geochronology reported herein and its interpretation SHOULD NOT BE USED, either for citation or as a basis for further research.

The dissertation committee of Austin Boles, listed below, approves this corrigendum and its insertion into the dissertation:

Ben van der Pluijm, Chair
Richard B. Rood
Jeffrey Alt
Rob Van Der Voo

Satur venter non studet libenter

A view of the Southern Alpine Orogen,
South Island, New Zealand.
Field photo (2014).

Austin Harold Boles
aboles@umich.edu; austin.boles@gmail.com
ORCID iD: 0000-0003-3072-3309

Dedication

I dedicate this volume to my two sons, Oliver and Calum. May they be ever curious and never lose their wonder.

Acknowledgments

I thank the many collaborators, colleagues, mentors, committee members and friends who have supported, encouraged, and taught me along the way: Anja Schleicher, Eliza Fitz-Diaz, Samantha Nemkin, Erin Lynch, Brice Lacroix, Jasmaria Wojtschke, Bernhard Schuck, Semih Can Ülgen, Celal Şengör, Halim Mutlu, I. Tonguç Uysal, Laurence Warr, Virginia Toy, Rupert Sutherland, John Townend, Timothy Little, the DFDP science team, Chris Hall, Nathan Niemi, Andreas Mulch, Zhongrui Li, Gordon Moore, Anne Hudon, Rob Van der Voo, Jeff Alt, Ricky Rood and many, many others. I thank my mentors at Shell Oil Co. for their insight, advice, and friendship: Kamran Zahid, Bill Lyons, Gina Gonzalez, and Ed Perry. I am grateful to Eugene Clark, Thomas Morris, and Ron Harris who inspired me to study geology and pursue a postgraduate degree. I am grateful to Ben van der Pluijm as an adviser, mentor, editor, and friend and for his unflagging patience, humor, and encouragement.

I am grateful for the funding that has supported my research during my tenure at the University of Michigan, including several Graduate Turner Awards and the Russell C. Hussey Scholarship from the UM Department of Earth and Environmental Sciences, several Research and Conference travel grants from the UM Horace H. Rackham School of Graduate Studies, Clay Minerals Society conference travel grants and the Robert C. Reynolds, Jr. Research Award, the Sedimentary Geology and Structural Geology and Tectonics Divisions of the Geological Society of America Stephen E. Laubach Research in Structural Diagenesis Award, and the International Continental Drilling Program's Training Course on Active Fault Zone Drilling support.

I am grateful to the students of structural geology and field camp that were unfortunate enough to have me as your teacher. I learned more than you did.

I thank my parents for a lifetime of teaching and sacrifice to engender in their children a love of learning. Finally, I thank my wife, Camilla, whose enduring love sustains me and whose spirit of adventure inspires me and ensures that we never bore.

Table of Contents

List of Figures

List of Tables

List of Appendices

Abstract

The various occurrences of clay neomineralization often coincide with zones of crustal deformation, making this family of minerals uniquely suited to record and retain the temperature, timing, and chemical conditions of upper crustal deformation. This dissertation comprises a suite of studies that employ various aspects of clay mineralogy, crystallography and clay chemistry to answer major questions in regional structural geology. These studies are diverse in their geography, timing and structural/tectonic setting, while united in their utilization of applied clay science. A key methodological tool used in these investigations is the illite polytype analysis method. An important contribution is the refinement of this method, both improving its accuracy by using state-of-the-art, Rietveld-type quantitative X-ray powder diffraction techniques, as well as broadening its application to include H isotopic analysis.

Chapter I serves to preface the dissertation and includes an introduction to practical aspects of clay mineralogy that distinguish them as geochronometers, geothermometers, and stable isotopic recorders. It outlines how the 3-dimensional arrangement of mineral populations and the properties of clays can be useful in understanding the structural history and mechanical behavior of deformed rock. Chapter II presents a new illite polytype analysis technique that represents significant advances on prior approaches, which is further utilized in subsequent chapters. Chapter III constrains the timing, temperatures, and mineralizing fluid characteristics of clays present in principal slip zone gouges from the Alpine Fault Zone (New Zealand), and concludes that both illitic and chloritic material in the fault zone are recent, surface-localized alteration. Chapter IV is an experimental study of temperature-dependent hydration behavior of natural smectite from the borehole of the Japan Trench Fast Drilling Project, which provides physical limits for estimates of coseismic heating during the 2011 Tohoku earthquake of <200ºC. Chapter V constrains illite mineralization timing in fault gouges along the trace of the modern North Anatolian Fault Zone, and indicates that the modern fault exploits pre-existing, weak clay material. Additionally, it shows that surface fluids infiltrated to depths >5 km in the upper crust. Chapter VI is a study of diagenetic

illite in mudstones of the Appalachian Plateau. The study presents evidence that mineralization timing (Early-Mid Triassic) coincides with the timing of maximum burial, and, therefore, hottest basinal temperatures, and that the fluid was surface-derived at spatial scales small enough to preserve a rain shadow effect from the nearby Appalachian orogen. This study challenges reigning views on tectonically-mobilized, older fluid flow for associated geologic processes. Chapter VII offers concluding remarks that highlight the main themes of this dissertation. Three appendices are included, presenting data tables and preliminary results of ongoing research efforts on pseudotachylytes from gneiss-dome bounding faults (Papua New Guinea), a fault dating campaign in the Istanbul Zone of northwest Turkey, and isotopic work on clay minerals recovered from principal slip zones in the San Andreas Fault Observatory at Depth borehole.

The overarching themes of the dissertation are the fingerprinting and timing of surface-derived (meteoric) signals in authigenic clay phases that formed at shallow to mid-crustal depths in major fault zones. This requires significant down-dip fluid flow. Emphasis is placed on how pre-existing, deep-seated weaknesses in the crust control deformation styles and facilitate fluid flow and mineralization, and on insights into the nature of deformation-related fluid flow and clay authigenesis.

Chapter I. Introduction

Clay minerals are a family of hydrous aluminosilicates with layered structures which, although they are characterized by extremely fine grain sizes (can be as small as a virus!), represent the most abundant minerals at the surface of the earth (Moore and Reynolds, 1997). Their study encompasses applied fields as diverse as pedology (the study of soils), radioactive waste disposal, the paper and chemical industries, ceramics, construction, hydrocarbon exploration and production, and even health sciences. As one of few families of minerals to form at low temperatures, clay minerals also fill an important information gap for the scientist investigating geologic processes between higher temperature systems that provide information about mid-crustal and deeper processes, and Earth's surface. Clay minerals can be particularly useful in the study of deformation of the brittle crust because their presence, properties, and chemistry are often direct results of the ways in which rocks respond to the application of tectonic forces and the generation of brittle structures. Indeed, the study of the interplay and feedbacks between mechanical deformation and chemical/mineralogical change at low temperatures is a rapidly growing field within the geosciences, recently coined "structural diagenesis" (Laubach et al., 2010). This introduction will outline the various ways in which clay minerals can be used in structural geology and serves as a preface the chapters of this dissertation that apply clay science toward resolving various questions in structural geology.

I.I Applied Clay Science in Structural Geology

A short summary of several key mineralogical features of individual clay minerals and clay mineral families is presented below to provide the background for their use as geochronometers, geothermometers, and isotopic tracers, and understanding how they can provide other useful types of information about deformation environments.

I.I.I. General Structure

Clay minerals are classified as phyllosilicates. Although there is a high degree of compositional and crystallographic variation among species that share this layered structure, all clay minerals are constructed from two basic building blocks: layer sheets of tetrahedrally-coordinated Si^{4+} (with Al^{3+} and Fe^{3+} commonly substituting) and layer sheets of octahedrally-coordinated Al^{3+} (or common alternatives Mg^{2+}, Fe^{2+}, Fe^{3+}, or other transition elements). A single sheet can achieve electrical neutrality by the position, charge, and abundance of these cations within a tetrahedral ring, leading to dioctahedral and trioctahedral species which feature two cations with 3+ charge or three cations with 2+ charge, respectively. The joining of two or more of these sheets along a shared junction plane of apical O and OH^- sites is what produces the two main types of clay layer, and the two main families of clay mineral. Much of what we know of the structure and crystal

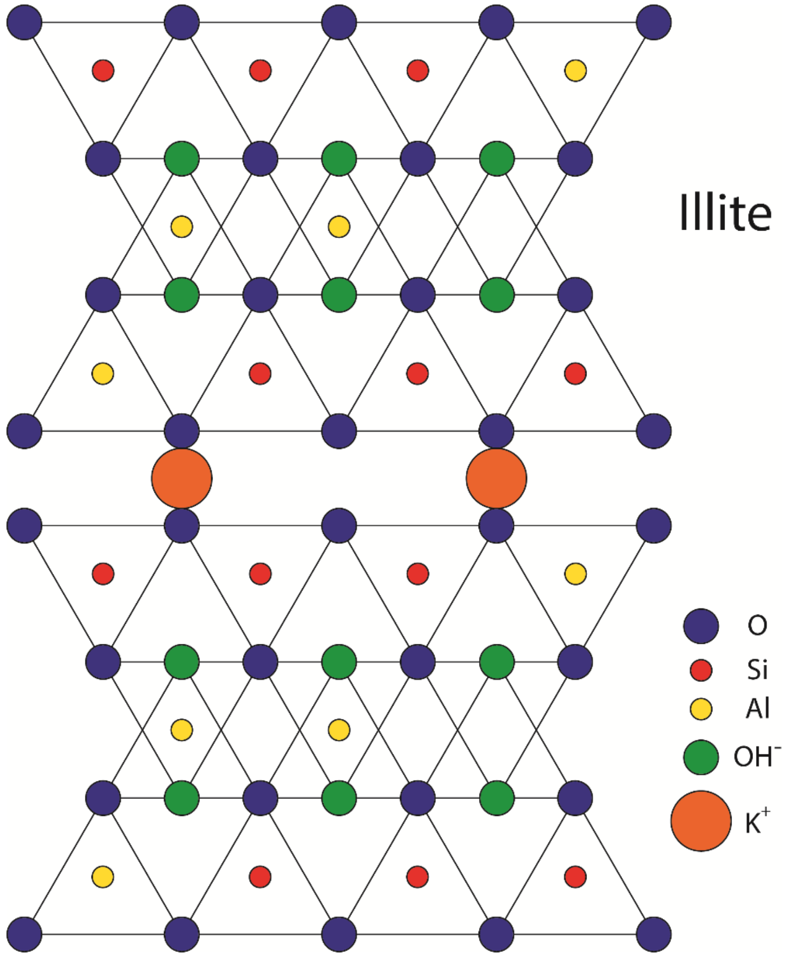

Figure I.I. Illite, a K-bearing, hydrous aluminosilicate that exhibits a 2:1 layer type structure.

habit of clay minerals comes from X-ray diffraction and scanning and transmission electron microscopy studies.

The first family of clay minerals features a 1:1 layer silicate structure. It joins a tetrahedral sheet and an octahedral sheet (TO) to create its fundamental layer type. Kaolinite and serpentine are minerals with a 1:1 layer type. The second clay mineral family adds an additional tetrahedral sheet by inverting it to make a tetrahedral-octahedral-tetrahedral (TOT) sandwich (figure I.I). 2:1 layer types are more compositionally diverse and include talc, smectite, vermiculite, illite, chlorite, and the true micas such as muscovite and biotite. It is the repetition of either the TO or TOT assemblage that makes the characteristic layered structure of clay minerals. This repetition also introduces electrical charge that must be neutralized by interlayer cations, or, in the case of chlorite, an additional octahedral sheet, between TOT assemblages. Perhaps even more surprising is the ability of smectite to recoverably expand along its c-axis to accommodate water and various organic molecules within the interlayer space in an effort to neutralize its layer charge – a property that is central to their use as cat litter and in other absorbents. Additionally, clay species can be interlayered with one another into superstructures, an example of which is illite-smectite. The resulting clay mineral family is a continuum of interlayer-type minerals, with end-members representing a pure species and the graduations representing various proportions of the two pure end-members, varied by layer stacking patterns and long range layer ordering systems.

In effect, it is the multiplicity of ways in which cations can be positioned and charged in tetrahedral layers, octahedral layers and interlayer sites, and the various ways layers can be stacked or intercalated that distinguish an individual clay species from others that may be closely genetically related within the truly diverse clay mineral family. This rich diversity is a large part of their practical appeal, as structural and compositional variation is the crystallographic memory of the formation conditions of a mineral. If mineralization of clay can be linked to deformation, this memory is the key to unraveling kinematic processes that encompass in their scope the temperature, fluid sources, and timing of deformation. See Bailey (1980), Brindley and Brown (1980), and Moore and Reynolds (1997) for in-depth treatment of clay mineral naming and classification conventions, structure and diversity.

I.I.II. Polytypism

Due to the ubiquitous presence of clay minerals of all species in the near-surface environment, and their very small size which precludes physical isolation of a mineral subset, distinguishing and

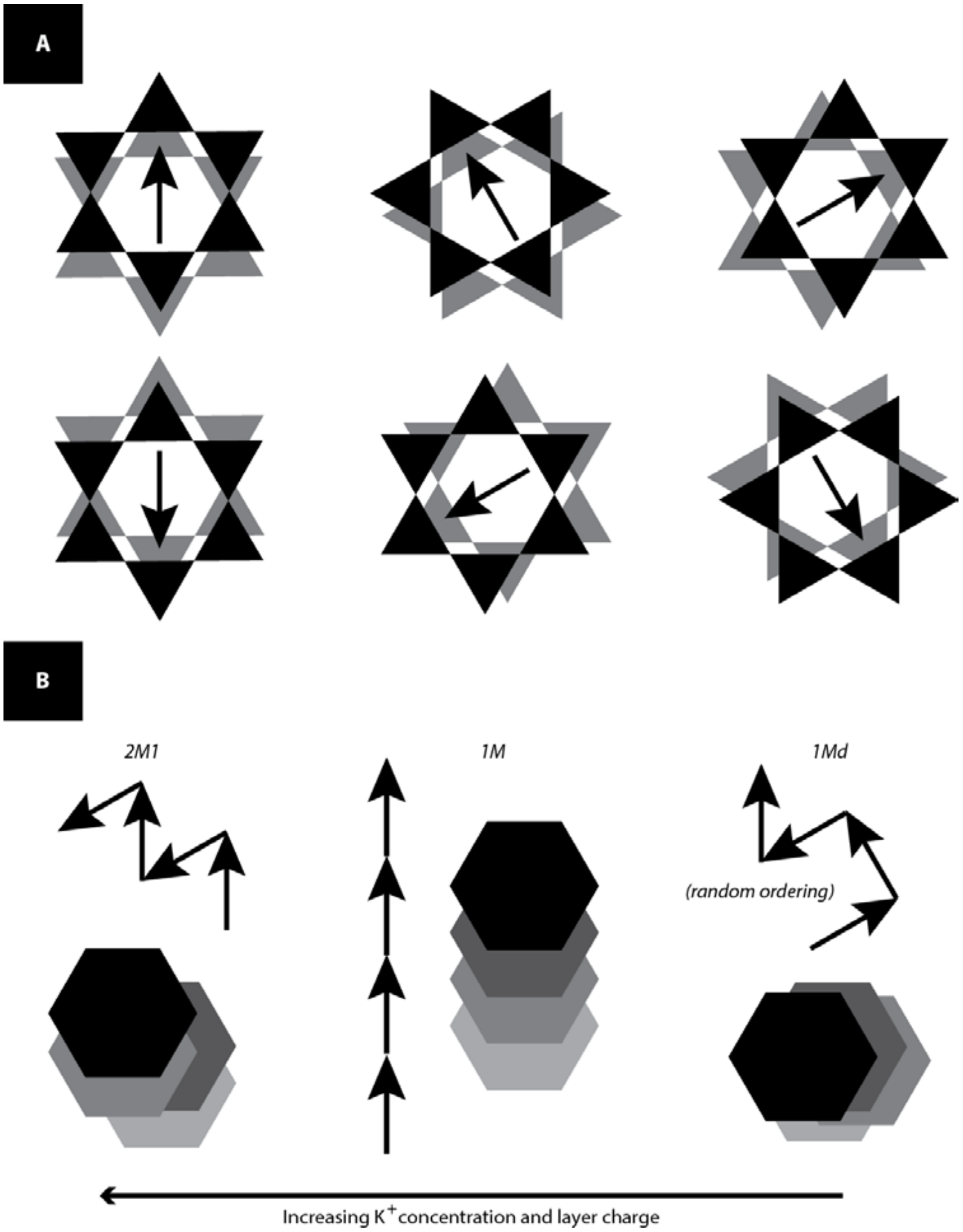

Figure I.II. A) The 6 possible shift vectors between the two tetrahedral sheets in a given TOT layer of illite. B) The three common polytypes of illite arranged by increasing stacking order complexity and K^+ concentration. This ordering also correlates to formation temperature.

unmixing the isotopic signals of co-existing populations (pre-existing clays and those related to deformation) is a prerequisite to their structural diagenetic interpretation. Fortuitously, several species of 2:1 layer type clay mineral exhibit forms of polytypism, a phenomenon that occurs whenever a given chemical compound exists in more than one structural form or arrangement. Polytypism is expressed in clay minerals as variations in layer stacking patterns. Chlorite, kaolinite, and illite all have common polytypes. Illite, a K-bearing phase useful for radiometric dating, has several polytypes (Velde and Hower, 1963). Well-ordered polytypes, such as 2M1, which display a long-range ordering structure, form at high temperature and are characteristic of detrital populations. Disordered illite polytypes (1Md), meaning clays whose layer ordering is more random, form at lower temperatures and are typically diagenetic or authigenic in nature. Figure I.II illustrates the layer stacking patterns of the most common polytypes of illite. These polytypes can be distinguished and their proportions quantified using X-ray diffraction (Grathoff and Moore, 1996; Ylagan et al., 2002). In addition to layer ordering, the different polytypes often differ in grain size, reflecting their distinct genesis; 2M1 polytype illite crystallites are much larger in size than the 1Md variety. These qualities allow the structural geologist to identify the signal of the illite population of interest—typically the authigenic population—that formed in response to brittle deformation in the crust.

I.I.III. Geochronology

As mentioned, illite is K-bearing, and can be used to date the timing of illite formation, and both K-Ar and ^{40}Ar/^{39}Ar geochronologic approaches have been used for this purpose (van der Pluijm et al., 2001; Hamilton, 2003; Clauer, 2013). The K-Ar system of illite is quite robust, with an Ar closure and resetting temperature of 300°C (Wijbrans and McDougall, 1986; Verdel et al., 2012). Issues regarding recoil effects due to small grain size, small sample amounts, and sample inhomogeneity have been addressed by encapsulation and the utilization of total gas Ar-Ar dating methodologies (Dong et al., 2000; van der Pluijm and Hall, 2015; Fitz-Díaz et al., 2016).

The Rb-Sr isotopic system also has a long tradition in clay mineralogy, and has been widely applied in the dating of clay minerals (Liewig et al., 1987; Mutlu et al., 2010). Finally, and somewhat less widespread as a technique, Sm-Nd geochronology has also yielded success in dating clay mineralization (Toulkeridis et al., 1994; Toulkeridis et al., 1998). These geochronometers can all be effective tools if the relevant signal corresponding to a well-characterized clay population can be isolated, and a link to deformation can be established.

I.I.IV. Geothermometry

Much literature exists that examines the temperature-dependent smectite-illite transition in sedimentary diagenetic environments (e.g. Burst, 1957; Hower et al., 1976; Pollastro, 1985; Pollastro, 1993; Huang et al., 1993; Altaner and Ylagan, 1997; Roaldset et al., 1998; Cuadros, 2006). Smectite, a low-temperature weathering product, is progressively converted to illite by the fixation of K^+ cations in the interlayer space in the following reactions:

If Al is considered a mobile element (Hower et al., 1976)

$$Eq\ I.I:$$

$$1\ smectite + K^+ + Al^{3+} \rightarrow 1\ illite + Na^+ + Ca^{2+} + Si^{4+} + Fe^{2+} + Mg^{2+} + H_2O$$

If Al is considered an immobile element (Boles and Franks, 1979)

$$Eq\ I.II:$$

$$1.6\ smectite + K^+ \rightarrow 1\ illite + Na^+ + Ca^{2+} + Si^{4+} + Fe^{2+} + Mg^{2+} + O^{2-} + OH^- + H_2O$$

This body of work represents the combined efforts of both academic and industrial research programs aimed at using clay mineralogy to predict subsurface temperatures in sedimentary basins, often with the application of predicting hydrocarbon generation and maturation of organic material within the sedimentary column. In addition to providing temperature information as an isotopic constraint, this mineralogical transition is thought to exert control over various structural processes, from growth fault distribution and generation to up-dip limits of seismicity in subduction zones (Bruce, 1984; Vrolijk, 1990; Moore and Saffer, 2001).

Chlorite is another species of clay mineral that is utilized as a geothermometer. Partitioning of Fe and Mg in chlorite in octahedral and tetrahedral cation sites is temperature-dependent. Several thermodynamic models have been developed to predict formation temperature from chlorite composition (Cathelineau, 1988; de Caritat et al., 1993; Inoue et al., 2009; Bourdelle and Parra, 2013). These models are based on various reactions including Fe and Mg exchange, the Tschermak exchange Si(Mg,Fe)=2Al, and dioctahedral to trioctahedral conversion X2Al=3(Mg,Fe) (Vidal et al., 2001; Vidal et al., 2005; Vidal et al., 2006).

Temperature-dependent phase stability of various species of clay minerals, including smectite and illite, can also provide important constraints on deformation-related clay mineralization. The process of smectite dehydroxylation and rehydration is temperature-dependent, and varies based on smectite composition (Wolters and Emmerich, 2007; Derkowski et al., 2012). Illite end-member compositions, polytypes, and interlayer structures have known thermodynamic stability fields (Aja et al., 1991; Pollastro, 1993; Yates and Rosenberg, 1997; Meunier and Velde, 2004). In addition, novel techniques such as temperature estimation based on Ar diffusion (Clauer et al., 1995) or B partitioning in illite-smectite (Williams et al., 2007) also provide insight into mineralization temperature conditions and the duration of thermal anomalies.

I.I.V. Stable Isotopic Systematics

The O and H in tetrahedral, octahedral and hydroxyl groups of clay minerals can be analyzed to understand the equilibrium fluid composition and temperature of mineralization. The two main controls that govern the fractionation behavior of stable isotopes of O and H in the natural environment are i) the difference between the masses of the isotopes and ii) the temperature at which the chemical reaction is taking place. The predominant physical law underpinning fractionation behavior of stable isotopes is that molecules containing a heavy isotope of an element are more thermodynamically stable than those containing only light isotopes of that element due to the decrease of molecular vibrational frequency associated with the increased molecular mass (Faure and Mensing, 2005). The changes of state associated with evaporation and condensation processes in the Earth's water cycle are described by mathematical relations, called the Rayleigh equations (Rayleigh, 1896), which predict that precipitation at the Earth's surface will form a linear data array with a fitted equation of $\delta D = (7.96 \pm 0.02)\delta^{18}O + 8.86 \pm 0.17$ (Rozanski et al., 1993). Figure I.III shows this meteoric water line, as well as the predicted ranges of various types

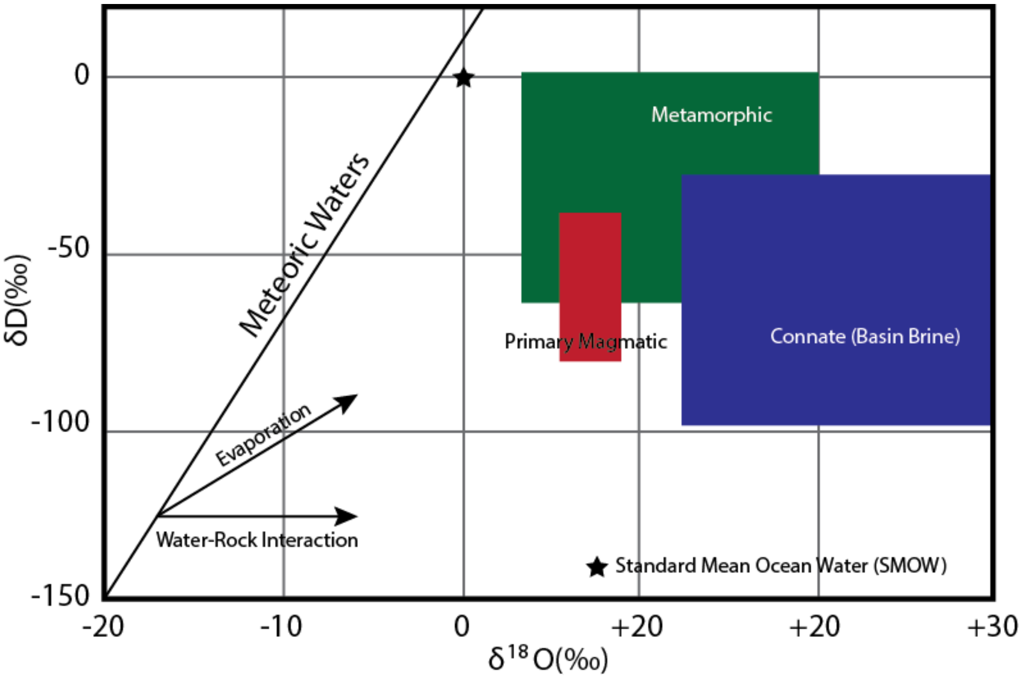

Figure I.III. O and H space (in δ notation) showing the range of meteoric water values and predictive compositional fields of various geologic origin.

of hydrous reservoirs in the earth. Meteoric water values become more negative with increasing latitude, increasing elevation and inland distance, and during geologic periods of ice house conditions when enhanced sequestration of light isotopes into polar ice caps occurs.

The systematics of these isotopes in clay-water systems have been subject to academic scrutiny since the 1960's (Sheppard et al., 1969; Savin and Epstein, 1970; Lawrence and Taylor, 1972; Sheppard and Gilg, 1996). A decrease in the environmental temperature corresponds to an increase in the magnitude of the fractionation between the mineral and the aqueous solution; however, the equations that relate isotopic fractionation to temperature have opposite slopes for H and O (figure I.IV). Low equilibrium temperatures in the clay-water system lead to a depletion of the heavy H isotope, whereas in the case of O the mineral phase is enriched in the heavy isotope (Delgado and Reyes, 1996).

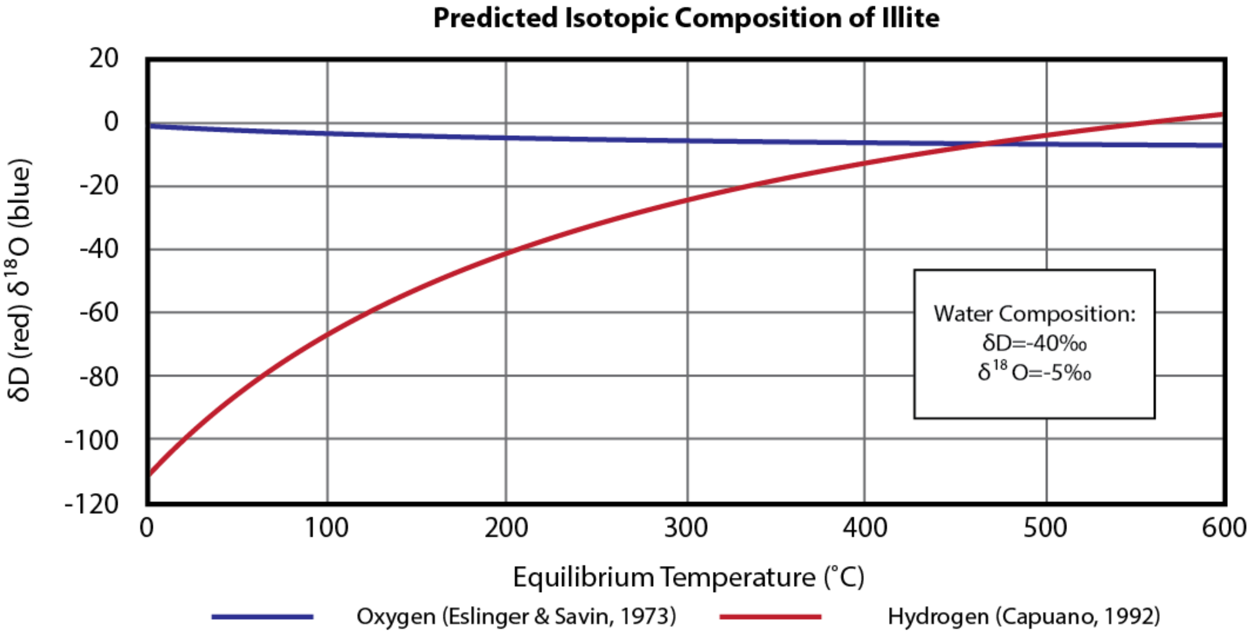

Figure I.IV. O and H isotopic composition of illite across a range of temperatures when in equilibrium with water of δD=-40 and δ^{18}O=-5.

These isotopic systems are robust, and remain resistant to post-crystallization isotopic exchange up to pressure-temperature-chemical conditions of their formation (Savin and Epstein, 1970; Morad et al., 2003). The low formation temperature of authigenic illite followed by geologically immediate exhumation along a fault means that the history of the authigenic material would be one of less extreme temperature and pressure conditions than that of formation. At temperatures <100ºC, the rates of recrystallization (which would lead to resetting of ages) are much slower than H isotopic re-equilibration, so they would be expected to retain an old signal if the clays themselves are old (Kyser and Kerrich, 1991). A test of post-crystallization isotopic resetting is the linearity of the mixing lines created during illite polytype analysis. A grain-size dependent process like H diffusion would likely create a parabolic curve in these mixing lines, with smaller size fractions being more effected by re-equilibration than larger size fractions. The mixing lines in this dissertation do not exhibit parabolic behavior; they are highly linear with R^2 often >0.9.

Workers have described the O and H fractionation behavior using codified equations for chlorite (Wenner and Taylor, 1971; Graham et al., 1987), illite (Eslinger et al., 1979; Suzuoki and Epstein, 1976; Capuano, 1992), smectite (Yeh and Savin, 1977; Yeh, 1980) and several other clay minerals. A combination of two of the three following variables, equilibrium temperature, stable isotopic composition of the crystal, or stable isotopic composition of the mineralizing fluid can predict the third variable. This provides a powerful tool in gaining an understanding of deformation-related fluid provenance and pathways when studying synkinematic clay minerals.

I.I.VI. Fabric Analysis

The three-dimensional arrangement of clay minerals in the spatial context of a deformed rock has implications for microstructural processes and mineral nucleation and growth. X-ray texture goniometry is a technique that utilizes transmission-mode diffractometry on thick sections of intact clay-rich material to quantify the crystallographic preferred orientation of minerals (van der Pluijm et al., 1994). This approach has been utilized, among other things, to characterize the fabric intensity across the damage zones of faults (Vrolijk and van der Pluijm, 1999; Solum, 2003; Schleicher et al., 2008; Haines et al., 2013; Schleicher et al., 2015b), to investigate the development of preferred orientation during diagenesis (Day-Stirrat et al., 2011; Day-Stirrat et al., 2008), and to characterize the fabric of post-failure mass transport deposits (Day-Stirrat et al., 2013).

I.I.VII. Physical Properties

Byerlee’s law predicts that Earth materials have a narrow range of coefficients of frictional sliding; ~0.6-0.85 (Byerlee, 1978). The sliding behavior of most faults can be explained by a coefficient of friction in this range and a geometric configuration where the fault is in an ideal orientation with respect to the stress field (see Faulkner et al., 2010 and references therein for recent review). Some faults, however, are thought to be “weak” because they slip outside of these bounds of Byerlee’s law. Two well-known examples of weak faults include the San Andreas Fault of California and the class of faults known as low-angle normal faults (LANFs). One solution to the weak fault paradox is to increase the fluid pressure within the fault zone to lower the effective normal stress;

another solution is to lower the frictional coefficient of fault materials to allow it to slide more easily. Studies of the frictional behavior of phyllosilicates indicate that several phases have coefficients of friction much lower than predicted by Byerlee's Law, as low as μ=0.2 (Morrow et al., 1982; Saffer et al., 2001; Saffer and Marone, 2003; Ikari et al., 2009; Carpenter et al., 2011). Specifically, in the San Andreas Fault Zone, evidence has accumulated that suggests that interconnected networks of weak phyllosilicate material dominates the weakening of the fault (Holdsworth, 2004; Collettini et al., 2009; Schleicher et al., 2010). Clay minerals in gouge zones and cataclastic fault rock lithologies can help explain, understand, and predict mechanical behavior of brittle structures. Understanding the mineralogy of such critical zone clays is key to understanding the spatial, temporal, compositional, and thermal limits to deformation processes.

I.II. Outline of Dissertation

This dissertation comprises a suite of studies that, although geographically unrelated, apply aspects of clay mineralogy to solving structural problems. They focus on well-known and societally important faults and sedimentary basins such as the Alpine Fault (New Zealand), the North Anatolian Fault (Turkey), the Japan Trench subduction zone, the Appalachian Basin, and the San Andreas Fault Zone (California). Many of these locations are at-risk from a geohazards perspective, or are important provinces for geologic resources.

I.II.I Chapter II. Quantitative X-ray Diffraction and the Illite Polytype Analysis Method: A Comparison of Analytical Techniques

Chapter II, submitted to *Clays and Clay Minerals* as Boles, Schleicher and van der Pluijm, presents a new methodological summary of the illite polytype analysis method. It introduces advances on prior approaches by using Rietveld-based quantitative X-ray powder diffraction for polytype characterization. The study compares the effectiveness of various polytype quantification techniques, and acts as a laboratory guide for new practitioners of the illite polytype analysis method. It is presented near the front of this dissertation, because illite polytype analysis is an approach utilized in subsequent dissertation chapters.

I.II.II. Chapter III. Clays in the Exhumed Alpine Fault Zone (New Zealand) are Late Surface Alteration

Chapter III, to be submitted to *Journal of Structural Geology*, addresses the presence of significant volumes of fault-hosted clay mineralization along the surface trace of the Alpine Fault Zone on New Zealand's South Island. Paradoxically, studies of the physical properties of the clay-rich gouge material indicate less-than-Byerlee frictional fault strength (characteristic of a “weak” fault) in a region of very high topography that is known for large magnitude seismic events. Electron microscopy, chlorite chemical geothermometry, and H isotopic characterization in this study help distinguish between different populations of clay minerals and suggest that surface and subsurface fault zone processes may be independent and differ significantly. This study highlights the need for further attempts at scientific drilling, following two near-surface drilling phases, to investigate the nature of this plate-bounding fault at seismogenic depths.

I.II.III. Chapter IV. Response of Natural Smectite to Seismogenic Heating and Potential Implications for the 2011 Tohoku Earthquake in the Japan Trench

Chapter IV, published in *Geology* as Schleicher, Boles and van der Pluijm in 2015, invokes the temperature-dependent dehydration behavior of smectite in a study of sheared principal slip zone gouge material involved in the 2011 M9.0 Tohoku earthquake. This plate-bounding subduction event featured ~50 m of coseismic displacement at Earth’s surface and was associated with a disastrous tsunami. The clay-rich gouge material used in this study was recovered in the fast-response scientific drilling effort J-FAST in 2012. We use novel X-ray based heating experiments on the smectite-rich gouge to put an empirical limit of <200°C on coseismic frictional heating in contrast to estimates >1000°C based on minor thermal perturbations in downhole thermal array measurements.

I.II.IV. Chapter V. Hydrogen and ^{40}Ar/^{39}Ar Isotope Evidence for Multiple and Protracted Paleofluid Flow Events within the Long-Lived North Anatolian Keirogen (Turkey)

Chapter V, published in *Geochemistry, Geophysics, Geosystems* as Boles, van der Pluijm, Mulch, Mutlu, Uysal and Warr (2015), presents isotopic evidence that indicates long-term, surface-derived fluid infiltration to upper mid-crustal depths into the damage zone of the long-lived North Anatolian Fault system. Ar-dating of illite shows a terrane-accretion type construction of northern Anatolia, identifying deformation pulses that include emplacement of ophiolites. Today’s transform fault, in this model, utilizes pre-existing weaknesses at terrane boundaries in its present geometry.

I.II.V. Chapter VI. Triassic, Surface-Fluid Derived Clay Diagenesis in the Appalachian Plateau, Northern U.S. Midcontinent

Chapter VI explores the linked deformational and diagenetic history of the Paleozoic cover sequence that overlays much of the North American midcontinent, using the lens of clay mineralogy. X-ray texture goniometry of illite establishes an association between diagenetic fabrics and Appalachian deformation, and indicates a progressive increase in strain toward the orogenic core. Illite is also used in polytype analysis, Ar-dating, and H isotopic analysis. After correcting for erosion and depth of burial by using conodont alteration index temperature zones, the stable isotopic results exhibit a typical orogenic rain-shadow pattern at mid-latitudes. Using Ar ages, we argue that this signature in diagenetic illite is related to tectonic stress regime change from contraction to extension. The results contradict the reigning orogenic fluid flow hypothesis, which advocates for far-travelled, tectonically-activated fluid flow into foreland basins of an evolving orogen.

I.II.VI. Chapter VII. Conclusions

Chapter VII summarizes the conclusions of this dissertation and draws together several meaningful contributions of each chapter in order to highlight the broader impacts of studying clay minerals as they relate to deformation processes.

I.II.VII. Appendix I. Timing of Crustal Accretion and Eastern Black Sea Rotation from Fault Dating of Thrusts within the Istanbul Zone, Western Turkey

Appendix I provides clay characterization for the future dating of brittle faults in the Istanbul Paleozoic terrane in order to answer questions pertaining to the tectonic history of this anomalous crustal block. Constraints on the historical extent of neotectonic strain in the highly populated Istanbul area would provide insight into the mechanics of the North Anatolian Fault Zone and allow for more robust geohazard risk assessment and mitigation. This work represents a collaboration between Semih Can Ülgen and Celal Şengör of the Department of Geological Engineering at the Istanbul Technical University, and laboratories at the University of Michigan.

I.II.VIII. Appendix II. Pseudotachylyte and Fault Gouge Dating of Mai'iu and Gwoira Faults Constrains the Late-Stage Exhumation Timing of the Dayman Gneiss Dome, Eastern Papua New Guinea

Appendix II, in collaboration with Timothy Little at the University of Victoria, Wellington (New Zealand), presents the first attempt to date friction melt and fault gouge from brittle structures involved in the exhumation of a low-angle normal fault and associated gneiss dome. The existence and origin of such structures remains controversial, and controls on exhumation rates and the timing of deformation are key pieces of information required to gain an understanding of regional kinematics.

I.II.IX. Appendix III. Meteoric fluid Cycling Recorded by Authigenic Illite in Clay-rich Zones of the San Andreas Fault Observatory at Depth (SAFOD) Borehole

Appendix III utilizes illite polytype analysis on clay mineral-bearing zones of the San Andreas Fault Observatory at Depth (SAFOD) borehole to investigate the nature of the fault-hosted mineralization fluid. Unique aspects of the San Andreas Fault gouge zone mineral assemblage and chemistry engender questions about fluid provenance, solute load, and heat transport characteristics of the fault. Notably, the H isotopic composition of both authigenic chlorite and illite minerals shows a significant surface-derived fluid component at depths >3 km. In addition, a methodology is presented to help account for non-illitic hydrous phase stable isotopic signals when using illite polytype analysis.

Chapter II. Quantitative X-ray Powder Diffraction and the Illite Polytype Analysis Method: A Comparison of Analytical Techniques

II.I. Abstract

This study presents a comparison of various quantitative X-ray powder diffraction (Q-XRPD) methodologies for practical application in the illite polytype analysis method. Q-XRPD results of WILDFIRE© modeling, End-member Standards Matching and Rietveld whole-pattern matching (BGMN®) are considered using both synthetic mixtures and natural fault gouge. Grain size aliquots of gouge were additionally investigated by Transmission Electron Microscopy (TEM) for polytypism, as well as laser particle size analysis for grain size distributions. End-member mixing plots illustrate the effectiveness of each method and indicate that the three analytical techniques produce similar results, but quantification of uncertainty is considerably better constrained by the Rietveld method. The application of illite polytype analysis to ^{40}Ar/^{39}Ar geochronology exhibits the full utility of the method.

II.II. Keywords

Illite, quantitative X-ray powder diffraction, Rietveld method, Transmission Electron Microscopy, fault gouge dating

II.III. Introduction

The illite polytype analysis method has been central to the dating of low-temperature deformation structures (see van der Pluijm and Hall, 2015 for recent review) and to the elucidation of the provenance of deformation-related fluids in the upper crust (Boles et al., 2015). A key step underpinning this method is the accurate identification and quantification of illite polytypes. The term illite, *sensu stricto*, does not refer to a single mineral, but rather a family of potassium- and aluminum-bearing mica-like, 1 nm basal-spacing dioctahedral minerals. It is non-expanding and has a 2:1 mica structure with a tetrahedral-octahedral-tetrahedral (TOT) sheet sequence.

Polytypism is expressed as differences in TOT layer stacking patterns, with 1M, 1Md (turbostratic), 2M1 and 3T polytypes having been identified. 3T is uncommon in nature, and often confused with the 1M *cis*-vacant variety (Reynolds and Thomson, 1993). Figure II.I is a comparison of model X-ray diffractograms, using WILDFIRE© generated end-members, of the three most common polytypes of illite. This figure illustrates the rationale behind using X-ray diffraction as a diagnostic tool to quantify relative proportions of illite polytypes in natural samples, as it emphasizes that the *hkl* reflections of each polytype are quite distinct. Indeed, using illite polytypism as a proxy for population provenance is the basis of the method.

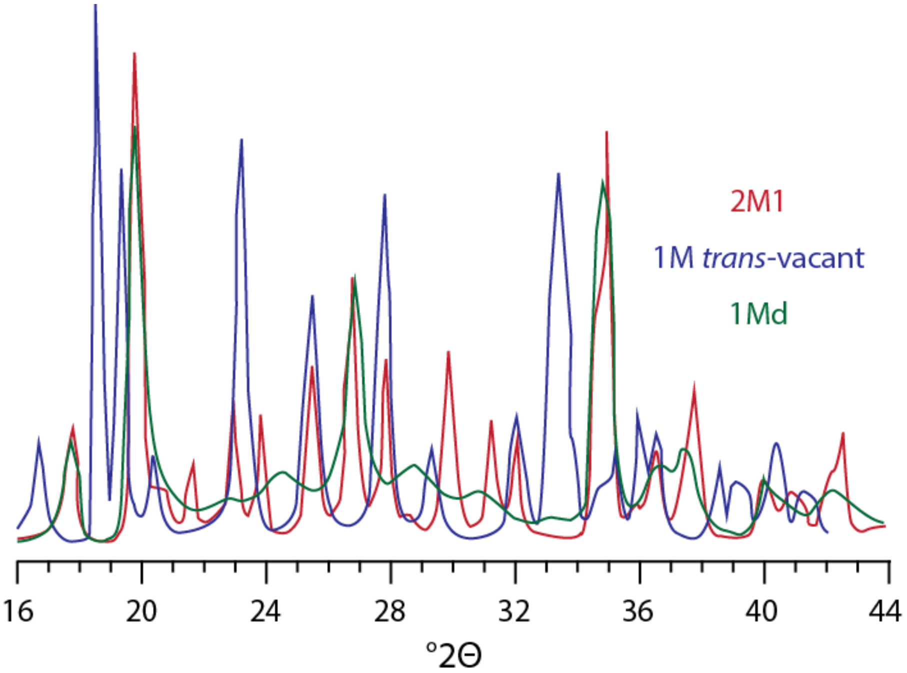

Figure II.I. WILDFIRE© generated X-ray diffractograms of three illite polytype end-members, illustrating the use of X-ray analysis to distinguish between various polymorphs of the mineral series.

In practice, natural samples are most often observed with two polytypes: 1Md and 2M1. The justification for a two end-member system lies in the observation that the formation of 1M illite requires compositional anomalies that do not occur in a normal prograde diagenetic/low-grade metamorphic sequence from 1Md to 2M1 (Peacor et al., 2002). This is further supported by the argument of Moore and Reynolds (1997) that 1M and 1Md polytypes likely have separate diagenetic paths to 2M1, instead of a 1Md->1M->2M1 path proposed by others. Observations from fault zones of various types show that the disordered polytype prograde series 1Md->2M1 is the predominant one in low-temperature, open system, near-surface environments (Solum et al., 2005; Haines and van der Pluijm, 2012; Hnat and van der Pluijm, 2014).

Early workers recognized a positive correlation between age and grain size in illite-bearing rocks (Hower et al., 1963), and this observation precipitated attempts to use these K-bearing micas as a geochronometer in natural systems (e.g. Hoffman et al., 1976; Covey et al., 1994). Separating the clay size fraction into a range of grain size aliquots yielded a positive correlation between grain size and age, which, by unmixing, could be extrapolated to end-member values, giving way to the main application, illite dating. The illite polytype analysis method has been used to date low-temperature, diagenetic illite in sedimentary basins or synkinematic illite growth associated with localized deformation in the brittle crust (Pevear, 1992; van der Pluijm et al., 2001; Dong et al., 2000). This methodology circumvents the obstacle of being unable to physically isolate diagenetic/authigenic illite from detrital illite in order to obtain crystallization ages of the secondary population.

Advances in the application of the method have included dating of more distributed deformation in folds of low metamorphic grade (Fitz-Diaz and van der Pluijm, 2013) and constraining paleo-hydrologic reservoirs and pathways using hydrogen isotopes (Boles et al., 2015; Haines et al., 2016). Additionally, Warr et al. (2016) proposed a similar age analysis technique to date smectite formation. Clauer et al. (2013) compared K/Ar and Ar/Ar geochronologic methodologies as used in illite age analysis and concluded that Ar/Ar dating has greater potential ability to date tectono-thermal activities and to deal with mixtures of multiple populations of illitic material due to the fine grain size and limited volumes of sample inherent to such studies. The conditions in shallow crustal settings are ideal for the use of illite polytype analysis as the mineralization temperatures of authigenic or diagenetic illite formation are likely the highest temperatures experienced by the rock before exhumation. Constraints on this temperature-time history of a natural sample are critical, first to ensure that high enough temperatures were reached in order to allow neocrystallization, and, second, because thermal resetting of the argon geothermometer in mica occurs >300°C (Wijbrans and McDougall, 1986; Verdel et al., 2012) and illite is resistant to stable isotopic re-equilibration at P-T conditions lower than that of formation (Savin and Epstein, 1970; Morad et al., 2003).

Various Q-XRPD methodologies constrain proportions of illite polytypes, following the tradition of Velde and Hower (1963) and Maxwell and Hower (1967). These all rely on a comparison of the relative diffracting power of the present phases. Some techniques compare characteristic peaks directly (Tettenhorst and Corbató, 1993; Dalla Torre et al., 1994) while others compare natural samples to synthetic diffraction patterns using forward model algorithms, such as NEWMOD© or WILDFIRE© (Reynolds, 1993; Grathoff and Moore, 1996; Ylagan et al., 2002; Haines and van der Pluijm, 2008). These efforts have used both mathematical and graphical methods to optimize fits between the model and natural samples. Similar to the graphical matches of simulated patterns, workers have mixed end-member polytype standards with good success (Boles et al., 2015). Others still have proposed crystal thickness distribution analysis by HRTEM or XRD (Uhlík et al., 2000; Dudek et al., 2002). Whole-pattern matching Rietveld analysis is a recent advance on the method, and represents a more inclusive approach to quantification that also allows more diverse compositions.

We contrast quantifications of the 1Md/2M1 polytype ratio for synthetic mixtures using i) models in a WILDFIRE© generated library ii) using end-member standards and iii) using Rietveld analysis. This paper describes the utility of these three Q-XRPD techniques as used in practical application of illite polytype quantification; it also aims to be a laboratory guide for practitioners that are new to this field. The first three sections introduce the samples used in the study, outline each Q-XRPD methodology, and present illustrative examples of TEM and X-ray analysis. The fourth section compares the results of the three Q-XRPD approaches by applying age analysis to a natural fault gouge sample. The manuscript concludes with a discussion of uncertainty estimates and with recommendations about the applicability of these Q-XRPD techniques in various circumstances.

II.IV. Sample Description

Samples were selected to illustrate the workings of the illite polytype analysis method in its variety of forms. Synthetic mixtures of 1Md and 2M1 illite, spiked with kaolinite as an interference phase are used as a control. A natural fault gouge sample was chosen to illustrate Ar/Ar geochronologic analysis as an application of the methods. Mineral standards were used to create the synthetic mixtures and for end-member matching. The 1Md standard used is the 0.05-0.2 μm size fraction of Clay Minerals Society standard IMt-1 from Silver Hill, Montana, USA. This size fraction was chosen because it is free from peak overlap of non-illite phases. The 2M1 standard used is the <2 μm fraction of pure muscovite from the Minas Gerais province of Brazil. The kaolinite standard used is the <2 μm fraction of the American Petroleum Institute reference sample series H-1 kaolinite from Murfreesboro, Arkansas, USA (http://www.clays.org/Sourceclays.html). Three synthetic mixtures were created using varying proportions of these standards. Synthetic mixture 1 (hereafter referred to as SM1) contains 25% kaolinite, 25% 1Md illite, and 50% 2M1 illite by weight. Synthetic mixture 2 (hereafter referred to as SM2) contains 25% kaolinite, 50% 1Md illite, and 25% 2M1 illite by weight. Synthetic mixture 3 (hereafter referred to as SM3) contains 10% kaolinite, 80% 1Md illite, and 10% 2M1 illite by weight. The fault gouge sample was collected from the surface trace of the North Anatolian Fault Zone near Gerede, Turkey and is identified as sample G2 (see Boles et al., 2015). G2 was separated into four grain size aliquots, as described in section IV (below): 2.0-1.0 μm (coarse), 1.0-0.2 μm (medium), 0.2-0.05 μm (fine), and <0.05 μm (very fine).

II.V. TEM Polytype Characterization and Grain Size Distribution Analysis

In order to confirm a 1Md-2M1 illite polytype end-member system, and to gain an understanding of illite population distributions across the grain size aliquots, we investigate the natural fault gouge sample G2 by Transmission Electron Microscopy (TEM) and laser particle size analysis.

Transmission Electron Microscopy work was conducted at the GFZ Potsdam using a FEI Tecnai G2 F20 X-Twin transmission electron microscope (TEM/AEM) equipped with a Gatan Tridiem energy filter, a Fischione high-angle annular dark field detector (HAADF), and an energy dispersive X-ray analyzer (EDS). The powdered samples were oriented, impregnated and prepared with a focused ion beam (FIB) device (FEI FIB200TEM; for more detailed information see Wirth, 2009).

The TEM investigation of the coarse size fraction of sample G2 provides direct imagery of both 1Md and 2M1 illite polytypes (figure II.II). Light- and dark-field images show a plate-like morphology of the illite crystallites that tapers toward the edges, in addition to accessory phases such as quartz. Lattice-fringe images and SAED diffraction patterns clearly distinguish between well-ordered 2M1 and disordered 1Md, with the poorly ordered illite exhibiting streaking of non-001 reflections. These images clearly confirm a 1Md-2M1 polytype system.

Laser particle size analysis of multiple aliquots of sample G2 was conducted at the University of Potsdam using a Sympatec HELOS BR laser diffraction analyzer with a measuring zone for the insertion of dry/wet dispersers or sample couplers for particle sizes between 0.1 to 875 μm. Figure II.III displays grain size abundance histograms for select grain size aliquots of sample G2. The finest size fractions were outside the resolution of the instrument, and therefore could not be

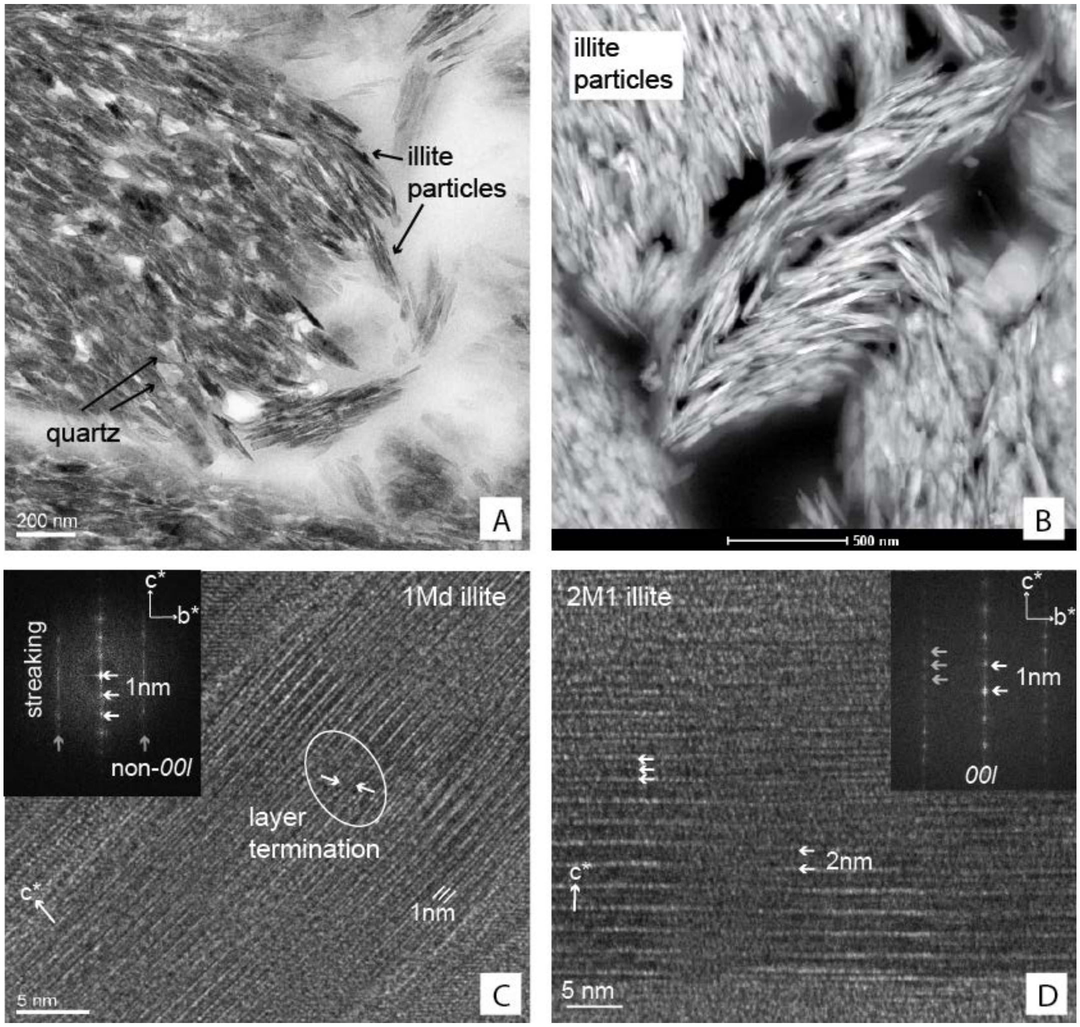

Figure II.II. A) TEM bright-field image of a SEM-FIB (scanning electron microscopy-focused ion beam) cut of impregnated illite particles. The image shows mostly very thin 1Md illite crystals together with small quartz grains. The particles get thinner toward the ends.
B) In this TEM dark field image, the average length of the illite packages is ~250nm, whereas the thickness is less than 50nm.
C) The lattice-fringe image of subparallel illite packets obtained along [hk0] indicates defects in the 1Md illite. Layer termination is marked in a circle with arrows. The SAED pattern contains well-defined 00l reflections with a lattice distance of 1nm (white arrows), and streaking of non-00l reflections (gray arrows), indicating the disordered 1Md stacking sequence.
D) Lattice fringe image of a 2M1 illite obtained along [hk0] showing TOT sheets represented by up to four lines, and the interlayer region presented by the brightest line (marked with arrow). In the SAED pattern, non-00l reflection dots are caused by ordered stacking of layers (gray arrow), and 00l reflections (white arrows) have a lattice distance of 1nm.

compared. The local maximum near 3 μm of the coarse grain size histogram, as well as the positively skewed tails of all histograms likely indicate the presence of coarser, non-clay minerals

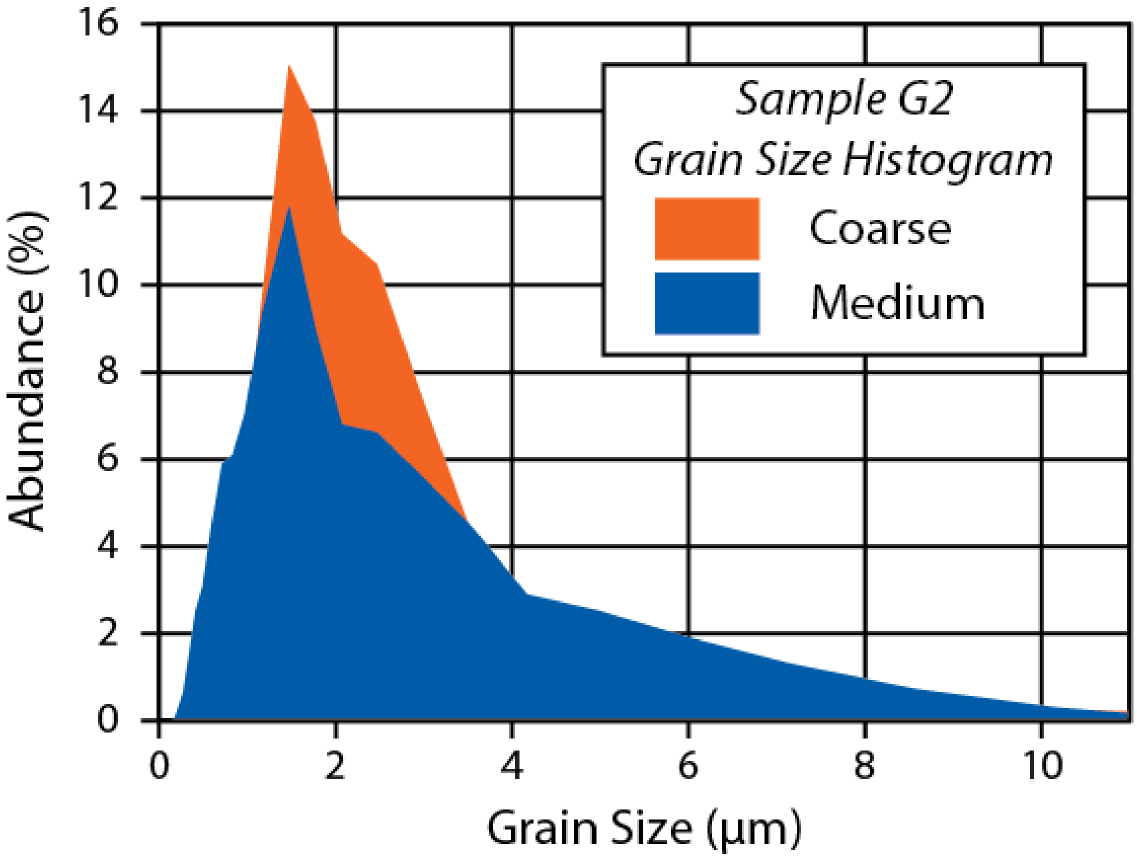

Figure II.III. Grain size histograms for G2-C and G2-M size aliquots. Local maxima at ~1 µm and between 1-2 µm indicate the presence of two distinct populations of clay minerals, likely of detrital and authigenic origin.

in these aliquots. This is corroborated by TEM imagery and Q-XRPD. A significant maximum between 1-2 µm likely represents coarse, detrital clay minerals, with a more subtle peak with a position ~1 µm in the medium grain size fraction representing the authigenic mineral population; indeed, the TEM light and dark field images of sample G2 show 1Md crystallites on that same length scale. We posit that the grain size separations do not therefore represent a continuous array of grain sizes with Gaussian distributions, rather that two dominant grain sizes, one composed of detrital grains and the other of authigenic, are mixed in various proportions in the different grain size aliquots. We believe that this is representative of most low-temperature mineralizing environments in the brittle crust.

II.VI. X-ray Analysis

Having imaged both 1Md and 2M1 illite in sample G2, and a dual grain size system, we use three Q-XRPD techniques (WILDFIRE© modeling, end-member standards matching, and Rietveld refinement using BGMN®) to quantify the relative abundance of 1Md and 2M1 in the fault gouge. In this section, sample preparation and qualitative assessment are discussed, and a detailed presentation of each quantitative methodology is included. Results from the analysis of synthetic samples are included to contrast the application of each technique.

II.VI.I. Sample Selection, Preparation, and Instrument Configuration

The most significant effort required in the illite polytype analysis process, in terms of time intensity, is the proper selection and characterization of a natural, mixed-phase sample in order to assess its suitability for further isotopic analysis. The steps here outlined are prerequisite to any isotopic study, and demand the bulk of the laboratory activity associated with the method. Having taken care in the field to collect mudstone or fault gouge samples from beneath the surface to be as free from surface alteration as possible, each sample is hand-crushed by percussion to avoid diminution or induced strain in the crystals in an agate mortar and pestle; the use of ceramic tools can be a source of clay contamination. Disaggregation by freeze-thaw cycles or using electrical disaggregation can also be non-damaging techniques (Liewig et al., 1987; Fujita et al., 2001). The sample is dispersed in de-ionized water using an ultrasonic bath for 5-15 minutes (the presence of dissolved solids could encourage clay mineral formation or exchange, cf. Harder, 1974). It can be washed, if needed, to remove salts. Sodium pyrophosphate, or a similar dispersant, can be added to neutralize surface charge and inhibit flocculation, but the total amount of dispersant should be <0.5 weight percent of the sample to prevent crystallization of sodium salts, such as nahcolite or nitratine, in the fine fractions that may lead to peak overlap or impair efforts to control clay orientation in later preparations for X-ray analysis.

An oriented slide of the bulk clay fraction of each sample can be analyzed as a first pass to identify candidate samples for grain size separation. Figure II.IV highlights the diagnostic 003+022 peak at ~27°2θ (for CuKα radiation) that is used. The *hkl* peaks, characteristic of an individual polytype, will not be present in such an oriented scan, as they require random preparations and longer scan times. Well-crystallized illitic material will have a narrow, sharp peak, in contrast to the broader peak of a disordered crystal structure. Furthermore, a background hump will be present in disordered samples; indeed, the greater the hump, the more disorder. Those samples with the most disorder are selected for further processing with the intention of creating grain size aliquots with a large spread of 1Md/2M1 ratios. The blue diffraction pattern shown in figure II.IV exhibits the most disorder, while the red diffraction pattern exhibits the least disorder. Both have the potential

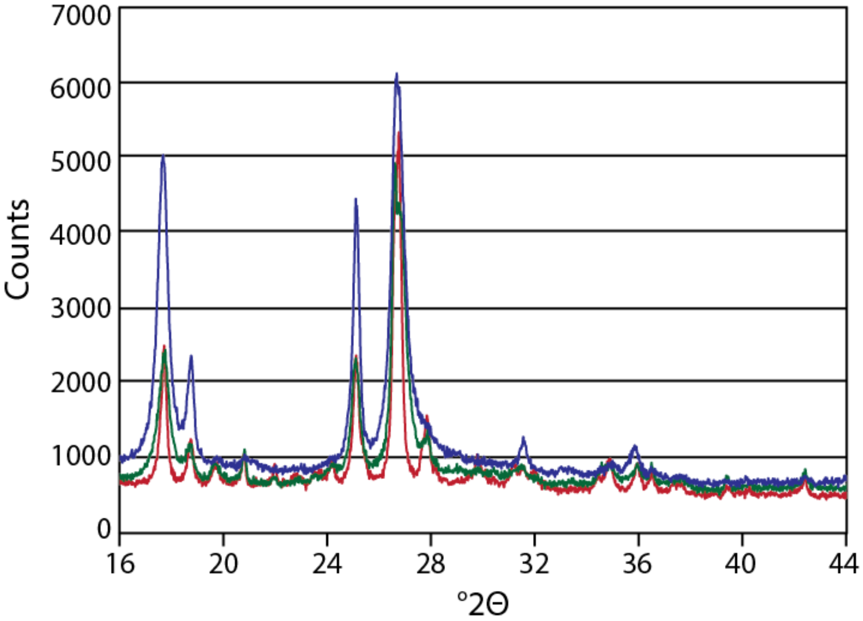

Figure II.IV. Diffractograms of three natural, illite-bearing samples showing increasing relative amounts of disorder in the illite structure, as seen in the 003+022 peak at ~27°2θ (for CuKα radiation). Samples ordered by increasing amounts of disorder are as follows: red, green and blue.

to be adequate samples for illite polytype analysis, but the sample with more disorder has a greater likelihood of having higher proportions of 1Md illite when separated into fine grain sizes, thereby improving statistical uncertainties during correlation and unmixing. This preliminary analysis can aid in selection of candidates for the full grain size separation as described below.

The clay-size fraction is extracted from the bulk rock using Stoke's Law. Gravity separation of particles down to 2µm are more effective as a first step than centrifugation in removing accessory minerals such as quartz, feldspar, calcite and oxides. We attribute this observation to the spherical particle shape assumption in Stoke's Law, with clay minerals settling more slowly due to their platy crystal habits. A centrifuge is used in further grain size separation into the various aliquots of clay-sized material needed for the method. The United States Geological Survey published procedural guides for clay separation by both gravity separation and centrifugation (Poppe et al., 2001).

The number of the clay-sized aliquots is not a trivial consideration, given the subsequent isotopic analysis of each aliquot and the significant cost of such isotopic techniques, but enough grain sizes (typically 3-6) should be separated to create a robust mixing line for multivariate regression analysis. The absolute grain size of these aliquots, however, is less important, with the result being the creation of various size fractions, each with a unique ratio of 1Md/2M1. Care should be taken to dry each aliquot in a fume hood or oven at temperatures <50°C to prevent the possibility of stable isotopic re-equilibration. Pyrex trays are convenient drying containers and the dried clay can be removed using a razor blade and gently re-powdered with an agate mortar and pestle. Alternatively, Millipore® filter products are useful for vacuum filtration for washing samples that contain salts, extracting clays from suspension for quick analysis or for quantitative preparation (Moore and Reynolds, 1997).

X-ray analysis in this study was conducted on a Rigaku Ultima IV diffractometer used in Bragg-Brentano geometry, with CuKα radiation, operated at 40 kV and 44 mA, and located at the Electron Microbeam Analysis Laboratory (EMAL) at the University of Michigan. Testing of the Rietveld results was conducted by analysis of the same samples on a PanAlytical Empyrean diffractometer at the Helmholtz-Center Potsdam, GeoForschungsZentrum (GFZ), with CuKα radiation and operated at 40 kV and 40 mA. For help optimizing optics, consult a reference text such as Jenkins and Snyder (1996).

II.VI.II. Qualitative Phase Assessment

Key to any of the Q-XRPD methods outlined below is a robust qualitative X-ray phase characterization of a <2 μm, oriented sample, which may include, but is not limited to, the following treatments: ethylene glycolation, high temperature treatment, acid treatment, cation exchange, clay interstratification and ordering estimation, etc. Care should be taken to set aside an aliquot of sample for isotopic analysis before any acid treatment, as the effect of acid on the stable isotopic composition of clays remains uncertain, although Clauer et al. (1993) showed that acid treatment has negligible effect on K/Ar systematics. In this study, oriented slides made by air-drying an aqueous suspension, such that sample density is 5 mg/cm^3, are used for qualitative analysis. Qualitative measurements were collected from 2-80°2θ, with a step size of 0.05°2θ, a 1 degree/minute scan rate and open divergence and receiving slits. Further treatment of clay preparations and characterization techniques are outlined in Brindley and Brown (1980) and Moore and Reynolds (1997).

Figure II.V shows X-ray diffraction patterns for the clay-sized fraction (<2.0 μm) of fault gouge sample G2 in air-dried and ethylene-glycolated conditions. The glycolated condition shows minor swelling behavior of the chlorite phase, likely with an *R0* chlorite (0.8-0.9)/smectite ordering structure, and the presence of discrete chlorite. The absence of interlayer smectite in illitic material is confirmed. Illite and chlorite are the major clay minerals present in the sample. Further qualitative assessment of sample G2 indicates the presence of quartz and calcite.

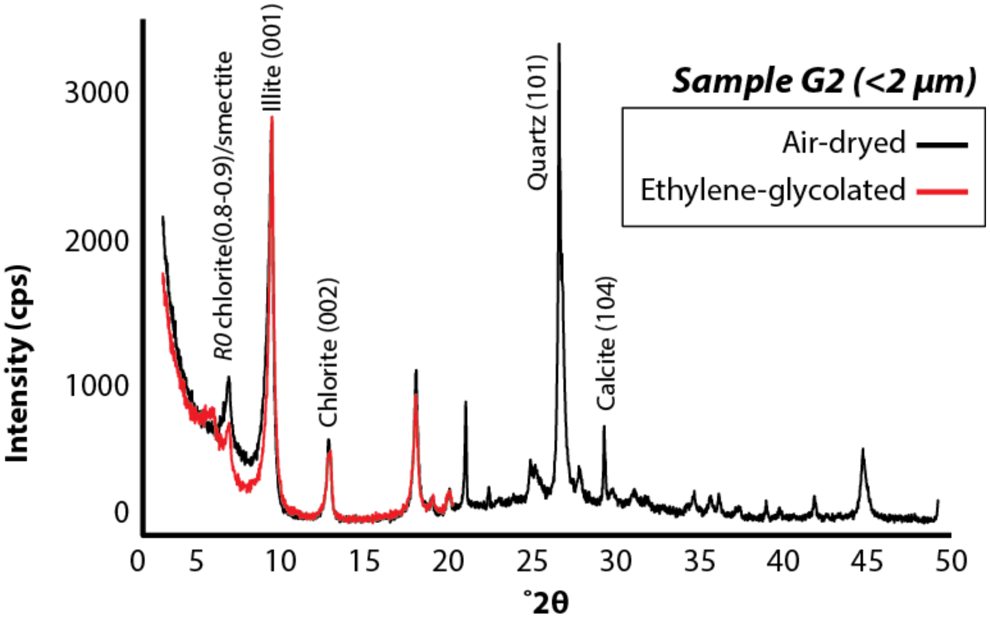

Figure II.V. Qualitative analysis of oriented X-ray diffraction patterns of sample G2 in air-dried and ethylene glycolated conditions indicates the presence of illite and chlorite clay minerals.

II.VI.III. Q-XRPD

The central tenet of any Q-XRPD technique is that the relative diffracting power of a phase is proportional to its abundance. General theory and considerations for Q-XRPD have been thoroughly examined in many books and articles, and we refer the reader to those comprehensive works for fuller treatment. The following consider many clay-specific problems: Bish et al. (1989), Bish and Reynolds (1993), Bish (1993), Bergmann et al. (1998), Hillier et al. (2000; 2003), Środoń et al. (2001), Środoń (2002), Omotoso et al. (2006). Mentioned here are two important aspects of preparation that are imperative to accurate quantification, i) achieving a random distribution of particles, and ii) ensuring constant X-ray absorption volume across all °2θ. Several preparation techniques have been developed to try to induce randomness into a powder sample that is a combination of minerals of all types of crystal habit. Platy minerals, such as clays, are the most difficult to randomize. Moore and Reynolds (1997) compared various methods. Effective (and time intensive) methods of creating random powder mounts of clay minerals are freeze-drying and spray-drying (Hillier, 1999). For reference-intensity-ratio (i.e. mineral intensity factor) Q-XRPD, these labor-intensive preparation techniques are likely required, but for pattern matching and Rietveld programs (such as BGMN®) that model anisotropy, careful use of back-, side- and top-loading methods provide quality results. In this study, the top-loading method for random preparation is used at the University of Michigan, with the surface retouched with a sharp edge to induce roughness. The back-loading method is used at the Helmholtz-Center Potsdam, GeoForschungsZentrum (GFZ).

A constant absorption volume is another aspect that must be considered. At small °2θ, the analyzed volume in contact with the incident X-ray beam is broad and thin (doesn't penetrate as far into the sample); at large °2θ, the analyzed volume is narrow but thick (i.e. penetrates further into the sample). This is a product of the Bragg-Brentano instrumental configuration. The total analysis volume, regardless of its changing dimensions throughout the measurement, must be constant. In order to ensure this, the user must take care that beam spillover onto the sample holder does not occur and that the sample is of "infinite thickness". Beam spillover may be a problem with round sample holders at low °2θ and may necessitate the use of square ones. An "infinite thickness" depends on the X-ray absorption and attenuation properties of the sample, but is typically achieved by filling the sample holder supplied with most diffractometers. In addition to the violation of the constant volume assumption, which can nullify quantitative results, beam spillover can produce ghost peaks in the resultant diffractogram, often at low angles, as the crystallinity of the sample holder itself is measured.

II.VI.III.I. Library of WILDFIRE©-Generated Illite Polytype End-Members

The computer program WILDFIRE© generates 3D diffraction forward models for pure and interlayered clay minerals (Reynolds, 1993). Along with inputs of machine geometric parameters, a user can vary layer rotational disorder, *cis*- vs *trans*- vacancy characteristics (octahedral cation occupancy), chemical substitutions, crystallographic orientation and crystallite thickness. Polytype quantification using WILDFIRE© has been illustrated by Grathoff and Moore (1996), Ylagan et al. (2002), Haines and van der Pluijm (2008), and others. Similar to these authors, we have generated nearly 700 variations of 1Md illite and 20 variations of 2M1 illite as candidate end-member polytype matches to natural samples. The approach to quantification of polytypes in a natural sample using WILDFIRE© generated libraries is to graphically compare the diffractogram of the natural sample to a composite diffractogram produced by adding a 1Md and a 2M1 pattern in varying proportions using the equation II.I:

$$Eq.II.I: W_p = (Ax + By)MF$$

Where W_p is the resultant sum of the 1Md and 2M1 combined WILDFIRE© patterns, A is the intensity of the 2M1 WILDFIRE©-generated pattern for a single step in °2θ, x is abundance of 2M1 in weight percent, B is the intensity of the 1Md WILDFIRE©-generated pattern for a single step in °2θ, y is the abundance of 1Md in weight percent (x+y=1), and MF is a scaling factor that accounts for the background radiation and intensity. An alternative to manually selecting end-members for graphical matching, which is cumbersome with so many end member options (something like 14,000 possible combinations!), is to run a least squares algorithm for first pass identification. Peaks chosen for fitting should be selected judiciously in order to avoid peak overlap of non-illite peaks, with emphasis on polytype differentiation (i.e. *hkl* reflections). Non-illite peaks invalidate the least squares calculation (the routine minimizes χ^2, which can yield graphically nonsensical results in the presence of extraneous peaks). In practice, this often means matching the polytype specific *hkl* reflections in the 16-44°2θ range while excluding peaks of chlorite,

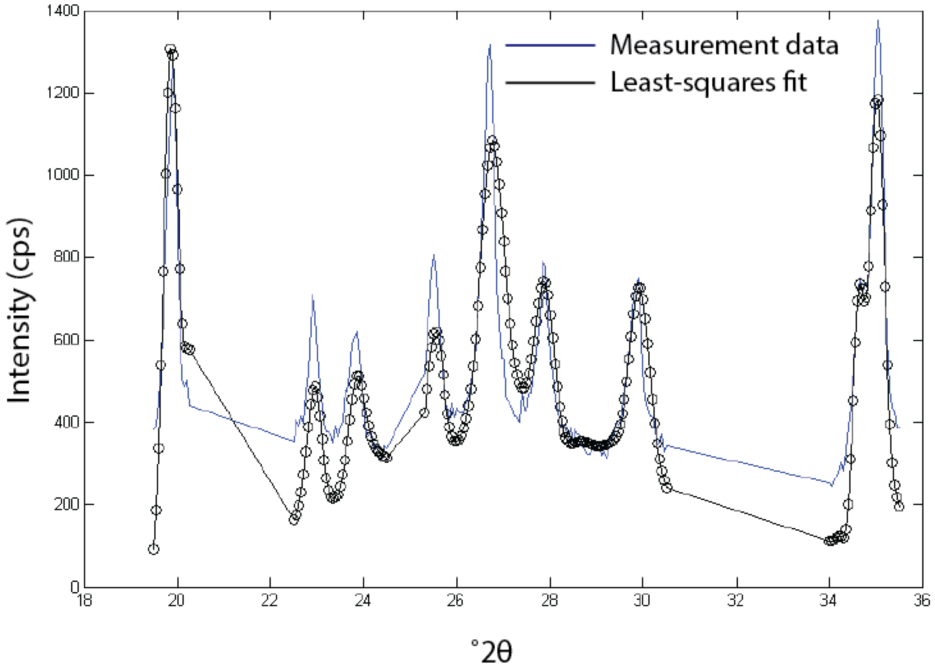

Figure II.VI. Result of a least-squares algorithm fit of a 1Md and 2M1 polytype mixture from the WILDFIRE© diffractogram library to a synthetic mixture (SM1), that illustrates its effective predicting power when non-illite peaks are disregarded in the match.

calcite, and feldspars that may occur. Uncertainty estimates are on the order of ±7-8% using this methodology.

Figure II.VI illustrates the use of the least-squares algorithm on synthetic sample mixture SM1, excluding °2θ ranges 20.25-22.5, 24.5-25.3, and 30.5-34. This synthetic mixture has a 1Md/2M1 ratio of 1:3, and the algorithm predicts a 1Md abundance of 1Md/(1Md+2M1)=30%. An iterative approach can be applied, with a least-squares calculation suggesting possible end-members, followed by graphical fitting using a mixing spreadsheet. This approach was applied in the current study.

II.VI.III.II. End-Member Natural Standards

A similar spreadsheet mixing program as with WILDFIRE©-calculated diffractograms is used in the End-member Standards Matching technique. The motivation to use natural 1Md and 2M1 illite polytype end-member standards instead of those calculated with a diffractogram generator is two-fold: i) the use of natural end-members of similar origin and grain size to those of the sample under investigation allow a good fit of many of the structural parameters inherent to the mineral, and ii) by measuring the end-members and the sample using the same diffractometer and optical set-up, the geometric characteristics, X-ray intensity, and background subtleties unique to a particular diffractometer can be matched. When the end-member standards are measured, they are mixed to create a composite diffractogram (using eq. II.I), and graphically fitted to the unknown sample to estimate relative proportions of 1Md and 2M1. Uncertainty estimates are less than 5% using this methodology.

II.VI.III.III. Rietveld Refinement by BGMN®

The third method used for polytype quantification is whole-pattern fitting X-ray powder diffraction, which was developed for structure refinement and structure solution in the absence of single crystal specimens (Rietveld, 1967; Rietveld, 1969). BGMN®, a powerful peak profile modeling program system, was introduced to separate the influences of experimental set-up from the contribution to the diffraction pattern of the measured sample, and allows users to quantitatively assess phase proportions of known minerals in an unknown mixture (Bergmann et al., 1998). The program is provided free for academic, non-commercial use by the authors, and can also be downloaded with a graphical user interface PROFEX that has both PC and MAC compatibility. The following paragraphs summarize at a high level the basic theory and necessary steps needed to implement the Q-XRPD technique (see program manual for detailed instruction; Bergmann, 2005).

The innovative approach taken by separating the influence of the device configuration from the measured diffraction pattern eliminates correlation between profile and structure parameters, as found in other Rietveld programs, and guarantees that the calculation converges in every case. Since the profile is investigated independently, the user is now able to insert boundary conditions for all parameters used in the fitting routine. Control over preferred orientation description and correction, crystallite size and strain is achieved. The algorithm generates synthetic mineral models from a structure file, varying the parameters as allowed by the boundary conditions, adding the instrument configuration, and optimizing the fit between the summed models and the unknown, to minimize a least-squares sum (Eq. II.II):

$$Eq. II.II\colon \sum_{i=1}^{M} w_i (y_i - y_{ic})^2$$

M is pattern length (number of data points), y_i is measured intensity at pattern data point i,y_{ic} is the computed intensity at pattern data point i, w_i is the weight at pattern data point i, and T_i is the counting time as preselected for pattern data point i. See Bergmann (2005) for further theoretical discussion.

Figure II.VII is a workflow that illustrates the steps required for Rietveld analysis in BGMN®. The following discussion is a summary of more in-depth instruction contained in the program manual, but is meant to give new users an overview of what is required for setup. Templates for the files discussed are provided in the program bundle. Many mineral structure files are also included with the program, and can be shared between users or generated from *.cif structure files publicly available in mineral databases. The basic control files required by the program to perform the refinement are an instrument configuration file (*.geq), a command control file (*.sav), and mineral structure files (*.str).

For a laboratory desiring to adopt this methodology, the biggest hurdle is the creation of the instrument configuration file. There are two ways to build such a file; by profile raytracing and by the learnt peak profile approach. Profile raytracing requires the input of several goniometer-specific parameters such as goniometer radius, slit choices, X-ray tube characteristics, etc. All of this information should be available in instrument manuals or can be measured directly on the goniometer. The geometric device data is used to model the device function at specific angular

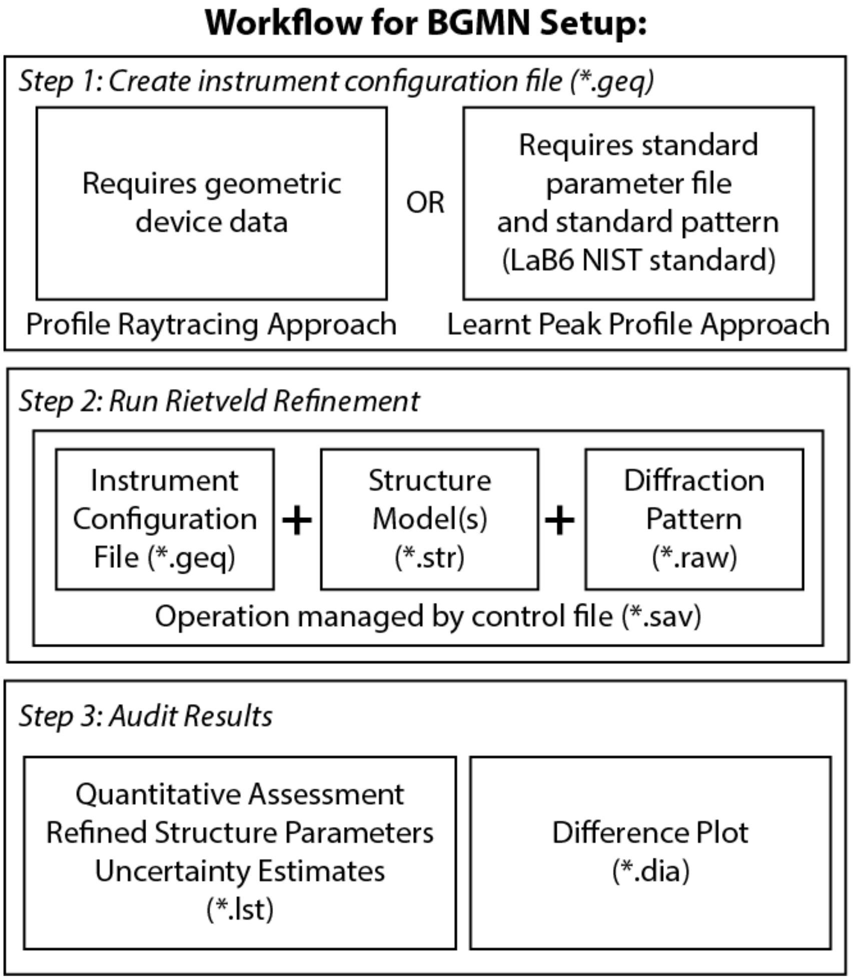

Figure II.VII. Workflow diagram illustrating the steps used for Rietveld refinement using BGMN®.

positions with an operation called GEOMET. The device function is further interpolated across the whole angular range using the MAKEGEQ operation. The learnt peak profile approach calls for a standard pattern (NIST standard 660c LaB_6) to be measured and deconvoluted using the VERZERR operation, and then interpolated using the MAKEGEQ operation. The resultant instrument configuration file from either approach is used in each calculation to account for nuances of experimental setup. With this file, the user is prepared to generate models for samples measured with that specific experimental setup.

After the creation of an instrument configuration file, model refinement is straightforward. Once a refinement has been completed, it is up to the user to assess the results and perhaps add/remove structures from the refinement, change the boundary conditions of individual parameters in a given mineral's structure file, or change the degrees of freedom in the Lagrangian polynomial used to model the background. This iterative approach is usually successful in achieving a good fit.

Uncertainty estimates are also important assessment tools. BGMN® returns a number of uncertainty estimates which can aid in understanding the validity of a model fit. These include various R-factors (reliability factors) and the Durban-Watson statistic. Low R-factors do not mean that the quantification is accurate, however R-factors >5% are a good indication that the fit is poor quality (Toby, 2006). A statistical error estimate is also provided for each phase, and is reported in the *.lst file next to the calculated quantity. These quantification errors represent lower bounds of the estimated standard deviation, as defined by the error propagation rules from counting statistics of pattern data, whereas the actual estimated accuracy of the measurements is ~2% for each phase (Ufer et al., 2008; Kleeberg, 2009; Kaufhold et al., 2012; Dietel, 2015). The reported statistical errors can be compared in practice to the reported phase quantity, and if the error is equal to or greater than the quantity, the fit should not be trusted.

II.VI.III.IV. Q-XRPD Results and Comparison

Using the three quantitative methods described above, and robust qualitative characterizations of sample G2, we list the calculated totals of each mineral in Table II.I. As mentioned above, the WILDFIRE© and End-member Standards Matching methods report polytype abundance as a

Table II.I. Q-XRPD results for WILDFIRE© (WF), End-member standards matching (STD) and Rietveld (BGMN) methodologies of each grain size of sample G2.

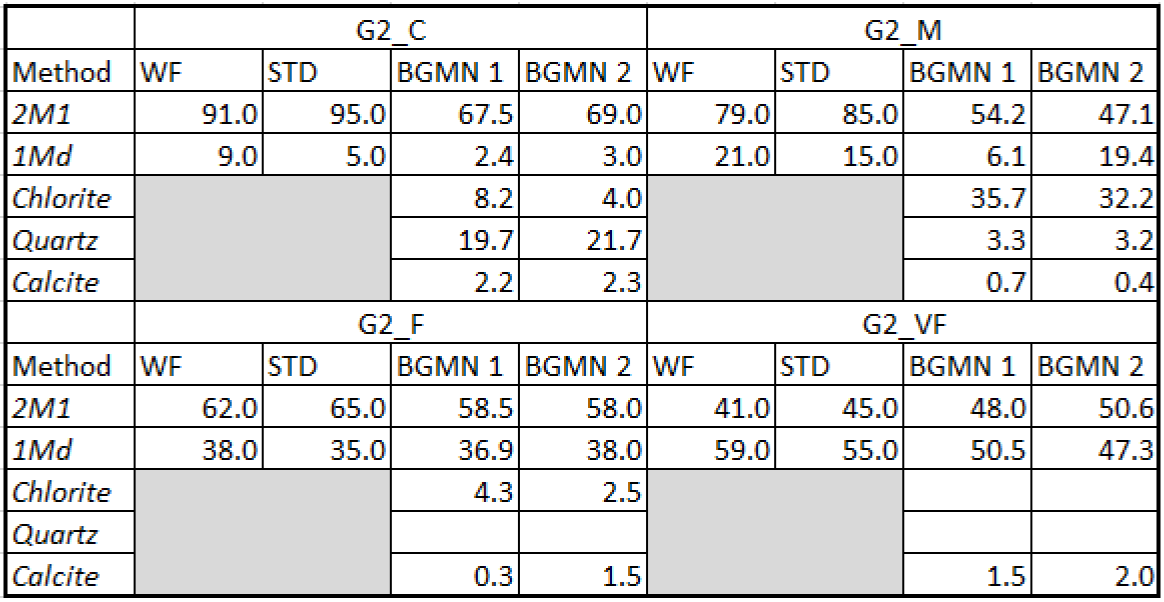

	G2_C				G2_M			
Method	WF	STD	BGMN 1	BGMN 2	WF	STD	BGMN 1	BGMN 2
2M1	91.0	95.0	67.5	69.0	79.0	85.0	54.2	47.1
1Md	9.0	5.0	2.4	3.0	21.0	15.0	6.1	19.4
Chlorite			8.2	4.0			35.7	32.2
Quartz			19.7	21.7			3.3	3.2
Calcite			2.2	2.3			0.7	0.4
	G2_F				G2_VF			
Method	WF	STD	BGMN 1	BGMN 2	WF	STD	BGMN 1	BGMN 2
2M1	62.0	65.0	58.5	58.0	41.0	45.0	48.0	50.6
1Md	38.0	35.0	36.9	38.0	59.0	55.0	50.5	47.3
Chlorite			4.3	2.5				
Quartz								
Calcite			0.3	1.5			1.5	2.0

proportion of total illite, whereas the Rietveld method reports phase abundance for each individual mineral as a proportion of the total mixture of minerals.

It is instructive to compare the fits of the different models to the data from synthetic mixtures to gain graphical understanding of the various uncertainty estimates associated with each methodology. Figure II.VIII displays the model fits of SM1, SM2 and SM3 for each Q-XRPD technique in red, against the measured sample in black. The Rietveld models also display the calculated 1Md contribution to the diffraction pattern in grey. The WILDFIRE© models successfully fit background disorder, as well as key peaks at 20, 27, and 35°2θ, but matching all *hkl* peaks remains a challenge. End-member standard matching provides satisfactory fitting of illite polytypes, and effectively "sees through" contaminating phases, but error estimates are ~5%. Rietveld refinement is the most successful in replicating the pattern data, yielding accurate results and providing robust estimates on error. It requires the most extensive laboratory preparations, but

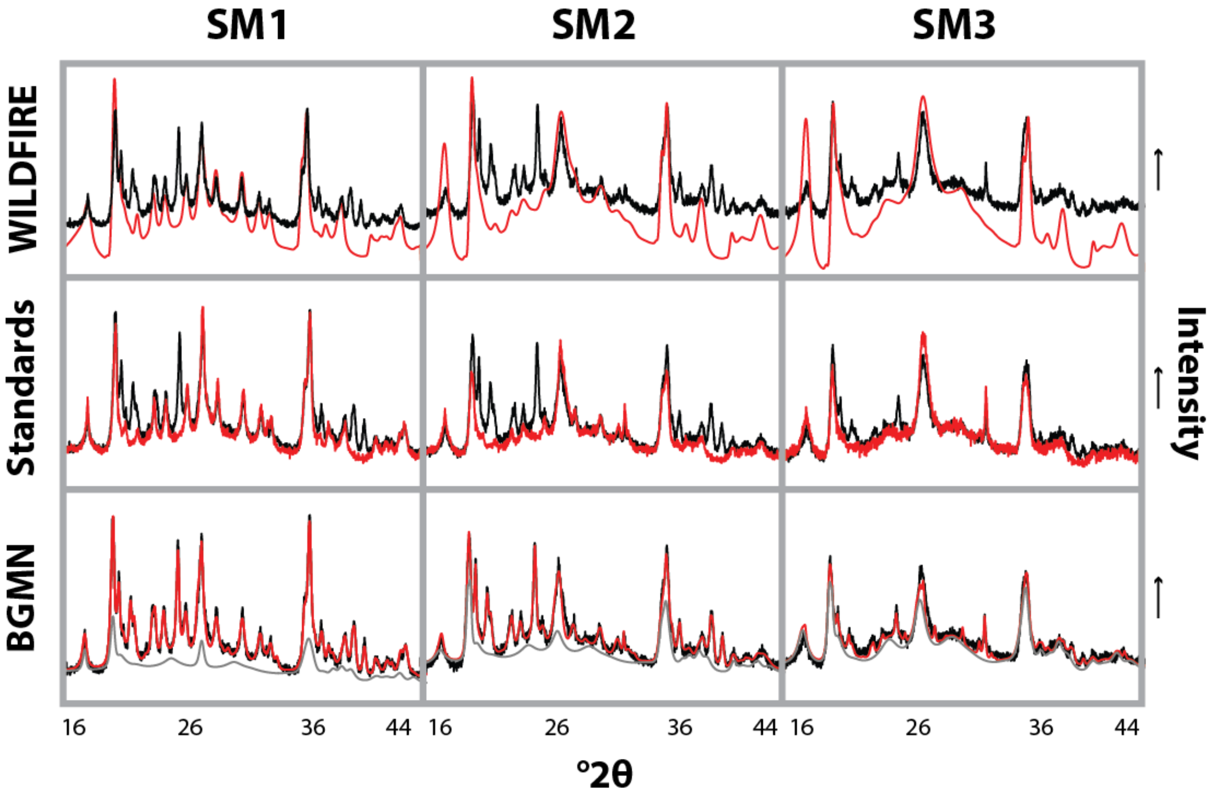

Figure II.VIII. A comparison of the model fits for the synthetic samples SM1, SM2, and SM3 for each of the analytical approaches undertaken: WILDFIRE© matching, end-member standards matching, and Rietveld refinement using BGMN ®. Measurement data is displayed in black, and models are displayed in red. BGMN® models also show 1Md illite polytype contributions in grey.

comparison of BGMN_1 (University of Michigan) and BGMN_2 (GFZ Potsdam) results in table II.I shows excellent repeatability across different experimental set-ups. The visual comparison of the model fits to synthetic samples for each Q-XRPD technique highlight the varying uncertainty associated with each approach.

II.VI.IV. Application of Illite Polytype Analysis to ^{40}Ar/^{39}Ar Geochronology

Having compared the quantitative assessments of the proportion of 1Md and 2M1 illite polytypes in each grain size of sample G2 with the WILDFIRE©, End-member Standards, and Rietveld approaches, we apply age analysis using ^{40}Ar/^{39}Ar geochronology to illustrate the utility of these methods. Four grain size aliquots of sample G2 were dated, and the results were correlated and unmixed to constrain the age of authigenic illite mineralization.

Ar-dating was conducted by the Noble Gas Laboratory at the University of Michigan using the encapsulation method (van der Pluijm and Hall, 2015). Scherrer thicknesses calculated from full-width at half maximum (FWHM) measurements of the illite 001 peak of each sample differentiate between the use of recoil and retention ages (Fitz-Díaz et al., 2016), and recoil (i.e. total gas) ages are used for sample G2. The measured ages are as follows 90.33±0.84 Ma for sample G2-C, 89.43±0.49 Ma for sample G2-M, 73.55±0.31 for sample G2-F, and 68.4±0.37 Ma for sample G2-VF. Using the radiometric ages for sample G2, and the Q-XRPD results reported in table II.I, the mixing lines for each of the three methodologies are compared in figure II.IX.

Multivariate linear regression is used for age analysis and other unmixing procedures (Boles et al., 2015).These correlations between isotopic composition and 1Md/2M1 abundance ratios have been calculated using both a modified York-type regression analysis (Mahon, 1996) and a Bayesian-type regression analysis (Staisch, 2014), yielding unmixing lines that are used to extrapolate to end-member 1Md and 2M1 illite population values. In York least-squares linear regression, the slope and intercept values have the following assumptions: they represent a Gaussian distribution, they are independent, and they are uncorrelated. If this approach is utilized, despite the high accuracy of the error on each of the x and y datasets independently and excellent correlations (high R^2), the unochron error can lead to large age uncertainty if the range of 1Md/2M1 abundance ratios is small (Pană and van der Pluijm, 2014). Therefore, samples exhibiting a large range of 1Md/2M1 abundance ratios across the grain size separates should be selected to limit this problem. We use York-type multivariate regression analysis in this study.

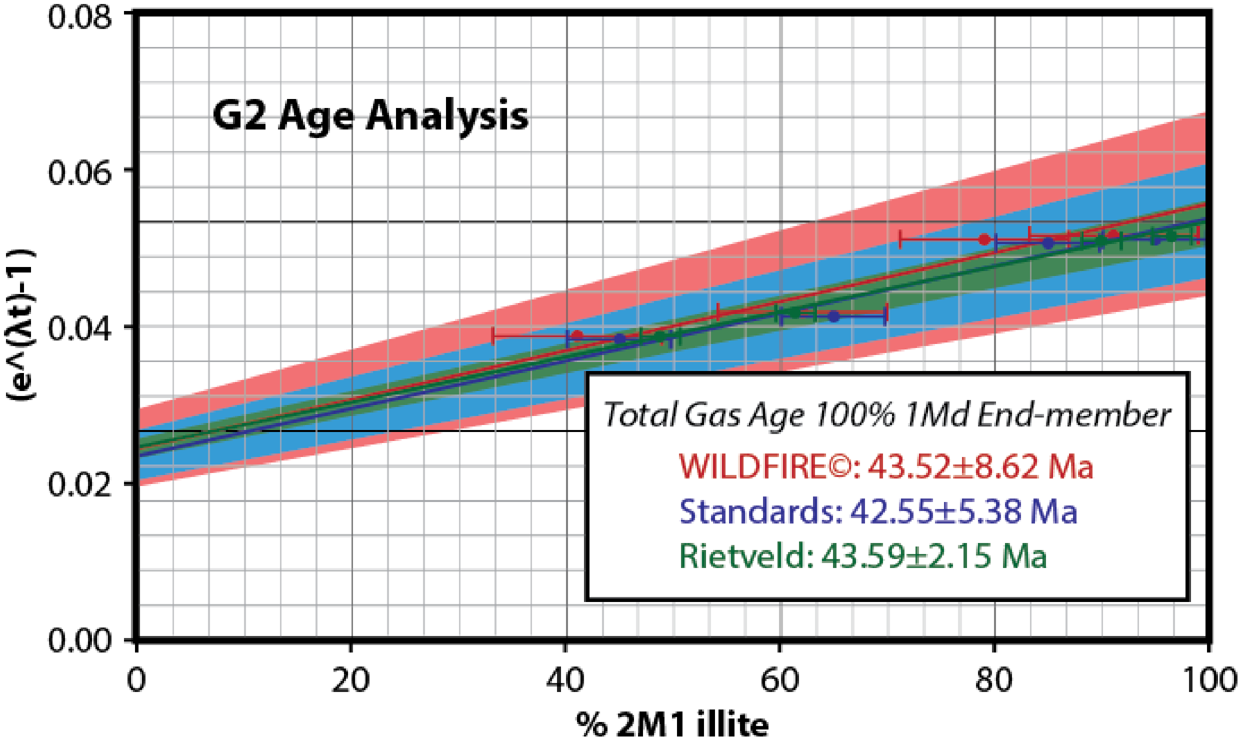

Figure II.IX. York-type regression analysis comparing the mixing lines for WILDFIRE© matching (red), End-member Standards Matching (blue) and Rietveld refinement using BGMN ® (green). Individual data points indicate error with brackets, and correspondingly colored fields represent error bounds for regression analysis, which become smaller in the methods order above.

Alternatively, Monte-Carlo modeled linear fits can test the likelihood of correlation with observed data in the Bayesian approach. With a sample size on the order of 10^6, the resultant posterior probability density functions constrain the range of illite ages and may provide a more statistically meaningful estimate of uncertainty, if calculated slope and intercept are not independent.

The uncertainties associated with each technique, highlighted in figure II.VIII, correspond to the uncertainty estimates of individual data points (brackets) and of the York-type regression line (and correspondingly colored fields) of the mixing lines in figure II.IX. Significantly, all methodologies produce statistically identical results for the ages of end-members, but the uncertainty estimation is most robust using the Rietveld method, and least robust with WILDFIRE© models. In addition, it is significant to note that all methods effectively model illite polytypism in the presence of non-illite peaks. As long as the isotopic signal investigated is not influenced by the presence of other phases, WILDFIRE© and end-member standard matching methods remain effectual analytical techniques for the illite polytype analysis method; otherwise the Rietveld method should be used.

II.VI.V. Discussion and Conclusions

Three analytical techniques, WILDFIRE© modeling, End-member Standards Matching, and Rietveld refinement using BGMN® offer effective approaches to quantifying proportions of illite polytypes for use in illite polytype analysis. Each method is able to accurately model illite polytypes in the presence of non-illite peaks, as long as preparation and X-ray diffraction best-practices are followed. In order of increasing statistical certainty and robustness, we rank the approaches as follows: WILDFIRE© modeling, End-member Standards Matching and Rietveld refinement using BGMN®.

We recommend End-member Standards Matching as the simplest method for new practitioners of the illite polytype analysis method for dating or stable isotopic fingerprinting of authigenic illite. The trade-off between statistical robustness and laboratory demands favors the simplicity of this approach. If, however, small error uncertainty is of high priority, we recommend use of Rietveld refinement for its improved statistical robustness. Perhaps even more important, if other populations of minerals contribute to the isotopic signal under investigation, quantification of all phases is required. BGMN® provides excellent model fits in addition to decreasing user dependency, while providing inter-laboratory repeatability. We anticipate further improvements to the illite polytype analysis method, such as the implementation of the methodology in other isotopic systems, such as O, H, Hg, B or Sr, for tracing deformation-related or diagenetic fluids in deformed upper crust.

II.VI.VI. Acknowledgments

This chapter was submitted to the journal *Clays and Clay Minerals* with co-authorship of Anja M. Schleicher and Ben van der Pluijm. We thank Jasmaria Wojatschke for development of Rietveld capabilities at the University of Michigan, Ross Maguire and Trevor Hines for the development of Matlab coding of the least-squares fitting algorithm. A MATLAB script for generating Bayesian-type linear regressions for x and y data with respective uncertainties can be requested from Eric Hetland at the University of Michigan (ehetland@umich.edu). John Solum originally generated the WILDFIRE© patterns used in this study. Heide Kraudelt is thanked for the Laser Particle Analyzer data and Richard Wirth for TEM analyses. Our research is supported by the National Science Foundation, most recently under EAR-1629805.

Chapter III. Clays in the Exhumed Alpine Fault Zone (New Zealand) are Late Surface Alteration

III.I. Abstract

Mineralogical and isotopic investigation of fault-hosted clays from the exhumed trace of the central Alpine Fault Zone (South Island, New Zealand) reveal a recent, near-surface alteration history. Two predominant clay phases ubiquitous in the exposed fault damage zone, illite and chlorite, are studied using 8 principal slip zone, hanging wall, and footwall fault gouge samples. Quantitative X-ray powder diffraction using BGMN® constrains mineral and illite polytype abundances. A modified illite polytype analysis methodology dates authigenic illite growth using encapsulated ^{40}Ar/^{39}Ar geochronology. H isotopic analysis preserves the source of mineralizing fluids responsible for both illite and chlorite growth. Dating of four size fractions of sample SC yielded values in negative age space, indicating recent illite authigenesis estimated at <0.5 Ma. Energy Dispersive Spectroscopy, Electron Microprobe Analysis, and chlorite chemical thermometry reveal the spatial distribution of chlorite and calculate sub-greenschist formation temperatures of 210-296ºC. Measured δD values of clay fraction separates range from -71 to -105‰, and calculated mineralizing fluid values from end-member extrapolation during polytype analysis delineate two distinct mineralizing fluid compositions. A population of chlorite in two samples has a mineralizing fluid range -36 to -45‰, which is in the metamorphic fluid range, but all other illite and chlorite fluid values are -55 to -75‰, similar to modern meteoric fluid in the area. Hanging wall and footwall isotopic compositions differ by -14‰, indicating a history of fault sealing behavior. Isotopic analysis also constrains illite growth to T<100ºC. The predominant clay populations at the surface formed recently, at low temperatures, and from a meteoric-dominated mineralizing fluid. We infer that these clays are unstable at depths >2 km (illite) and >5 km (chlorite), and, therefore, that surface and deep fault rock may significantly differ.

III.II. Key Words

Alpine Fault Zone, H isotopic analysis, $^{40}Ar/^{39}Ar$ geochronology, Chlorite chemical geothermometry, illite polytype analysis

III.III Introduction

Results from drilling programs that target active fault zones have highlighted the mechanical importance of fault-hosted clay mineralization. For example, the presence of low-friction chlorite-smectite minerals in the San Andreas Fault Observatory at Depth (SAFOD) borehole has helped explain the "weak" behavior of the fault, previously constrained by measurements of heat flow, stress orientation, and seismological observations to slip at a low frictional coefficient of ~0.2 (Brune et al., 1969; Hickman and Zoback, 2004; Boness and Zoback, 2006; Schleicher et al., 2010; Lockner et al., 2011; Carpenter et al., 2012). The temperature-dependent hydration behavior of smectite was used to experimentally constrain coseismic heating estimates on Japan Trench Fast Drilling Project (J-FAST) principal slip zone (PSZ) material (Schleicher et al., 2015a). Studies from the Wenchuan earthquake Fault Scientific Drilling project (WFSD) and the Taiwan Chelungpu-fault Drilling Project (TCDP) similarly use PSZ clay mineral constituents to make inferences about the mechanical behavior, thermal history, and chemical activity of geologic processes in these deformation zones (Hirono et al., 2008; Kuo et al., 2009; Kuo et al., 2011; Si et al., 2014; Zhang et al., 2014).

The stated goal of the Deep Fault Drilling Project (DFDP), which aims to investigate the nature of the Alpine Fault Zone (AFZ) in New Zealand, is to examine how rocks exposed at the surface relate to seismogenic and tectonic processes at depth (Townend et al., 2009). One prominent attribute of Alpine Fault surface geology is the presence of significant amounts of clay minerals in the exposed damage zone of the fault, which vary in volume, mineralogy, and prominence along strike (Sibson et al., 1981; Warr and Cox, 2001; Norris and Cooper, 2007). The frictional properties of Alpine Fault Zone clay gouge have previously been tested using PSZ material both sampled at the surface and recovered from the DFDP phase 1 shallow borehole (<150 m depth). These studies indicate that some types of Alpine Fault gouge have frictional coefficients as low as 0.31 (Boulton et al., 2012; Boulton et al., 2014; Ikari et al., 2014).

Considering the Alpine Fault's large magnitude (M_w~8.0) earthquakes, the presence of low-friction material at depth in this fault zone would present a mechanical paradox (Sutherland et al., 2000; Beavan et al., 1999; Norris and Cooper, 2000; Sutherland et al., 2007). Additional observations, such as the very high measured geothermal gradient of ~125ºC/km from the DFDP-2B borehole, or more conservative albeit still high geothermal gradient measurements ~63ºC/km from the DFDP-1 borehole, indicate that many species of clay mineral are out of their respective thermodynamic stability fields within only a few km from the surface in this area, far above the load-bearing, seismogenic portion of the crust whose base is ~10-12 km (Allis and Shi, 1995; Shi et al., 1996; Beavan et al., 1999; Leitner et al., 2001; Boese et al., 2012; Sutherland et al., 2015; Sutherland et al., 2012).

In light of these contrasting observations, we investigate the nature of AFZ clay mineralization using 8 fault gouge surface samples collected from main thrust of the Alpine Fault and from hanging wall and footwall subsidiary faults in the vicinity of the DFDP-2 drill site in Westland, New Zealand. Specific focus is given to the two dominant populations of clay minerals, 1Md polytype illite and chlorite (chlinochlore). Quantitative X-ray powder diffraction (Q-XRPD) using BGMN® constrains mineral and polytype abundances and increases the accuracy of the illite polytype analysis method. Also, H isotopic analysis, paired with traditional ^{40}Ar/^{39}Ar geochronology, broadens the scope of the illite polytype analysis methodology and is used to discriminate between mineralizing fluid compositions responsible for illite and chlorite growth. Scanning Electron Microscopy (SEM) and Energy Dispersive Spectroscopy (EDS) large-area mapping, Electron Microprobe Analysis (EMPA), and chlorite chemical geothermometry constrain the spatial distribution, composition, and formation temperature of chlorite. We use these mineralogical and isotopic constraints to determine the genesis of surface clays and their relationship to the mechanical behavior of the fault.

III.IV. Geologic Background

III.IV.I. Alpine Fault Zone Structure

The New Zealand subcontinent is a Gondwanan-affiliated fragment of continental crust, rifted from the margins of Australia and Antarctica in the Late Cretaceous (Kamp, 1986). It is currently situated between two subduction zones of opposite polarity, the Puysegur Trench to the southeast, and the Hikurangi subduction zone to the northwest (figure III.I, inset map). The dextral-reverse AFZ, located on the western margin of the South Island, links these subduction zones and represents the plate boundary between the Australian and Pacific plates. It juxtaposes meta-sediments and granitoids of the Western Province Basement and Quaternary gravels against sub-amphibolite-facies Alpine Schist. It produces the dramatic topography of the Southern Alps with peaks that reach >3.5 km above sea-level, and has displaced basement markers >450 km (Cooper and Norris, 1994; Norris and Cooper, 2000; Sutherland et al., 2006). Geodetic studies indicate no aseismic creep at the surface and a relative plate motion of 39-42 mm/yr., 50-70% of which is accommodated on the main fault plane (Beavan et al., 1999; Norris and Cooper, 2007; DeMets et al., 2010). The occurrence of pseudotachylyte, buried fault scarps, and seismological evidence are indications that large magnitude (M_w~8.0) earthquakes occur on this margin with a recurrence interval ~300 years, and that the fault is in the late stages of its seismic cycle (Sibson and Toy, 2006; Toy et al., 2011; Sutherland et al., 2007; De Pascale and Langridge, 2012; Townend et al., 2013; Warr et al., 2007).

DFDP phases 1 & 2, completed in 2012 and 2015, respectively, have significantly contributed to our understanding of this major plate-bounding fault. DFDP-1 was located at Gaunt Creek, retrieved core from two pilot holes drilled to depths of 100.6 m and 151.4 m located ~80 m from each other, and successfully intersected the PSZ in both cores (Sutherland et al., 2012; Toy et al., 2015). DFDP-2 was located near the mouth of Whataroa River, and achieved a maximum depth of 893 m, where technical failure of the casing string necessitated premature termination of drilling before the fault zone was intersected, but not before cuttings and hanging wall core were retrieved and a geophysical observatory was installed (Sutherland et al., 2015).

DFDP activities corroborate fault rock architecture models. The fault zone comprises plastic deformation regime mylonites and ultramylonites, with both hanging wall and footwall protoliths that have been overprinted by cataclastic-series brittle deformation. Damage is generally more pervasive near the fault, but varies by lithology, as shown by CT imaging of DFDP-2 hanging wall core (Williams et al., 2016). The PSZ is identified by clay-rich gouge with sharp, but not necessarily parallel, upper and lower boundaries. Clay gouge is variable in color, thickness, foliation, and cementation characteristics. The clay mineralogy of AFZ gouges has been well-described from surface samples by Warr and Cox (2001) and from DFDP-1 core by Schleicher et al. (2015b), showing the dominant presence of illite and chlorite minerals, with variable amounts of interlayered smectite. Modal mineralogy varies by gouge color and sampling location (Boulton and Moore, 2014). Significant physical properties, petrophysical, and geophysical information has also been produced from DFDP data (e.g. Carpenter et al., 2014; Boulton and Moore, 2014; Ikari et al., 2014; Townend et al., 2013)

III.IV.II. Sample Site Descriptions

The samples used in this study were collected during DFDP-2 activities in the region surrounding the DFDP-2B borehole, and were originally intended for use as a comparison with PSZ material recovered at depth; unfortunately no deep gouge was recovered. Figure III.I indicates sampling locations, and coordinates are reported in table III.I. The main thrust of the Alpine Fault was sampled in four locations; Cataclasite Creek (CC), Gaunt Creek (GC), Stony Creek (SC), and Waikukupa River (WR). Two hanging wall faults were sampled at Hari Mari Creek (HM1 & HM2). Two footwall faults were sampled at Whataroa Quarry (WQ) and Smithy's Creek (SmC). Most hanging wall faults and footwall faults have kinematic indicators implying that these comprise elements of the damage zone of the greater Alpine Fault deformation regime.

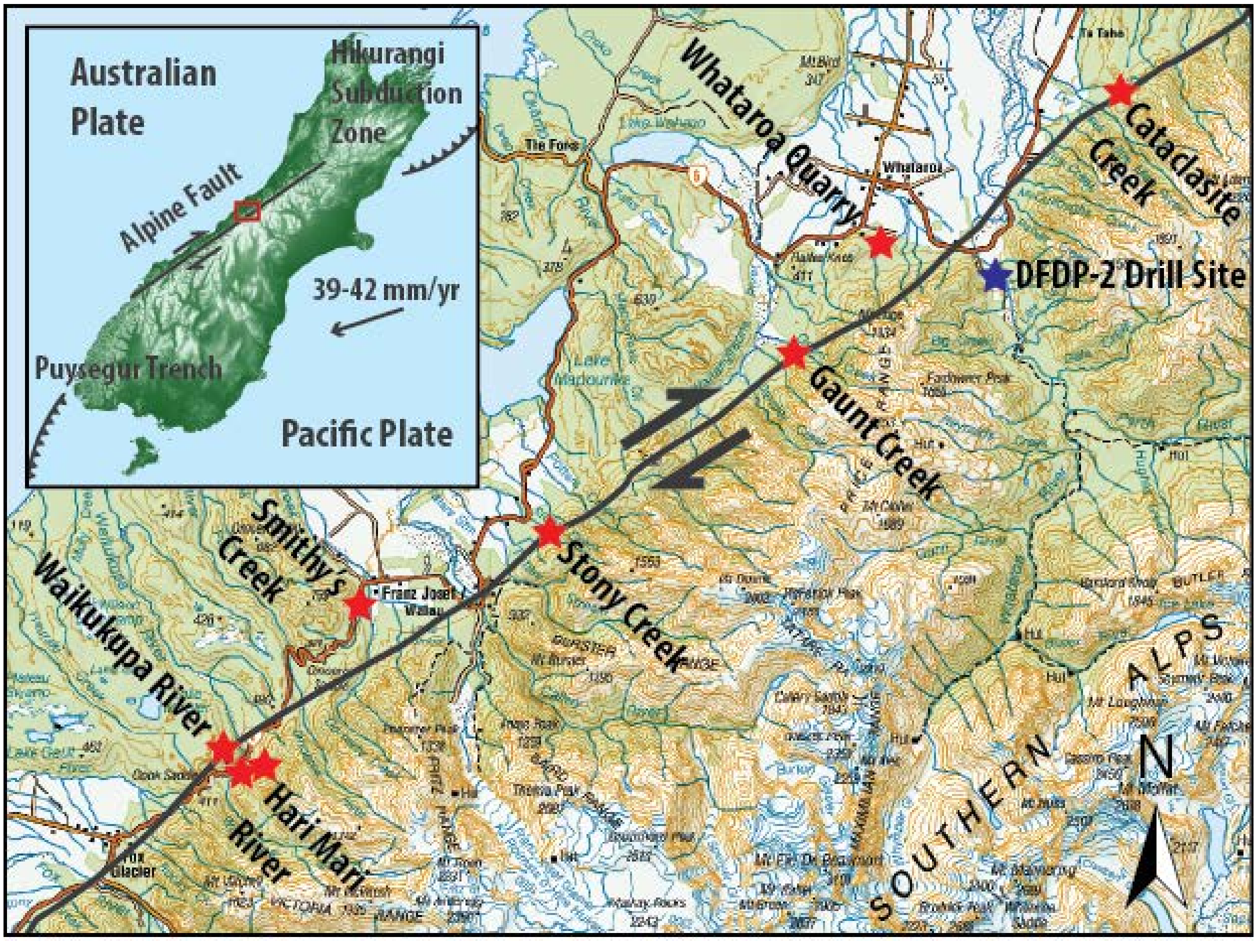

Figure III.I. Map of study area and sampling locations. Plate motion vector from DeMets et al. (2010).

The four main thrust sampling locations are mesoscopically similar, with hanging wall cataclastic-series rocks separated from footwall Quaternary gravels by several centimeters of PSZ gouge. Much of the damage zone at the Gaunt Creek location is greenish in color, indicating high chlorite content, and the sampled PSZ is a well-defined zone ~10 cm in width of brown/green gouge with sharp edges. Calcite veins are observed in and above the gouge zone, and are perpendicular to the plane of the fault.

The Stony Creek location also includes a greenish cataclastic zone, but the PSZ gouge is thicker (~15 cm), and features stratified, unfoliated light grey, dark green, and brown clay. Limited sample access necessitated mixing of stratified layers into a composite gouge during acquisition.

Stream cover prevented proper description of lithologic relationships at the Cataclasite Creek location, and the recovered clay-rich sample is estimated to have been within 1 m of the PSZ, though may not represent the PSZ proper. The sampled clay-rich material is greenish-grey in color and lacks foliation fabric; it contains coarser grained clasts than other main thrust samples, and possibly represents cataclasite-series fault rock.

The Waikukupa Thrust Sheet is described by Norris and Cooper (1997) as an ‘out-of-sequence’, imbricate thrust sheet that was abandoned during glaciation-controlled rapid river erosion because of geometrical constraints of critical wedge theory. The Waikukupa River sampling location is the basal detachment of the Waikukupa Thrust Sheet. It features a 3-5 cm thick brown/green gouge with subparallel, sharp edges separating greenish-colored hanging wall cataclasite from very poorly sorted footwall Quaternary gravel. This sampling location experiences high erosion rates, and the fault zone outcrop is well-exposed, with all fault architectural components represented.

Both hanging wall samples were collected in the incised valley of the Hari Mari River. These small-scale slip zones are sub-parallel to dominant Southern Alps schistosity, and the wall rock of these gouge zones is mylonitic. Interbedded chert layers are observed in the mylonite, above and below the gouge zones. The two slip zone locations feature very thin (3-5 cm) bands of dark brown, unfoliated clay-rich gouge with no associated cataclasite, damage, or alteration halo.

Footwall fault gouges were sampled at two locations. A well-developed, scaly gouge of greyish-brown color was sampled at Whataroa Quarry. Gouge contacts are undulating, and both hanging wall and footwall lithologies comprise tectonized granitoids of the Greenland Group. Gouge is variably 10-30 cm thick, and a further brecciated damage zone of 50 cm on either side of the fault is observed. The fault has an opposite dip direction than the Alpine Fault, at ~45º W. No displacement markers could be located.

The footwall fault gouge sampling location known as Smithy's Creek Fault zone has been described by Lund-Snee et al. (2014). It is dextral-oblique and is associated with a 100 m wide damage zone and 8 m wide fault core. The fault is unfavorably oriented in the modern stress regime but has kinematics compatible with neotectonic deformation Wall rock lithology is metamorphosed plutonic rock of mafic composition. Clay-rich foliated gouge ~0.5 m thick is greenish-grey in color, with sharp upper and lower contacts.

Table III.I Sampling Locations

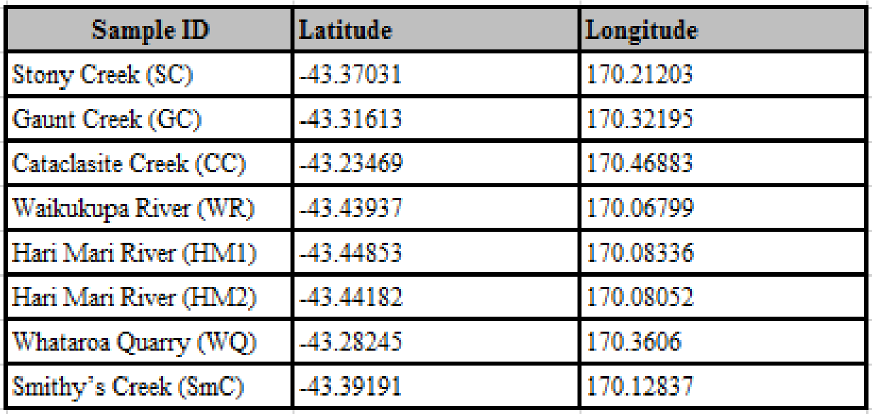

Sample ID	Latitude	Longitude
Stony Creek (SC)	-43.37031	170.21203
Gaunt Creek (GC)	-43.31613	170.32195
Cataclasite Creek (CC)	-43.23469	170.46883
Waikukupa River (WR)	-43.43937	170.06799
Hari Mari River (HM1)	-43.44853	170.08336
Hari Mari River (HM2)	-43.44182	170.08052
Whataroa Quarry (WQ)	-43.28245	170.3606
Smithy's Creek (SmC)	-43.39191	170.12837

III.V. Methods

III.V.I. Illite Polytype Analysis

The primary methodology utilized in this study is a modified version of the illite polytype analysis method (van der Pluijm and Hall, 2015; Boles et al., 2015). Illite polytype analysis is used to resolve the end-member isotopic signal of two coexisting populations of the K-bearing clay mineral illite. Polytypism in illite is expressed as differences in layer stacking patterns of phyllosilicate sheets, and different polytypes have different thermodynamic stability ranges. The high-temperature illite polytype 2M1 is well-ordered, and forms in the temperature range 150-300 ºC, whereas the low-temperature illite polytype 1Md is poorly-ordered ('d' in 1Md stands for disorder), and forms at temperatures 80-150 ºC (Meunier and Velde, 2004). 2M1 illite is known to represent detrital, or pre-existing clay populations, in fault zones and 1Md illite grows authigenically in the fault zone, with the potential to record the temperature, fluid composition, and timing of formation (van der Pluijm et al., 2001; van der Pluijm and Hall, 2015).

By separating the clay portion of a fault gouge (< 2 μm) into multiple size fractions and correlating the 1Md:2M1 illite ratio and isotopic composition measured in each size fraction, a mixing line is obtained and used to extrapolate to pure end-member 1Md and 2M1 isotopic compositions. York-type multivariate linear correlation is utilized (Mahon, 1996). X-ray diffraction is the technique used to differentiate between and quantify the proportions of each illite polytype, in addition to any other minerals present. The traditional application of this methodology has been the dating of brittle deformation using K/Ar and Ar/Ar techniques (e.g. Haines and van der Pluijm, 2008; Clauer, 2013). Boles et al. (2015) broadened the application of the illite polytype analysis method by the unmixing of the H isotopic composition of each end-member polytype, deriving the isotopic composition of the mineralizing fluid from known illite fractionation behavior. The current study applies a more rigorous quantitative X-ray powder diffraction (Q-XRPD) approach that involves Rietveld-type whole-pattern decomposition using BGMN®, in order to address the compositionally diverse mineralogy of Alpine Fault gouges.

III.V.I.I. Sample preparation

The 8 fault gouge samples were hand-crushed using an agate mortar and pestle and disaggregated in deionized water in an ultrasonic bath for ~10 min. Sodium pyrophosphate was used as a deflocculant, as necessary. Each sample was separated into 6 grain size fractions (VF<0.05 μm, F=0.05-0.1 μm, M=0.1-0.5 μm, MC=0.5-1.0 μm, C=1.0-1.5 μm, and VC=1.5-2.0 μm) by centrifugation according to Stoke's Law. Clay suspensions were dried in Pyrex pans in a flume hood at T<40ºC, and gently re-powdered after drying. Each 6 grain size fractions of each of the 8 samples was analyzed by Q-XRPD, for H isotopic composition, and select samples were analyzed by ^{40}Ar/^{39}Ar geochronology for subsequent correlation and unmixing of the isotopic signals.

III.V.I.II. X-ray Analysis

X-ray analysis was conducted at the Electron Microbeam Analysis Laboratory (EMAL) at the University of Michigan on a Rigaku Ultima IV diffractometer operated at 40 kV and 44 mA, equipped with a scintillation detector, in Bragg-Brentano geometry, using Cu Kα radiation.

III.V.I.II.I. Qualitative analysis

The bulk mineralogy of each of the 8 samples was characterized by qualitative X-ray powder diffraction using oriented suspension mounts dried on glass slides (Moore and Reynolds, 1997). A robust qualitative interpretation is a prerequisite for subsequent Q-XRPD. The oriented mounts emphasize the basal peaks of the clay minerals for ease in identification. Samples were analyzed in both air-dried and ethylene glycolated conditions to test for the presence of swelling minerals; ethylene glycol occupies interlayer sites of smectite species clay minerals, causing them to swell along the c-axis which, in turn, diagnostically changes the X-ray diffraction pattern. Diffraction patterns were collected from 2-50º2θ at 0.05 step size and scan rate of 1 º2θ/minute, and were characterized using MacDiff software mineral libraries.

III.V.I.II.II. Quantitative X-ray Powder Diffraction using BGMN®

Various X-ray methodologies have been utilized to quantify the proportion of 1Md to 2M1 illite in mixed population natural samples. These include WILDFIRE© modeling and end-member standards matching (Grathoff and Moore, 1996; Boles et al., 2015). These approaches have quantitative accuracies on the order of ±8% (WILDFIRE©) and <±5% (end-member standards matching), and are adequate approaches for Ar-dating because 1Md and 2M1 illite are the only K-bearing phases at clay grain-size fractions. If a mixing line is to be created using H isotopic composition in the presence on non-illitic clay minerals such as chlorite, the true proportions of all hydrous minerals present must be known. In addition, the relative proportions of H contributed by a structural unit of each clay phase must be understood and corrected for.

Rietveld-method full-pattern fitting tools, such as BGMN®, are known as ‘state-of-the-art’ quantitative assessment techniques that decompose an X-ray spectrum into its constituent mineral contributions; these are known to provide accuracies as good as ±2%, decrease user dependency, and ensure interlaboratory repeatability (Bergmann et al., 1998; Ufer et al., 2008; Kleeberg, 2009; Kaufhold et al., 2012; Dietel, 2015). We utilize these advances in this study.

BGMN® requires two basic types of information to create a model fit. It utilizes structure files containing mineralogical information for each mineral present, which include both basic crystallographic descriptions, as well as information pertaining to disorder, strain, and crystallographic preferred orientation of the phase. It also utilizes an instrument configuration file that contains information specific to the goniometer in use, with information such as goniometer radius, radiation type, etc. In this way, the fitting routine minimizes the error between the measured and model spectra by taking into account machine parameters and mineralogical information. Statistical R-factors about the fit are provided to assess the quality of the Rietveld calculation, and an R-factor of <5% was used as a cutoff in this study (Toby, 2006).

Random powder mounts of each size fraction of the 8 fault gouge samples were prepared by the front-loading method (Moore and Reynolds, 1997). Diffraction patterns were collected from 2-

80º2θ at 0.03 step size and scan rate of 0.3º2θ/minute. Each size fraction was analyzed using BGMN® for mineral and polytype modal percentages.

III.V.I.III. H Isotopic Analysis

δD values were measured at the Joint Goethe University – BiK-F Stable Isotope Facility Frankfurt using a ThermoFinnigan MAT 253 mass spectrometer in continuous flow mode coupled to a high temperature conversion elemental analyzer (TC-EA). A sample weight of 1 mg was wrapped into Ag foil and dried overnight at 150°C in a stainless steel tray. Samples were rapidly transferred to a zero-blank autosampler in the stainless steel tray and the autosampler was immediately purged with helium gas to prevent rehydration of interlayer spacing or water adsorption on clay surfaces from ambient air moisture. Standards were run in-line with unknowns and reproduced with an error below ±2 ‰. All δD values are reported relative to standard mean ocean water (VSMOW).

III.V.I.IV. $^{40}Ar/^{39}Ar$ Geochronology

Ar isotope analysis was conducted at the University of Michigan's Noble Gas Laboratory. Vacuum encapsulated samples were irradiated for 90 MWh at location 8C of the McMaster Nuclear reactor at McMaster University in Hamilton, Ontario in irradiation package mc51. Each capsule had a packet of standard mineral MMhb-1 placed above and below the capsule. Measurement procedures for encapsulated clay samples follow the procedures outlined in Hall (2013), Vacuum capsules were made from 2 mm OD, 1 mm ID fused silica (i.e. quartz) tubing. Sections of tubing were cut into 10 cm long segments and each segment was heated in the middle with a methane-O_2 torch while pulling apart each half, thereby collapsing the center into two 5 cm long pieces with breakseal tips. Clay samples were first resuspended in 1 mL of deionized water and then centrifuged in a 1.5 mL tube. The water was then decanted and the remaining clay pellet was allowed to dry in a laminar flow hood. Small (~0.5 mg) pieces of the clay pellets were cut from the dried pellet and loaded into the quartz breakseal tubes and then attached to a vacuum manifold. Procedures for evacuating the breakseal tubes and analyzing the encapsulated samples are outlined in detail in Hall (2013). Encapsulated samples were not baked prior to analysis in order to reduce the possibility of outgassing the sample, thereby complicating the measurement of Ar release purely due to recoil effects. Encapsulated samples were laser step-heated *in situ* until complete fusion was achieved using a defocused beam from a 5 W Coherent Innova continuous Ar-ion laser operated in multi-line mode. For each degassing step, the system was programmed to heat each grain in turn for 60 seconds.

Ar isotopes were measured using a VG1200S mass spectrometer with a source operating at 150 μA total emission and equipped with a Daly detector operating in analog mode. Mass discrimination was monitored daily using ~4x10^{-9} ccSTP of atmospheric Ar. Fusion system blanks were run every five fusion steps and blank levels from argon masses 36 through 40 (~2 x 10^{-14}, ~3 x 10^{-14}, ~1 x 10^{-14}, ~3 x 10^{-14}, and 2 x 10^{-12} ccSTP respectively) were subtracted from sample gas fractions. Corrections were also made for the decay of ^{37}Ar and ^{39}Ar, as well as interfering nucleogenic reactions from K, Ca and Cl as well as the production of ^{36}Ar from the decay of ^{36}Cl. Standard hornblende MMhb-1 was used as a neutron flux monitor with an assumed age of 520.4 Ma (Samson and Alexander, 1987).

III.V.II. Chlorite Distribution and Chemistry

To constrain chlorite formation and to derive a corresponding temperature for stable isotopic conversion in the chlorite-water system of micrometer-scale chlorites, optical and electron microscopic techniques were employed. SEM/EDS were used to identify candidate chlorite mineral sites which were subsequently analyzed by EMPA for composition. The compositional results are inputs into thermodynamic models of Fe-Mg partitioning to estimate chlorite formation temperature.

III.V.II.I. Optical Microscopy

Thin sections of select samples were prepared for optical microscopy at Wagner Petrographic, Inc. (Lindon, Utah). Standard thin section preparation techniques were used that resulted in 24x46 mm slides with a thickness of 30 μm. Photomicrographs were collected at various levels of zoom in both plane and polarized light for mineralogical and microstructural interpretation.

III.V.II.II. Electron Microscopy

Microanalysis work was conducted at the University of Michigan EMAL, using Scanning Electron Microscopy, Energy Dispersive Spectroscopy, and Electron Microprobe Analysis.

III.V.II.II.I. Sample Preparation

Gouge samples were prepared for SEM/EDS and EMPA using progressive introduction of low viscosity (L.R. White) resin, as described in Kim et al. (1995). The resin impregnation method arrests the swelling behavior of clay minerals and penetrates any sample pores. The samples were fixed to thin-section slides, cut to thick sections of 1-2 mm, progressively hand smoothed using 600-1200 grit sandpaper, and polished with a polishing wheel using 1.0 μm and 0.3 μm corundum grit. Samples were washed in deionized water, cleaned in an ultrasonic bath, and carbon-coated for electron beam examination.

III.V.II.II.II. Energy Dispersive Spectroscopy Large-Area Mapping

SEM images and EDS maps were collected on a JEOL-7800FLV field emission gun, high-vacuum and variable-pressure scanning electron microscope operated at 15 kV and optimized beam current with an Oxford EDS detector, AzTec software, and large area mapping image montage capability. Fe and Mg concentration maps were used to constrain the spatial distribution of chlorites and identify candidates for detailed EMPA compositional analysis with the goal of using the chemical analyses to calculate formation temperature.

III.V.II.II.III. Electron Microprobe Analysis

Candidate chlorite sites identified using EDS were selected for chemical analysis for the elements Si, Fe, Mg, Al, Ti, Ca, and Na. EMPA data were collected with a Cameca SX-100 electron microprobe analyzer using wavelength dispersive spectroscopy and operated at 20 kV, 10 nA, and 3 μm beam diameter. The small size of the chlorite limited their analyses to a single point. The following standards were used: jadeite, geikielite, K feldspar, wollastonite, uvarovite, rhodonite, and ferrosilite.

III.V.II.III. Chlorite Geothermometry

Chlorite formation temperatures were determined using EMPA data in the chemical thermometer developed by Vidal et al. (2005; 2006) and Inoue et al. (2009), similar to Lacroix et al. (2012). This thermodynamic model is based on Fe-Mg partitioning in aluminous trioctahedral chlorites using the following end-members:

- Clinochlore $(Mg_5Al)[Si_3AlO_{10}](OH)_8$
- Daphnite $(Fe_5^{2+}Al)[Si_3AlO_{10}](OH)_8$
- Amesite $(Mg_4Al_2)[Si_2Al_2O_{10}](OH)_8$ and $(Fe_4^{2+}Al_2)[Si_2Al_2O_{10}](OH)_8$
- Sudoite $(Mg_2Al_3)[Si_3AlO_{10}](OH)_8$

These end-members allow for the description of the Fe-Mg, Tschermak, and dioctahedral-trioctahedral substitutions. XFe^{3+} and XFe^{2+} were estimated simultaneously for the Chl-Qtz-H_2O assemblage with pressure equal to 1 kbar, a temperature difference of 20ºC, and a_{water} using a temperature scatter of 20ºC and a criterion based on the convergence of equilibria as described by equations 1-4 in Vidal et al. (2005). Ideal chlorite EMPA results for such analysis have elemental

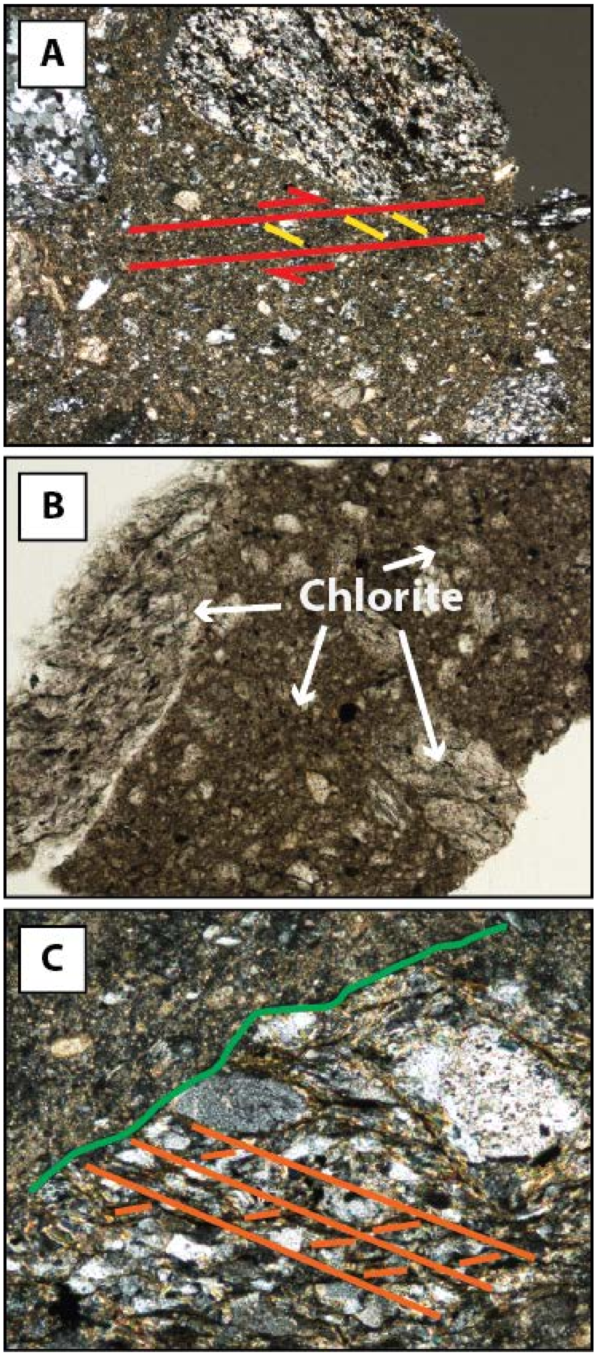

Figure III.II. Unoriented thin sections photomicrographs of the clay gouge sample from Stoney Creek. A) 5x magnification, unpolarized light. B) 5x magnification, polarized light. C) 20x magnification, polarized light. Red and yellow lines highlight the development of deformation bands in the incohesive fault rock. Green lines show pressure solution. Orange lines show shear bands within mylonitic host rock clasts.

oxide weight percent totals 85-89%, and K/Na contents <0.5 weight percent. Due to the high stiffness contrasts prohibiting smooth surface polish and the fine grain sizes (often <5 μm) inherent in fault gouge material, it was sometimes difficult to obtain consistent results from the chlorite EMPA point analysis sites; however, several sites yielded good quality data.

III.VI. Results

The results below are presented in terms of the two predominant clay minerals present in Alpine Fault Zone gouges, chlorite and illite.

III.VI.I. Chlorite

Optical spectroscopy, SEM/EDS, and EMPA identify the location, spatial distribution, and composition of chlorite as inputs into the chlorite chemical thermometer.

III.VI.I.I. Optical Microscopy

Petrographic investigation of the Stoney Creek gouge (figure III.II) shows many characteristic elements of cataclastic fault rocks, such as isolated, angular fragments of Alpine schist, proto-mylonite, and mylonitic wall rock in a fine-grained matrix (Warr and Cox,

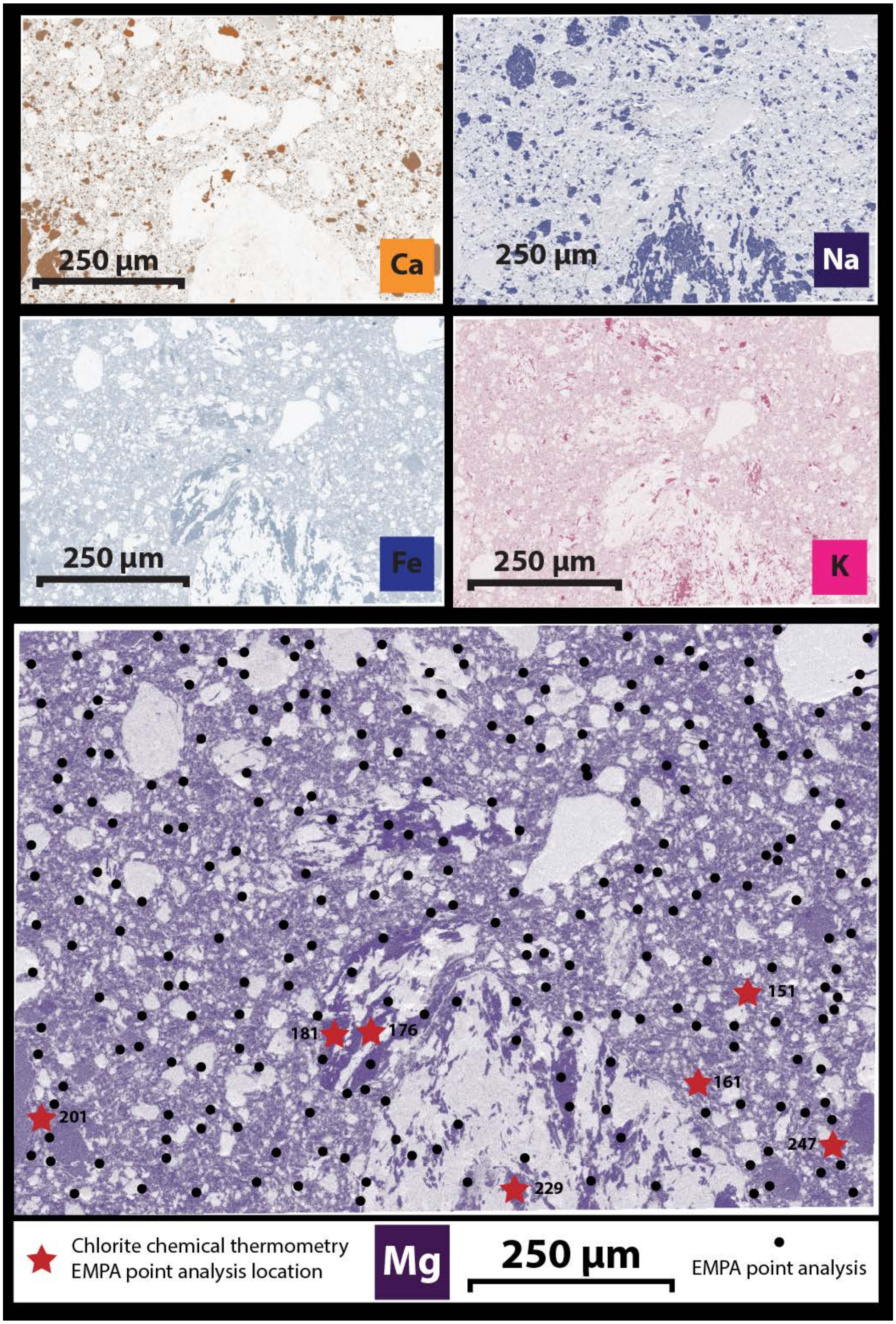

Figure III.III. EDS large-area elemental maps of select elements of the fault gouge from Stoney Creek. EMPA point analysis locations are indicated by black dots on Mg element distribution map; red stars indicate successful chlorite chemical geothermometry sites with numbers specifying the EMPA point analysis identifier.

2001; Passchier and Trouw, 2005). Mm-scale deformation bands with subsidiary (Riedel) shears can be identified in isolated locations within the matrix material. The matrix has near-uniform extinction that may reflect preferred orientation of matrix constituents. Pressure solution features and asymmetric stress shadows can also be identified. The fine-grained nature of the chlorite overprint, as seen in thin section, necessitated the use of electron beam methods for the identification of candidate chlorites for geothermometric analysis.

III.VI.I.II. SEM/EDS

SEM/EDS element maps were created for O, C, Ti, Si, Al, Mg, Fe, Ca, P, S, Na, and K of the PSZ fault gouge sample from Stoney Creek. Figure III.III shows the spatial distribution of select elements (Fe, Mg, Ca, Na, and K). These elemental maps further emphasize the cataclastic nature of the fault gouge, as imaged in optical microscopy. For example, the K distribution map highlights micas deformed by indentation of more competent minerals or clasts. Mg and Fe concentrations from elemental EDS large-area mapping were utilized to identify candidate chlorite locations for subsequent EMPA analysis and chemical thermometry.

III.VI.I.III. EMPA

About 250 candidate chlorite sites identified by SEM/EDS Mg and Fe concentration maps of the fault gouge sample from Stoney Creek were analyzed by EMPA. 7 of these chlorites yielded good quality EMPA results and were within the 4-end-member compositional space to allow for chlorite formation temperatures to be calculated. This large attrition is likely due to sampling bias. Table III.II lists the EMPA results of these 7 point analyses that are relevant for geothermometric analysis.

Table III.II Select chlorite EMPA and geothermometry results

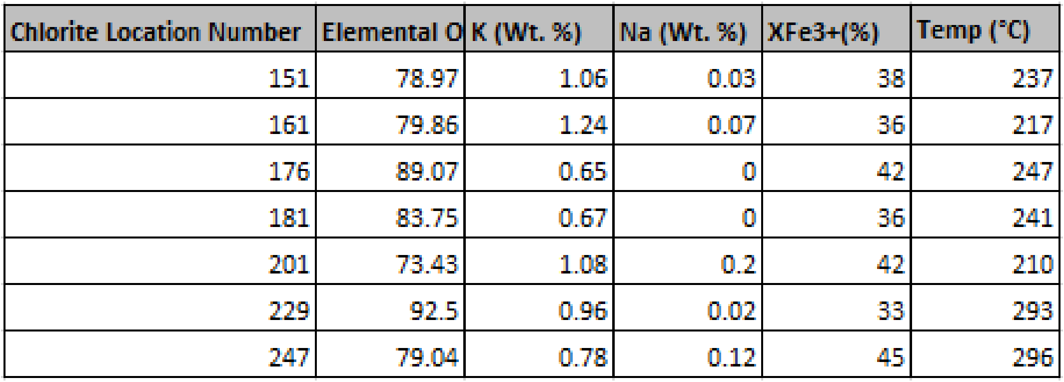

Chlorite Location Number	Elemental O	K (Wt. %)	Na (Wt. %)	XFe3+(%)	Temp (°C)
151	78.97	1.06	0.03	38	237
161	79.86	1.24	0.07	36	217
176	89.07	0.65	0	42	247
181	83.75	0.67	0	36	241
201	73.43	1.08	0.2	42	210
229	92.5	0.96	0.02	33	293
247	79.04	0.78	0.12	45	296

III.VI.I.IV. Chlorite Geothermometry

In addition to the EMPA results, the calculated XFe^{3+} and chlorite formation temperature determined from the thermometer are reported in table III.II. The 7 successfully analyzed sites have a range of temperatures of 210-296ºC (anchizone/sub-greenschist facies). This is consistent with observations from mineralogy of Warr and Cox (2001), who estimated chlorite formation at <320ºC based on composition, recrystallization, and disordered stacking. No noticeable spatial or textural variation in temperature across the area of investigation is identified. Chlorite point analyses from within host-rock clasts, as well as chlorite point analyses within matrix material formed within the same temperature range.

III.VI.II. Illite

III.VI.II.I. Qualitative and Quantitative X-ray Powder Diffraction

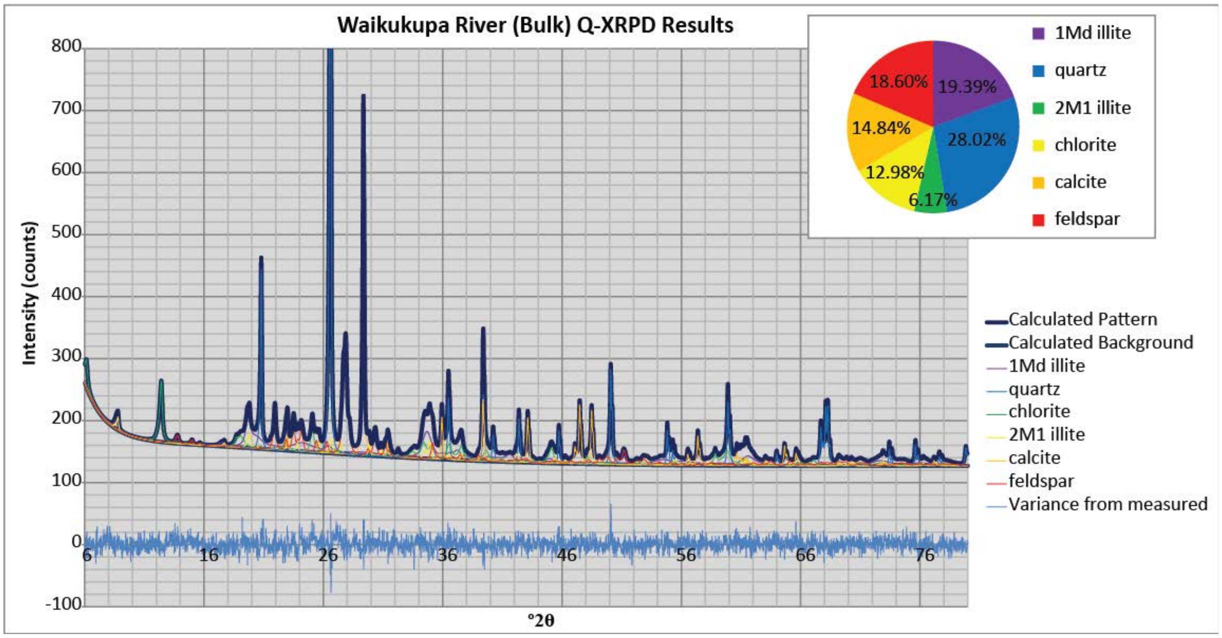

Figure III.IV. Diffractogram of the bulk clay gouge sample from Waikukupa River modeled using Rietveld refinement program BGMN®. The calculated pattern is the sum of each component mineral phase. The curve plotting variance from measured is calculated by taking the difference between the raw data and the calculated pattern. The pie chart shows the calculated modal composition by mineral phase in weight percent.

In contrast to Warr and Cox (2001) and Schleicher et al. (2015b), our qualitative analysis of the 8 fault gouge samples in this study indicates that smectite is a minor clay constituent in the Alpine Fault damage zone, occurring only in small amounts at the Gaunt Creek sampling location. This difference is likely due to the variability of Alpine Fault gouge mineralogy, both mesoscopically

Table III.III. Q-XRPD results from BGMN® analysis (reported values are in weight percent with error ±2 %.)

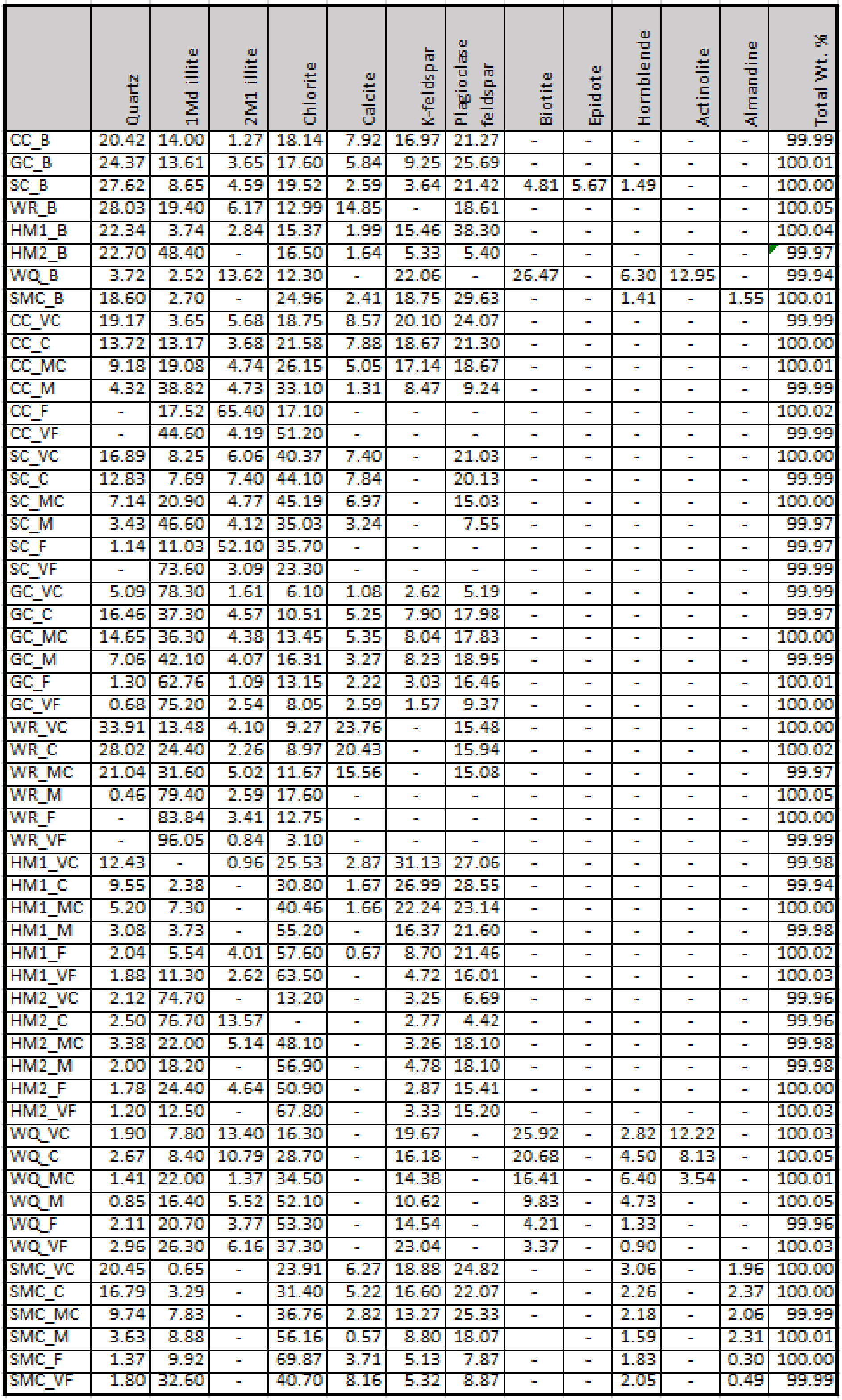

	Quartz	1Md illite	2M1 illite	Chlorite	Calcite	K-feldspar	Plagioclase feldspar	Biotite	Epidote	Hornblende	Actinolite	Almandine	Total Wt. %
CC_B	20.42	14.00	1.27	18.14	7.92	16.97	21.27	-	-	-	-	-	99.99
GC_B	24.37	13.61	3.65	17.60	5.84	9.25	25.69	-	-	-	-	-	100.01
SC_B	27.62	8.65	4.59	19.52	2.59	3.64	21.42	4.81	5.67	1.49	-	-	100.00
WR_B	28.03	19.40	6.17	12.99	14.85	-	18.61	-	-	-	-	-	100.05
HM1_B	22.34	3.74	2.84	15.37	1.99	15.46	38.30	-	-	-	-	-	100.04
HM2_B	22.70	48.40	-	16.50	1.64	5.33	5.40	-	-	-	-	-	99.97
WQ_B	3.72	2.52	13.62	12.30	-	22.06	-	26.47	-	6.30	12.95	-	99.94
SMC_B	18.60	2.70	-	24.96	2.41	18.75	29.63	-	-	1.41	-	1.55	100.01
CC_VC	19.17	3.65	5.68	18.75	8.57	20.10	24.07	-	-	-	-	-	99.99
CC_C	13.72	13.17	3.68	21.58	7.88	18.67	21.30	-	-	-	-	-	100.00
CC_MC	9.18	19.08	4.74	26.15	5.05	17.14	18.67	-	-	-	-	-	100.01
CC_M	4.32	38.82	4.73	33.10	1.31	8.47	9.24	-	-	-	-	-	99.99
CC_F	-	17.52	65.40	17.10	-	-	-	-	-	-	-	-	100.02
CC_VF	-	44.60	4.19	51.20	-	-	-	-	-	-	-	-	99.99
SC_VC	16.89	8.25	6.06	40.37	7.40	-	21.03	-	-	-	-	-	100.00
SC_C	12.83	7.69	7.40	44.10	7.84	-	20.13	-	-	-	-	-	99.99
SC_MC	7.14	20.90	4.77	45.19	6.97	-	15.03	-	-	-	-	-	100.00
SC_M	3.43	46.60	4.12	35.03	3.24	-	7.55	-	-	-	-	-	99.97
SC_F	1.14	11.03	52.10	35.70	-	-	-	-	-	-	-	-	99.97
SC_VF	-	73.60	3.09	23.30	-	-	-	-	-	-	-	-	99.99
GC_VC	5.09	78.30	1.61	6.10	1.08	2.62	5.19	-	-	-	-	-	99.99
GC_C	16.46	37.30	4.57	10.51	5.25	7.90	17.98	-	-	-	-	-	99.97
GC_MC	14.65	36.30	4.38	13.45	5.35	8.04	17.83	-	-	-	-	-	100.00
GC_M	7.06	42.10	4.07	16.31	3.27	8.23	18.95	-	-	-	-	-	99.99
GC_F	1.30	62.76	1.09	13.15	2.22	3.03	16.46	-	-	-	-	-	100.01
GC_VF	0.68	75.20	2.54	8.05	2.59	1.57	9.37	-	-	-	-	-	100.00
WR_VC	33.91	13.48	4.10	9.27	23.76	-	15.48	-	-	-	-	-	100.00
WR_C	28.02	24.40	2.26	8.97	20.43	-	15.94	-	-	-	-	-	100.02
WR_MC	21.04	31.60	5.02	11.67	15.56	-	15.08	-	-	-	-	-	99.97
WR_M	0.46	79.40	2.59	17.60	-	-	-	-	-	-	-	-	100.05
WR_F	-	83.84	3.41	12.75	-	-	-	-	-	-	-	-	100.00
WR_VF	-	96.05	0.84	3.10	-	-	-	-	-	-	-	-	99.99
HM1_VC	12.43	-	0.96	25.53	2.87	31.13	27.06	-	-	-	-	-	99.98
HM1_C	9.55	2.38	-	30.80	1.67	26.99	28.55	-	-	-	-	-	99.94
HM1_MC	5.20	7.30	-	40.46	1.66	22.24	23.14	-	-	-	-	-	100.00
HM1_M	3.08	3.73	-	55.20	-	16.37	21.60	-	-	-	-	-	99.98
HM1_F	2.04	5.54	4.01	57.60	0.67	8.70	21.46	-	-	-	-	-	100.02
HM1_VF	1.88	11.30	2.62	63.50	-	4.72	16.01	-	-	-	-	-	100.03
HM2_VC	2.12	74.70	-	13.20	-	3.25	6.69	-	-	-	-	-	99.96
HM2_C	2.50	76.70	13.57	-	-	2.77	4.42	-	-	-	-	-	99.96
HM2_MC	3.38	22.00	5.14	48.10	-	3.26	18.10	-	-	-	-	-	99.98
HM2_M	2.00	18.20	-	56.90	-	4.78	18.10	-	-	-	-	-	99.98
HM2_F	1.78	24.40	4.64	50.90	-	2.87	15.41	-	-	-	-	-	100.00
HM2_VF	1.20	12.50	-	67.80	-	3.33	15.20	-	-	-	-	-	100.03
WQ_VC	1.90	7.80	13.40	16.30	-	19.67	-	25.92	-	2.82	12.22	-	100.03
WQ_C	2.67	8.40	10.79	28.70	-	16.18	-	20.68	-	4.50	8.13	-	100.05
WQ_MC	1.41	22.00	1.37	34.50	-	14.38	-	16.41	-	6.40	3.54	-	100.01
WQ_M	0.85	16.40	5.52	52.10	-	10.62	-	9.83	-	4.73	-	-	100.05
WQ_F	2.11	20.70	3.77	53.30	-	14.54	-	4.21	-	1.33	-	-	99.96
WQ_VF	2.96	26.30	6.16	37.30	-	23.04	-	3.37	-	0.90	-	-	100.03
SMC_VC	20.45	0.65	-	23.91	6.27	18.88	24.82	-	-	3.06	-	1.96	100.00
SMC_C	16.79	3.29	-	31.40	5.22	16.60	22.07	-	-	2.26	-	2.37	100.00
SMC_MC	9.74	7.83	-	36.76	2.82	13.27	25.33	-	-	2.18	-	2.06	99.99
SMC_M	3.63	8.88	-	56.16	0.57	8.80	18.07		-	1.59	-	2.31	100.01
SMC_F	1.37	9.92	-	69.87	3.71	5.13	7.87	-	-	1.83	-	0.30	100.00
SMC_VF	1.80	32.60	-	40.70	8.16	5.32	8.87	-	-	2.05	-	0.49	99.99

and along strike. Some DFDP studies also identify smectite-rich and smectite-poor gouges (Boulton et al., 2014). The qualitative results, used as inputs into BGMN® modeling, are reported with quantitative results of the bulk samples and each grain size fraction in table III.III (Sample ID's are denoted using abbreviated sampling location identifiers from table III.I, concatenated with grain size fraction identifiers VF<0.05 µm, F=0.05-0.1 µm, M=0.1-0.5 µm, MC=0.5-1.0 µm, C=1.0-1.5 µm, and VC=1.5-2.0 µm). Figure III.IV illustrates the decomposition calculation employed by the Rietveld method on the bulk sample from the Waikukupa River PSZ, and highlights the exceptional model fits achieved by BGMN®.

In addition to modal percentages of minerals, the BGMN® routine differentiates between 1Md and 2M1 illite. Figure III.IV and the Q-XRPD data indicate that the dominant illite polytype in fault gouges of the AFZ is 1Md illite (the low-temperature, poorly-ordered species). Additionally, the finer size fractions are more enriched in 1Md illite, as is typical of fault gouge zones (Haines and van der Pluijm, 2012). Figure III.V displays only the 1Md illite

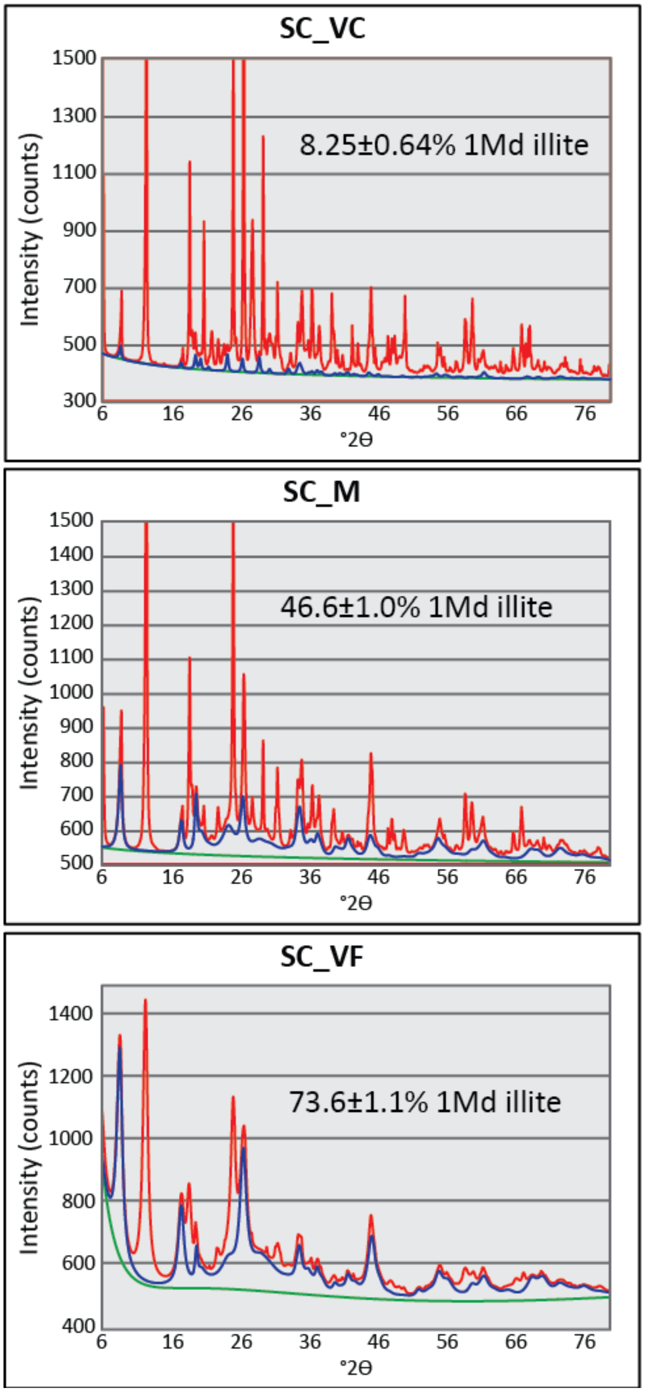

Figure III.V. Modeled diffractograms of three clay-size fractions of the clay gouge sample from Stoney Creek. The red line includes all mineral phases, the blue line shows the 1Md illite contribution, and the green line indicates the background used in the model. The proportion of disordered illite is negatively correlated with grain size.

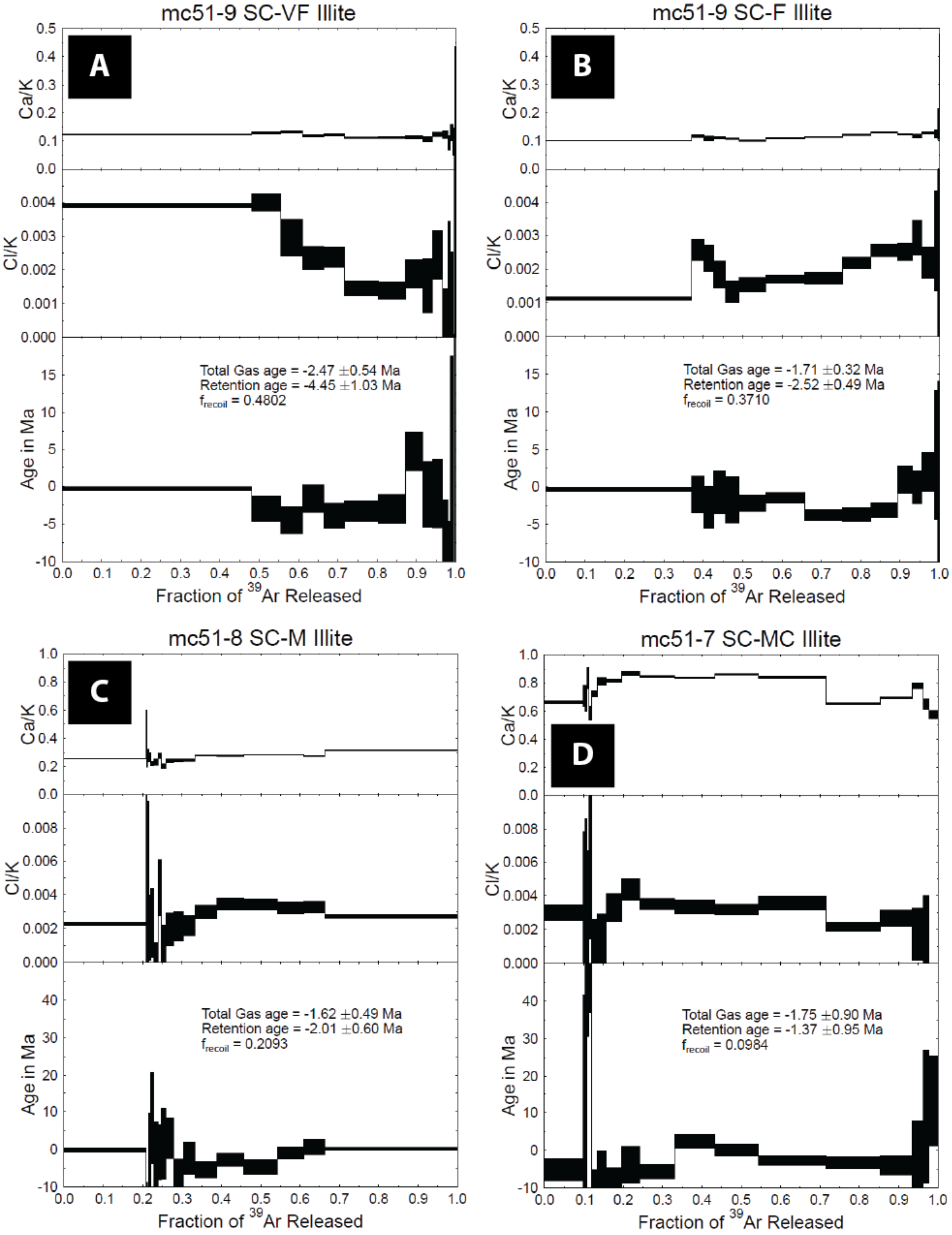

Figure III.VI. Ar degassing spectra for A) SC-VF B) SC-F C) SC-M and D) SC-MC.

contribution to the total measured spectrum of several grain sizes of sample SC, as calculated by BGMN®, to illustrate this negative correlation between grain size and 1Md illite proportion. 1Md illite proportions, with respect to the other hydrous phases (2M1 illite and chlorite), are noticeably less in hanging wall and footwall fault gouges than in the main thrust. This may indicate less total amounts of exhumation on these structures, or less active hydrologic systems due to smaller or non-existent damage zones of auxiliary faults.

III.VI.II.II. $^{40}Ar/^{39}Ar$ Geochronology

Four grain size fractions of the fault gouge from Stoney Creek were selected for age dating. An active Alpine Fault PSZ sampling location was chosen in order to constrain the age of faulting, as opposed to hanging wall or footwall deformation. Of the three candidate samples that fit that criteria (Cataclasite Creek, Stoney Creek, and Gaunt Creek), the sample from Stoney Creek had the most robust Q-XRPD results with the wide range of 1Md/2M1 ratios needed to avoid the "unochron error" as described by van der Pluijm and Hall (2015).

Figure III.VI displays the degassing spectra for each of the four size fractions of sample SC that were dated. All age dates, both total gas and retention, are in negative age space due to an integrated $^{40}Ar/^{39}Ar$ ratios below the atmospheric value of 295.5. No correlation with grain size is identified. The samples most likely fractionated initial argon. Moreover, high Cl/K and Ca/K ratios in several of the grain size fractions lend uncertainty to the results due to recoil artifacts. For sub-micron samples with relatively high initial Ar and low K, our age estimate is <0.5 Ma.

III.VI.II.III. H Isotopic Analysis

Results of the hydrogen isotopic analysis of each of the 6 size fraction for each of the 8 samples are presented in table III.IV, and are arranged by fault type (hanging wall fault gouge, footwall fault gouge, or main thrust fault gouge). Some samples are more depleted in deuterium in the finer fractions, while others are not. Measured values of hanging wall fault gouge clay fractions are in the range of -95 to -105‰, footwall fault gouge clay fractions are in the range of -78 to -100‰, and main thrust gouge clay fractions are in the range of -71 to -103‰.

III.VI.II.IV. Illite Polytype Analysis

In order to parse the measured isotopic signal, which is a composite of H contributed by 1Md illite, 2M1 illite and chlorite, we utilize illite polytype analysis. We extract the H signal inherent to authigenic 1Md polytype illite by correlating measured δD with % contribution of 1Md illite to the total measured signal using γ, defined in equation III.I, and extrapolating to end-member values:

$$Eq. III.I\ \gamma = \frac{\%1Md\ illite}{(\%\ 1Md\ illite + \%\ 2M1\ illite + \%\ chlorite)} * 100$$

Table III.IV. Results of Hydrogen Isotopic Analysis

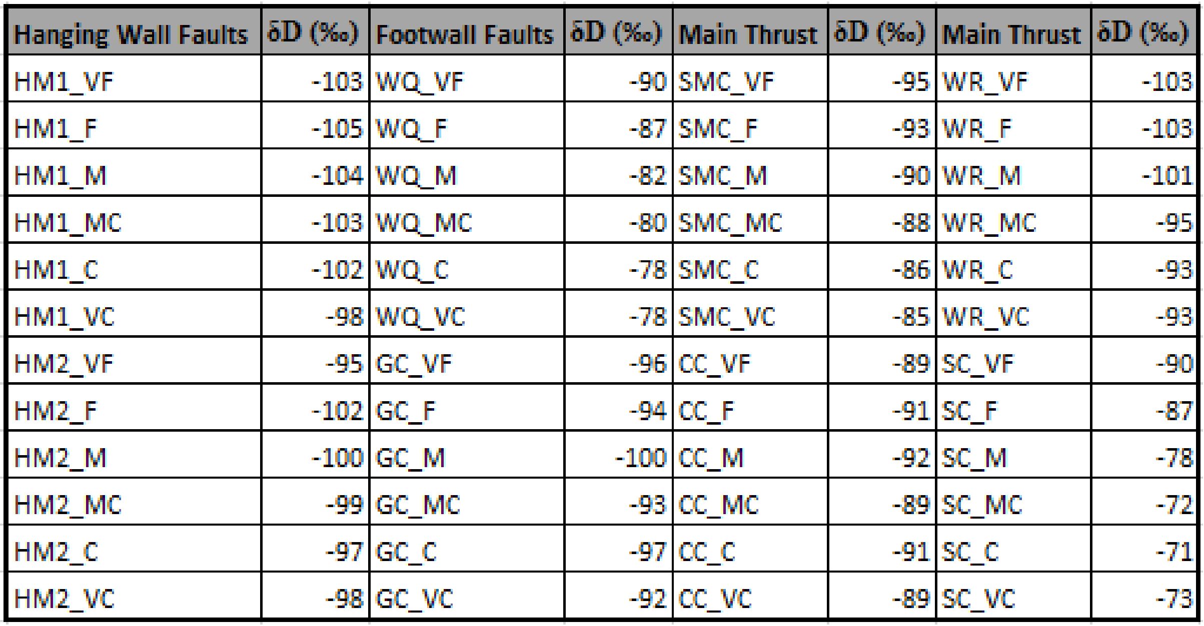

Hanging Wall Faults	δD (‰)	Footwall Faults	δD (‰)	Main Thrust	δD (‰)	Main Thrust	δD (‰)
HM1_VF	-103	WQ_VF	-90	SMC_VF	-95	WR_VF	-103
HM1_F	-105	WQ_F	-87	SMC_F	-93	WR_F	-103
HM1_M	-104	WQ_M	-82	SMC_M	-90	WR_M	-101
HM1_MC	-103	WQ_MC	-80	SMC_MC	-88	WR_MC	-95
HM1_C	-102	WQ_C	-78	SMC_C	-86	WR_C	-93
HM1_VC	-98	WQ_VC	-78	SMC_VC	-85	WR_VC	-93
HM2_VF	-95	GC_VF	-96	CC_VF	-89	SC_VF	-90
HM2_F	-102	GC_F	-94	CC_F	-91	SC_F	-87
HM2_M	-100	GC_M	-100	CC_M	-92	SC_M	-78
HM2_MC	-99	GC_MC	-93	CC_MC	-89	SC_MC	-72
HM2_C	-97	GC_C	-97	CC_C	-91	SC_C	-71
HM2_VC	-98	GC_VC	-92	CC_VC	-89	SC_VC	-73

The illite polytype analysis mixing plots for H created by the correlation of δD and γ are displayed in figure III.VII. In order for this approach to be viable, due to the different contributions to the measured H signal of chlorite (8 H atoms per structural unit) vs. illite (2 H atoms per structural unit), the produced correlation must be highly linear. A linear correlation between δD and γ (when multiple phases contribute to the measured signal) indicates that either i) each of the phases are present in the exact same proportion in all of the measured size fractions, which is highly unlikely based on sample preparation methodology, or ii) the two high temperature phases 2M1 illite and chlorite have identical isotopic compositions. We rely on the latter, that 2M1 illite and chlorite carry the same isotopic signal, based on overlap of the thermodynamic range of 2M1 illite and the calculated chlorite formation temperature range of this study (Meunier and Velde, 2004).

Extrapolation to end-member values along the York-type linear regression lines in figure III.VII yields 1Md illite H composition on one side of the diagram and 2M1/chlorite H composition on the other. Two types of behavior are observed in these mixing plots. Figure III.VIIa displays samples that exhibit grain size dependent δD behavior; figure III.VIIb displays samples whose δD

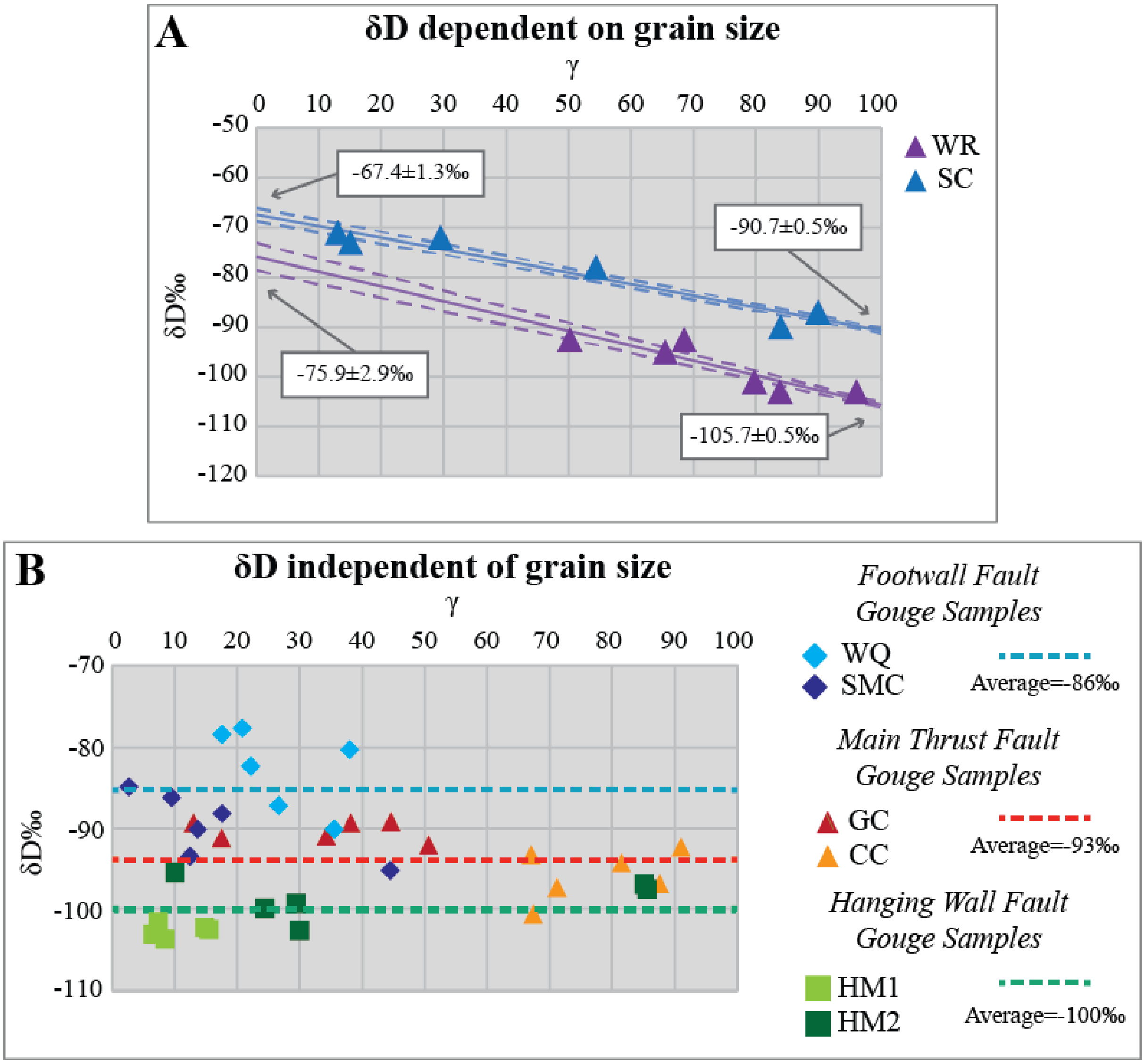

Figure III.VII. Illite polytype analysis mixing plots. As defined by eq. III.I in the text, γ represents the %1Md illite normalized by the modal % of the total hydrous phases present (1Md illite, 2M1 illite, and chlorite). A) Two main thrust fault gouge samples (WR and SC) display grain size dependent H isotopic behavior. York-type linear correlations (solid lines), error envelopes (dashed lines), and end-member extrapolations are displayed for each sample. B) All other fault gouge samples display grain-size independent H isotopic behavior. Footwall fault gouges are diamond symbols, main thrust fault gouges are triangles, and hanging wall fault gouges are squares. Dashed lines indicate average compositions based on fault type.

composition does not vary with grain size. Only two samples display grain-size dependent H isotopic behavior, from Waikukupa River and Stoney Creek (figure III.VIIa). All other samples have H isotopic behavior independent of grain size (figure III.VIIb). Footwall fault gouge samples have an average composition of -86‰, hanging wall fault gouge samples have an average composition of -100‰, and main thrust fault gouge samples from Gaunt Creek and Cataclasite Creek have average δD of -93‰. A -14‰ difference between hanging wall and footwall fault gouge clays is observed, with hanging wall gouges more depleted in deuterium. The 1Md illite end-member of all mixing plots has an isotopic range of -86 to -105‰. 2M1/chlorite end-members of δD independent fault gouges (7b) have a similar range, -86 to -100‰. The 2M1/chlorite end members of samples WR and SC, however, have an isotopic range of -67 to -76‰.

We use the fractionation equations of Graham et al. (1987) and Capuano (1992) to convert these values to equilibrium fluid values for chlorite and illite, respectively. At an average chlorite formation temperature of 250ºC (obtained from chemical thermometry), the average footwall fault gouge composition of -86‰ yields a chlorite mineralizing fluid value of -55‰, the average hanging wall fault gouge composition of -100‰ yields a chlorite mineralizing fluid value of -69‰, and the average composition of main thrust samples GC and CC of -93‰ yields a chlorite mineralizing fluid value of -62‰. The illite fractionation equation yields the same results using a mineralogically-consistent temperature value of 100±25ºC, allowing for both illite and chlorite in these samples to have formed in equilibrium with the same fluid.

Using the same chlorite formation temperature, the mineralizing fluid compositions for chlorite in samples WR and SC are -46 and -36‰, respectively. A temperature of 100±25ºC, consistent with the 1Md illite in the previous samples, yields illite mineralizing fluid compositions of -75 and -60‰ for samples WR and SC, respectively. As a summary, chlorite in 6 of the 8 samples and 1Md illite in all of the samples formed in equilibrium with fluid in the δD range of -55 to -75‰, whereas chlorite in the other two samples formed in equilibrium with fluid in the δD range of -36 to -45‰.

III.VII. Discussion

III.VII.I. Chlorite

The fine-grained and pervasive nature of the Mg-chloritization event experienced by these fault rocks is highlighted by electron microscopic analysis. Fine-grained Mg-rich chlorite is ubiquitous to the PSZ gouges. Given consistent formation temperatures between 210-296ºC, this chlorite likely represents a retrograde alteration of higher metamorphic facies Alpine Schist rocks as they are exhumed along the AFZ, with the following (Craw et al., 2009):

$$metamorphic\ chlorite \rightarrow hydrothermal\ chlorite$$
$$(negligible\ compositional\ change)$$

Using the extreme temperature gradient measured in the DFDP-2B borehole of 125ºC/km (Sutherland et al., 2015), the chlorite formed at a minimum of 2 km depth; the measured geothermal gradient of the DFDP-1B borehole of 63ºC/km (Sutherland et al., 2012), which is more consistent with finite element models of the near surface (Allis and Shi, 1995; Shi et al., 1996), a maximum chlorite formation depth can be constrained at 5 km. An exhumation rate of 10 mm/yr in the central Alpine Fault region (Cooper and Norris, 1994; Norris and Cooper, 2000), from a depth of 5 km, indicates a crystallization age of <0.5 Ma, consistent with the maximum illite crystallization age estimate from Ar geochronology.

In the majority of the samples, the chlorite has equilibrium fluid values in the range of modern meteoric fluid of -50 to -80‰ in this area (Rogers et al., 2012). Two samples (CC & GC), however, have δD values that are more enriched in deuterium, and the equilibrium fluid for the chlorite in these samples is likely dominated by a metamorphic fluid component. Experimental studies of the H-diffusion behavior of well-crystallized phyllosilicates indicate that post-crystallization re-equilibration on 10^5 year timescales and at temperatures 200-300ºC will be near complete (Graham, 1981). We envision a chlorite retrograde reaction scenario similar to Craw et al. (2004) and Craw (2009), and that near-complete overprint by topographically-driven meteoric fluid occurs during late-stage exhumation. It is also possible that along-strike variations in the dominant fault-related fluid flow direction preferentially preserved or overprinted the isotopic signal of the chlorite material (e.g. Muir-Wood, 1994; López and Smith, 1995).

III.VII.II. Illite

The geothermal gradients of 125ºC/km and 63ºC/km from the DFDP boreholes constrain 1Md illite neocrystallization and thermodynamic stability to depths <2 km. This temporally necessitates a post-chlorite formation that occurs at a shallower crustal level along the AFZ exhumation pathway. Illite likely formed from the following reaction (Craw et al., 2009):

$$Metamorphic\ muscovite + albite \rightarrow hydrothermal\ muscovite\ (\rightarrow illite)$$

$$KFe_{0.2}Mg_{0.2}Al_{2.0}Si_{3.3}O_{10}(OH)_2 + 0.2\ Al^{3+}_{(albite)}$$

$$\rightarrow KFe_{0.05}Mg_{0.05}Al_{2.2}Si_{3.3}O_{10}(OH)_2 + 0.15\ Fe^{2+}_{(pyrite,chlorite)} + 0.15\ Mg^{2+}_{(chlorite)}$$

Equilibrium fluid values are in the range of modern meteoric water, similar to most chlorite samples, and the <0.5 Ma crystallization estimate indicates that 1Md illite authigenesis is, indeed, a recent, near-surface phenomenon.

III.VII.III. Implications for Fault Behavior

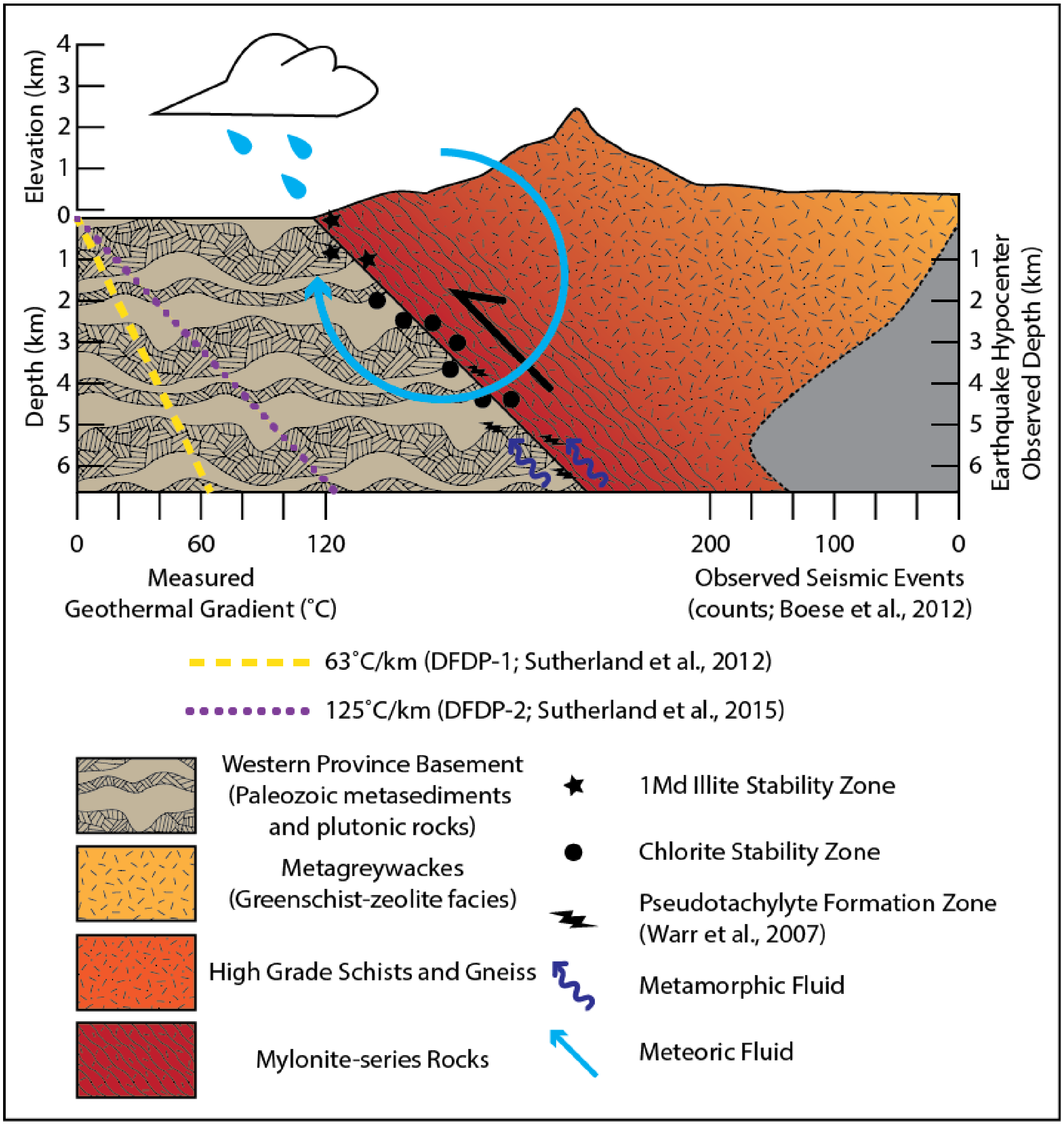

Figure III.VIII. An idealized cross-section of the central Alpine Fault Zone that indicates that the thermodynamic stability of fault-hosted clay reaches its down-dip limit above the main load-bearing portion of the seismogenic crust.

Figure III.VIII is an idealized cross section of the central Alpine Fault Zone that indicates thermodynamic stability ranges of fault-hosted 1Md illite and chlorite mineralization, pseudotachylyte generation depths (Warr et al., 2007) as well as a histogram of observed earthquake hypocenter depths (Boese et al., 2012). Friction melts related to Alpine Fault Zone deformation have been estimated to form at depths between 3.5-11 km in this orogen (Warr et al., 2003; Warr et al., 2007). The main load-bearing portion of the crust is observed from seismicity to be from 5-12 km depth (Beavan et al., 1999; Leitner et al., 2001; Boese et al., 2012). From these observations, we see that the thermodynamic stability of fault-hosted clay mineralization is greatly attenuated by seismogenic depths, and likely very little clay constituents are present in the PSZ of the Alpine Fault at these seismic rupture depths. The seeming paradox of a "strong" fault behavior and an exhumed PSZ filled with "weak" fault material is, therefore, resolved by clay material in the Alpine Fault as a surface alteration product that has little relevance for deeper fault rupture processes.

III.VIII. Conclusions

Both chlorite and illite clay populations present in fault gouge samples from the central Alpine Fault Zone, New Zealand, preserve late-stage, surface-localized histories. Chlorite formed at temperatures between 210-296°C as a retrograde alteration product. We posit that its mineralizing fluid was originally metamorphic in origin, but that significant isotopic overprinting due to H diffusion occurred, resulting in the dominance of a meteoric fluid signal from these chlorite minerals. 1Md illite formed at temperatures ~100°C, with a distinct meteoric fluid signal, and with an Ar age of <0.5 Ma. These isotopic constraints corroborate the temperature limits on clay mineralization presented by Warr and Cox (2001) and others, and imply topography-driven infiltration of meteoric fluid to depths as great as 5 km. In addition, a -14‰ δD difference between hanging wall and footwall fault zone gouges indicates a history of fault sealing behavior.

We conclude that the voluminous, mechanically weak clay material that is a distinctive feature of the Alpine Fault Zone surface geology is limited to depths <2 km for illite and <5 km for chlorite. This resolves the apparent paradox of large magnitude earthquakes along the fault and the presence of frictionally weak material in exhumed fault gouge. It is likely that deeper fault zone architecture, in terms of lithology and chemistry, differs significantly from the surface exposures, highlighting the need for a continuation of Deep Fault Drilling Project activities aimed at intersecting the Alpine Fault at greater structural depths.

III.IX. Acknowledgments

We thank the DFDP research team for field support and suggestions on surface sampling locations; no clay-rich principal slip zone samples were obtained from drilling. We benefitted from discussions with DFDP team members, particularly Schleicher, Sutherland, Townend and Toy on the geology of the Alpine Fault. We thank Brice Lacroix for help and conversations about chlorite geothermometry. Jasmaria Wojatschke contributed to the development of Q-XRPD analysis at Michigan. Chris Hall (Michigan) and Jens Fiebig (Frankfurt) offered expert support for Ar geochronology and stable isotope geochemistry, respectively. Our fault rock research is supported by the National Science Foundation, most recently under EAR-16PAF03738. We thank Nick Timms and an anonymous reviewer, who greatly improved this work.

Chapter IV. Response of Natural Smectite to Seismogenic Heating and Potential Implications for the 2011 Tohoku Earthquake in the Japan Trench

IV.I. Abstract

The sensitivity of smectite during brief and protracted heating intervals can provide crucial information about the temperature history of faults during seismogenic slip and creep. Pelagic-sourced smectite is the most abundant clay mineral that is incorporated into the slip zone that was drilled during the Japan Trench Fast Drilling Project (JFAST) Expedition 343 in the Japan Trench, located ~820 m below seafloor. This study investigates the potential for abundant smectite to preserve a record of coseismic frictional heating associated with the Tohoku earthquake in May 2011 by laboratory examination of mineral hydration and dehydration in JFAST drill core samples during brief (maximum of 5 min) and protracted (5 h) heating sequences. Using a real-time heating stage that is connected to an X-ray diffractometer, we observe that (1) both brief and protracted heating causes reduction of water interlayers in smectite, (2) smectite recovers faster to the original hydration state after quick heating than long heating, and (3) nonrecoverable collapse of all smectite occurs at >200 °C for brief and protracted heating rates. Because hydrated, smectite clays are widely present in the fault rocks, we conclude that frictional heating within the slip zone of the Tohoku fault zone cannot have reached significantly elevated temperatures.

IV.II. Introduction

The Magnitude 9.0 Tohoku earthquake in the Japan Trench in March 2011 caused large coseismic slip (50 m) on the shallow portion of the fault, which propagated to the trench and produced a disastrous tsunami (e.g., Lay et al., 2013). In order to understand the conditions and associated hydromechanical processes during seismogenic slip, we investigate the properties of fault-related mineral reactions that may occur. The study of clay minerals has contributed greatly to our understanding of permeability and frictional properties in slip zone environments (e.g., Saffer et al., 2001), and the nature of discrete smectitic clays place constraints on the ambient conditions of fault zones, as they are typically not stable at persistent temperatures above ~150–200 °C (e.g. Freed and Peacor, 1989). In contrast to regional heating, temperature changes during seismogenic slip are fast and may dissipate quickly. Clay-rich gouges are quickly heated and effectively undrained, especially when wet, in association with changing cation content or layer charge (Perry and Hower, 1970; Huang et al., 1994). Thermal pressurization may occur (Rice, 2006), which would inhibit large temperature increases in the area within and adjacent to the principal slip zone (e.g., Chen et al., 2013). In this study we examine the behavior of smectite clay minerals that were collected from the Japan Trench Fast Drilling Project (JFAST), using elevated temperatures at brief and protracted intervals, reflecting a range of natural conditions. The question examined is whether smectite can withstand quick, frictional heating during seismogenic movement, without permanently changing the internal structure or undergoing phase transformation. If so, then smectite clays would be a proxy of maximum temperature conditions along seismogenic faults.

IV.III. Geology, Samples, and Analytical Methods

The JFAST drill site is located off Oshika Peninsula, west of the axis of the Japan Trench, where the Pacific plate thrusts underneath northeastern Honshu, Japan (Chester et al., 2012; Mori et al., 2012). During Expedition 343 of the Integrated Ocean Drilling Program (IODP), three holes were drilled 12 months after the 9.0 Tohoku earthquake at Site C0019, to investigate the mechanics and mineralogy of great subduction earthquakes (Chester et al., 2013). At Hole C0019E, ~55 m of discontinuous core was recovered; the top of the geologic plate boundary is ~820 m below seafloor (mbsf; Kirkpatrick et al., 2015). A ~1-m-thick shear zone of scaly clay was observed in the pelagic clay layer between 821.5 and 822.65 mbsf. The fabric defines a spaced, anastomosing foliation that bounds variably shaped and sized lenses of clay. A borehole temperature observatory was installed 16 months after the earthquake (Expedition 343T), in order to investigate the temperature directly at the plate boundary fault (Fulton et al., 2013). Small rock chips (~1 × 1 cm) of five samples from Hole C0019E were taken for mineralogical analysis. One sample was taken ~60 cm below a localized slip zone (shown as fault B of Kirkpatrick et al., 2015; Figure IV.I, sample 17R_01_86–87.5), and a second rock chip was taken ~2 cm below the localized slip zone (sample 17R_01_20). Both samples are dark brown and show an intense scaly fabric (Chester et al., 2013; Figure IV.IB). For mineralogical comparison, three samples of the surrounding hanging wall and the footwall were also investigated. The mineral assemblages were determined using a Rigaku Ultima IV X-ray diffractometer (XRD) operating at 40 kV and 44 mA with Cu-Kα radiation. Bulk

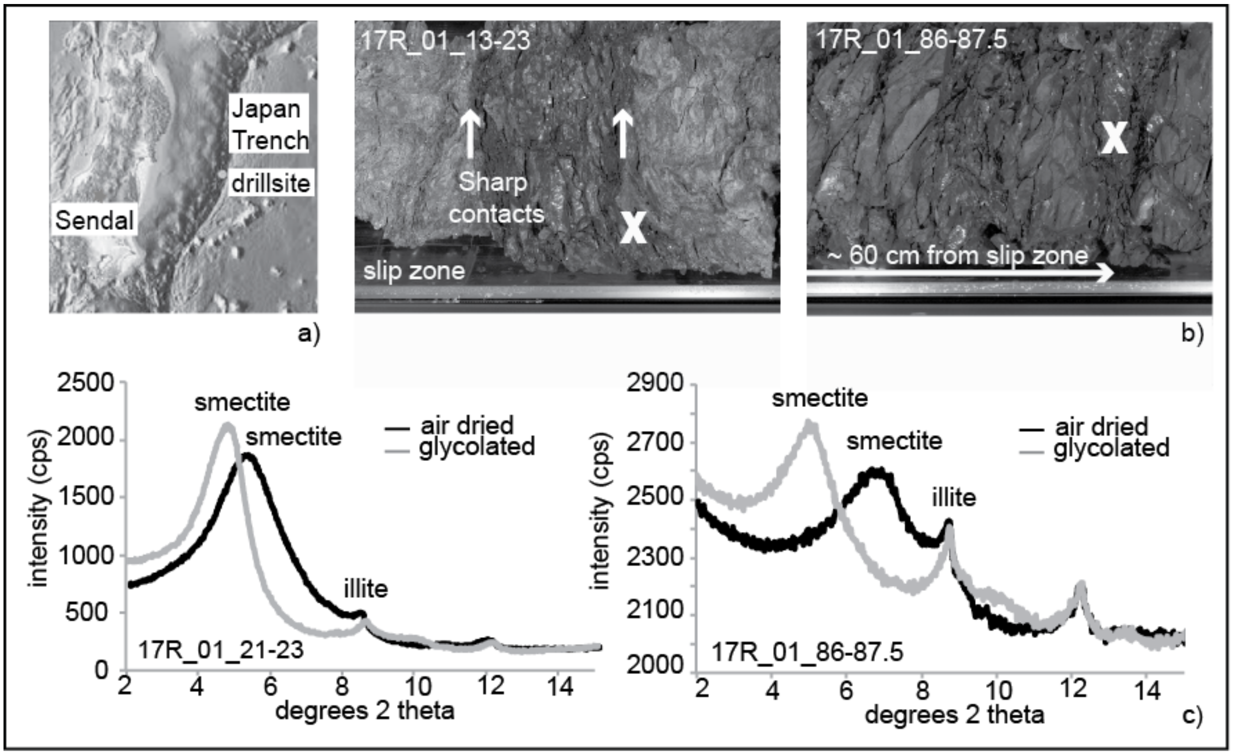

Figure IV.I. A: Location of the Japan Trench Fast Drilling Project (JFAST) drill site in the Japan Trench, modified after the Japan Agency for Marine-Earth Science and Technology/ Integrated Ocean Drilling Program (JAMSTEC/IODP) website (www.jamstec.go.jp/chikyu/e/exp343 /science.html). B: Zoom images from the sample areas of core C0019E-17R. C: X-ray diffraction patterns of the clay size fraction (<2 μm).

rock powder samples were analyzed for general mineralogic composition, and oriented clay-sized mineral analysis (<2 mm) was conducted to determine the clay mineralogy (Moore and Reynolds, 1997). After general mineralogical analysis, a chamber with digital temperature control was installed into the XRD for sample heating experiments (figure IV.II). In order to measure only smectitic clay minerals, the grain size fraction 0.05–0.1 mm was used. Two measurement sets were done: brief heating (5 min) and protracted heating (5 h). For brief heating, eight analyses of each sample were performed in total. An XRD pattern was obtained at 25 °C, after which the chamber (including the sample) was heated within 3–5 min to the specific peak temperatures (50, 75, 100, 125, 150, 175, 200, or 225 °C), and XRD patterns were immediately collected at each temperature step. After each measurement, the chamber was cooled down to 25 °C (10–20 min) and a final XRD pattern was obtained, as well as 1–3 days after the first measurements. A similar procedure was used for protracted heating, except that the chamber was held at the high-temperature target for 5 h at specific peak temperatures before taking the XRD patterns. Temperature, holding time,

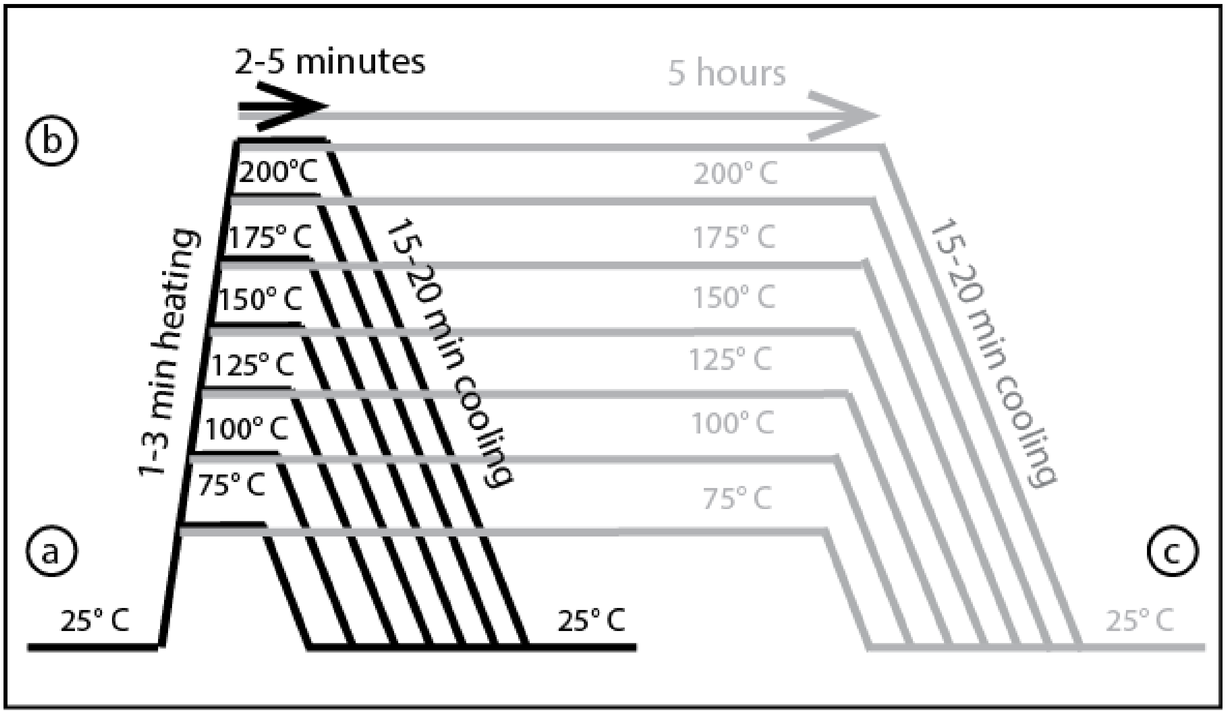

Figure IV.II. Powdered samples were measured after 5 min (black) and 5 h (gray). A: Pre-heating at 25 °C, ~30% RH (relative humidity). B: At 50, 75, 100, 125, 150, 175, 200, and 220 °C. C: Post-heating at 25 °C, ~30% RH.

measure time, and range were computer controlled. The range of heating rate and duration reflect likely conditions in the natural fault zone during the Tohoku earthquake, so the results enable us to make inferences about the effects of heating under natural conditions.

IV.IV. Results

IV.IV.I. Mineralogy and Chemical Composition

All samples investigated contain the clay minerals chlorite/kaolinite, illite, and smectite (see also Kameda et al., 2015). Illite is the main mineral in footwall and hanging-wall rocks. Within the gouge zone (Figure IV.I), smectite is the principal mineral constituent. The X-ray pattern of the clay size fraction (<2 mm) of the sample next to the slip zone (Kirkpatrick et al., 2015, fault B therein) shows a characteristic smectite peak with a d‑value of 1.5 nm, reflecting ~2 water layers under air-dried conditions (25 °C, ~30% relative humidity, RH; Figure IV.IC). This peak moves to 1.7 nm after ethylene glycolation, which reflects as many as three water layers (2 sheets of ethylene glycol molecules). A small peak at 1.0 nm implies that some discrete illite is present. The X-ray pattern of the sample ~60 cm below the slip zone shows a similar characteristic smectite peak with a d-value of 1.4 nm, reflecting ~1–2 water layers under air-dried conditions. This peak also increases to 1.7 nm after glycolation. The chemical composition of smectite shows a montmorillonite with Fe and Mg as the most abundant major rock-forming elements, with Fe2O3 9.61 wt%, MgO 3.26 wt%, and K2O 2.14 wt%.

IV.IV.II. High-Temperature Analyses

Figure IV.III shows the X-ray diffraction patterns of smectite at brief and protracted heating times and at different temperatures. Because of the relatively steady temperature of ~20 °C and constant

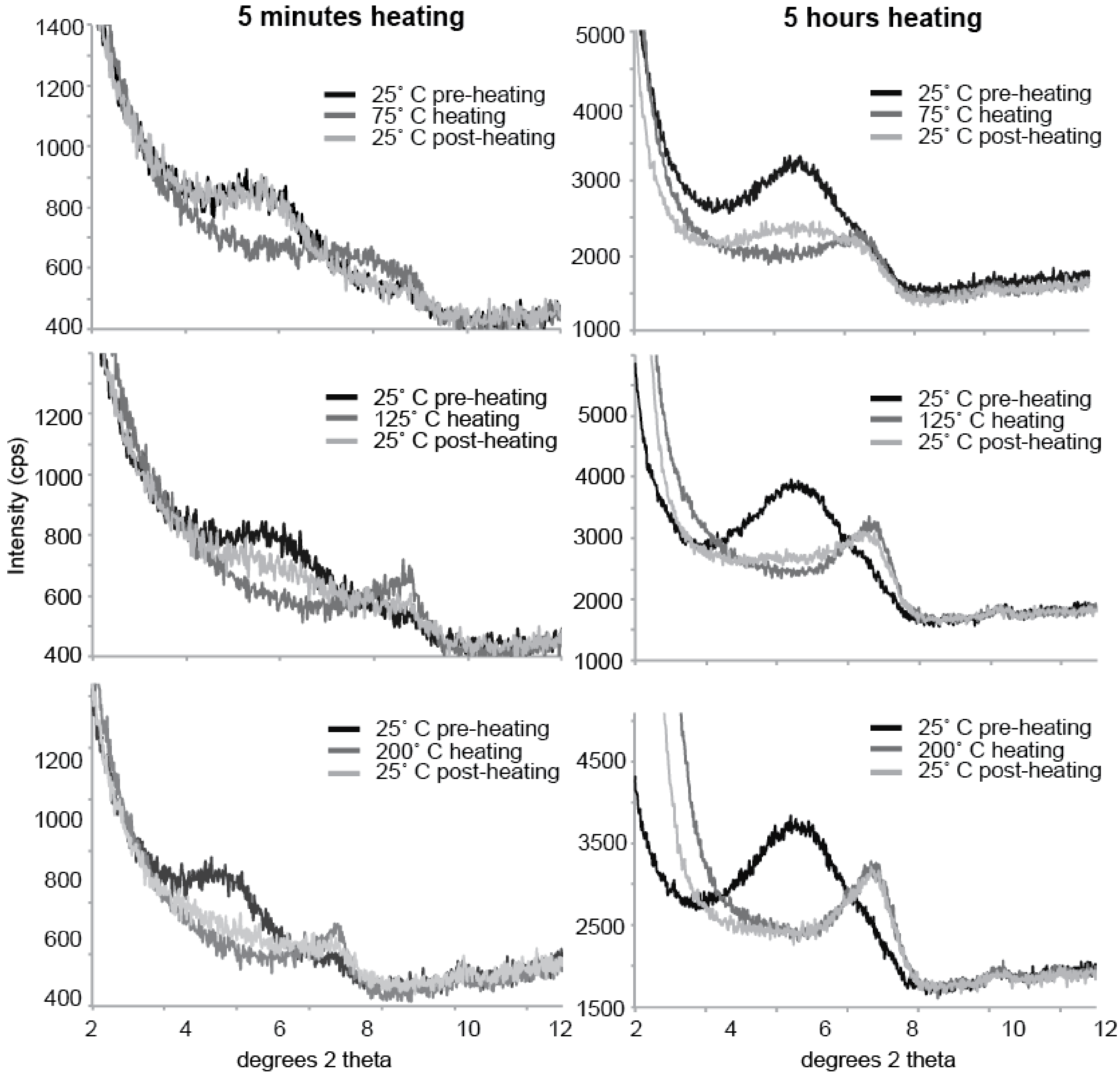

Figure IV.III. High-temperature analysis of the Japan Trench Fast Drilling Project (JFAST) sample 17R_01_67‑68, ~60 cm below the slip zone area.

RH of ~30% in the laboratory, all samples analyzed at 25 °C show smectite peaks ranging between 1.3 nm and 1.4 nm (1–2 water layers). For comparison, samples were also measured at 25 °C and ~30% RH 1 day and as many as 3 days after the experiment.

IV.IV.II.I. Brief Heating Response

The first sample measured at 25 °C and ~30% RH shows a smectite peak at ~1.4 nm, which is typical for air-dried smectite (Figure IV.IIIA). After quick heating to 50 and to 75 °C, most, but not all, of the water is expelled from the interlayers, leaving an irregular peak shape with 2 maxima at ~1.1 nm and 1.0 nm. This shape occurs because of the relatively fast temperature increase, so water was not able to vacate the interlayers completely. After quick cooling back to 25 °C, water reentered the interlayers and the smectite peak returned to 1.4 nm, identical to the first measurement. This pattern remained unchanged one day after the initial measurement. Similar peak behavior was observed between 100 °C and 125 °C heating temperatures. A permanent change is recognized at a heating temperature of 150 °C (Figure IV.IIIB); here, the water was almost completely expelled during quick heating, and a single peak at 1.0 nm reflects the dry smectite phase. After cooling back to 25 °C, some water reentered the interlayer space of smectite, but the new value did not reach its original dimension. One day after the initial measurement, however, the initial water layers were mostly recovered. In contrast, a permanent change is observed at 200 °C. After quick heating to this temperature, the water was completely expelled from the crystal structure (Figure IV.IIIC), and no water was able to reenter the interlayers after cooling down to 25 °C. This hydration process of smectite possesses a notable hysteresis curve, and the difference between pre-heating and post-heating may be related to the maximum extent of collapse (e.g., Bérend et al., 1995). Even after several days, no water had reentered the interlayers.

IV.IV.II.II. Protracted Heating Response

The same types of experiments as above were conducted for protracted heating analysis (Figures IV.IIID-F). Here, the sample was heated quickly and held at temperature for 5 h prior to remeasurement. The smectite peak at 1.4 nm that occurs at 25 °C and ~30% RH reflects 1–2 water layers in the interlayer sheets. However, after heating the sample to 50 and to 75 °C, water was expelled almost completely from the interlayers, leaving a single dry smectite peak at 1.0 nm (Figure IV.IIID). After cooling back to 25 °C, the peak at 1.4 nm reappears, albeit with a lower intensity. The intensity of this peak increases one day post-heating. Similar patterns were observed between 100 and 125 °C. At a heating temperature of 150 °C, water was completely expelled from the interlayer sheets (Figure IV.IIIE), and the intensity of the dry smectite peak at 1.0 nm increased. After cooling back to 25 °C, the sample shows a very small and broad peak, indicating that smectite is still able to recover. After one day, the water was able to reenter the interlayer sheet. At 200 °C, however, the structure of the smectite was permanently altered, such that no water was able to reenter the interlayer site even after several days.

IV.V. Discussion

Ideal conditions exist for smectite minerals at the JFAST drill Site C0019, with a relatively low ambient temperature of 26 °C ~820 mbsf and the presence of ample fluid (Chester et al., 2012). Smectite is observed in the entire core of Hole C0019E, and, notably, the slip zone at ~820 mbsf is composed mostly of smectitic minerals that are incorporated into the fault rock (Figure IV.I; Kameda et al., 2015). Smectite is also common at other drill sites along the Japan Trench, so our observations are applicable to other areas. Ocean Drilling Program (ODP) Sites 1150 and 1151, which are located in the deep-sea terrace on the landward side of the Japan Trench, show similar sedimentary sequences with various silty-clay to claystone lithologies (Sacks et al., 2000). In Deep Sea Drilling Project (DSDP) Legs 56 and 57, drilled in the Japan Trench transect, sandstone, siltstone, and claystone alternate throughout the hole. Leg 56 (Site 436) is particularly relevant, because the basal sediments on the outer rise of the Pacific plate show a lithology similar to the subhorizontal strata below ~820 mbsf of the JFAST drill Site C0019 (Chester et al., 2013; Mann and Mueller 1980). Units 4–7 of Site C0019 correlate to Site 436 unit 3, which matches the smectite-rich brown clay at Site 436 and the multicolored smectitic clays close to the slip zone at Site C0019. The slip zone likely utilized the mechanically incompetent clay layer, incorporating preexisting, weak, pelagic smectite into the fault gouge. During the Tohoku earthquake in March 2011, large fault displacement significantly affected pressure temperature conditions in the rocks, as proposed by Chester et al. (2013) and Ujiie et al. (2013). Sudden slip was postulated to have quickly generated high local heat, with temperatures in a narrow slip zone increasing briefly, as proposed by Fulton et al. (2013). Assuming a slip duration of 50 s and a slip zone thickness <1 mm, Fulton et al. (2013) proposed a maximum peak temperature within the slip zone as high as 1250 °C, combined with a very low coefficient of friction of 0.08. Thicker zones would have had slightly lower temperatures, but even a ~4-cm thick shear zone produces a temperature of 200 °C. Frictional heating during large slip displacement earthquakes should therefore significantly change the hydromechanical properties of smectite in these rocks. Our experiments show that even a brief heat pulse could not have exceeded 175–200 °C without permanently altering the observed smectite clay minerals. In JFAST samples there is no indication of such change to smectite minerals, whether they are very close to (~2 cm) or near (~60 cm) the presumed main slip surface. Instead, the samples investigated show abundant smectite with indistinguishable swelling behavior (Figure IV.I), containing one to two water layers that increase to three layers after ethylene glycolation. Whereas minor discrete illite occurs in conjunction with smectite in both samples near the slip zone, there is less illite in the sample closest to the slip surface. Dehydrated smectite is structurally distinct from illite, and remains a smectite family mineral even in a collapsed state unless its lattice arrangement is permanently modified. In contrast, Yamaguchi et al. (2011) proposed a transformation of smectite to illite clay minerals in the Nankai Trough subduction zone, caused by frictional heat based on geochemical X-ray fluorescence mapping and XRD analysis. Yamaguchi et al. (2011) argued that a higher content of illite in illite-smectite mixed layered clays in the fault gouge was caused by frictional heating effects, suggesting that seismic slip can propagate to very shallow levels along the megasplay fault system. Because there is abundant smectite and little illite in the JFAST sample closest to the slip zone, evidence for local high-temperature transformation of smectite to illite is not present.

IV.VI. Implications for Fault Slip

Smectite is common in fault rocks around the world (e.g., Vrolijk and van der Pluijm, 1999), and may persist as a major component to depths of several kilometers, below which a thermally driven transformation into illite-smectite and illite would occur (e.g., Colten-Bradley, 1987). Figure IV.IV schematically illustrates the smectite hydration state that would occur during quick slip at variable temperatures along the décollement that is sampled in Hole C0019E based on our results. Smectite can exist in a fully hydrated state only in the shallow portion of a fault, because smectite hydration is temperature dependent, and has chemical and mechanical properties that change significantly with depth. Based on our experiments, smectite cannot endure high temperatures of short duration without permanent change, so its property places an important constraint on a fault's thermal history. Slip that causes heat exceeding 75–125 °C has no damaging effect on the hydration behavior of smectite, as water is able to reenter the interlayer space after cooling. Slip that exceeds 150 °C causes partial damage to the smectite structure, and the hydration state is not fully recovered after heating. At temperatures >200 °C, the smectite in the JFAST samples is permanently damaged, and no water is able to re- enter the structure after cooling. Fulton et al.

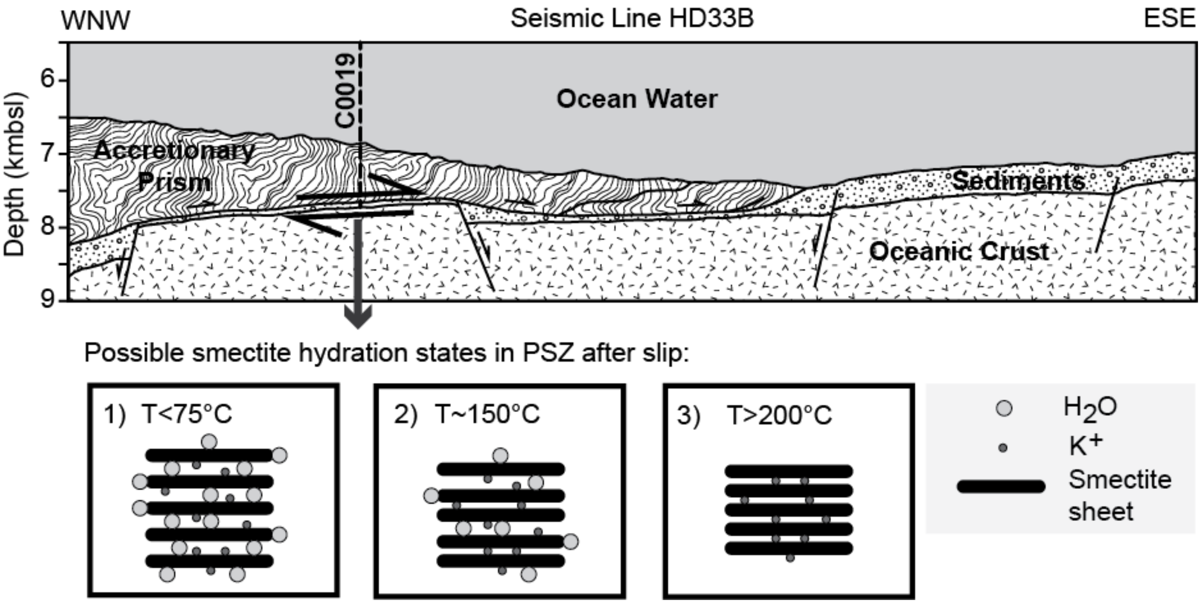

Figure IV.IV. Idealized cross section of the Japan Trench along seismic line HD33B (see Chester et al., 2013). Smectite hydration within the principle slip zone (PSZ) is temperature dependent, and three post-displacement scenarios are illustrated. T-temperature; bsl below sea level.

(2013) proposed temperatures as high as 1250 °C in the JFAST drill hole during displacement in the shallow portion of the Tohoku slip zone, assuming that the slip zone was very narrow (to 1 mm). In that case, highly efficient refrigeration of the damaged host rock would be required to keep it at sub-200 °C temperatures, in order to explain the preservation of hydrated smectite. Alternatively, slip along a much wider zone, perhaps capitalizing on the ubiquitous presence of weak clays (Chester et al., 2013), would not reach such high temperatures; this better fits our observations on the state of smectitic clays in the fault zone.

IV.VII. Conclusions

Slip within the pelagic clay zone located along the plate boundary fault is the defining surface characteristic of the Tohoku shallow earthquake fault, with smectitic clay providing regional control on displacement localization. Based on protracted and brief heating experiments, reflecting a range of seismogenic conditions of natural clay samples collected from drill core, we find systematic reductions of water interlayers in smectite. Smectite recovers more quickly to its original hydration state after brief heating than protracted heating. In both sets of experiments, smectite structure recovery is 100% to 125 °C, but only partial recovery occurs at higher temperatures, until non-recoverable collapse of smectite at >200 °C, regardless of the heating duration. This places a firm upper bound on the local temperature conditions. Thus, based on the behavior of smectitic clay in samples from JFAST core, we conclude that the slip zone investigated did not undergo distributed frictional heating over 200 °C.

IV.VIII. Acknowledgments

This chapter was published in *Geology* as Schleicher, Boles and van der Pluijm (2015). We thank the Japan Trench Fast Drilling Project (JFAST) community for valuable discussions, especially Christie Rowe, Jamie Kirkpatrick, and Patrick Fulton, and reviewers Michael Underwood, Brett Carpenter, Matt Ikari, Nick Hayman, Peter Vrolijk, and an anonymous reviewer. We also thank Virginia Toy and Jun Kameda for kindly providing samples, and James Gleason for inductively coupled plasma–optical emission spectrometry analysis at the University of Michigan. National Science Foundation grant EAR-11-18704 funds our studies of clays in fault rock.

Chapter V. Hydrogen and $^{40}Ar/^{39}Ar$ Isotope Evidence for Multiple and Protracted Paleofluid Flow Events within the Long-lived North Anatolian Keirogen (Turkey)

V.I. Abstract

We present a new approach to identifying the source and age of paleofluids associated with low-temperature deformation in the brittle crust, using hydrogen isotopic compositions (δD) and $^{40}Ar/^{39}Ar$ geochronology of authigenic illite in clay gouge-bearing fault zones. The procedure involves grain size separation, polytype modeling, and isotopic analysis, creating a mixing line that is used to extrapolate to δD and age of pure authigenic and detrital material. We use this method on samples collected along the surface trace of today's North Anatolian Fault (NAF). δD values of the authigenic illite population, obtained by extrapolation, are -89±3‰, -90±2‰, and -97±2‰ (VSMOW) for samples KSL, RES4-1, and G1G2, respectively. These correspond to δD fluid values of -62‰ to -85‰ for the temperature range of 125°C ±25°, indistinguishable from present-day precipitation values. δD values of the detrital illite population are -45±13‰, -60±6‰, and -64±6‰ for samples KSL, G1G2, and RES4-1, respectively. Corresponding δD fluid values at 300°C are -26 to -45‰ and match values from adjacent metamorphic terranes. Corresponding clay gouge ages are 41.4 ±3.4 Ma (authigenic) and 95.8±7.7 Ma (detrital) for sample G2 and 24.6 ±1.6 Ma (authigenic) and 96.5±3.8 Ma (detrital) for sample RES4-1, demonstrating a long history of meteoric fluid infiltration in the area. We conclude that today's NAF incorporated pre-existing, weak clay-rich rocks that represent earlier mineralizing fluid events. The samples preserve at least three fluid flow pulses since the Eocene and indicate that meteoric fluid has been circulating in the upper crust in the North Anatolian Keirogen since that time.

V.II. Introduction

Active fault zones of the upper-crustal, brittle deformation regime are dynamic and variable environments, both spatially and temporally. Multiple parameters directly or indirectly control the morphology and character of fault zones, including wall-rock lithology, three-dimensional fault geometry, rate and amount of displacement, pre-existing structure, and fluid-rock interaction (e.g., Sibson, 1977; Scholz, 1987; Bruhn et al., 1990; Caine et al., 1996). These primary controls determine fault zone features such as permeability and porosity structure, fluid flux, and mineralization suites, and lead to the resulting peculiarity of fault zones to behave either as fluid flow barriers or fluid flow conduits (Oliver, 1986; Sibson, 1992; Hickman et al., 1995; Person et al., 2007; Sutherland et al., 2012). Fault rock formation is a result of interactions between physical and chemical processes, with characteristics that evolve throughout the displacement cycle.

Recent work has highlighted the importance of low-temperature clay mineral authigenesis and transformations in this upper-crustal zone, and has documented their importance in governing fault mechanical behavior (Schleicher et al., 2010; Si et al., 2014; Warr et al., 2014; Kameda et al., 2015) and their utility as deformation geochronometers (Haines and van der Pluijm, 2008; Zwingmann et al., 2010; Hetzel et al., 2013; Bense et al., 2014; Hnat and van der Pluijm, 2014; Mancktelow et al., 2015). The clay mineral illite, specifically, has garnered attention due to structurally bound K, O, and H in its lattice, the fact that it forms at low temperatures, and that we can differentiate between detrital and authigenic populations of the mineral (e.g., Hetzel et al., 2013). Integral to this discussion is the presence and circulation of a fluid that acts as the agent of mineralization and that can govern mechanics; the composition of this fluid acts as an added control on the evolving character of a fault zone (Wintsch, 1995; Mulch et al., 2006; Faulkner et al., 2010). Constraints on mineralizing fluid composition allow for a more thorough understanding of fault zone maturation processes throughout the displacement cycle, and can also have implications for fault-compartmentalized hydrocarbon reservoir and fault-hosted metal deposit formation and extraction, earthquake risk assessment, and other physico-chemical processes of the brittle crust (Simpson and Wintsch, 1989; Levielle et al., 1997; Berger et al., 2003; Agosta et al., 2008).

Results by Fitz-Diaz et al. (2014) corroborate the longstanding hypothesis that the oxygen isotope composition of a fluid in the subsurface can equilibrate with the host rock before low-temperature illite authigenesis occurs, but that the absence of hydrogen in most rock-forming phases allows the authigenic minerals to retain a memory of the fluid's original hydrogen isotopic composition (Criss and Taylor, 1986; Sheppard, 1986). This is true in the upper crust and as deep as the brittle-plastic transition (e.g. Mulch et al., 2004; Mulch and Chamberlain, 2007; Gebelin et al. 2012; Campani

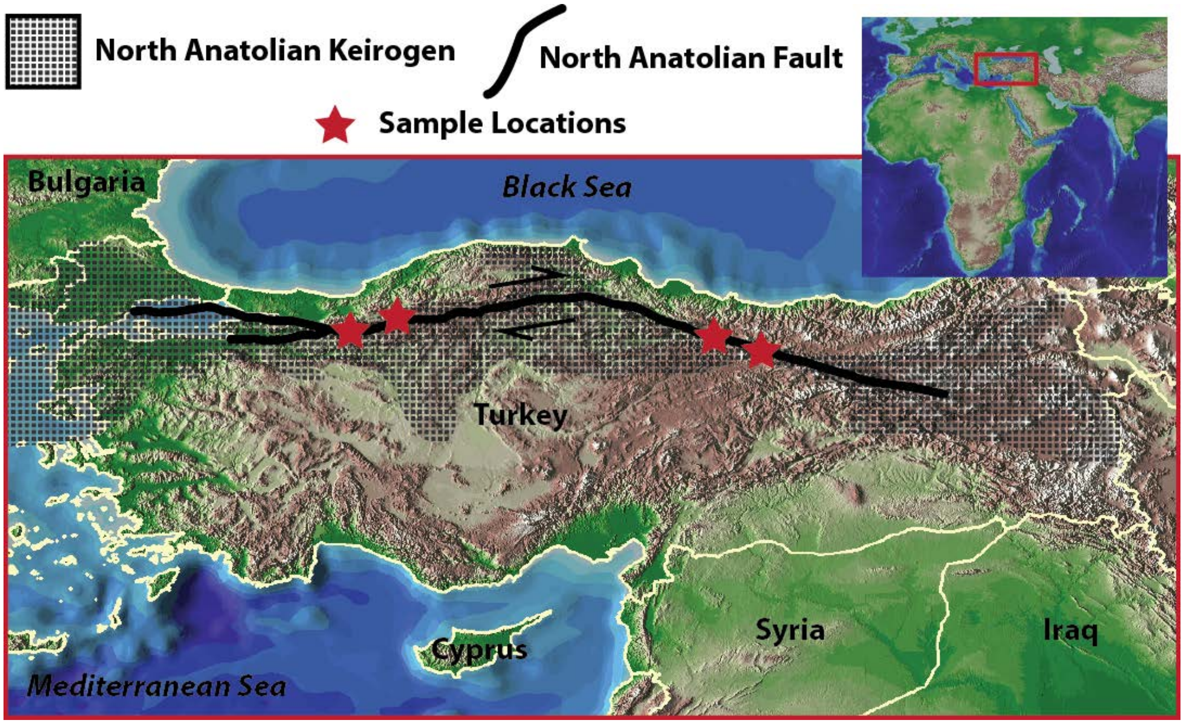

Figure V.I. Regional map of Turkey showing sample locations in the North Anatolian Keirogen that includes today's North Anatolian Fault.

et al., 2012). For this reason, we focus on the hydrogen composition of neoformed clay minerals in this study.

Given the common mixture of detrital and authigenic illite in natural fault rocks, we adapted the illite age analysis (IAA) approach toward characterizing the hydrogen isotopic composition of fluids present in the upper-crustal environment during active deformation. This represents a novel advance in our ability to constrain the formation conditions of authigenic clays. Key to our approach is the integration with dating to ascertain the timing of mineralizing fluids of samples obtained along the long-lived North Anatolian Keirogen (NAK) in which the North Anatolian Fault (NAF) currently resides.

V.III. Methodologies

The fluid fingerprinting methodology described below is based on the premise that our ability to physically isolate authigenic material from natural rock samples is limited to cases where no detrital clay is present. By separating a single sample into several size fractions that comprise quantifiable ratios of authigenic to detrital material, extrapolation to pure end-member phases is possible using a mixing line (van der Pluijm et al., 2001). This methodology is used in illite age analysis (IAA) with a well-ordered, higher temperature illite polytype (2M1) representing the detrital population, and a more disordered, lower temperature illite polytype (1Md) representing the authigenic illite populations. Our approach similarly requires use of grain-size separation and polytype quantification toward hydrogen isotope analysis.

Samples used in this study were characterized by X-ray diffraction (XRD) for mineralogy and polytypism, ^{40}Ar/^{39}Ar radiometric dating using the IAA method, all at the University of Michigan, and by continuous flow isotope ratio mass spectrometry for hydrogen isotope compositions at the Joint Stable Isotope Facility at Goethe University Frankfurt.

V.III.I. Sample Preparation

Samples were collected in northern Turkey at 8 sites in four different locations along the surface trend of today's NAF representing an aerial extent of > 750 km (Figure V.I). Limited by suitable outcrop, two of the locations are on the west and the other two are on the eastern part of the North Anatolian Fault Zone. In the lab, gouge samples were hand-crushed in an agate mortar, repeatedly washed with distilled water to remove salts, and placed in an ultrasonic bath ~15 minutes to disaggregate and deflocculate clay minerals. The samples containing illite were centrifuged according to Stoke's Law to separate each sample into four different size fractions: 2.0-1.0 µm (coarse), 1.0-0.2 µm (medium), 0.2-0.05 µm (fine), and <0.05 µm (very fine). Aliquots were split for ^{40}Ar/^{39}Ar geochronology and isotope measurements before chemical treatment, as the effects of acid treatment on the Ar and H activity in poorly ordered, fine-grained clay minerals are not well understood. These untreated aliquots were used for isotope measurements, while the remaining material was treated for XRD characterization as follows: samples containing carbonate minerals were treated with 1N HCl at 50°C for 1 hour to eliminate peak overlap in X-ray patterns. Oriented powder mounts of each size fraction were prepared on glass slides with a sample density of 5 mg/cm2. Random powder mounts of each size fraction were prepared by the side-loading method of Moore and Reynolds (1997).

V.III.II. X-ray Diffraction

X-ray diffraction of both oriented samples (used for mineral identification) and randomly oriented samples (used for polytype quantification) was conducted at the Central Campus Electron Microbeam Analysis Laboratory at the University of Michigan. Measurements were taken on a Rigaku Ultima IV diffractometer with CuKα radiation operated in Bragg-Brentano geometry at 40 kV and 44 mA. Oriented slides were measured both in air-dried conditions and after ethylene glycolation from 2-80°2θ for mineralogic characterization. Randomly-oriented mounts were measured from 16-44°2θ for polytype quantification. Less than 2μm phases common to fault rock include kaolinite, smectite, chlorite, illite, and metal oxides. Other contaminants include feldspar and quartz. Care was taken to avoid samples with even minor amounts of K-feldspar for Ar dating. Samples/size fractions containing illite and <5 wt. % other phases were selected for isotopic analysis (mineral proportions were assessed qualitatively, based on full-width-half-maximum and peak area measurements of prominent mineral peaks).

V.III.III. Polytype quantification

Previous studies (see van der Pluijm and Hall, 2015, for review) using illite dating involved the synthetic XRD pattern calculator WILDFIRE© (Reynolds, 1993) to generate end-member polytypes, which were mixed to match the pattern of the natural sample toward quantifying its 1Md/2M1 ratio. This application introduces complexity into the quantification due to the array of machine parameters that must be carefully constrained and inserted into the model. We avoid such complications in this study by utilizing natural samples of 2M1 and 1Md illite as end-member standards, measured at the same grain size and with the same machine parameters as the natural samples of interest (Haines and van der Pluijm, 2008). Standards used were the 2M1 muscovite from the Owl Creek pegmatite (Wind River Mtns.) and the Clay Mineral Society 1Mt-1 1Md illite standard (Hower and Mowatt, 1966). These standard materials were processed in the same manner as the natural samples. We noticed that the use of clay standards as end-members allows for better resolution of pattern matches and reduces error, as many effects of machine calibration are eliminated. Polytype quantification errors are estimated at ±2-3%. Figure V.II is an example of illite polytype quantification, using sample RES4-1. The results show that the four size fractions derived from RES4-1 have various 1Md/2M1 ratios, and that these ratios systematically correlate with grain size.

V.III.IV. Isotopic Analysis

V.III.IV.I. $^{40}Ar/^{39}Ar$ radiometric dating

^{40}Ar/^{39}Ar geochronology was conducted by the Noble Gas Laboratory at the University of Michigan using the encapsulation method. The small crystallite size of clay minerals increases recoil during irradiation. Mixed age populations combined with this recoil effect typically lead to degassing spectra and ages that are not defined by plateaus. Encapsulation in quartz tubes during irradiation captures the released argon, which is then measured in bulk, circumventing the problem of recoil (Dong, et al., 1995). Mean illite crystallite size was calculated to be 10-20 nm for dated samples, as obtained by means of the Scherrer equation (Moore and Reynolds, 1997). This crystallite size is used to determine whether the total gas or retention age is appropriate, and for these samples total gas age is used. Note that Ar age errors are a fraction of a percent, but that extrapolated ages incorporate the greater error (2-3%) of polytype characterization, resulting in a larger age error than typical for Ar dating only. See van der Pluijm and Hall (2015) for a recent overview of this method.

V.III.IV.II. Hydrogen Isotopic Analysis

About 1 mg of dried sample material was wrapped into Ag foil and kept overnight at 200°C under vacuum. Samples were rapidly transferred to a zero-blank autosampler in a stainless steel tray and the autosampler was immediately purged with helium gas to avoid rehydration with ambient air moisture. δD values were measured at the Joint Goethe University – BiK-F Stable Isotope Facility Frankfurt using a ThermoFinnigan MAT 253 mass spectrometer in continuous flow mode coupled

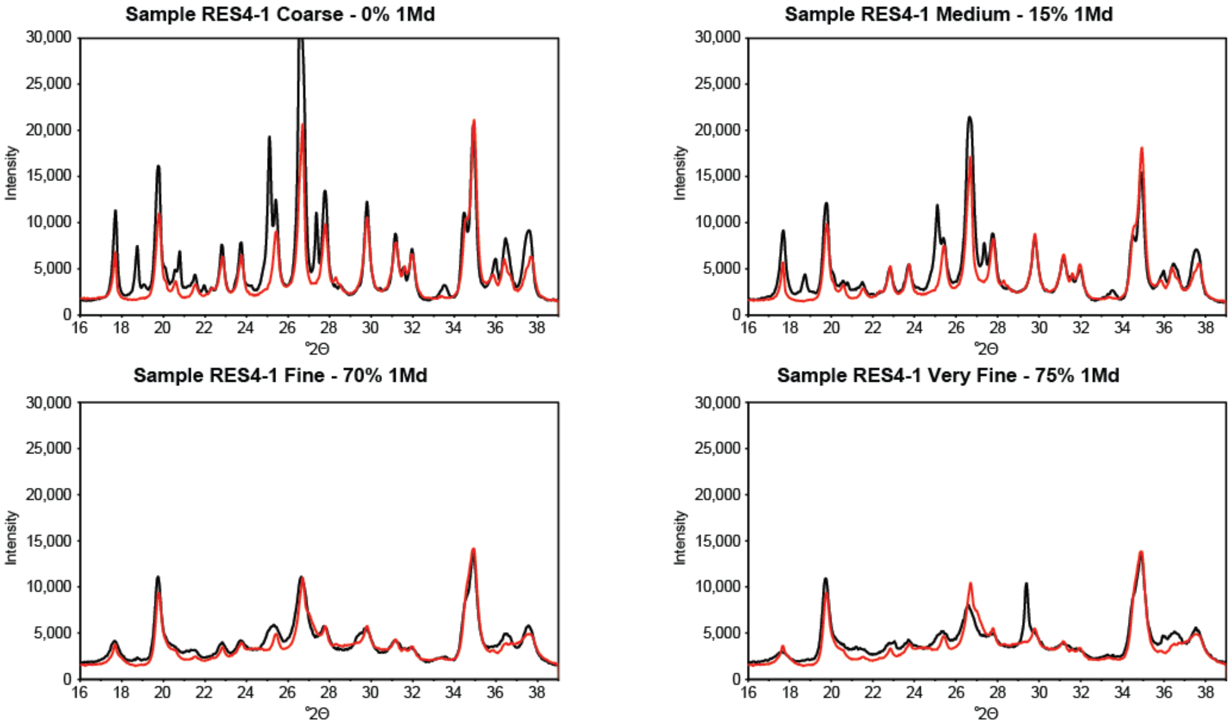

Figure V.II. X-ray diffractograms used for polytype quantification of the four size fractions of sample RES4-1. The black pattern is the natural sample and the red pattern is the synthetic match created by mixing the end-member $2M_1$ and $1M_d$ polytype standards. $1M_d/2M_1$ ratios systematically increase with decreasing grain size, indicating an increased abundance of authigenic minerals in the finer fractions.

to a high temperature conversion elemental analyzer (TC-EA). In-house and three international standards were run with the samples and yielded δD = -64.8 ‰ (NBS30 biotite), δD = -117.9 ‰ (NBS22 oil), and δD = -103.2 ‰ (CH7 polyethylene foil). Standards were run in-line with unknowns and reproduced with an error below ±2 ‰. All δD values are reported relative to standard mean ocean water (VSMOW).

V.III.IV.III. Mixing Plots and Isotopic Model

The key step in our methodology combines the results from multiple grain size fractions into two relations: one calculates δD for end-member authigenic and detrital illite, and the second constrains their ages. By plotting each size fraction of a sample in terms of the % authigenic illite and isotopic composition, and fitting these data with a York-type regression (Mahon, 1996), the intercepts of these lines are extrapolated end-member isotopic values. This is summarized in the idealized mixing plots in Figure V.III. The high correlation of the data (R^2 often exceeds 0.9) indicates several important features. First, there are mixtures of two populations of illite in the sample. The line would be horizontal if there was a single population or if multiple populations had undergone post-crystallization isotopic re-equilibration. More than two populations of illite would not plot on a linear trend unless all fractions fortuitously contained each population in the exact ratio across grain sizes, which is unlikely due to the mechanical mixing of each sample. Second, hydrogen and argon are not

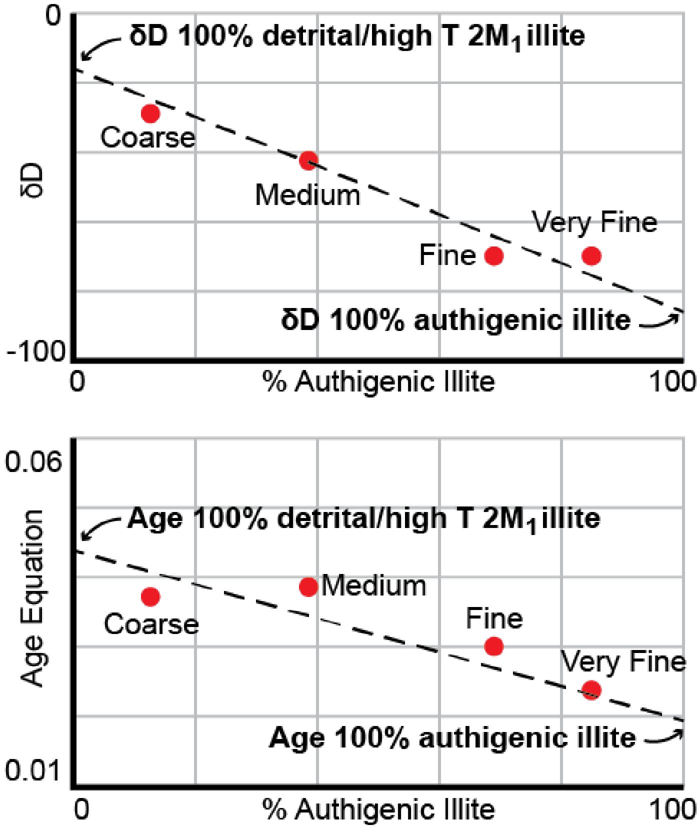

Figure V.III. Schematic mixing diagrams plotting size fractions of a single sample in terms of their isotopic composition and % authigenic material. Data is fitted with a regression method; the lower and upper intercepts give values of pure end-member compositions.

influenced by grain-size dependent diffusion at the temperatures to which these samples have been subjected. If diffusion was occurring, the line would be parabolic, with the smaller grain sizes being more affected than the larger grain sizes, because of changing surface area to volume ratios across the size spectrum. This precludes an argument that a single clay population incompletely experienced isotopic re-equilibration to create the mixing line. Finally, we note that the minerals were never subjected to pressure/temperature conditions that exceeded their formation, as the material would have undergone recrystallization and would not exist in two distinct polytypes (Morad et al., 2003). These characteristics are consistent with an upper crustal origin and shallow exhumation of the rocks.

V.IV. Application: the North Anatolian Keirogen

V.IV.I. Geological Setting and Sample Description

The tectonic evolution of Northern Turkey has a complex, prolonged history of subduction, terrane accretion, rifting, and escape tectonics. Şengör and Yilmaz (1981) describe its development in two phases, defined by the evolution of the Paleo-Tethys and Neo-Tethys Oceans. Phase one: Pangean rifting in the Permian separated Laurasia from Gondwana by the opening of the Paleo-Tethys Ocean. This was subsequently closed by south-dipping subduction underneath the Cimmerian ribbon continent that originated from northern Gondwana. Phase two: The rifting of the Cimmerian Continent from Gondwana opened the Neo-Tethys Ocean. Several terranes of various origins, located in the Neo-Tethys, were accreted to the Eurasian Plate by a series of north-dipping, Cenozoic-aged subduction zones and thrust belts. This convergence marked the closure of the Neo-Tethys, and culminated with the collision of the Arabian Plate with Eurasia in the Miocene (13-11 Ma), initiating the escape tectonic regime—facilitated by the NAF and other faults—that has dominated until the present time (Tapponnier et al., 1982; Şengör, 1985; Bozkurt and Mittwede, 2001; Şengör et al., 2005; Şengör et al., 2014).

This history illustrates that the area currently occupied by the NAF has been a long-lived tectonic zone since the Late Paleozoic, and it has experienced many and varied deformation events. We capture that prolonged history by using the term North Anatolian Keirogen (NAK), which includes all areas of current deformation in northern Turkey, as well as all underlying Tethyside accretionary complexes (Şengör and Natal'in, 1996; Şengör et al., 2005). Further evidence of a prolonged deformation history is provided by the studies of Uysal et al. (2006) and Mutlu et al., (2010) that obtained K-Ar and Rb-Sr ages of fault rocks with ages from the Paleocene to the

Miocene in locations along the trace of today's North Anatolian Fault (NAF). Samples of this study are from locations similar to that of Uysal et al. (2006) and Mutlu et al., (2010). The contrasting results of this paper and those—both from a clay mineralogy perspective and an isotopic compositional perspective—can be reconciled by (i) the fact that there are likely faults of various origin and age in the same locality and samples of this study could be different from those of the other studies, or (ii) that if the refined method described in this work was applied to the isotopic results of the other studies, the apparent differences would likely be resolved.

Eight fault gouge samples were collected for this study along the surface trace of the NAF (Figure V.I), spanning >750 km eastward of Istanbul. About 0.5-1 kg of sample was collected below the immediate surface to reduce the influence of surface contamination. Samples are typical fault zone clay gouge that is fine-grained, of various color, and friable. Sample G3 is from a carbonate-cemented conglomerate exposed 1 km south of Sultanbeyli village of the city of Bolu. Samples G1 and G2 were collected from the metamorphic rocks on the Bolu-Gerede road. Sample KSL is located near the town Koyulhisar. At this location, the fault gouge sample was taken from a landslide zone comprising interbedded sandstone and shale units. Sample KHS was collected from intensely altered peridotite unit on a roadcut between the towns of Koyulhisar and Resadiye. Sample RES4-1 is from the ultramafic units between sampling locations of samples KSL and KHS. The last two sampling sites, namely KO1 and KO3, are taken from peridotites located along the Kelkit River. Further sample description details and structural context can be found in Uysal et al. (2006) and Mutlu et al. (2010), which use material from the same locations. Sample location and mineralogic characterizations are listed in Table V.I. Only size fractions from samples G1, G2,

Table V.I. Sample details (Qtz=quartz, I=illite, Chl=chlorite, Kln=kaolinite, Fsp=feldspar, Py=pyrite, Cal=calcite, S=smectite)

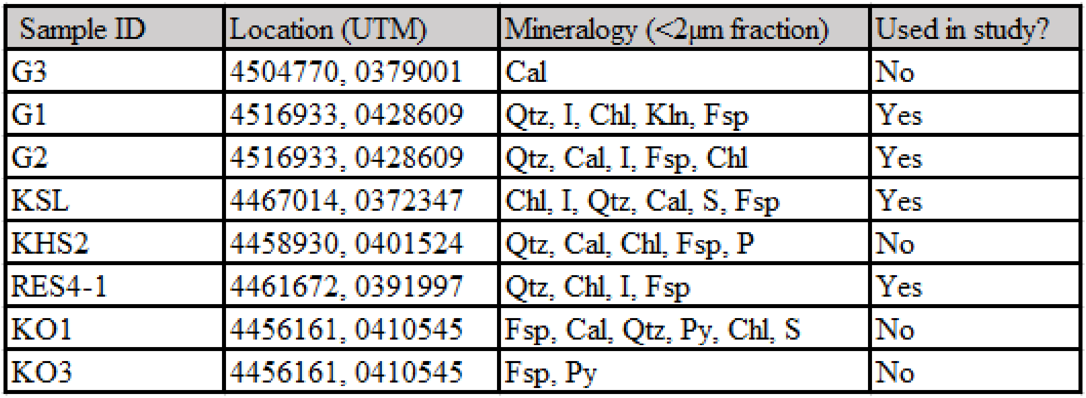

Sample ID	Location (UTM)	Mineralogy (<2μm fraction)	Used in study?
G3	4504770, 0379001	Cal	No
G1	4516933, 0428609	Qtz, I, Chl, Kln, Fsp	Yes
G2	4516933, 0428609	Qtz, Cal, I, Fsp, Chl	Yes
KSL	4467014, 0372347	Chl, I, Qtz, Cal, S, Fsp	Yes
KHS2	4458930, 0401524	Qtz, Cal, Chl, Fsp, P	No
RES4-1	4461672, 0391997	Qtz, Chl, I, Fsp	Yes
KO1	4456161, 0410545	Fsp, Cal, Qtz, Py, Chl, S	No
KO3	4456161, 0410545	Fsp, Py	No

KSL, and RES4-1 met the criteria for isotopic investigation by containing mostly illite and <5% contaminating phases; the four other samples include significant chlorite and other phases, or contain insufficient illite. Illite in the selected samples occurs both in discrete diffracting domains, as well as interlayered with smectite. The illite-smectite of these samples was remarkably similar between samples, and was evaluated based on 002/003 peak position (d=4.92-5.04 Ǻ) which indicates that it has long-range ordering (R≥3) and is illite rich (>90%) (Moore and Reynolds, 1997).

V.IV.II. Hydrogen Isotope Results

The results of hydrogen isotopic analysis for the samples investigated, as well as their polytype quantifications, are reported in Table V.II. The very fine fraction of samples G1 and KSL did not contain enough illite to model the proportions of detrital and authigenic populations above the noise of small crystallite size peak broadening, background radiation, and contaminating phases, and were therefore omitted. The results of the analyses for samples G1 and G2 are combined because they were collected at the same locality and are otherwise indistinguishable.

Table V.II. Hydrogen Isotope and Polytype Quantification Results

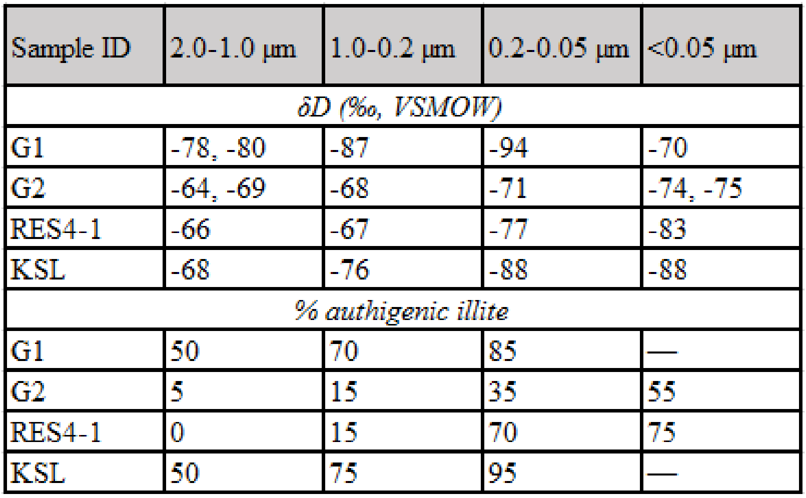

Sample ID	2.0-1.0 μm	1.0-0.2 μm	0.2-0.05 μm	<0.05 μm
δD (‰, VSMOW)				
G1	-78, -80	-87	-94	-70
G2	-64, -69	-68	-71	-74, -75
RES4-1	-66	-67	-77	-83
KSL	-68	-76	-88	-88
% authigenic illite				
G1	50	70	85	—
G2	5	15	35	55
RES4-1	0	15	70	75
KSL	50	75	95	—

Figure V.IV displays mixing plots for three sites, showing the success of our approach. Authigenic end-member δD compositions are -89±3‰, -90±2‰, and -97±2‰ for samples KSL, RES4-1 and G1G2, respectively. This range of values is restricted, and implies a common fluid origin for all authigenic populations analyzed, regardless of location.

A crystallization temperature can be estimated by various methods in order to calculate δD fluid compositions. Maden et al. (2014) calculated a geothermal gradient for the Eastern Anatolian Plateau of 32.2°C/km. Unpublished fault gouge data from samples from the Rwenzori Mountains of East Africa indicates a minimum depth of 3-5 km is needed for authigenesis to occur (Haines, personal communication). This indicates a growth window of ~100-150°C for authigenic minerals. Alternatively, using the smectite-to-illite kinetic reaction model of Huang et al. (1993), and assuming a typical [K+] of 200 ppm and growth time of 1 Ma, we calculate a temperature of

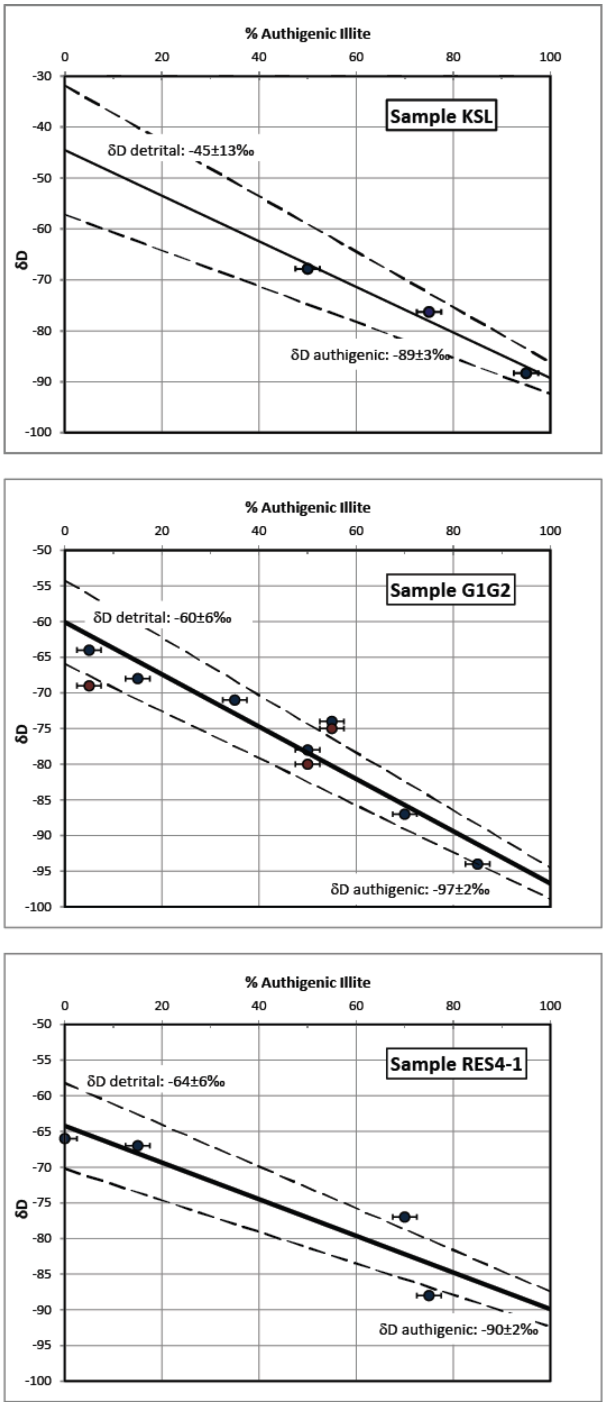

Figure V.IV. Mixing line diagrams plotting measured δD composition of illite vs. % authigenic illite. Data points each represent a single size fraction of sample; ratios of illite polytype populations vary among the multiple size fractions of the sample. This data is fitted with a York-type regression line (solid line) with standard error envelopes (dashed lines). Duplicate measurements not used in regression analysis are displayed in red.

formation of ~130°C. This model assumes the likely progression from an intermediate smectite phase (Boles and Franks, 1979; Hower et al., 1976). A third estimate considers the long range (R≥3) ordering pattern of I/S interlayers. The minimum temperature needed to achieve this ordering structure in burial sedimentary basin environments characterized by lower [K+] is 170°C. Therefore, using a temperature window of 100-150°C and the illite fractionation equation of Capuano (1992), calculated δD values for the water from which illite precipitated range from -59 to -83‰.

Detrital end-member δD compositions are -45±13‰, -60±6‰, and -64±6‰ for samples KSL, RES4-1 and G1G2, respectively. These values fall well into the range of muscovite δD values commonly observed in metamorphic rocks. A similar argument as above follows for the detrital populations, that the restricted range of values indicates a common fluid origin for each sample analyzed. The formation temperature for well-ordered 2M1 illite is above 300°C (Frey, 1987). Using 300°C as a minimum temperature, and the muscovite fractionation equation of Suzuoki and Epstein (1976), δD values of the fluid from which the detrital population of micas precipitated are calculated as -27 to -45‰. The gap of 15‰ between detrital and authigenic phases is significant and would represent an unlikely shift of almost 20° in latitude if these samples were precipitated at surface conditions and latitudinal isotope gradients in precipitation were wholly responsible for setting δD of meteoric water.

V.IV.III. Illite Dating Results

In order to distinguish between ancient fluid mineralization and modern weathering, two samples were selected for dating. Figure V.V shows the combined results of illite dating using 8 size fractions. Sample G2, collected from the western portion of the fault, near the city Gerede, yields an authigenic end-member age of 41.4 ±3.4 Ma. Sample RES4-1, collected from the eastern portion of the fault near the city of Resadiye, yielded a younger, authigenic end-member age of 24.6 ±1.6 Ma. Also, both samples yield detrital end-member ages of ~96 Ma (95.8±7.7 Ma for sample G2 and 96.5±3.8 Ma for sample RES4-1), indicating a common history for detrital material that is a significant distance apart today.

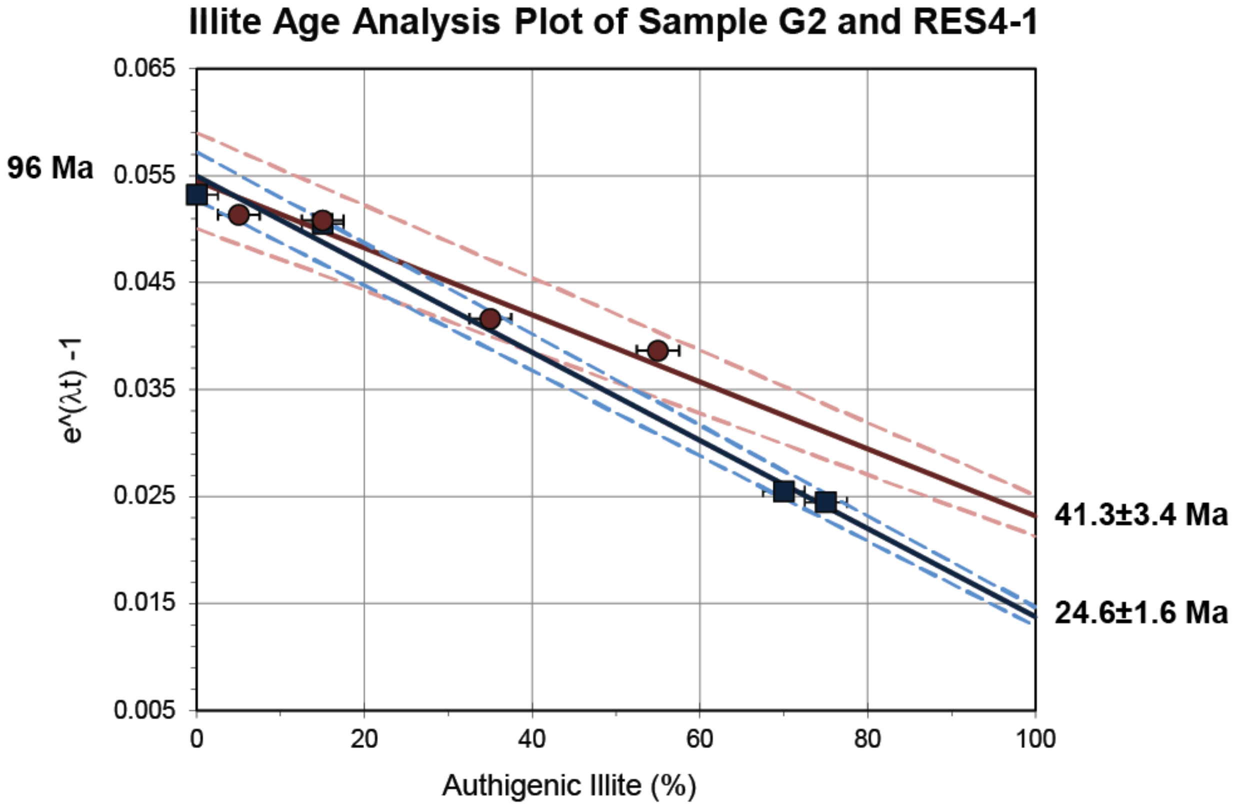

Figure V.V. Illite dating plot of samples G2 (red) and RES4-1 (blue). The diagram plots age (in Ar-Ar age equation form) vs. % authigenic illite. The authigenic mineralization age of sample G2 is 41.4±3.4 Ma and of sample RES4-1 is 24.6±1.6 Ma. Detrital mineralization ages of the two samples are the same within error; G2 is 95.8±7.7 Ma and RES4-1 is 96.5±3.8 Ma.

V.V. Discussion and Conclusions

There is a clear compositional demarcation between fluids from which the end-member illite/mica populations precipitated (Figure V.VI). Fluids associated with authigenic mineralization occupy the range of modern-day precipitation values (Schemmel et al., 2013), whereas the fluid associated with detrital minerals is in the range of values that are reported from various metamorphic terranes adjacent to the fault zone (Bozkaya et al., 2007; Canbaz and Gökce, 2014; Satir and Taubald, 2001).

The main factors that may influence the isotopic composition of meteoric fluids in faults and shear zones include climate, altitude and latitude. For example, Early Eocene global climate has been inferred from proxy data to be the warmest period during the Cenozoic, with deep ocean water temperature ~12°C warmer than current temperatures, and tropical conditions that extended 10-12° latitude poleward of their present positions (Douglas and Woodruff, 1981; Zachos et al., 2008). These, and lesser extremes since that time, do not significantly affect our distinction between authigenic fluid and metamorphic fluid. The NAK has experienced little vertical deformation or exhumation since the Miocene, and occupied a broad, low valley for much of its ~1200 km trace (Koons et al., 2003). Stable isotope studies addressing the role of the Pontide Mountains in

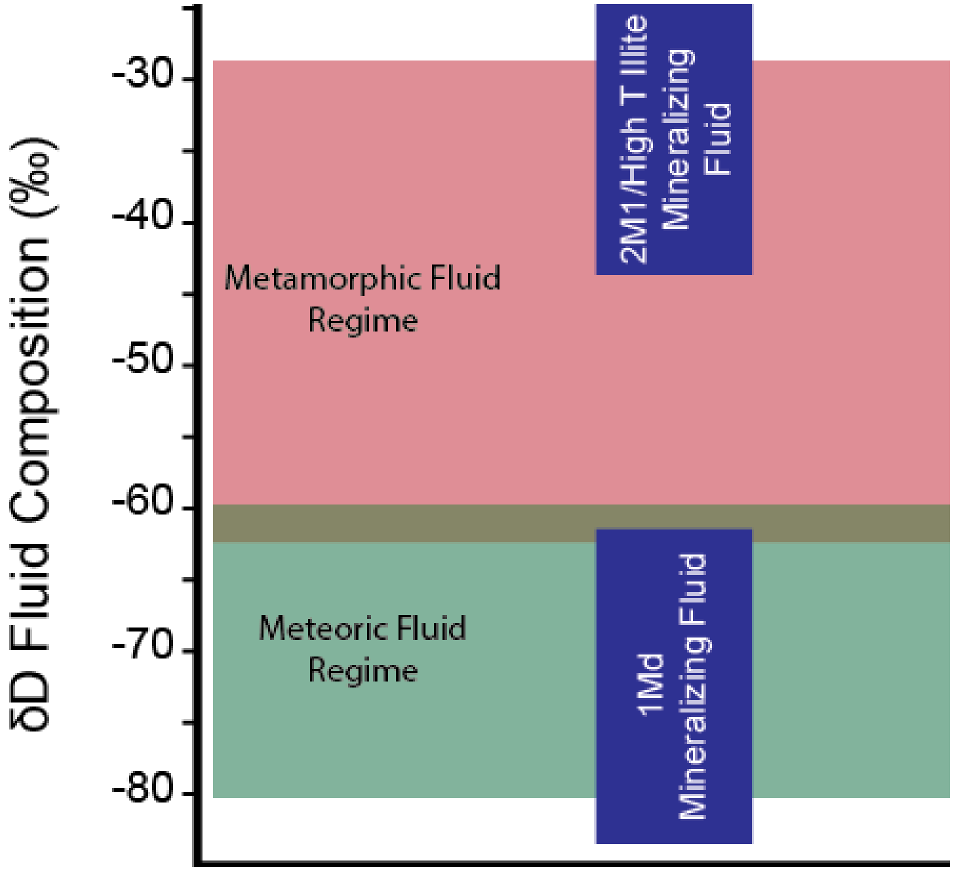

Figure V.VI. Comparison of δD fluid values of this study (blue) with fluids of metamorphic origin adjacent the fault (red) and modern-day precipitation (green) (Satir and Taubald, 2001; Bozkaya et al., 2007; Schemmel et al., 2013; Canbaz and Gökce, 2014). Measured mineral δD values from referenced sources were converted to fluid values based on temperatures, and were converted to VSMOW for comparison.

controlling precipitation patterns (and associated change in δD of precipitation) are scarce. However, there is increasing stable isotope evidence that the Pontide Mountains did not influence isotope in precipitation patterns at least as far back as the Oligocene (Mazzini et al. 2013; Lüdecke et al., 2013). The latitude of the NAK has been essentially unchanged throughout the Cenozoic, and has been defined by the southern extent of the stable Eurasian landmass; the orogenic suture zone has likely moved less than 4° latitude since the Paleocene (Van der Voo, 1993), with the greatest amount of depletion attributed to this latitudinal change of <6‰. Thus, we conclude that climate, elevation and latitude do not vary enough since the Miocene to affect our conclusions about the origins of distinct fluid sources in the area.

Using the nature and ages of mineralization, three fluid flow events can be recognized. The timing and composition of the oldest event is constrained by the detrital end-member populations of the samples at ~96 Ma, with a paleofluid that was metamorphic in nature and produced 2M1 illite. These clays were subsequently incorporated into the modern NAF and are today preserved

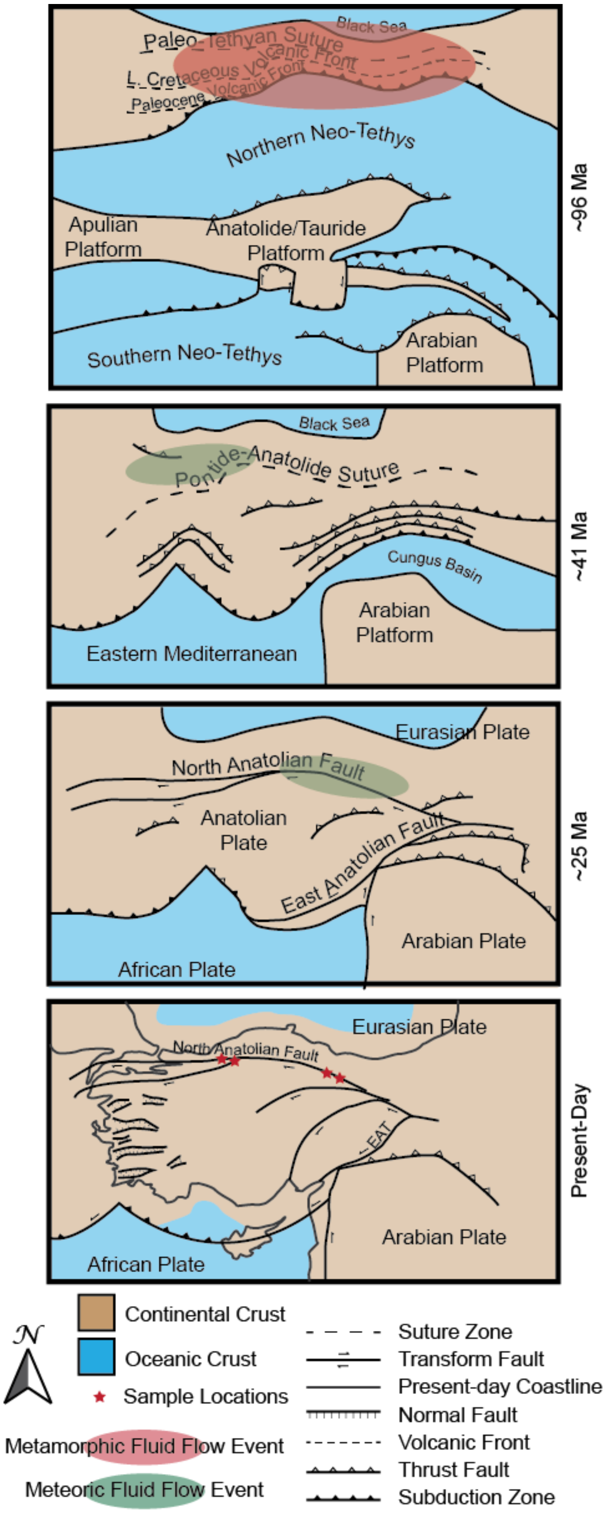

Figure V.VII. Paleogeographic maps since the late Cretaceous time showing multiple fluid flow/clay mineralization events and illite-bearing sample locations related to tectonic activity in the North Anatolian Keirogen. Maps adapted from Şengör and Yilmaz, 1981.

in samples located >400 km apart. We also note that this age is remarkably similar to the age (95-90 Ma) of metamorphic soles of ophiolites that directly overlie Eurasian crust and mark the suture between Sakarya (a Eurasian terrane) and the Anatolid-Tauride Block that makes up a large portion of modern Turkey (van Hinsbergen et al., 2010; Gülyüz et al., 2013). We surmise that during the tectonic emplacement of these terranes, metamorphic fluids were generated by dehydration reactions. These processes, in turn, influenced upper-crustal permeability and porosity structures, and initiated mineralization series that included illite.

The two younger events record meteoric fluid activity in the upper several kilometers of the crust. The depth range of 1Md crystallization is dependent on the geotherm, and is typically constrained to be <4-5 km from the surface (Hower et al., 1976). The timing of the event on the west side of the area is ~41 Ma. During the mid-Eocene, arc magmatism and associated bentonite deposition continued in the NAK—bentonites are commonly associated with 1Md illite formation (Pevear, 1999). Furthermore, fold-and-thrust belt formation occurred in this time period, providing pathways for fault-related fluid flow and clay generation. The event on the east side of the sampling area is ~25 Ma. Late Oligocene deformation included the transport and emplacement of several nappes and crystalline massifs along southerly-imbricated detachments (Şengör and Yilmaz, 1981). Volcanism was restricted to a smaller region, and the initiation of today's North Anatolian Fault was only a few million years away. Regardless of the varied tectonic environments, our isotopic results show that ancient fluids with compositions similar to that of modern-day precipitation have been circulating in the upper crust of the NAK since Early Cenozoic time.

Our dating shows that clay gouge present in today's North Anatolian Fault is older than modern strike-slip fault initiation. We conclude that older Cenozoic deformation and associated clay formation created zones of weakness in the area that the present-day NAF continues to exploit (figure V.VII). This is consistent with various studies indicating across-fault compositional, viscosity and age differences that point toward large-scale, deep discontinuities between allochthonous terranes of the NAK (Şengör et al., 2005; Bozkurt and Mittwede, 2010; Zattin et al., 2010; Fichtner et al., 2013; Yamasaki et al., 2014). As the nascent NAF propagated through Northern Turkey during a shift from subduction-dominated tectonics to an escape tectonics regime in the Miocene (Şengör et al., 2005), it navigated the terrane aggregate of the region and preferentially utilized weak, clay-rich zones that had been generated during earlier deformation.

Using hydrogen isotopes of clay size fractions for fluid source characterization and associated dating of neoformed and detrital illite, we are able to constrain the nature of mineralizing paleofluids and the timing of fluid circulation pulses within the North Anatolian Keirogen. Our method resolves the complications from mixed sample populations with extremely fine grain sizes, so has potential for application in many other areas, as illitic clays are common in deformation zones. Illite is a robust recorder of formation conditions, preserving a rich source of information about the type, timing and nature of fluids that are associated with regional deformation.

V.VI. Acknowledgments

Research was supported by the US National Science Foundation EAR 1118704 (BvdP) and the University of Michigan Turner Fund (AB). AM acknowledges support through the US National Science Foundation Continental Dynamics CAT project. We thank Chris Hall (Michigan) for Ar dating, J. Fiebig (Frankfurt) for laboratory support, and Volkan Karabacak (Eskisehir Osmangazi University) for field support. This manuscript was improved by comments from Cin Ty Lee and an anonymous reviewer.

Chapter VI. Triassic, Surface-fluid Derived Clay Diagenesis in the Appalachian Plateau, Northern U.S. Midcontinent

VI.I. Abstract

Integrated investigation of authigenic clays in the Appalachian Plateau of the northeastern US Midcontinent using X-ray goniometry illite polytype analysis, H isotopic analysis and ^{40}Ar/^{39}Ar geochronology yields novel insights about the structural diagenetic history of the North American sedimentary cover sequence. Texture analysis by High Resolution X-ray Texture Goniometry preserves bedding-parallel diagenetic fabrics that indicate a burial depth of ~2-5 km. Illite mineralization temperatures are spatially variable, and range from 80-190ºC, correlating to depths of ~3-6 km. Mineralizing fluid is surface-derived, with δD values ranging from -48 to -72‰ (in the range of predicted Pangea meteoric fluid). In addition, we find a spatial dependence, with mineralizing fluid δD values increasing away from the hinterland, interpreted as the rain shadow effect from the high elevation Appalachian orogen, and consistent with a locally-derived fluid source. The diagenetic age is constrained to ~225-250 Ma (Triassic) and displays no spatial trend, reflecting protracted, regional diagenesis. We postulate that the transition from burial to exhumation in a compressional to extensional tectonic regime facilitated the opening of pathways for meteoric fluid infiltration into the shallow crust, resulting in regional diagenesis and mineralization at depth. This model challenges reigning views about the timing and role of previously proposed tectonically-forced fluid flow.

VI.II. Keywords

Illite polytype analysis, hydrogen isotopes, Appalachian Basin, structural diagenesis, ^{40}Ar/^{39}Ar geochronology

VI.III. Introduction

The theory of plate tectonics divides the lithosphere (the crust and upper mantle) into thin, rigid blocks that mostly interact with one another at their boundaries (Morgan, 1968). Within this established framework, however, intraplate deformation may also occur in both continental and oceanic settings (Molnar, 1988). Examples include the Central Indian Basin, a 3,000 km wide deformation zone in the Indian Ocean (Neprochnov et al., 1988; Bull, 1990; Singh et al., 2017), and the Ancestral Rockies, Laramide orogeny, and intracratonic basins of the North American craton (e.g. van der Pluijm et al., 1997; Marshak et al., 2000). The existence of intraplate deformation, and a memory of the stress field retained by the cratonic cover rocks (e.g. Craddock et al., 1993), indicate that far-field stresses from boundary zone deformation belts are transferred deep into cratonic interiors. The orientation, style, and magnitude of this diffuse strain experienced by the plate are often focused on preexisting structures in basement rock (Marshak et al., 2000). The intraplate, brittle crust remains inherently strong, maintaining a state of critical stress, near-hydrostatic pore pressures, and high permeability (Townend and Zoback, 2000; Zoback and Townend, 2001).

One manifestation of intraplate deformation, epeirogeny—long-wavelength, vertical movements in cratonic settings—is particularly notable in the North American midcontinent (figure IV.I). In addition to domes, arches and basins, many through-going discontinuities have been identified in the basement rocks of the Eastern United States (Hay et al., 1988; Marshak et al., 2000). Although the kinematics of such structural features remain poorly understood, their existence and ubiquity are striking, arguing against the common view of a rigid plate interior. Many of these structures have been temporally linked to plate boundary deformation, diagenesis, and fluid flow (e.g. Bethke, 1986; Carlson, 1994; Howell and van der Pluijm, 1999; Grathoff et al., 2001).

The long-range mobilization of fluids in foreland basin sedimentary rocks due to far-field tectonic activity was first postulated by Oliver (1986). In his conceptual model, orogenesis expedites sediment compaction deep within the foreland basin wedge, while inducing laterally migrating hot, solute-rich basinal brine away from the orogen. It has provided a simple, convenient and compelling explanation for several temporally- and spatially-linked geologic phenomena in the North American midcontinent, including brine-derived Mississippi Valley-type (MVT) ore deposits (Hearn et al., 1987), regional potassium metasomatism (Buyce and Friedman, 1975; Elliott and Aronson, 1987; Lu et al., 1991; Schedl et al., 1993), anomalously high thermal histories of shallowly-buried sediments (Cathles and Smith, 1983; Sverjensky, 1986), correlation of hydrocarbon accumulations to distant source rocks (Momper, 1978; Clayton and Swetland, 1980), and widespread paleomagnetic remagnetization (Manning and Elmore, 2012; Van der Voo and Torsvik, 2012).

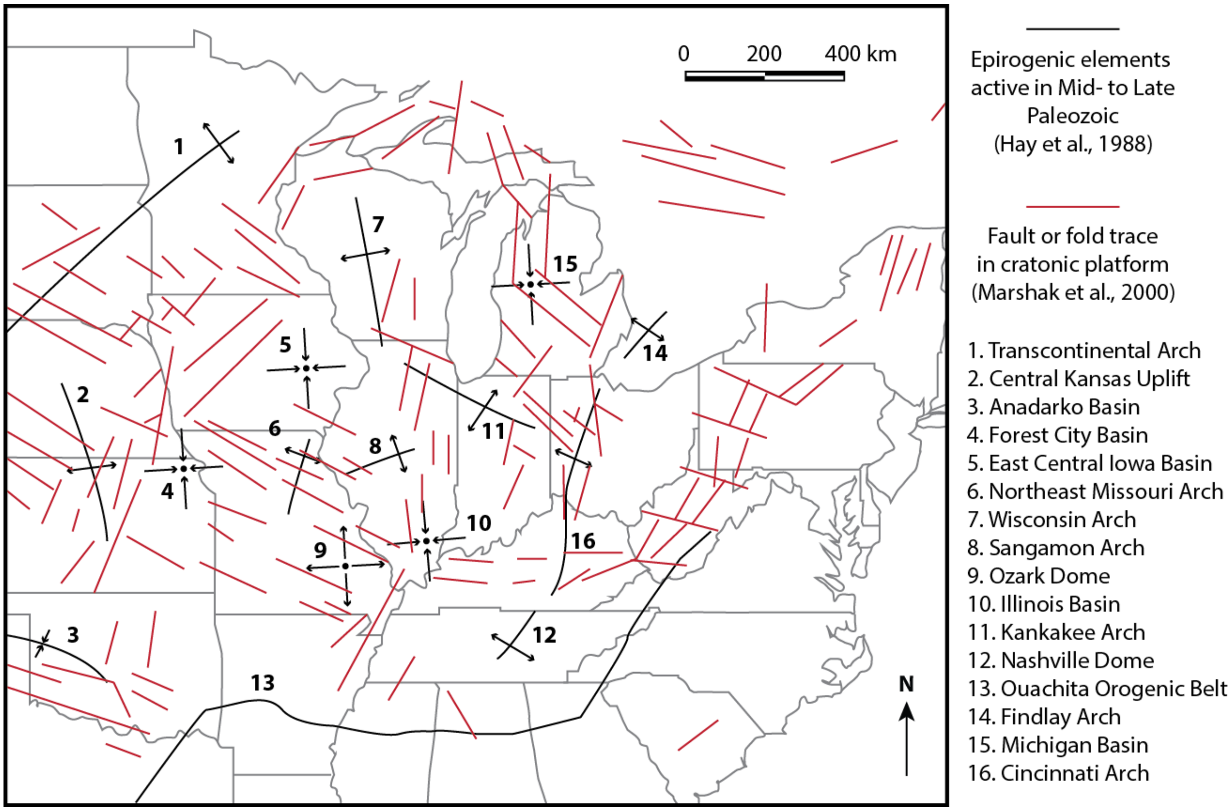

Figure VI.I. Structural features of the North American midcontinent that include both epeirogenic elements and basement faults and folds. Modified after Hay et al. (1988) and Marshak et al. (2000).

The seminal paper of Bethke and Marshak (1990) examines the lines of evidence in detail and concludes that brine migrations can achieve the length scale of an orogenic belt and transfer geofluid many hundreds of kilometers into plate interiors (see also Garven, 1995; Person and Baumgartner, 1995 for reviews). Several other observations, however, controvert the claim that geofluid has the ability to flow laterally within a sedimentary package across such distances, and retain elevated temperatures:

(1) The structurally-induced permeability anisotropy of the deformed rock that is expected for a compressional system is predicted to preferentially direct a significant proportion of fluid flow along-strike; i.e., parallel—not perpendicular—to the orogen (Sibson, 2005).

(2) Fluid flow, regardless of the forcing mechanism, will always be down hydraulic gradients, but competition between deformation processes which maintain connectivity and those which close pathways will determine permissible fluid volumes and flow rates (Knipe and McCaig, 1994). In compressional, sedimentary systems at low temperatures, permeability restriction by pressure solution, compaction and cementation is likely to be greater than permeability enhancement by the opening of fractures and grain boundary voids or chemical dissolution.

(3) Primary permeability distribution is anisotropic, and highly dependent on sedimentary facies (Bjorlykke, 1993). Adherence to Walther's Law ("…only those facies and facies-areas can be superimposed primarily which can be observed beside each other at the present time"; Middleton, 1973) suggests lateral primary permeability variations that would significantly affect horizontal flow. Moreover, these variations and the observed mineral reactions would require flow rates and durations of flow that are not attainable by compaction-driven flow without extreme focusing of that flow, which precludes regional alteration events (Schedl, 1992; Bjorlykke, 1994).

(4) Time-dependent numerical models of fluid, heat and solute transport indicate that the high fluid velocities required to carry heat across a basin rapidly exhausts solute supply provided by compaction-driven flow (Deming et al., 1990; Deming and Nunn, 1991). This mechanism can, therefore, only explain regional brine migration if flow is focused into spatially restricted discharge zones, and sets fundamental limitations on the ability of either compaction-driven or topographically-driven flow to continuously transport significant heat across a basin for an extended period of time (Nunn and Deming, 1991).

(5) A model assuming a single hydrostratigraphic system that dominates the whole of the Appalachian Basin is simplistic, and the reality is likely an interplay between several flow systems, each competing, mixing and interfering with the others (Bachu, 1995).

The current study challenges this widely-used "orogenic squeegee" scenario in its type area by studying one product of potassium metasomatism that is widespread in the North American midcontinent, the clay mineral illite, and utilizes recent advances in the illite polytype analysis method to constrain the diagenetic age of illite and the geofluid source from hydrogen isotopic composition in mudstone samples across the northern Appalachian Basin. We conclude—based on the results of age and fluid source analyses—that pre-existing structural features and intracratonic stress realignment mobilized locally-sourced, surface-derived fluid and lead to widespread and protracted diagenesis within the continental sedimentary cover of the Appalachian Plateau. A locally-sourced fluid resolves many problems related to long-range fluid mobilization (volume and temperature), while the timing of clay mineralization represents post-Appalachian deformation in the region.

VI.IV. Geologic Background

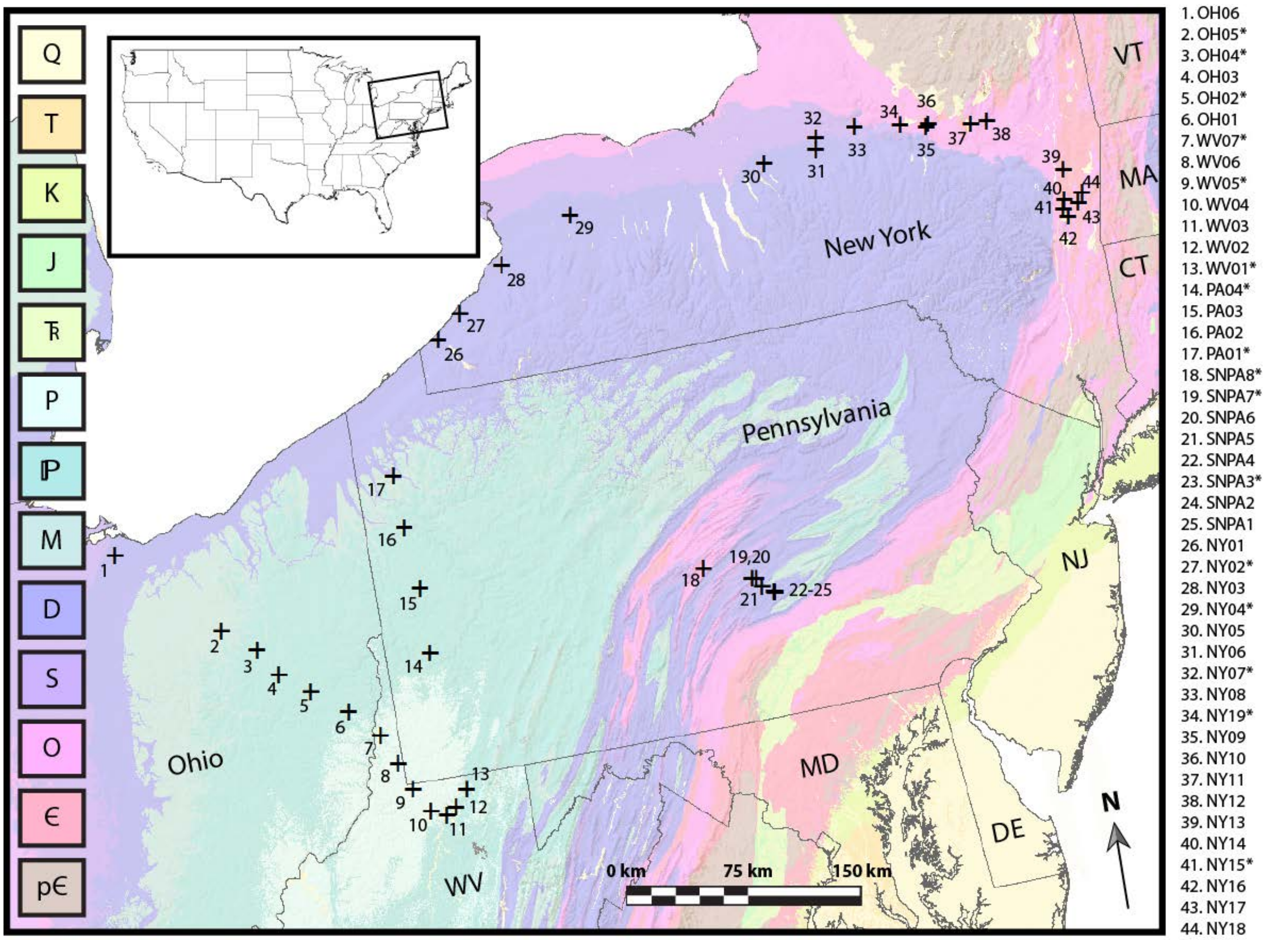

Figure VI.II. Generalized geologic map of the Northern Appalachian Basin. Mudstone surface sample locations are denoted with cross symbols.

The Appalachian Plateau is a tectonic province of the central Appalachian orogenic belt that is characterized by flat-lying to gently-folded Paleozoic strata deposited in the foreland basin (Quinlan and Beaumont, 1984; Mitra, 1987; Hatcher, 2010). Figure VI.II shows the locations of 44 mudstone samples that were collected in this region. Sample location GPS coordinates are included in Table VI.I. Fine-grained lithologies were targeted to maximize the clay content for

Table VI.I. Sample locations, ages, and lithologies (asterisk denotes samples selected for illite polytype analysis).

Sample ID	Lat	Long	Location	Age	Outcrop Description
NY01	42.30842	-79.57702	Westfield, NY	Dev	Thinly-bedded shale and sandstone
NY02*	42.43811	-79.33451	Fredonia, NY	Dev	Massive shale
NY03	42.67973	-78.87865	Eden, NY	Dev	Laminated shale with sandstone boudins
NY04*	42.89985	-78.17754	East Bethany, NY	Dev	Massive shale
NY05	42.97419	-76.33455	Marcellus, NY	Dev	Massive black shale
NY06	42.98646	-75.84591	Chittenango, NY	Dev	Interbedded limestone, siltstone, and shale
NY07*	43.05820	-75.82658	Chittenango, NY	Sil	Shale
NY08	43.07466	-75.45280	Clinton, NY	Sil	Massive black shale
NY09	42.99578	-74.78839	Little Falls, NY	Ord	Interbedded limestone and black shale
NY10	42.98215	-74.81390	Little Falls, NY	Ord	Interbedded limestone and black shale
NY11	42.93971	-74.40204	Fultonville, NY	Ord	Massive shale
NY12	42.93588	-74.25807	Amsterdam, NY	Ord	Massive shale
NY13	42.54460	-73.67372	Nassau, NY	Cam	Deformed shale
NY14	42.37235	-73.73354	Stuyvesant, NY	Ord	Deformed shale
NY15*	42.31531	-73.75588	Hudson, NY	Cam	Massive shale
NY16	42.26567	-73.73564	Hudson, NY	Cam	Massive shale
NY17	42.33323	-73.61142	Ghent, NY	Ord	Interbedded, near-vertical limestone and shale
NY18	42.38660	-73.55775	Chatham, NY	Ord	Shale (slate?)
NY19*	43.02855	-75.03789	Frankfort, NY	Ord	Massive shale
PA01*	41.55385	-80.18088	Cochranton, PA	Miss	Interbedded shale and sandstone
PA02	41.23796	-80.16005	Jackson Center, PA	Penn	Massive shale
PA03	40.86274	-80.10997	Harmony, PA	Penn	Massive shale
PA04*	40.47227	-80.11752	Coraopolis, PA	Penn	Silty shale
SNPA1	40.451317	-77.021117	Ducannon, PA	Dev	Shale
SNPA2	40.455817	-77.024117	Ducannon, PA	Dev	Shale
SNPA3*	40.459617	-77.025633	Ducannon, PA	Dev	Shale
SNPA4	40.462633	-77.027867	Ducannon, PA	Dev	Shale
SNPA5	40.503567	-77.128117	Newport, PA	Dev	Shale
SNPA6	40.556183	-77.16555	Millerstown, PA	Sil	Shale
SNPA7*	40.565367	-77.194083	Millerstown, PA	Sil	Shale
SNPA8*	40.6789	-77.606317	Reedsville, PA	Ord	Shale
WV01*	39.63674	-79.99847	Morgantown, WV	Penn	Decimeter-scale interbedded sandstone and shale
WV02	39.54012	-80.11959	Rivesville, WV	Penn	Interbedded shale and sandstone
WV03	39.50348	-80.20872	Fairmont, WV	Penn	Interbedded shale and sandstone
WV04	39.54213	-80.34347	Mannington, WV	Perm	Siltstone and shale
WV05*	39.69082	-80.46216	WV	Perm	Thick shale with interbedded sandstone
WV06	39.85826	-80.55627	WV	Perm	Sandstones and shale
WV07*	40.03886	-80.67164	Wheeling, WV	Penn	Sandstones and shale
OH01	40.20625	-80.91568	OH	Penn	Interbedded shale and sandstone
OH02*	40.35903	-81.21669	Scio, OH	Penn	Interbedded shale and sandstone
OH03	40.48853	-81.47231	New Philadelphia, OH	Penn	Interbedded shale and sandstone
OH04*	40.65504	-81.62455	Beach City, OH	Penn	Sandstone and siltstone.
OH05*	40.79837	-81.91261	Wooster, OH	Miss	Sandstone and shale
OH06	41.33999	-82.75567	Sandusky, OH	Dev	Siltstone

illite polytype analysis. About 2 kg of sample was collected at each location, from beneath the surface to avoid recent contamination. Two transects of the Appalachian plateau, oriented orthogonally to the Appalachian Mountains in New York and Ohio, West Virginia, and Pennsylvania, respectively, were targeted. Further sampling in the Valley and Ridge Province in central Pennsylvania was conducted to gain lateral continuity of samples representing undeformed to highly strained material. As such, the sample suite represents a variety of rock types (shale, siltstone, argillaceous limestone; Table VI.I), which range from Early to Late Paleozoic age.

VI.V. Methods

High resolution X-ray texture goniometry is utilized in this study to quantify and interpret diagenetic fabric. Illite polytype analysis for both H isotopic composition and Ar radiometric age are utilized to determine the timing of diagenesis and to constrain the source of the mineralizing fluid active in the diagenetic environment at the time of 1Md illite authigenesis. H isotopic analysis of clays was selected over O isotopic analysis because H isotopic change is not expected in a fluid undergoing fluid-rock interaction, as hydrous rock-forming minerals in the crust are an inadequate buffer, while the O isotopic composition of the fluid will equilibrate with the host rock, thus yielding little information about fluid sourcing (Fitz-Diaz et al., 2011).

VI.V.I. X-ray Texture Goniometry

High-resolution X-ray texture goniometry (XTG) was conducted on an ENRAF-Nonius CAD4 automated single-crystal diffractometer using a Mo source, operated at 23 mA and 43 kV, and located in the University of Michigan's Electron Microbeam Analysis Laboratory (van der Pluijm et al., 1994). By using transmission mode, crystallographic preferred orientation is measured and a pole figure generated for the 1 nm 001 d-spacing clay mineral illite. A multiple of random distribution (MRD) value is also calculated that quantifies crystallite orientation. The resultant magnitude of the MRD value describes the calculated probability of illite misorientation with respect to a material with uniformly distributed misorientations (an MRD value equal to 1 is a perfectly random distribution; higher MRD values indicate greater levels of fabric anisotropy).

The samples were first investigated over a 2θ range of 0.5-6.0º (corresponding to 1-13º2θ Cu) to determine the exact diffraction angle at which textural data should be collected. Next, a "pole-figure scan" (Ho et al., 1995) was completed wherein diffracted X-ray intensity data were collected every 2.5º from 0-360º along an axis parallel to a line between the goniometer and the detector, and in 9 steps between 0-40º around a second axis oriented normal to the first. A total of 1296 intensity measurements were made, corrections were made for sample absorption, grain density, and specimen thickness, and intensity data were smoothed, rotated, and displayed on pole figure diagrams (van der Pluijm et al., 1994). Eight samples were selected for XTG analysis representing two transects, orthogonally oriented to the Appalachian orogen, in New York and West Virginia. A ~0.2-0.5 mm thick section of each sample was prepared so that X-rays are transmitted through the sample in an orientation parallel to bedding.

VI.V.II. Hydrogen Isotopes

The δD values were measured at the Joint Goethe University – BiK-F Stable Isotope Facility Frankfurt using a ThermoFinnigan MAT 253 mass spectrometer in continuous flow mode coupled to a high temperature conversion elemental analyser (TC-EA). A sample weight of 1 mg was wrapped into Ag foil and dried overnight at 150°C in a stainless steel tray. Samples were rapidly transferred to a zero-blank autosampler in the stainless steel tray and the autosampler was immediately purged with helium gas to avoid re-hydration with ambient air moisture. Standards were run in-line with unknowns and reproduced with an error below ±2 ‰. All δD values are reported relative to standard mean ocean water (VSMOW).

VI.V.III. $^{40}Ar/^{39}Ar$ Geochronology

Ar isotope analysis was conducted at the University of Michigan's Noble Gas Laboratory. Vacuum encapsulated samples were irradiated for 90 MWh at location 8C of the McMaster Nuclear reactor at McMaster University in Hamilton, Ontario in irradiation package mc53. Each capsule had a packet of standard mineral MMhb-1 placed above and below the capsule. Measurement procedures for encapsulated clay samples follow the procedures outlined in Hall (2013), Vacuum capsules were made from 2 mm OD, 1 mm ID fused silica (i.e. quartz) tubing. Sections of tubing were cut into 10 cm long segments and each segment was heated in the middle with a methane-O_2 torch while pulling apart each half, thereby collapsing the center into two 5 cm long pieces with breakseal tips. Clay samples were first suspended in 1 mL of deionized water and then centrifuged in a 1.5 mL tube. The water was then decanted and the remaining clay pellet was allowed to dry in a laminar flow hood. Small (~0.5 mg) pieces of the clay pellets were cut from the dried pellet and loaded into the quartz breakseal tubes and then attached to a vacuum manifold. Procedures for evacuating the breakseal tubes and analyzing the encapsulated samples are outlined in detail in Hall (2013). Encapsulated samples were not baked prior to analysis in order to reduce the possibility of outgassing the sample, thereby complicating the measurement of Ar release due to recoil effects. Encapsulated samples were laser step-heated *in situ* until complete fusion was achieved using a defocused beam from a 5 W Coherent Innova continuous Ar-ion laser operated in multi-line mode. For each degassing step, the system was programmed to heat each grain in turn for 60 seconds.

Ar isotopes were measured using a VG1200S mass spectrometer with a source operating at 150 μA total emission and equipped with a Daly detector operating in analog mode. Mass discrimination was monitored daily using ~4x10^{-9} ccSTP of atmospheric Ar. Fusion system blanks were run every five fusion steps and blank levels from argon masses 36 through 40 (~2 x 10^{-14}, ~3 x 10^{-14}, ~1 x 10^{-14}, ~3 x 10^{-14}, and 2 x 10^{-12} ccSTP respectively) were subtracted from sample gas fractions. Corrections were also made for the decay of ^{37}Ar and ^{39}Ar, as well as interfering nucleogenic reactions from K, Ca and Cl and the production of ^{36}Ar from the decay of ^{36}Cl. Standard hornblende MMhb-1 was used as a neutron flux monitor with an assumed age of 520.4 Ma (Samson and Alexander, 1987). The utilization of either total gas or retention age is determined by crystallite thickness; total gas ages are used in this study as mandated for small crystallite 1Md illite material (Hnat and van der Pluijm, 2014; Fitz-Díaz et al., 2016).

VI.V.IV. Illite Polytype Analysis

The illite polytype analysis method utilizes quantitative X-ray powder diffraction (Q-XRPD) techniques to appraise relative proportions of low- and high-temperature illite polytype end-members in a plurality of grain sizes of a single sample for the purpose of unmixing the isotopic signals of coexisting illite populations in natural rocks (van der Pluijm et al., 2001; van der Pluijm and Hall, 2015). Quantitative examination of illite polytypes is possible by X-ray diffraction, as polytypism in clays is expressed as differences in layer stacking patterns, leading to distinct *hkl* reflections for each polytype. The 2M1 polytype is a higher temperature, well-ordered phase that is typically detrital in origin in low-grade sedimentary rocks. The 1Md polytype is a low-temperature, disordered phase that is secondary (diagenetic) in origin. A quantitative assessment of polytype proportions and an isotopic measurement are acquired for each grain size aliquot of a sample. These are then correlated using York-type linear regression (Mahon, 1996) and the extrapolated end-member values represent the unmixed illite population isotopic compositions.

X-ray diffraction was conducted using a Rigaku Ultima IV diffractometer equipped with CuKα radiation, operated at 40 kV and 44 mA, and located in the Electron Microbeam Analysis Laboratory at the University of Michigan. Oriented slides were measured in both air-dried and ethylene glycolated conditions for qualitative assessment. The front-loading method for random preparations was used for quantitative characterization (Moore and Reynolds, 1997).

A new application of Rietveld whole-pattern matching software BGMN® was used for quantitative analysis (Bergmann et al., 1998). As shown recently (Boles et al, in submission; Chapter II), the Rietveld method for illite polytype quantification is superior to other quantification methods when applying illite polytype analysis to H isotopic composition, because the proportions of additional populations of hydrous clay minerals can be quantified to create the mixing line. This approach also yields more robust error statistics (±2%) and further decreases user dependency (Kleeberg, 2009).

The recent successes in utilizing the H isotopic composition of illite (Boles et al., 2015) and the implementation of Rietveld analysis for Q-XRPD (Boles, in submission) have broadened the scope and increased the accuracy of illite polytype analysis. These advances were used in this study. To create H mixing plots, weight percent 1Md illite is normalized by the total weight percent of all hydrous minerals using equation VI.I:

$$Eq.VI.I:$$

$$\gamma = \frac{\%1Md\ illite}{(\%\ 1Md\ illite + \%\ 2M1\ illite + \%\ chlorite + \%\ other\ hydrous\ minerals)} * 100$$

The extrapolated end-members are 1Md illite on one side of the diagram, and a high-temperature aggregate signal of 2M1 illite, chlorite, and other hydrous phases on the other. A highly linear correlation indicates that the high-T clay phases all have the same isotopic composition; it is highly unlikely that varying proportions of each mineral constituent in each size fraction would produce bulk isotopic measurements that correlate linearly with grain size. In the majority of samples, this signal is dominated by chlorite.

A total of 16 of the 44 samples were selected for illite polytype analysis based on spatial distribution and the presence of illite (these are indicated in table VI.I with an asterisk). Samples were crushed in an agate mortar and pestle, washed, and disaggregated in an ultrasonic bath. Sodium pyrophosphate was used as needed for deflocculation. Each sample was separated into five grain sizes by centrifugation, using Stoke's Law. The resulting grain sizes are: very coarse (2-1 μm), coarse (1-0.5 μm), medium (0.1-0.5 μm), fine (0.05-.01 μm), and very fine (<0.05 μm). H isotopic analyses is conducted on each grain size aliquot, and select samples are dated by $^{40}Ar/^{39}Ar$ geochronology.

VI.VI. Results and Analysis

VI.VI.I. X-ray Texture Goniometry

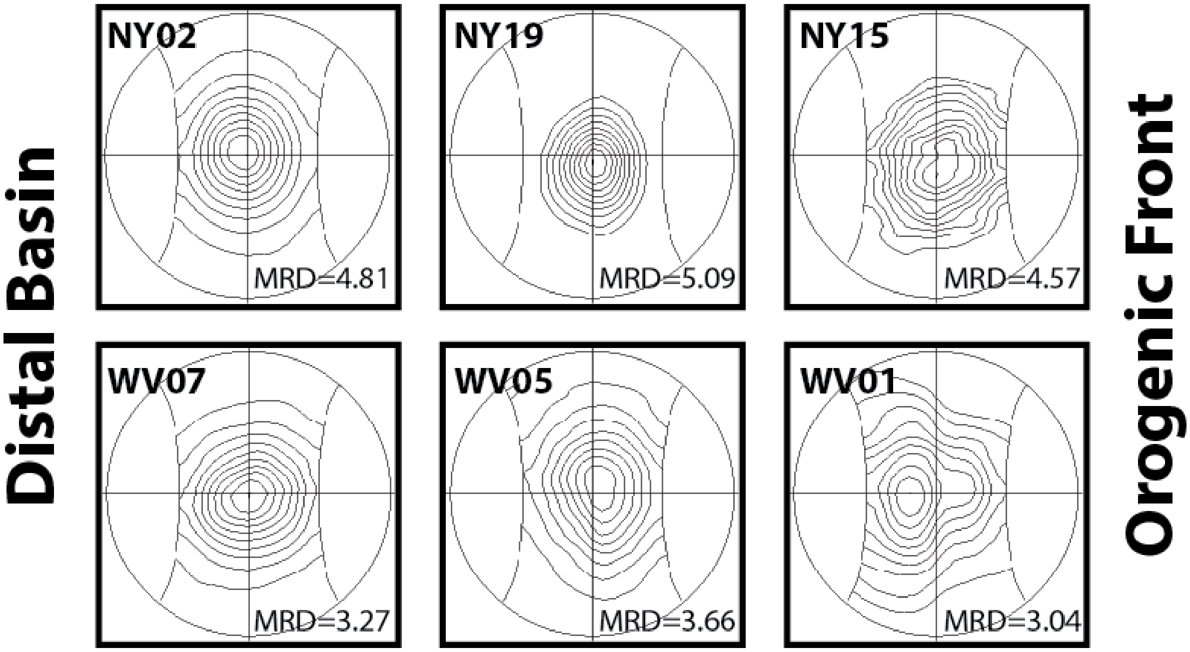

Figure VI.III. Pole-figure diagrams describing the CPO of illite in mudstone samples from two transects across the Appalachian Basin. A single maximum with a circular pattern in all measured samples indicates a burial diagenetic fabric.

Figure VI.III displays the results of 6 X-ray texture goniometry (XTG) analyses; 3 from the New York transect, 3 from the West Virginia transect. These pole figures are arranged by geographic proximity to the orogenic belt. The illite CPO fabric of all samples have symmetrical, circular patterns, which reflect a post-sedimentation, homogeneous compaction fabric overprinted by diagenetic illite growing in a preferred orientation parallel to bedding (Day-Stirrat et al., 2008; Day-Stirrat et al., 2012). Minor elongation is recorded in the samples closest to the orogen, which may indicate the presence of an incipient cleavage (cf. Ho et al., 1999; Ho et al., 2001).

The MRD values expected for unconsolidated sediments at the time of deposition are ~ 1.7-2.0 (Matenaar, 2002), ~6.0 at the onset of metamorphism (Day-Stirrat et al., 2008), and as high as ~12.0 for metamorphic pelites (Jacob et al., 2000). The values recorded in these samples, MRD ~3-5, correspond to burial depths of 2-5 km (Ho et al., 1999; Day-Stirrat et al., 2010).

VI.VI.II. Illite Polytype Analysis

Q-XRPD results from the Rietveld analysis of each of 5 size fractions for 16 sample sites are presented in table VI.II, with an error of ±2 weight percent. The very fine size fractions of samples

Table VI.II. Q-XRPD results (k=kaolinite, g=gypsum, d=dolomite, hb=hornblende, fl=fluorite, ap=apatite)

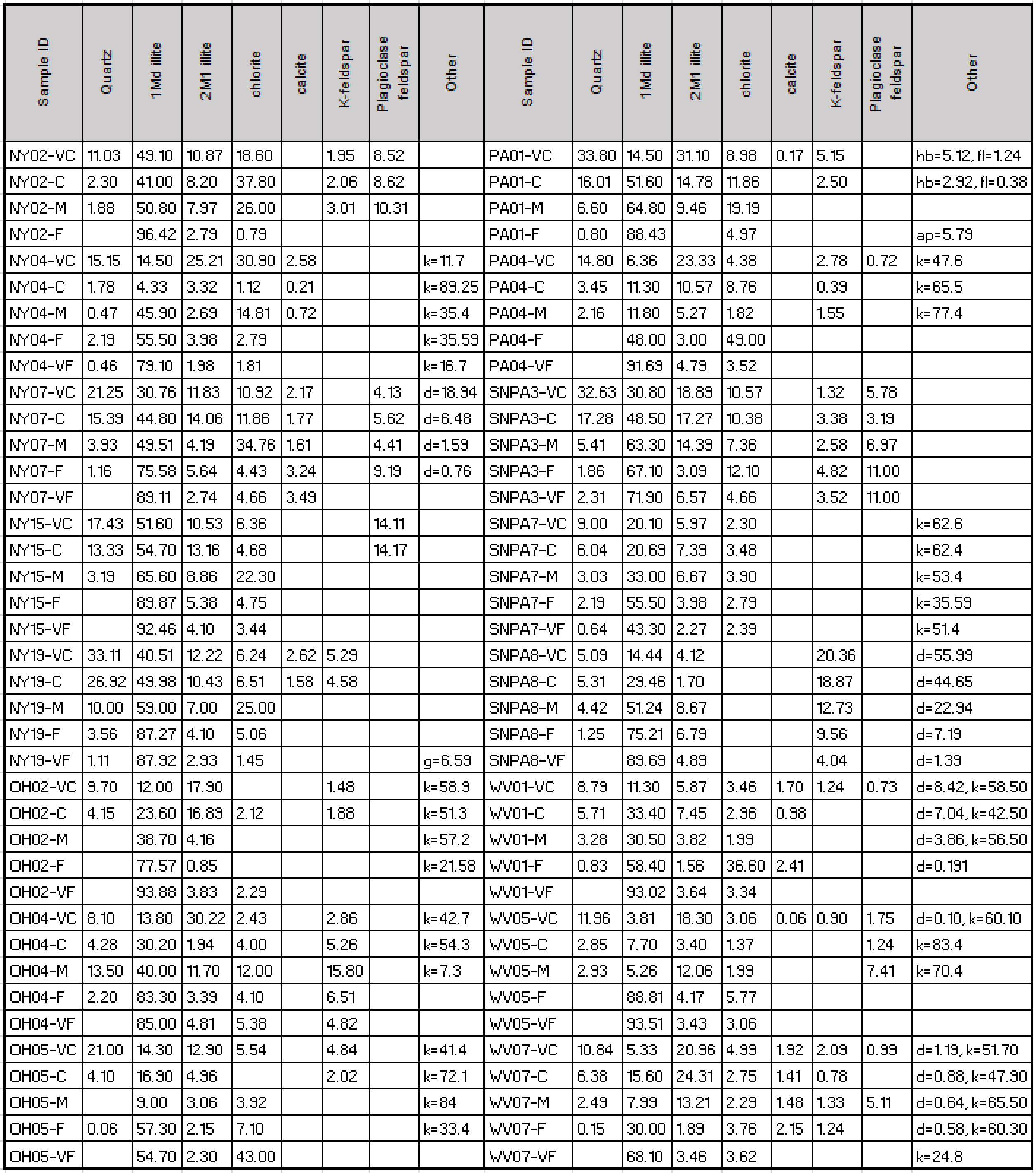

Sample ID	Quartz	1Md illite	2M1 illite	chlorite	calcite	K-feldspar	Plagioclase feldspar	Other	Sample ID	Quartz	1Md illite	2M1 illite	chlorite	calcite	K-feldspar	Plagioclase feldspar	Other
NY02-VC	11.03	49.10	10.87	18.60		1.95	8.52		PA01-VC	33.80	14.50	31.10	8.98	0.17	5.15		hb=5.12, fl=1.24
NY02-C	2.30	41.00	8.20	37.80		2.06	8.62		PA01-C	16.01	51.60	14.78	11.86		2.50		hb=2.92, fl=0.38
NY02-M	1.88	50.80	7.97	26.00		3.01	10.31		PA01-M	6.60	64.80	9.46	19.19				
NY02-F		96.42	2.79	0.79					PA01-F	0.80	88.43		4.97				ap=5.79
NY04-VC	15.15	14.50	25.21	30.90	2.58			k=11.7	PA04-VC	14.80	6.36	23.33	4.38		2.78	0.72	k=47.6
NY04-C	1.78	4.33	3.32	1.12	0.21			k=89.25	PA04-C	3.45	11.30	10.57	8.76		0.39		k=65.5
NY04-M	0.47	45.90	2.69	14.81	0.72			k=35.4	PA04-M	2.16	11.80	5.27	1.82		1.55		k=77.4
NY04-F	2.19	55.50	3.98	2.79				k=35.59	PA04-F		48.00	3.00	49.00				
NY04-VF	0.46	79.10	1.98	1.81				k=16.7	PA04-VF		91.69	4.79	3.52				
NY07-VC	21.25	30.76	11.83	10.92	2.17		4.13	d=18.94	SNPA3-VC	32.63	30.80	18.89	10.57		1.32	5.78	
NY07-C	15.39	44.80	14.06	11.86	1.77		5.62	d=6.48	SNPA3-C	17.28	48.50	17.27	10.38		3.38	3.19	
NY07-M	3.93	49.51	4.19	34.76	1.61		4.41	d=1.59	SNPA3-M	5.41	63.30	14.39	7.36		2.58	6.97	
NY07-F	1.16	75.58	5.64	4.43	3.24		9.19	d=0.76	SNPA3-F	1.86	67.10	3.09	12.10		4.82	11.00	
NY07-VF		89.11	2.74	4.66	3.49				SNPA3-VF	2.31	71.90	6.57	4.66		3.52	11.00	
NY15-VC	17.43	51.60	10.53	6.36			14.11		SNPA7-VC	9.00	20.10	5.97	2.30				k=62.6
NY15-C	13.33	54.70	13.16	4.68			14.17		SNPA7-C	6.04	20.69	7.39	3.48				k=62.4
NY15-M	3.19	65.60	8.86	22.30					SNPA7-M	3.03	33.00	6.67	3.90				k=53.4
NY15-F		89.87	5.38	4.75					SNPA7-F	2.19	55.50	3.98	2.79				k=35.59
NY15-VF		92.46	4.10	3.44					SNPA7-VF	0.64	43.30	2.27	2.39				k=51.4
NY19-VC	33.11	40.51	12.22	6.24	2.62	5.29			SNPA8-VC	5.09	14.44	4.12			20.36		d=55.99
NY19-C	26.92	49.98	10.43	6.51	1.58	4.58			SNPA8-C	5.31	29.46	1.70			18.87		d=44.65
NY19-M	10.00	59.00	7.00	25.00					SNPA8-M	4.42	51.24	8.67			12.73		d=22.94
NY19-F	3.56	87.27	4.10	5.06					SNPA8-F	1.25	75.21	6.79			9.56		d=7.19
NY19-VF	1.11	87.92	2.93	1.45				g=6.59	SNPA8-VF		89.69	4.89			4.04		d=1.39
OH02-VC	9.70	12.00	17.90			1.48		k=58.9	WV01-VC	8.79	11.30	5.87	3.46	1.70	1.24	0.73	d=8.42, k=58.50
OH02-C	4.15	23.60	16.89	2.12		1.88		k=51.3	WV01-C	5.71	33.40	7.45	2.96	0.98			d=7.04, k=42.50
OH02-M		38.70	4.16					k=57.2	WV01-M	3.28	30.50	3.82	1.99				d=3.86, k=56.50
OH02-F		77.57	0.85					k=21.58	WV01-F	0.83	58.40	1.56	36.60	2.41			d=0.191
OH02-VF		93.88	3.83	2.29					WV01-VF		93.02	3.64	3.34				
OH04-VC	8.10	13.80	30.22	2.43		2.86		k=42.7	WV05-VC	11.96	3.81	18.30	3.06	0.06	0.90	1.75	d=0.10, k=60.10
OH04-C	4.28	30.20	1.94	4.00		5.26		k=54.3	WV05-C	2.85	7.70	3.40	1.37			1.24	k=83.4
OH04-M	13.50	40.00	11.70	12.00		15.80		k=7.3	WV05-M	2.93	5.26	12.06	1.99			7.41	k=70.4
OH04-F	2.20	83.30	3.39	4.10		6.51			WV05-F		88.81	4.17	5.77				
OH04-VF		85.00	4.81	5.38		4.82			WV05-VF		93.51	3.43	3.06				
OH05-VC	21.00	14.30	12.90	5.54		4.84		k=41.4	WV07-VC	10.84	5.33	20.96	4.99	1.92	2.09	0.99	d=1.19, k=51.70
OH05-C	4.10	16.90	4.96			2.02		k=72.1	WV07-C	6.38	15.60	24.31	2.75	1.41	0.78		d=0.88, k=47.90
OH05-M		9.00	3.06	3.92				k=84	WV07-M	2.49	7.99	13.21	2.29	1.48	1.33	5.11	d=0.64, k=65.50
OH05-F	0.06	57.30	2.15	7.10				k=33.4	WV07-F	0.15	30.00	1.89	3.76	2.15	1.24		d=0.58, k=60.30
OH05-VF		54.70	2.30	43.00					WV07-VF		68.10	3.46	3.62				k=24.8

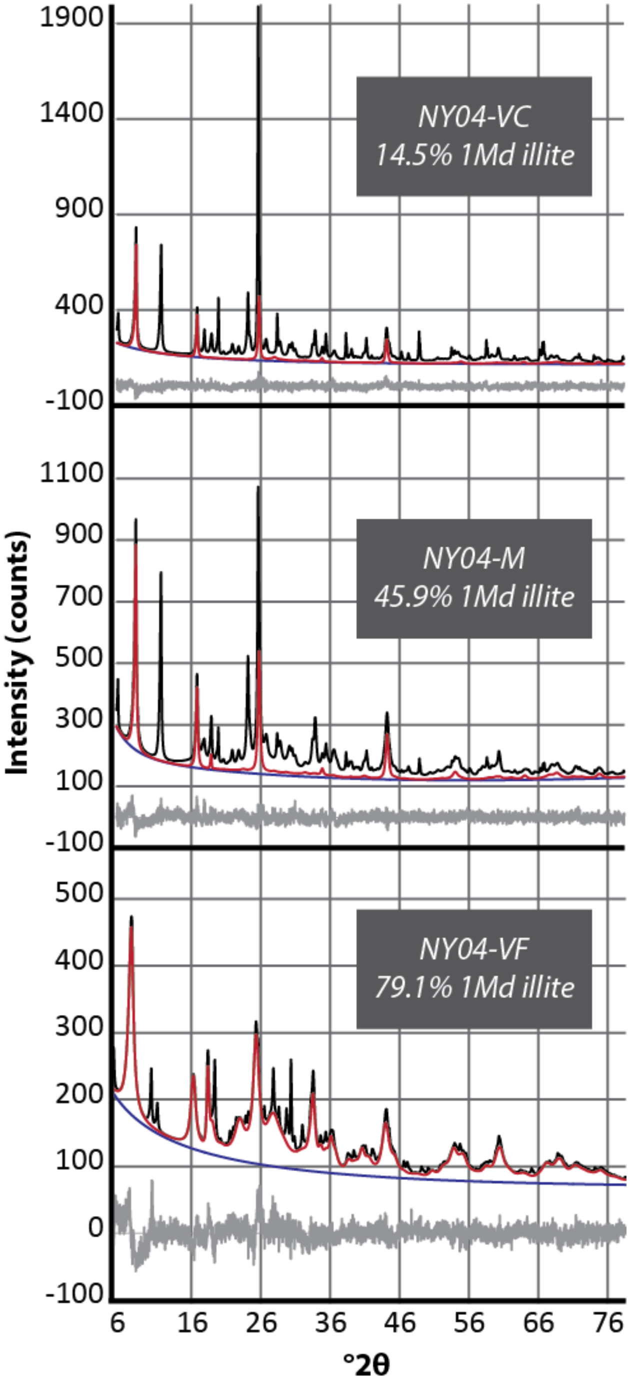

Figure VI.IV. X-ray diffractograms of three grain size fractions of sample NY04. Sample measurement data (black line), modeled 1Md illite (red line), calculated background (blue line), and difference between Rietveld model and measured spectrum (grey line) are displayed.

NY02 and PA01 were dominated by amorphous material, and illite polytypes could not be modeled using Q-XRPD. Figure VI.IV highlights the robust model fits achieved by BGMN ®, and the negative correlation between grain size and the proportion of authigenic illite for multiple size fractions of sample NY04.

VI.VI.III. Hydrogen Isotopes

The results of H isotopic analysis of each of the 5 size fractions for 16 samples are reported in Table VI.III. Using the measured H isotopic compositions and Q-XRPD results of each grain size, mixing plots are created for those samples located within the Appalachian Plateau (Figure VI.V). This excludes samples SNPA3, SNPA7, and SNPA8 which were collected in the Valley and Ridge province. The anomalously low value in sample PA01-VF is attributed to the presence of organic material or apatite, and, because the size fraction cannot be modeled by Q-XRPD, it is not used to calculate a mixing line for that sample. The extrapolated authigenic (1Md) clay end-member values and the extrapolated high-T hydrous mineral aggregate end-member values, after York regression analysis, are reported in Table VI.IV.

In order to convert the end-member isotopic values to equilibrium fluid compositions, constraints on the temperature of crystallization are needed. Figure VI.VI overlays the sample locations onto the conodont alteration index map of Harris (1979), and gives the fractionation temperature utilized for each of the samples. Using this temperature constraint in the fractionation equation of Capuano (1992), the equilibrium fluid values are calculated. These values and their corresponding temperatures are reported in Table VI.IV. In addition, to get an estimate of the mineralizing fluid of the high-temperature end-member (typically comprising 2M1 illite, chlorite), using the assumption that each of these phases have the same isotopic composition (which

Table VI.III. H isotopic results

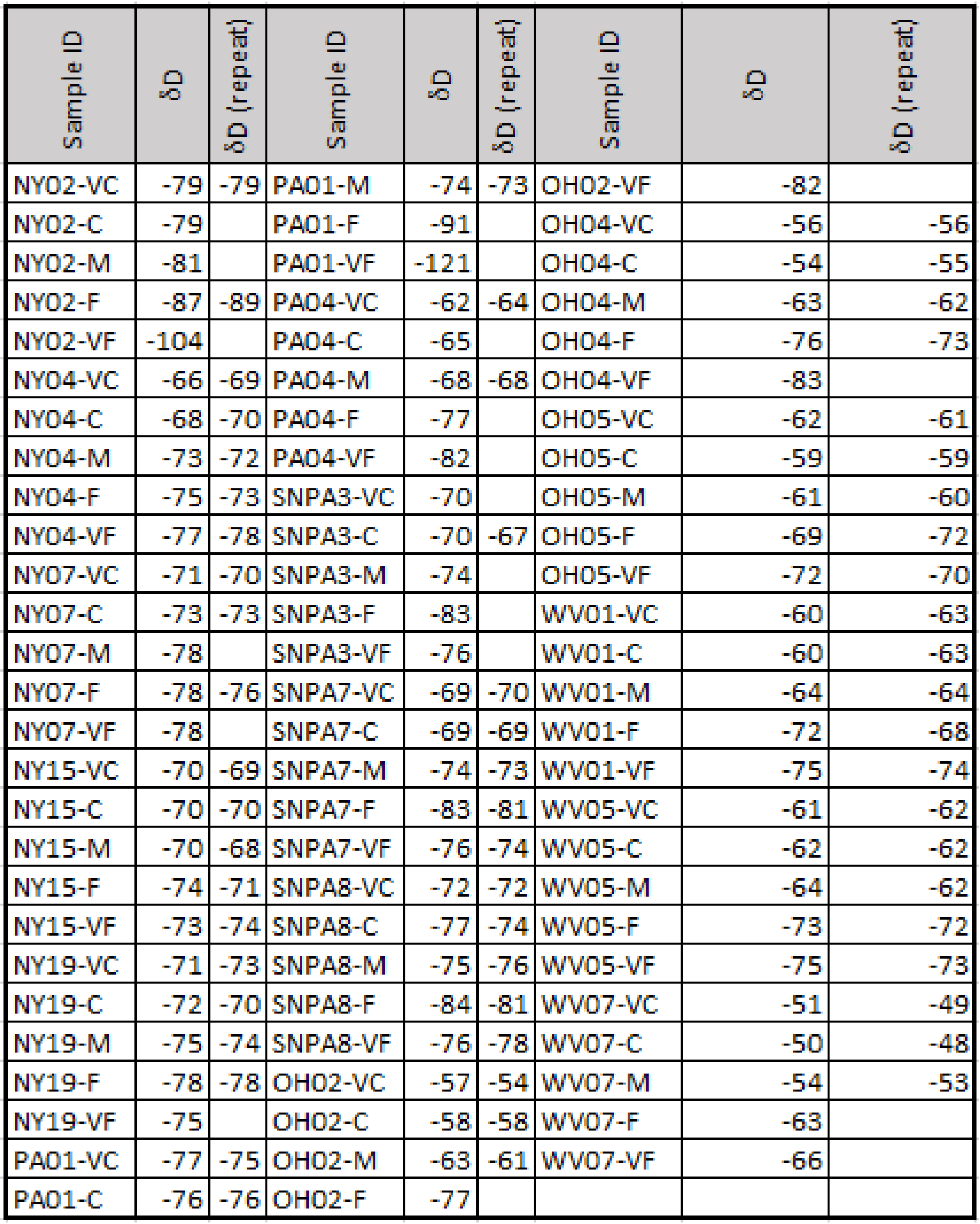

Sample ID	δD	δD (repeat)	Sample ID	δD	δD (repeat)	Sample ID	δD	δD (repeat)
NY02-VC	-79	-79	PA01-M	-74	-73	OH02-VF	-82	
NY02-C	-79		PA01-F	-91		OH04-VC	-56	-56
NY02-M	-81		PA01-VF	-121		OH04-C	-54	-55
NY02-F	-87	-89	PA04-VC	-62	-64	OH04-M	-63	-62
NY02-VF	-104		PA04-C	-65		OH04-F	-76	-73
NY04-VC	-66	-69	PA04-M	-68	-68	OH04-VF	-83	
NY04-C	-68	-70	PA04-F	-77		OH05-VC	-62	-61
NY04-M	-73	-72	PA04-VF	-82		OH05-C	-59	-59
NY04-F	-75	-73	SNPA3-VC	-70		OH05-M	-61	-60
NY04-VF	-77	-78	SNPA3-C	-70	-67	OH05-F	-69	-72
NY07-VC	-71	-70	SNPA3-M	-74		OH05-VF	-72	-70
NY07-C	-73	-73	SNPA3-F	-83		WV01-VC	-60	-63
NY07-M	-78		SNPA3-VF	-76		WV01-C	-60	-63
NY07-F	-78	-76	SNPA7-VC	-69	-70	WV01-M	-64	-64
NY07-VF	-78		SNPA7-C	-69	-69	WV01-F	-72	-68
NY15-VC	-70	-69	SNPA7-M	-74	-73	WV01-VF	-75	-74
NY15-C	-70	-70	SNPA7-F	-83	-81	WV05-VC	-61	-62
NY15-M	-70	-68	SNPA7-VF	-76	-74	WV05-C	-62	-62
NY15-F	-74	-71	SNPA8-VC	-72	-72	WV05-M	-64	-62
NY15-VF	-73	-74	SNPA8-C	-77	-74	WV05-F	-73	-72
NY19-VC	-71	-73	SNPA8-M	-75	-76	WV05-VF	-75	-73
NY19-C	-72	-70	SNPA8-F	-84	-81	WV07-VC	-51	-49
NY19-M	-75	-74	SNPA8-VF	-76	-78	WV07-C	-50	-48
NY19-F	-78	-78	OH02-VC	-57	-54	WV07-M	-54	-53
NY19-VF	-75		OH02-C	-58	-58	WV07-F	-63	
PA01-VC	-77	-75	OH02-M	-63	-61	WV07-VF	-66	
PA01-C	-76	-76	OH02-F	-77				

otherwise would not correlate linearly), the chlorite fractionation equation of Graham et al. (1987) is used. In contrast, an anchizone-greenschist facies boundary temperature of 300°C is used to obtain an estimate of the mineralizing fluid composition of the high temperature (2M1) clays. These fluid values are also reported in Table VI.IV.

Table VI.IV. Extrapolated end-member and calculated fluid δD results

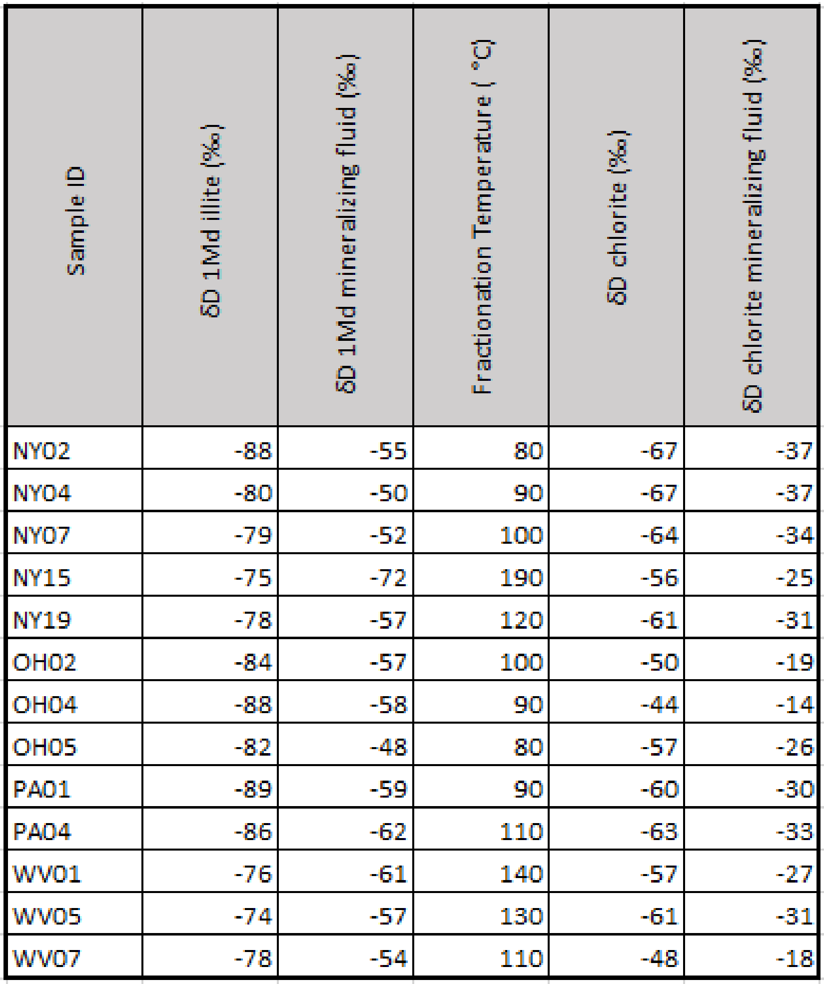

Sample ID	δD 1Md illite (‰)	δD 1Md mineralizing fluid (‰)	Fractionation Temperature (°C)	δD chlorite (‰)	δD chlorite mineralizing fluid (‰)
NY02	-88	-55	80	-67	-37
NY04	-80	-50	90	-67	-37
NY07	-79	-52	100	-64	-34
NY15	-75	-72	190	-56	-25
NY19	-78	-57	120	-61	-31
OH02	-84	-57	100	-50	-19
OH04	-88	-58	90	-44	-14
OH05	-82	-48	80	-57	-26
PA01	-89	-59	90	-60	-30
PA04	-86	-62	110	-63	-33
WV01	-76	-61	140	-57	-27
WV05	-74	-57	130	-61	-31
WV07	-78	-54	110	-48	-18

VI.VI.IV. ^{40}Ar/^{39}Ar Geochronology

Samples NY04, NY07, NY15, and NY19 were selected for Ar dating toward a r transect across the Appalachian Plateau. The results of the dating for each size fraction of these samples are presented in table VI.V. Sample NY19-VF exhibited extreme Cl/K ratios during degassing and was excluded from age analysis. Age analysis calculates an end-member 1Md illite formation age of 250.3±4.2 Ma and a 2M1 illite formation age of 494.2±13.4 Ma for sample NY04; a 1Md illite formation age of 231.8±11.0 Ma and a 2M1 illite formation age of 759.3±52.1 Ma for sample

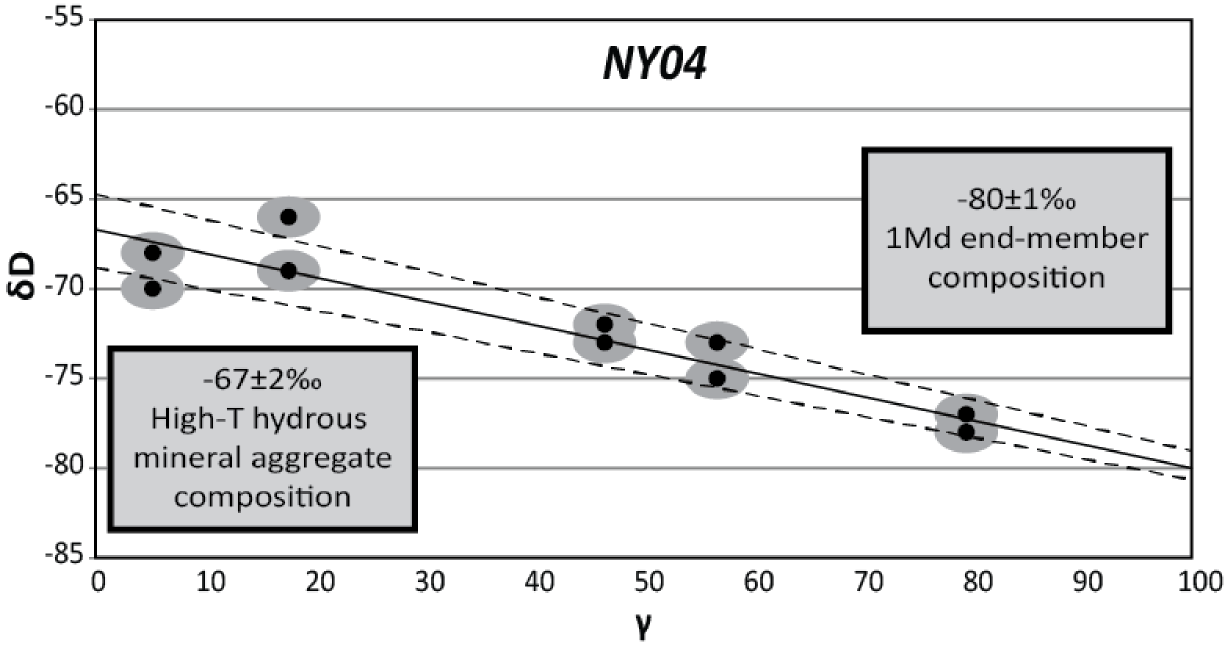

Figure VI.V. Mixing line with York-type linear regression analysis between H isotopic composition and abundance of authigenic illite (γ is defined in equation VI.I of the text). Uncertainty is indicated by grey spheres and dashed lines. Extrapolated end-member isotopic compositions for 1Md illite and a chlorite-dominated high-T hydrous clay mineral aggregate are displayed.

NY07; a 1Md illite formation age of 237.6±18.0 Ma and a 2M1 illite formation age of 944.1±116.4 Ma for sample NY15; and a 1Md illite formation age of 226.1±34.5 Ma and a 2M1 illite formation age of 1222.4±187.5 Ma for sample NY19 (figure VI.VII). Due to the limited range of 1Md:2M1 ratios exhibited by samples NY07, NY15, and NY19, the uncertainty estimates reported from the regression analysis are affected by the unochron error (the result of a much smaller range in %1Md

Table VI.V. 1Md:2M1 ratio and total gas age for each of the dated size fractions

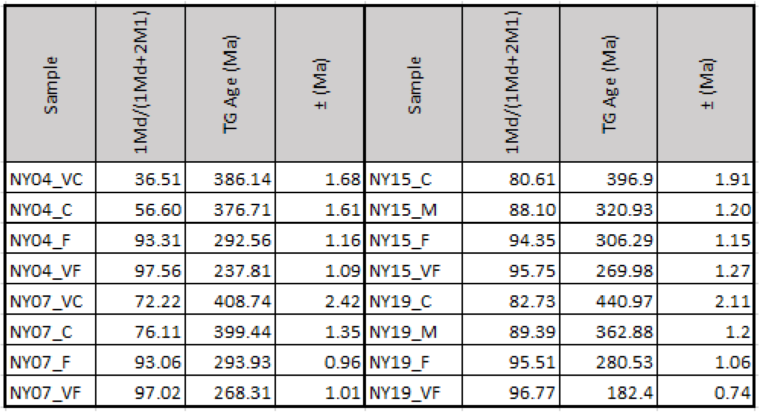

Sample	1Md/(1Md+2M1)	TG Age (Ma)	± (Ma)	Sample	1Md/(1Md+2M1)	TG Age (Ma)	± (Ma)
NY04_VC	36.51	386.14	1.68	NY15_C	80.61	396.9	1.91
NY04_C	56.60	376.71	1.61	NY15_M	88.10	320.93	1.20
NY04_F	93.31	292.56	1.16	NY15_F	94.35	306.29	1.15
NY04_VF	97.56	237.81	1.09	NY15_VF	95.75	269.98	1.27
NY07_VC	72.22	408.74	2.42	NY19_C	82.73	440.97	2.11
NY07_C	76.11	399.44	1.35	NY19_M	89.39	362.88	1.2
NY07_F	93.06	293.93	0.96	NY19_F	95.51	280.53	1.06
NY07_VF	97.02	268.31	1.01	NY19_VF	96.77	182.4	0.74

than the range in age), however the high proportions of 1Md illite in these samples give high confidence to the calculated end-member 1Md illite age (van der Pluijm and Hall, 2015).

VI.VII. Discussion

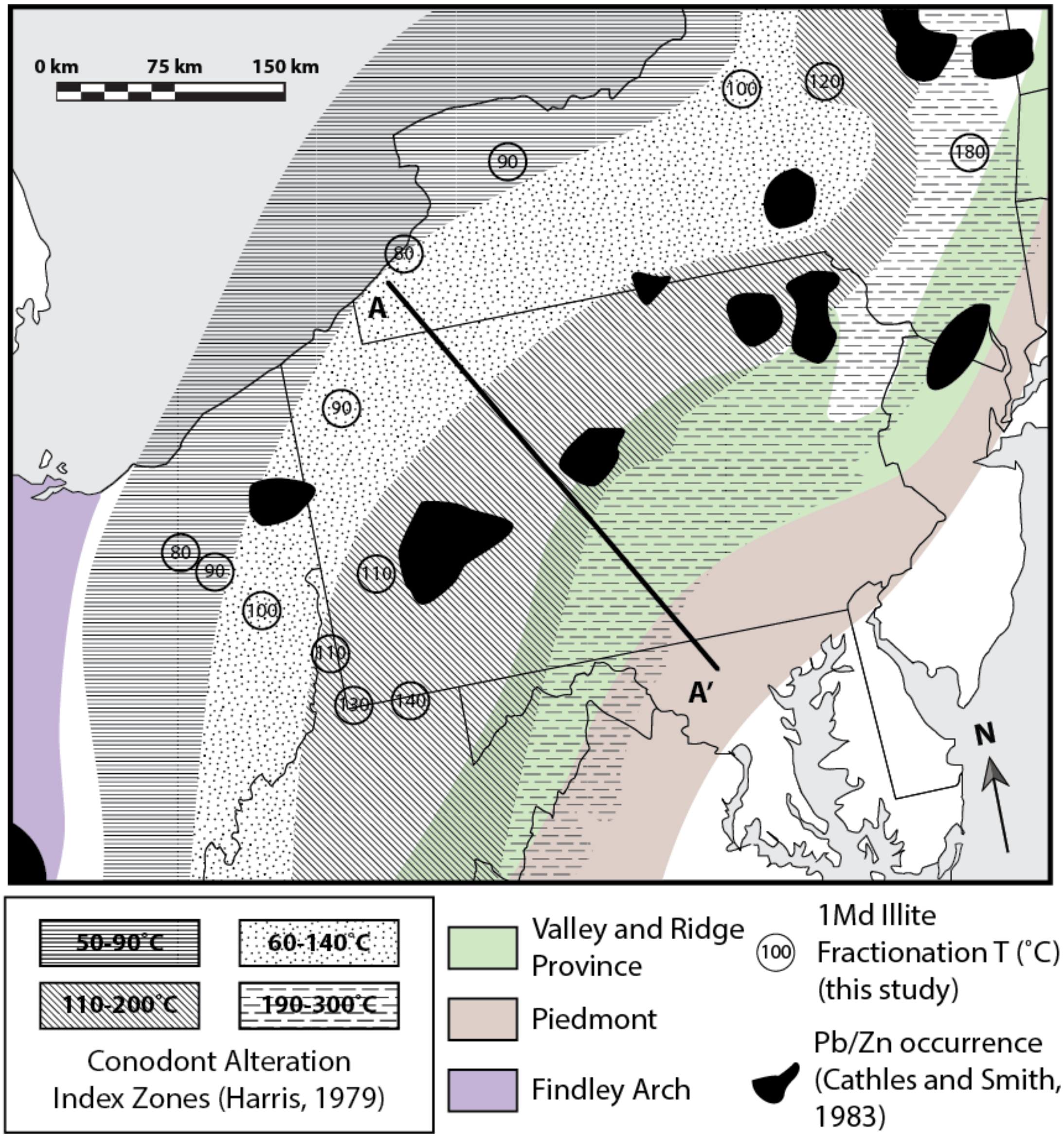

Figure VI.VI. Map of study area, overlaying select Appalachian Plateau samples onto the conodont alteration zones of Harris (1979). The numbers in the sample location circles indicate the chosen formation temperature utilized in H isotopic fractionation calculations. The cross-section line A-A' of figure VI.VIII is displayed.

To gain an understanding of the geographic variability of mineralizing fluid compositions, figure VI.VIII projects the data by distance from the Appalachian orogenic front onto a composite cross section line A-A' of figure VI.VI (geology from Cleaves et al., 1968; Ryder et al., 2009). In this

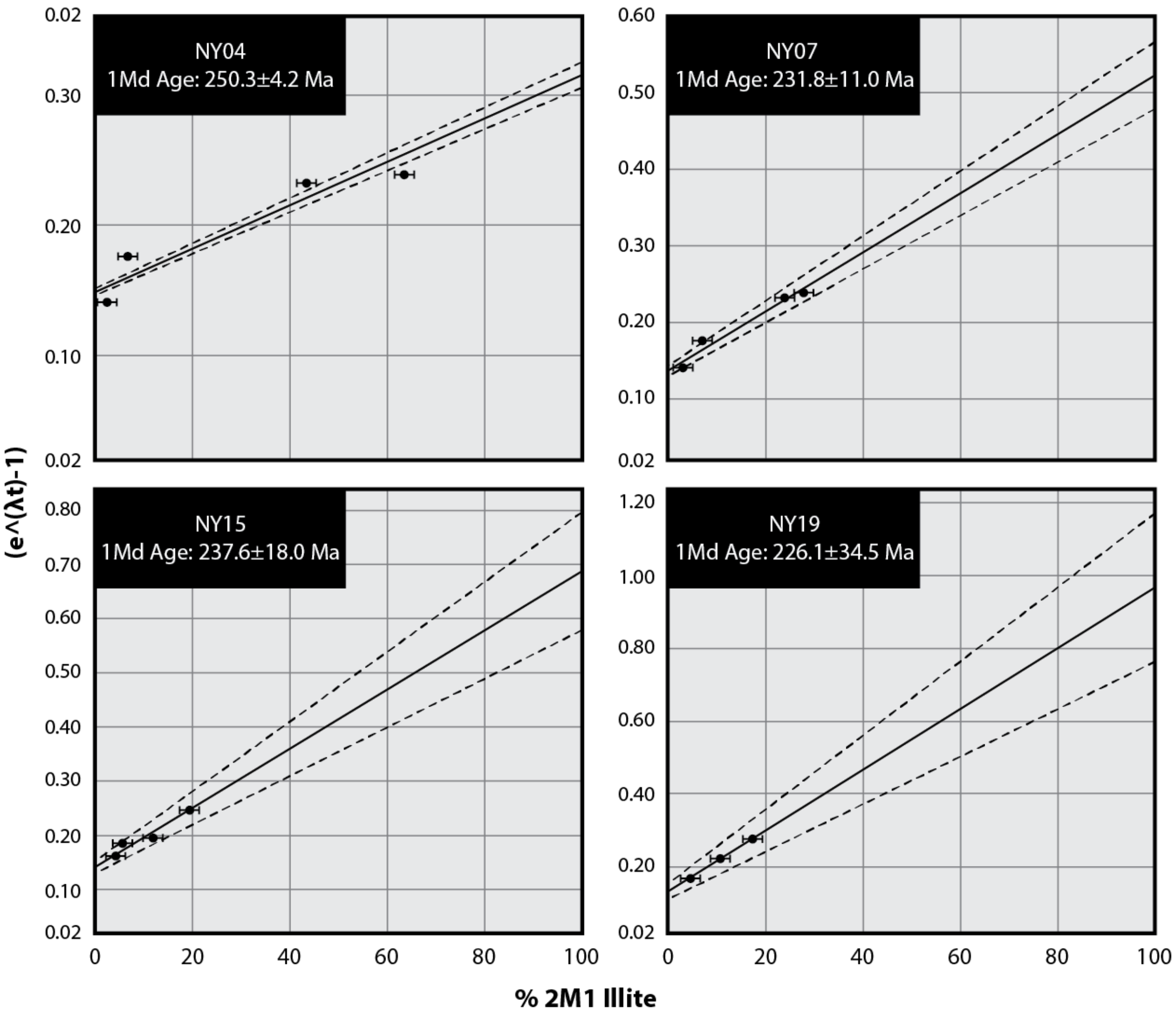

Figure VI.VII. Age analysis of samples NY04, NY07, NY15, and NY19.

generalized section, a negative correlation between 1Md illite δD composition and geographic proximity to the orogenic front is recognized, with samples located further into the craton displaying more negative 1Md illite compositions. When paired with the observation that a sampling transect of the modern day surface of the Appalachian Plateau represents rocks that occupied increasingly deeper stratigraphic levels and higher diagenetic grades (and thus higher formation temperatures) towards the orogen, the calculated mineralizing fluid compositions display a positive correlation with geographic proximity to the orogenic front. This pattern is predicted by clay-fluid H isotopic partitioning that yields higher and more deuterium-enriched fractionations at lower temperatures. Depositional geothermal gradient estimates in the Appalachian Basin are 25-30ºCkm^{-1} (Reed et al., 2005), so at formation temperatures of 80-190ºC,

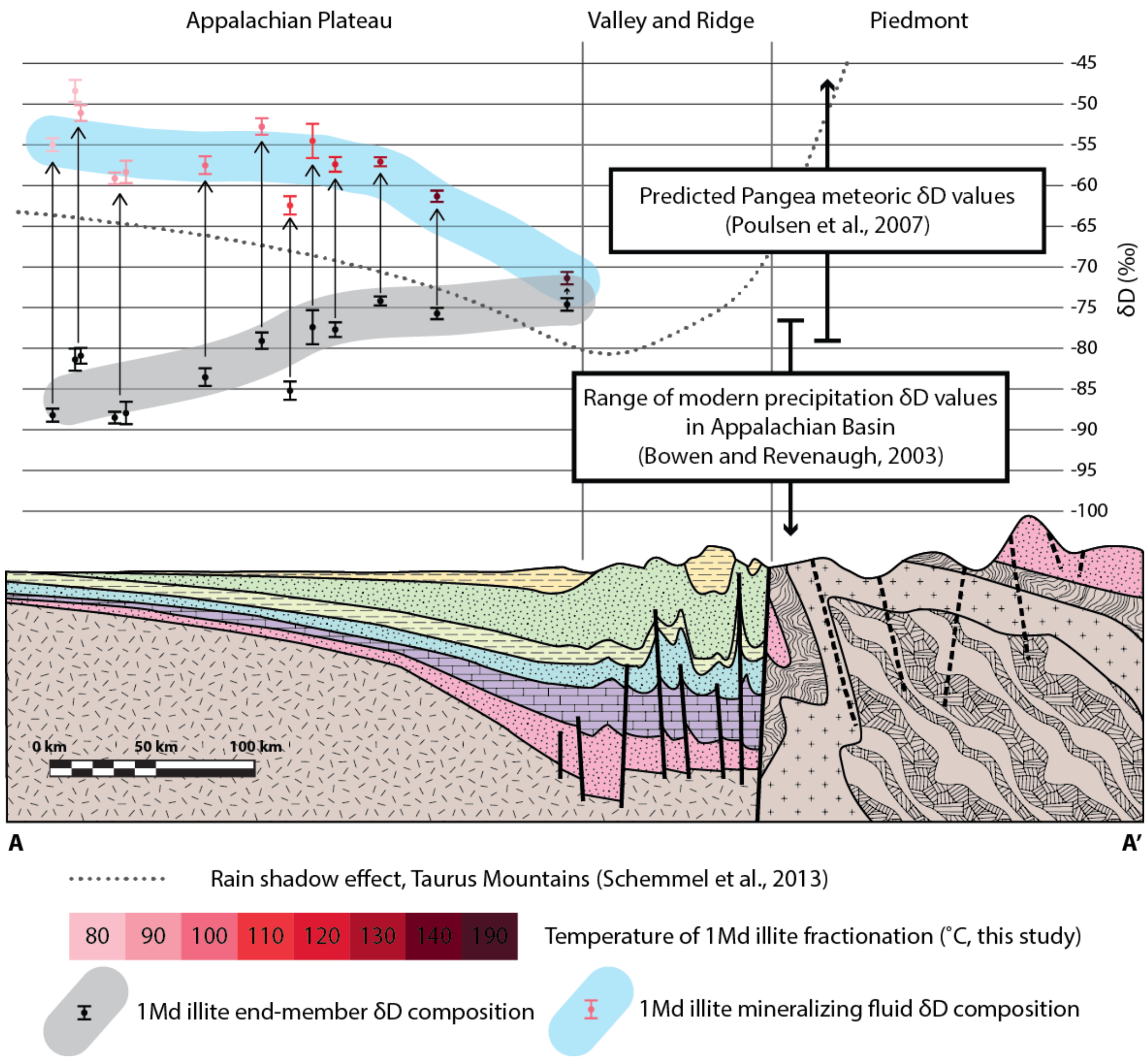

Figure VI.VIII. Composite idealized cross-section of the central Appalachian plateau and orogen. Both illite and mineralizing fluid compositions are displayed, color coded by utilized fractionation temperature. δD ranges of modeled Late Paleozoic meteoric fluid and modern Appalachian Basin meteoric fluid are displayed, as are rain shadow trends from modern orogens.

diagenesis and 1Md illite neocrystallization occurred at depths of ~3-6 km. Estimates of erosion from the Appalachian Plateau, based, variously, on coal rank, conodont alteration index, critical wedge theory, apatite fission track analysis, Atlantic-margin sediment volume calculations, and more, postulate 2-9 km of denuded topography, which accounts for the decreasing formation temperatures away from the orogen (Mathews, 1975; Friedman and Sanders, 1982; Slingerland and Furlong, 1989; Blackmer et al., 1994; Reed et al., 2005).

The calculated mineralizing fluid compositions are less negative than the range of modern precipitation in this region of North America, which is consistent with a more southerly Early Triassic paleogeographic latitude of North America and elevated mean surface temperatures during that time (Ziegler et al., 1983; Zharkov and Chumakov, 2001; Van der Voo, 1988; Peyser and Poulsen, 2008; Bowen and Revenaugh, 2003; Torsvik et al., 2012). The late Early Triassic was a period of dramatic climate change, likely due to changing atmospheric CO_2 concentrations, that led to a change from global hot-house conditions to latitudinally differentiated climatic zones (Galfetti et al., 2007; Preto et al., 2010). Our calculated mineralizing fluid compositions fall within the predicted range, and display the anticipated trend of modeled Pangea meteoric fluid values (using $\delta D \approx 8 * \delta^{18}O$; Poulsen et al., 2007). The geographic dependent behavior displayed by the mineralizing fluid compositions is congruent with a rain shadow effect that is widely observed in modern day orogenic belts, such as the Taurus mountains and the Southern Alpine mountains (Mulch and Chamberlain, 2007; Schemmel et al., 2013).

The high-T aggregate end-member isotopic composition of the 13 samples has no geographic trend and all occupy a narrow range of values with an average value of -55‰. The average high-T fluid composition of all 16 samples is -25‰, well within the predicted metamorphic fluid range (Sheppard, 1986; Schedl et al., 1993). We interpret this narrow range of values within the metamorphic field as confirmation that high temperature clays are indeed detrital, reflecting the composition of their orogenic provenance area.

The timing of diagenesis and 1Md illite neocrystallization represent a protracted window from ~225-250 Ma, within the lower half of the Triassic Period. In contrast, previous studies have suggested that the timing of K-alteration in the North American midcontinent was linked to orogenic fluid expulsion of the Alleghenian orogeny, with anticipated dates in the range of 320-270 Ma (Schedl et al., 1993; Elliott and Aronson, 1987; Hay et al., 1988; Hearn et al., 1987; Clauer et al., 2013). Instead, the ages of end-member 1Md illite mineralization from this study demonstrate a younger age for regional diagenesis that indicates mineralization post-dating final orogenic activity. Our new results challenge these reigning views.

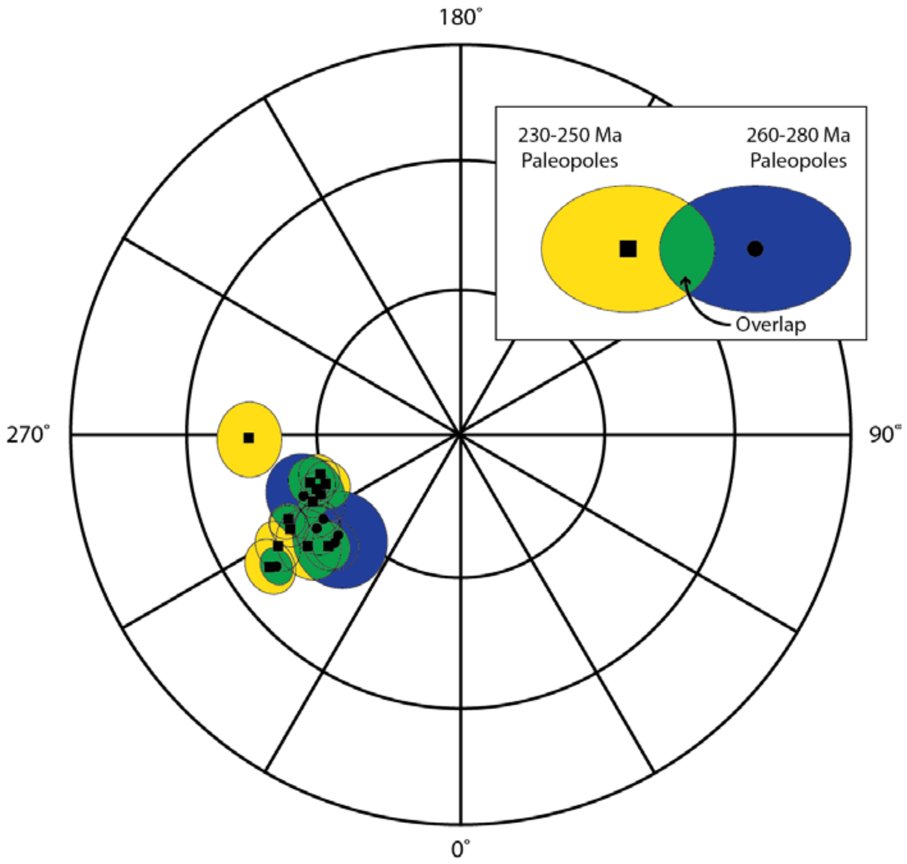

Figure VI.IX. Comparison of 6 paleopoles from Alleghenian time (260-280 Ma, circles with blue α_{95}) and 13 Early to Middle Triassic paleopoles (230-250 Ma, squares with yellow α_{95}). Significant overlap occurs, as indicated by green field (lower-hemispheric projection).

Widespread paleomagnetic remagnetization is among the foreland geologic phenomena in the area (Van der Voo and Torsvik, 2012). Interestingly, the comparison of paleopoles from remagnetized sedimentary strata in the Appalachian Plateau with apparent polar wander paths indicates a window of remagnetization that was previously interpreted as Late Paleozoic based on tectonic events and the orogenic fluid flow hypothesis (Scotese et al., 1982; Miller and Kent, 1988; McCabe et al., 1989). A critical reexamination of this data, however, shows that Alleghenian poles (260-280 Ma) overlap significantly with Early-Mid Triassic poles (230-250 Ma), and, thus, that remagnetization could similarly be younger (figure VI.IX; North America paleopoles from Torsvik et al., 2012). The analysis in this study indicates that either i) paleomagnetic remagnetization represents a longer and later time than previously postulated, or ii) a decoupling of 1Md illite neoformation and Valley & Ridge remagnetization processes.

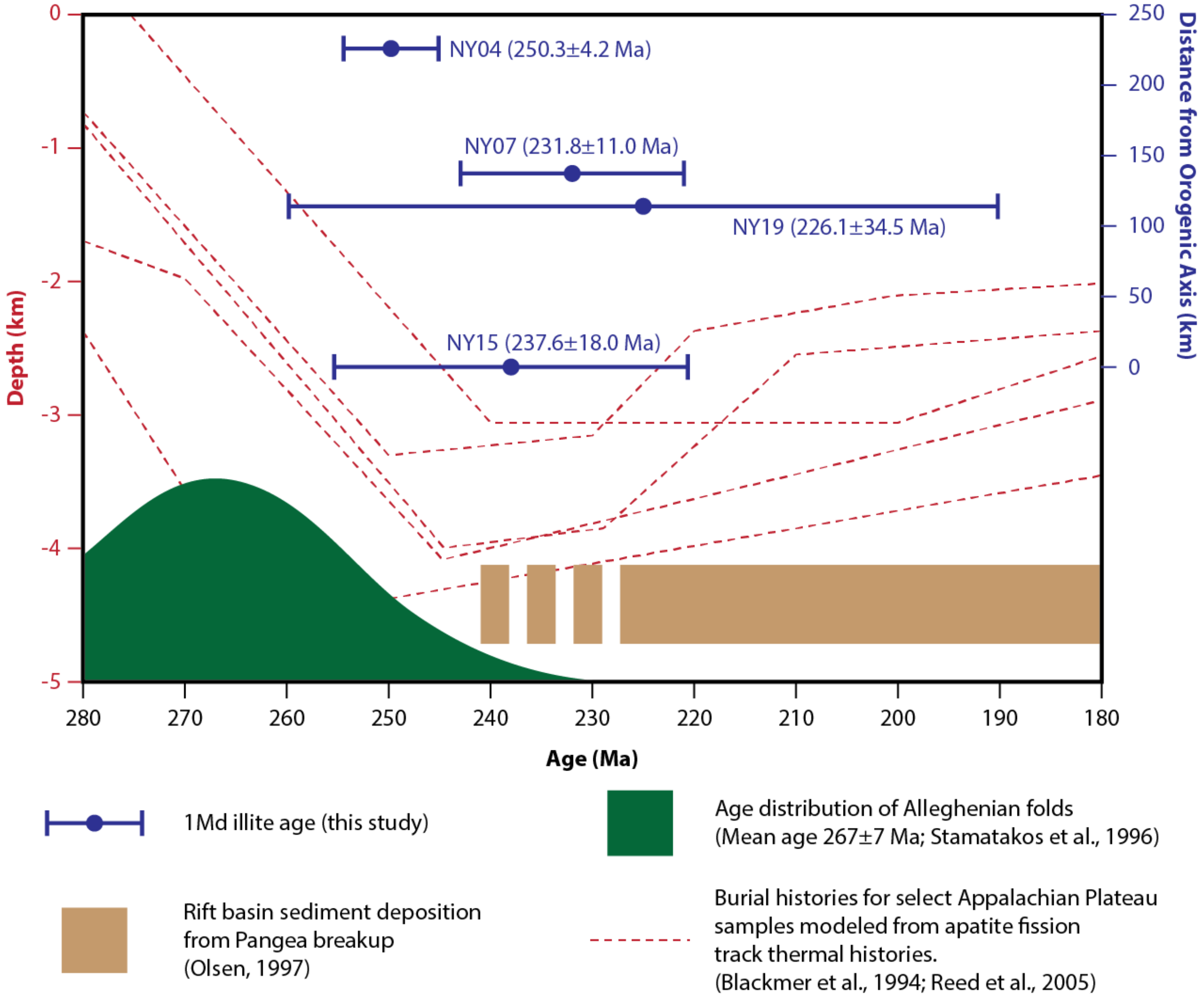

Figure VI.X. Diagenetic ages are plotted in context of the tectonic activity in the Appalachian Plateau. The ages are compared to apatite fission track analysis, Alleghenian fold timing, and Pangea break-up synrift strata deposition timing. The ages span the transition period from burial to exhumation and compressional to extensional tectonics.

Mississippi Valley-Type deposit genesis is conspicuously absent during Pangea breakup (Leach et al., 2001), with various radiometric and paleomagnetic dates constraining global MVT mineralization timing to two dominant Phanerozoic times, ~400-260 Ma and ~180-40 Ma, although Brannon et al. (1997) report a Th/Pb calcite age of 251±11 Ma. Successful MVT dating has focused on U/Pb and U/Th systems of calcite, Rb/Sr of sphalerite, Ar-Ar and K-Ar of feldspar. Approximations on the duration of MVT mineralization events have produced widely variable estimates, from <1 Ma to >25 Ma (Leach et al., 2001). The 1Md illite mineralization recorded in this study may therefore be unrelated to MVT deposit generation.

Figure VI.X plots the mineralization ages with respect to the tectonic evolution of Eastern North America and shows no spatio-temporal trend that would be expected if a chemically active alteration front was passing through the strata in a westward-driven, time-dependent regional fluid flow scenario. Instead, the diagenetic event was widespread and long-lasting across the Appalachian Plateau in lower Triassic times.

The newly-obtained Triassic ages are striking in their relation to the tectonic history of the region (Hatcher et al., 1989). They straddle the time space between Alleghenian folding, estimated by Stamatakos et al. (1996) with a mean age of ~267 Ma, and commencement of deposition of syn-rift strata related to Pangea breakup starting in the Lower Triassic (Olsen, 1997). In addition, apatite fission track analysis of Paleozoic rocks of the Appalachian Plateau shows that around this time isostatic rebound initiated, with the ensuing history of the Appalachian Basin one of progressive exhumation (Blackmer et al., 1994; Reed et al., 2005). These studies conclude that burial rates were on the order of 0.1 mm/yr, and that exhumation rates from late Permian to the early Cretaceous were ~0.01 mm/yr. This coincidence between the timing of maximum subsidence, i.e. the time peak basinal temperatures, and diagenesis is recorded by our age analysis of clay authigenesis and the diagenetic textures at depths 2-5 km of 1Md mica from the fabric analysis (XTG) data.

Maximum subsidence in a basin's history corresponds to a time when joint formation is most productive (Engelder and Lacazette, 1990). The systematic and pervasive joint sets that are exposed today in the Appalachian Plateau were derived both from burial and earlier deformation during Alleghenian deformation (Nickelsen and Hough, 1967; Engelder, 1985; Engelder et al., 2009). Their reactivation provided ubiquitous, vertical fluid pathways.

The diagenetic event we describe in our study spans the transition from burial to exhumation, and from compressional to extensional tectonics. We posit that the stress reorientation commensurate with this changing tectonic regime facilitated the infiltration of locally-sourced, surface-derived fluid to crustal depths of several kilometers, possibly by hydraulic fracturing of joints at the time of peak basin subsidence. The critically stressed brittle crust of intracratonic settings assisted in the opening of such fluid conduits, related to damage zones of pre-existing or new discontinuities that are ubiquitous in the North American Midcontinent.

VI.VIII. Conclusions

The pairing of H isotopic analysis and Ar dating of authigenic clays in the sedimentary rocks of the Appalachian Plateau provides a powerful tool to understand the conditions and timing of diagenesis. Our investigation of 1Md illite shows that authigenesis occurred at temperatures between 80-190ºC and at depths of 3-6 km, and that the provenance of the mineralizing fluid was predominantly meteoric in nature. Fluid was localized on spatial scales small enough to preserve a rain shadow effects of the high elevation Appalachian orogen in the Late Paleozoic-Early Mesozoic eras. The timing of regional clay diagenesis postdates the main stage of Alleghenian deformation and, instead, coincides with the onset of Triassic rifting of Pangea, when Appalachian Plateau deposits changed from a burial environment to exhumation.

We conclude that there is no evidence for long-range, lateral fluid migration to explain widespread illite mineralization in the Appalachian Plateau, and associated geologic processes (including chemical remagnetization), resolving problems related to the challenges of major lateral fluid flow that include volume, temperature and duration of flow. The lower Triassic age of diagenesis from ~230-250 Ma is protracted, and unrelated to older contraction in the nearby Appalachian orogen. Instead, we posit that the release of compressional stresses and initiation of exhumation are the driving forces behind surface fluid infiltration into the upper crust.

VI.IX. Acknowledgments

We thank Andreas Mulch and Chris Hall for H isotopic analysis and Ar dating, respectively. We thank Samantha Nemkin for field efforts that provided preliminary samples from the Valley and Ridge Province of Pennsylvania. We thank the Sedimentary Geology Division and Structural Geology and Tectonics Division of the Geological Society of America for the Stephen E. Laubach Research in Structural Diagenesis Award that supported this research. We also thank the Clay Minerals Society for the Robert C. Reynolds, Jr. Research Award that supported this research. Our work on clay mineralization is supported by the National Science Foundation, most recently under EAR-16PAF03738.

Chapter VII. Conclusions

This final chapter is organized into two broad categories in an effort to abridge and generalize the outcomes of this dissertation, with subjects that span both time (from Paleozoic to neotectonic deformation) and space (North America, Japan, Turkey, New Zealand, and Papua New Guinea):

i) Advances achieved by these studies on the application of clay mineralogy to the resolution of structural questions; and

ii) Broader contributions of these studies toward the understanding of deformation processes and conditions of the upper (brittle) crust.

VII.I. Clays in Deformation Zones

The diversity of composition and structure within and among clay minerals, and their low-temperature formation and stability, make them appealing phases for understanding the conditions of deformation in the brittle crust. They are powerful geochronometers, geothermometers, tracers of geofluids, 3-dimensional deformation fabric recorders, and predictors of the crust's mechanical behavior and deformation styles. This dissertation has focused on the development and application of several of these tools, with the specific goal to widen the scope and increase the accuracy of the illite polytype analysis method. Deformation zone clays are also used in several ways to constrain ambient temperature conditions and link crystallographic preferred orientation to deformation.

Chapters II, III, V, and VI present a range of applications of illite polytype analysis methodology in deformation studies. Key contributions of this dissertation to the application of illite polytype analysis are:

- The use of whole pattern Rietveld-type quantitative X-ray powder diffraction techniques;
- The application of stable isotopic systematics of fine-grained illite.

Quantitative Rietveld-based tools like BGMN® (Bergmann et al., 1998) are utilized to improve the uncertainty estimation of polytype quantification in illite analysis. This facilitates greater total accuracy and precision for unmixing of isotopic signals in multiphase populations. The new method also decreases user dependency and yields results with inter-laboratory repeatability (chapter II). Furthermore, the measured isotopic signal of a clay-rich sample can be decomposed into its constituent signals using Rietveld analysis when confronting samples that include non-illitic clay mineral species (chapter V-VI and appendix III).

The novel integration of H isotopic analysis and illite polytype analysis significantly augments the utility of the approach, decidedly broadening its appeal. The ability to both date the timing of synkinematic illite growth and constrain the composition of the mineralizing fluid active in the deformation zone extends the range of answers that can be provided by its use. Specifically, chapters III, V, and VI illustrate the effectiveness of using H isotopic composition as a discriminator between clay populations, and allow robust inferences about geofluid provenance and pathways, and reaction temperature. Similar approaches, tailored to isotopic systems such as O, Sr, B, or others, are promising future avenues of structural diagenetic research for tracing deformation-related fluid in the brittle crust.

Several clay mineral geothermometers are used throughout this dissertation. Chapter III utilizes chlorite chemical thermometry, and limits fault-hosted chlorite mineralization to low temperatures, with the attendant corollary that near-surface and subsurface fault properties likely differ significantly. Chapter IV utilizes smectite hydration behavior to test coseismic heating estimates with mineralogical observations, rejecting the high frictional temperatures inferred by some workers. Chapters V and VI utilize the thermodynamic stability of illite polytypes as constraints on equilibrium temperatures for use in isotopic composition conversions between mineral and fluid.

Chapter VI also integrates the application of X-ray texture goniometry to affirm the diagenetic texture of illite material. The timing of diagenesis is constrained and these observations are used to postulate about post-Alleghenian cratonic deformation.

VII.II. Contributions to the understanding the nature of upper-crustal brittle deformation

Several recurring ideas in this dissertation that contribute to the understanding of the nature of brittle deformation include:

- Large-scale crustal discontinuities exert major control over the hydrologic architecture of the upper (brittle) crust. Deformation zones focus vertical fluid flow with geologic permeabilities that are orders of magnitude greater than surrounding host rock. The H isotopic composition of fault-hosted authigenic illite in the Alpine Fault (chapter III), the

San Andreas Fault (appendix III), and the North Anatolian Fault (chapter V) all show significant involvement of surface fluid reservoirs. A large component of down-dip fluid flow must occur in crustal-scale fault systems.

- The coupling of Ar and H isotopic analysis of illite is a powerful tool to elucidate both deformation timing and deformation fluid characteristics (chapters III, V, and VI).
- Coseismic frictional heating temperatures may be overestimated by modeling, and need to be grounded in mineralogical observations (chapter IV).
- Pre-existing, deep seated weaknesses in continental crust are reactivated during orogenesis and facilitate fluid flow. Transcurrent faulting in Northern Anatolia utilized pre-existing zones of weak clay-rich material, formed by previous deformation events and terrane accretion, as motion on the North Anatolian Fault system initialized (chapter IV). Post-Alleghenian diagenesis in the Appalachian orogen (chapter VI) occurred during the period of far-field stress reorientation and a shift to exhumation of the Appalachian Plateau. The reactivation of existing discontinuities during this transition was inferred to create pathways for surface-derived fluids that infiltrated to upper mid-crustal depths and formed low-temperature illite. These observations are supported by exhumation studies that estimate the removal of 3-6 km in the Appalachian Plateau and Valley and Ridge province.
- In opposition to widely-cited claims of far-travelled fluid migrations in response to tectonism, illite polytype analysis favors a model whereby tectonically-activated mineralizing fluids promote K metasomatism in the North American midcontinent, which are locally derived (chapter VI).

Applied clay science in structural geology is an exciting and continually evolving field that provides new insights and contributes to the understanding of fundamental geologic processes in Earth’s upper (brittle) crust.

Appendix I: Timing of Crustal Accretion and Eastern Black Sea Rotation from Fault Dating of Thrusts within the Istanbul Zone, Western Turkey

APPI.I. Abstract

The paleogeographic affinity and deformation history of the Istanbul Zone in western Turkey are both contested. Competing models variously propose Gondwanan or Eurasian origins of the block and Paleozoic, Mesozoic, and even neotectonic deformation settings. Age analysis of illite-rich fault gouge from brittle structures within the Istanbul Zone provides geochronologic constraints on permissible scenarios of the area's tectonic history. Recent advances in the use of the illite polytype analysis method were utilized to quantify the proportion of illite polytypes using BGMN® for each of 4 size fractions of 10 samples, in support of future ^{40}Ar/^{39}Ar geochronology. Age analysis awaits the outcome of a funding proposal that was submitted to the Istanbul Technical University's Department of Geological Engineering.

APPI.II. Keywords

Istanbul Zone, illite dating, ^{40}Ar/^{39}Ar geochronology

APPI.III. Introduction

The Istanbul Zone (Şengör and Yilmaz, 1981), also known as the 'Paleozoic of Istanbul' or the Istanbul Nappe, is a distinct tectonic block in northwest Anatolia that features a conformable succession of marine and marginal marine sediments that record the development of a south-facing Atlantic-type continental margin (Gorur et al., 1997). The units unconformably overlie Precambrian metamorphic basement, which, in turn, is unconformably overlain by continental red-beds of the lower Triassic age (Okay, 1989). Ordovician units comprise 1000 m of arkosic sandstone and coarse conglomerate, overlain by several hundred meters of fossiliferous Silurian limestones and Devonian shale. A thick Carboniferous turbidite sequence (called the Thracian flysch) tops the conformable succession (Gorur et al., 1997).

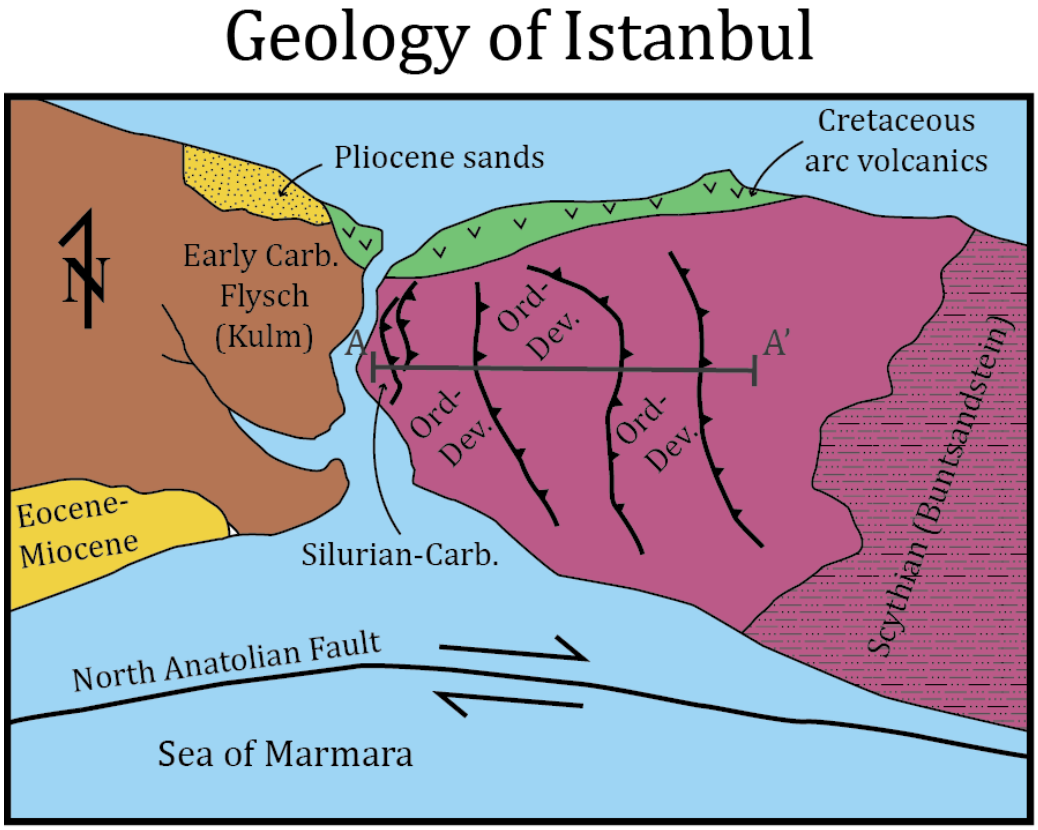

Figure APPI.I. Generalized geologic map in the vicinity of Istanbul, western Turkey. A-A' line is gouge sampling transect across thrust fault zones.

The Istanbul Zone is unique in composition, metamorphic history, and deformation style among the geologic provinces in northwestern Anatolia, and compositionally closely resembles Variscan belt Paleozoic sequences of the Moesian platform and the European coal basins (Gorur et al., 1997). Its provenance has been contested, with competing models proposing a Eurasian or Gondwanan origin (Ustaömer and Robertson, 1993). Its northern affinities—as well as geochronologic evidence from Neoproterozoic basement (Chen et al., 2002) and a unique diagenetic history (Bozkaya et al., 2012)—imply an exotic origin of the continental block. Okay et al. (1994) proposed a tectonic model with the Istanbul Zone originating along the Odessa shelf, between the Moesian platform and Crimea. In this model, the terrane is rifted from Eurasia during Albian-Aptian time and transported by two large transform fault systems—due to back-arc spreading and the opening of the western Black Sea—before accreting to Anatolia adjacent to the Sakarya Zone. The rotation of the eastern Black Sea continued to cause further thrusting and deformation through Miocene time. Due to the lack of geochronologic data in the Istanbul Zone,

Table APPI.I Fault gouge sample GPS locations

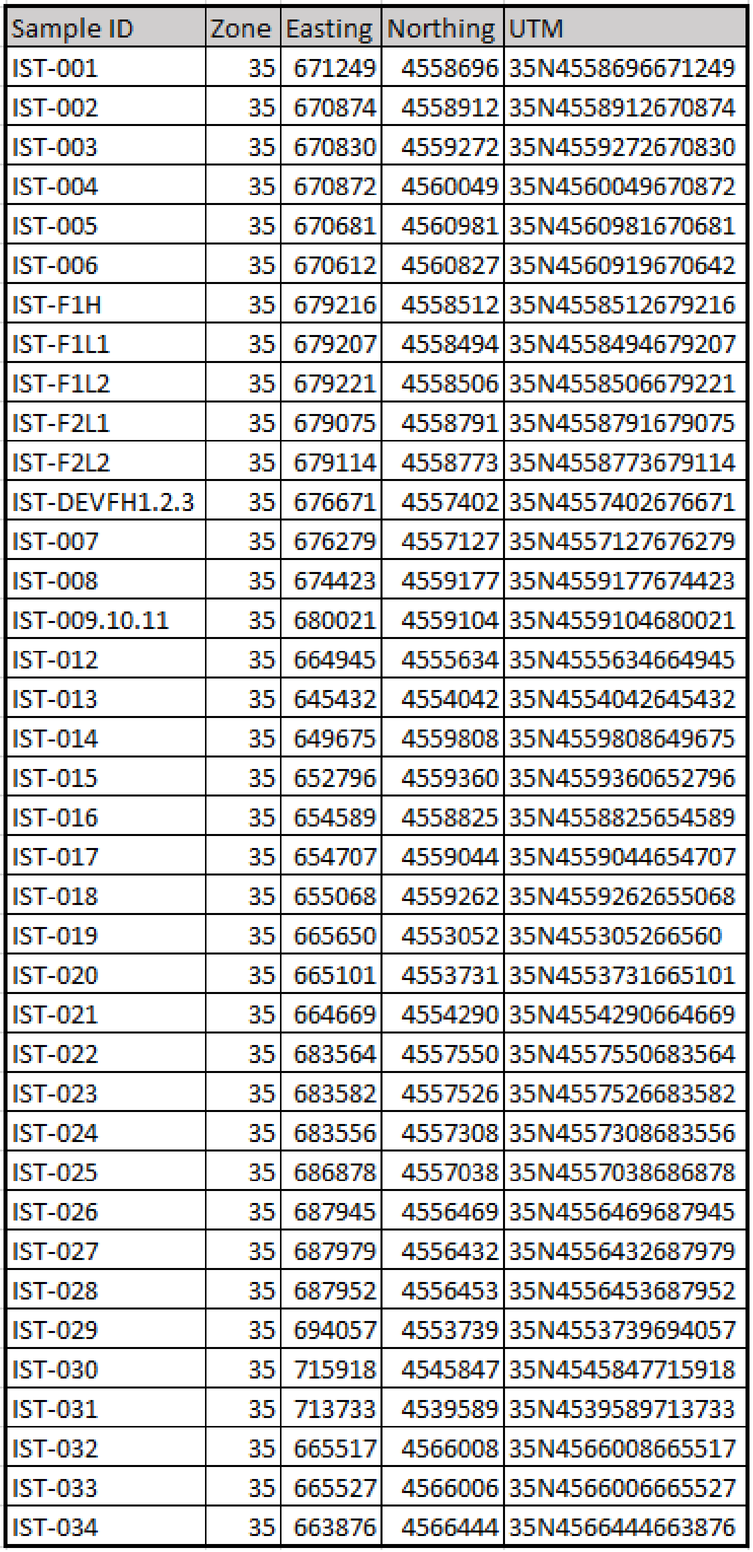

Sample ID	Zone	Easting	Northing	UTM
IST-001	35	671249	4558696	35N4558696671249
IST-002	35	670874	4558912	35N4558912670874
IST-003	35	670830	4559272	35N4559272670830
IST-004	35	670872	4560049	35N4560049670872
IST-005	35	670681	4560981	35N4560981670681
IST-006	35	670612	4560827	35N4560919670642
IST-F1H	35	679216	4558512	35N4558512679216
IST-F1L1	35	679207	4558494	35N4558494679207
IST-F1L2	35	679221	4558506	35N4558506679221
IST-F2L1	35	679075	4558791	35N4558791679075
IST-F2L2	35	679114	4558773	35N4558773679114
IST-DEVFH1.2.3	35	676671	4557402	35N4557402676671
IST-007	35	676279	4557127	35N4557127676279
IST-008	35	674423	4559177	35N4559177674423
IST-009.10.11	35	680021	4559104	35N4559104680021
IST-012	35	664945	4555634	35N4555634664945
IST-013	35	645432	4554042	35N4554042645432
IST-014	35	649675	4559808	35N4559808649675
IST-015	35	652796	4559360	35N4559360652796
IST-016	35	654589	4558825	35N4558825654589
IST-017	35	654707	4559044	35N4559044654707
IST-018	35	655068	4559262	35N4559262655068
IST-019	35	665650	4553052	35N455305266560
IST-020	35	665101	4553731	35N4553731665101
IST-021	35	664669	4554290	35N4554290664669
IST-022	35	683564	4557550	35N4557550683564
IST-023	35	683582	4557526	35N4557526683582
IST-024	35	683556	4557308	35N4557308683556
IST-025	35	686878	4557038	35N4557038686878
IST-026	35	687945	4556469	35N4556469687945
IST-027	35	687979	4556432	35N4556432687979
IST-028	35	687952	4556453	35N4556453687952
IST-029	35	694057	4553739	35N4553739694057
IST-030	35	715918	4545847	35N4545847715918
IST-031	35	713733	4539589	35N4539589713733
IST-032	35	665517	4566008	35N4566008665517
IST-033	35	665527	4566006	35N4566006665527
IST-034	35	663876	4566444	35N4566444663876

it is difficult to constrain paleogeographic reconstructions because of the uncertain nature of crustal accretion within the Tethyan belt near Anatolia.

The dominant structural feature of the Istanbul Zone is a series of north-south striking thrust faults that duplex the Paleozoic strata (figure APPI.I). The timing of this deformation is contested. Some authors have proposed a late Paleozoic (Variscan?) deformation event, related to the closure of the Intra-Pontide ocean (Şengör et al., 1984; Okay et al., 1994). Such an event would have entailed a north-south zone of compression, creating east-west striking structural features and would, therefore, require crustal block rotation since that time to attain the current fault geometry. Attempts to identify this rotation with paleomagnetism were unsuccessful due to widespread remagnetization within the block (Nalan Lom, Istanbul Technical University, personal communication). A Mesozoic age of deformation may also be possible, related to the accretion of the Istanbul Zone to Anatolia, with Cretaceous volcanism in the Istanbul zone as evidence for

Figure APPI.II. Field photo of well-developed clay gouge (sample IST-026) along a brittle fault that juxtaposes altered Ordovician rocks over unmetamorphosed Neogene lacustrine sedimentary rocks. The dip and dip direction of this fault are 52°→170°, corresponding to the predicted trend of synthetic Riedel shears of the North Anatolian Fault Zone.

Mesozoic subduction and accretion. Lastly, neotectonic processes related to the North Anatolian shear zone have likely overprinted earlier deformation events or reactivated existing structures.

We plan to confirm the timing of crustal accretion of the Istanbul Zone, the neotectonics of the North Anatolian Fault, and the temporal extent of eastern Black Sea rotation, by dating the imbricate thrust faults within the Istanbul zone through illite polytype analysis and ^{40}Ar/^{39}Ar geochronology. We utilize recent advances in illite polytype analysis by using Rietveld refinement techniques for the quantification of polytype proportions (Boles et al., in submission; Chapter II). Figure APPI.I is a generalized geologic map of the region immediately surrounding the city of Istanbul, Turkey, and the line A-A' indicates the fault sampling transect that was completed during the summer 2016 field season. We posit that the timing of deformation within the Istanbul Zone will constrain crustal accretion processes in NW Turkey and resolve outstanding controversies in the tectonic history of the Mediterranean Cimmerides.

APPI.IV. Methods

APPI.IV.I. Field Campaign

A successful field campaign in August 2016 yielded a promising suite of 43 fault gouge samples from fault structures along the transect in figure APPI.I; sample locations are listed in table APPI.I. Preliminary field observations are that much of the deformation is partitioned into discrete zones that have undergone localized folding and faulting, and that these deformed zones are separated by relatively undeformed Paleozoic strata. Many of the structures have orientations compatible with subsidiary (R') orientations along the North Anatolian Fault, and, if dating confirms young ages, the shear zone at the terminus of this continental-scale transform fault would be much wider than previously recognized (figure APPI.II). Metamorphic grade in the region increases to the west, with greenschist facies mineralization occurring within the Paleozoic strata in the region surrounding Sazlidere Baraji. Also of note is the first-reported discovery of a mixed orthoconic and platycone ammonoidea, ornamented trilobite and brachiopod fossil-rich Devonian shale location (figure APPI.III). Figure APPI.IV overlays sampling sites onto the geologic map of the Istanbul Municipality, and highlights the fault gouge zones selected for age analysis with red triangles.

APPI.IV.II. Sample Preparation

After obtaining approximately 0.5 kg of clay-rich material from the surface trace of Istanbul Zone thrust faults, surface weathering material was removed, and the samples were crushed, soaked in

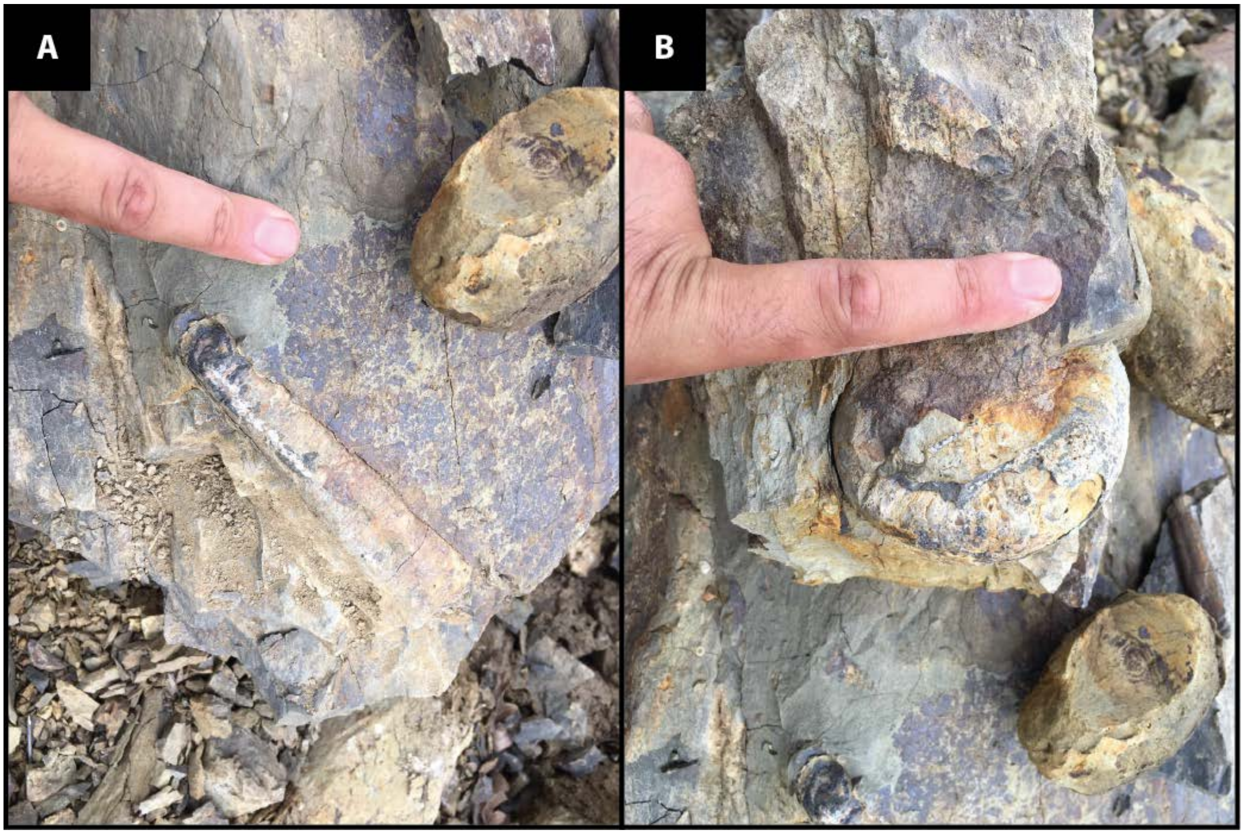

Figure APPI.III. First report of mixed A) orthoconic and B) platyconic ammonoid, ornamented trilobite, and generally fossiliferous Devonian shale location in the Istanbul Zone.

de-ionized water to remove salts, and disaggregated by ultra-sonic bath. Stoke’s Law centrifugation techniques wer used to separate the material into four grain size fractions, each less than 2.0 µm in size (<0.05 µm, 0.05-0.2 µm, 0.2-1.0 µm, and 1.0-2.0 µm). Resultant aliquots represent mixtures of authigenic and detrital material, with each size fraction having a different authigenic/detrital ratio. Age dating of each aliquot, and a multivariate linear regression analysis between age and proportion of authigenic illite will allow for a mixing line to be created that can be used to extrapolate to end-member ages of each illite population. Oriented slides and random powder mounts were prepared for X-ray diffraction using techniques described in Moore and Reynolds (1997) for each grain size of each sample.

APPI.IV.III. X-ray analysis

X-ray work was conducted on a Rigaku Ultima IV diffractometer used in Bragg-Brentano geometry, with CuKα radiation, operated at 40 kV and 44 mA, and located at the Electron Microbeam Analysis Laboratory (EMAL) at the University of Michigan. Preliminary qualitative

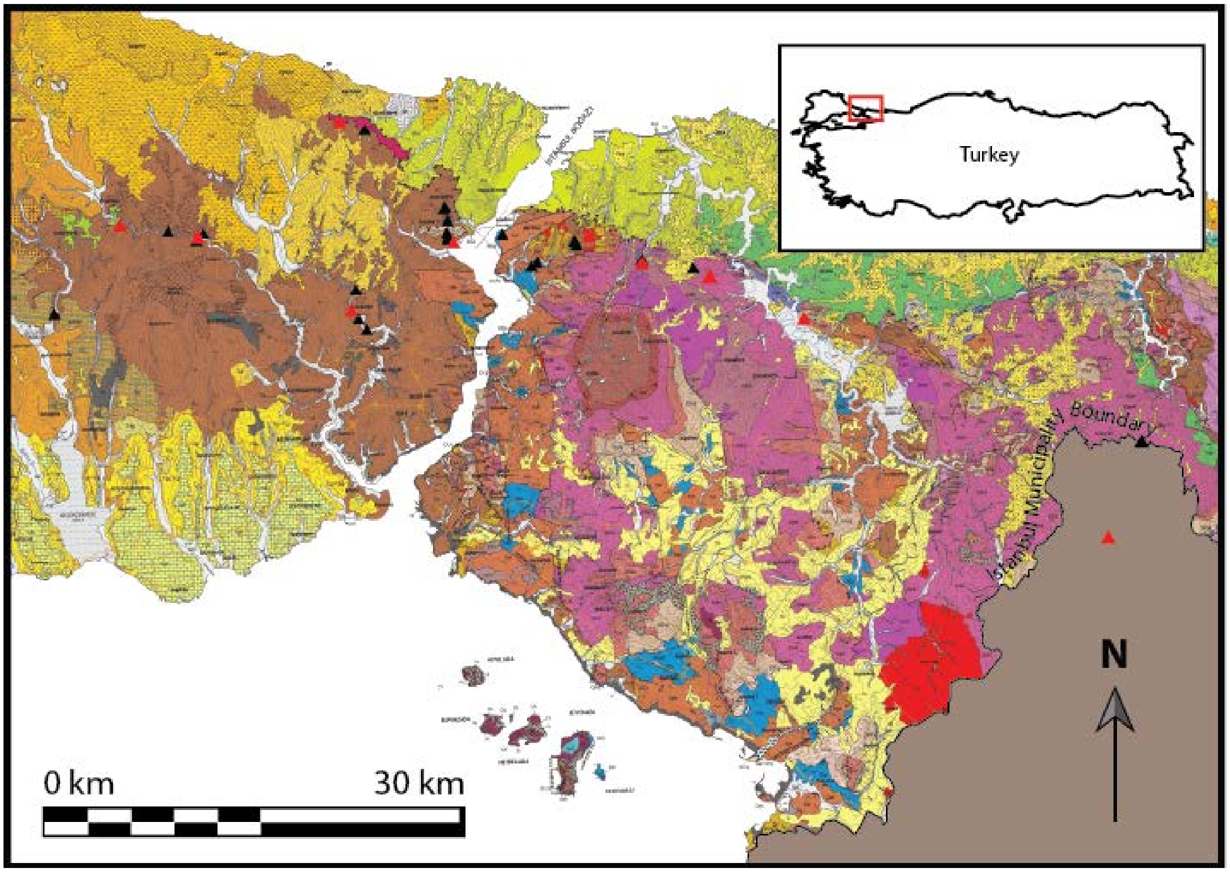

Figure APPI.IV. Geologic map of Istanbul, with sampling locations indicated by triangles. Red triangles denote sampling locations of fault gouges that were selected for detailed characterization and age analysis in this study.

scans on oriented slides were used to enhance the basal reflections of clay minerals, and these were analyzed under both air-dried and ethylene glycolated conditions. From these patterns, the mineralogy and illite crystallinity, a measure of crystallographic ordering, of the samples was determined and 10 samples were selected for grain size separation and future Ar dating. The random powder mounts were analyzed using Rietveld refinement software BGMN© (Bergmann et al., 1998) and these results were used to determine illite polytypism, as reported in table APPI.II (Boles et al., in submission; Chapter II).

APPI.IV.IV. Age Analysis

$^{40}Ar/^{39}Ar$ geochronology will be conducted by the Noble Gas Laboratory at the University of Michigan using the encapsulation method (see van der Pluijm and Hall, 2014 for recent review). Scherrer thicknesses calculated from full-width at half maximum (FWHM) measurements of the illite 001 peak of each sample will be used to differentiate between whole gas and retention ages

(Fitz-Díaz et al., 2016). Age analysis is awaiting the results of a funding proposal submitted to the Department of Geological Engineering at the Istanbul Technical University.

APPI.V. Results

The use of our Rietveld whole-pattern matching technique (using BGMN®) in this study was very successful in quantifying the proportion of authigenic (1Md) and detrital (2M1) illite in each of 4 grain sizes of the 10 samples selected for age analysis (figure APPI.V). Table APPI.II presents the results of this quantitative X-ray powder diffraction investigation, as well as the calculated proportion of 1Md, relative to all illite. Samples IST-021-VF and IST-034-VF were unsuitable for quantitative analysis due to the absence of identifiable 1Md illite among the noise of fine-grain

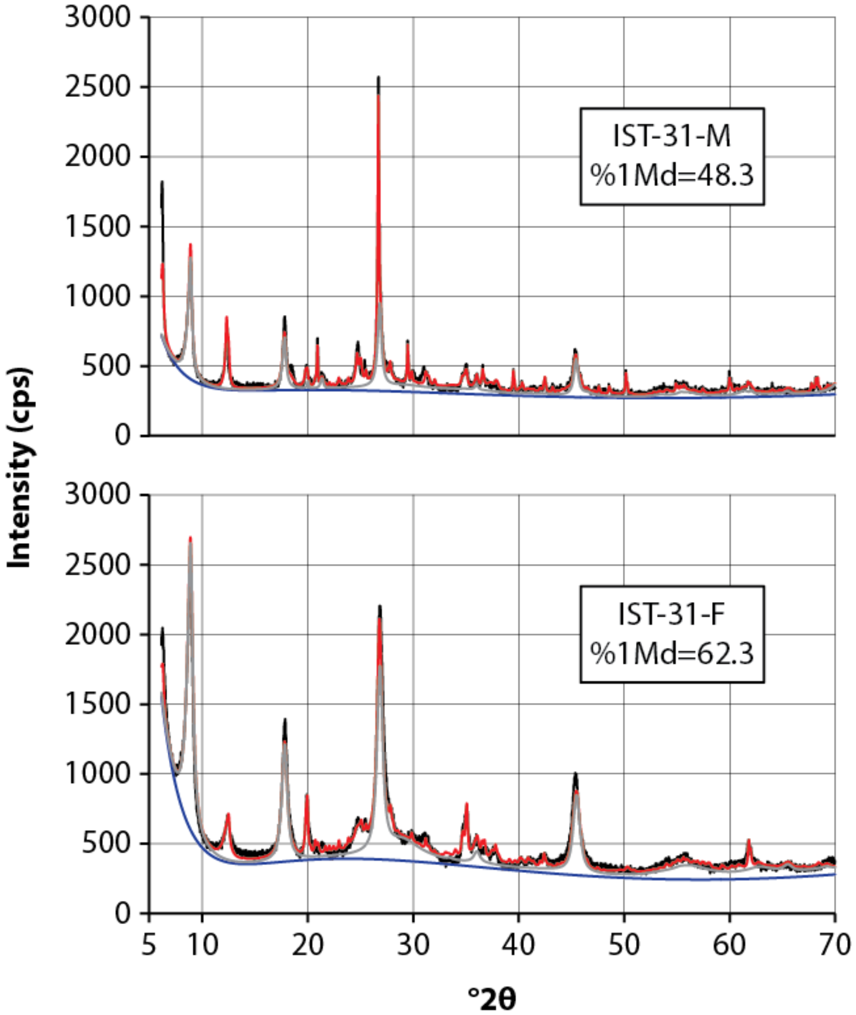

Figure APPI.V. X-ray diffraction patterns of two size fractions of sample IST-031, showing increasing proportions of 1Md illite in smaller grain sizes. The black line is measurement data, the red line is BGMN modeled fit, the grey line is 1Md illite contribution to the BGMN model, and blue line is the modeled background.

size peak broadening and contamination from salts. The absence of any accessory K-bearing phases gives additional confidence that these clay-rich fault gouges are suitable for dating.

APPI.VI. Conclusion

Constraints on the timing of deformation within the Istanbul Zone can illuminate the tectonic accretion history of NW Turkey and resolve questions about the timing of neotectonic activity and eastern Black Sea rotation. The illite polytype analysis method uniquely lends itself to this problem because of the nature of the brittle faults and the presence of clay-rich gouge zones. Our quantitative analysis of four size fractions of 10 fault gouge samples from a transect across the Istanbul Zone has yielded promising results. We await the decision on a funding proposal that will allow for the dating of these characterized samples to commence.

APPI.VII. Acknowledgments

This work was completed in collaboration with Semih Can Ülgen and Celal Şengör from the Istanbul Technical University's Department of Geological Engineering. We thank the Horace H. Rackham School for Graduate Studies for a research grant that funded the field component of this work.

Table APPI.II. Q-XRPD Results. c=calcite; h=halite; gt=goethite; gp=gypsum; gb=gibbsite; hm=hematite; rt=rutile; m=monazite

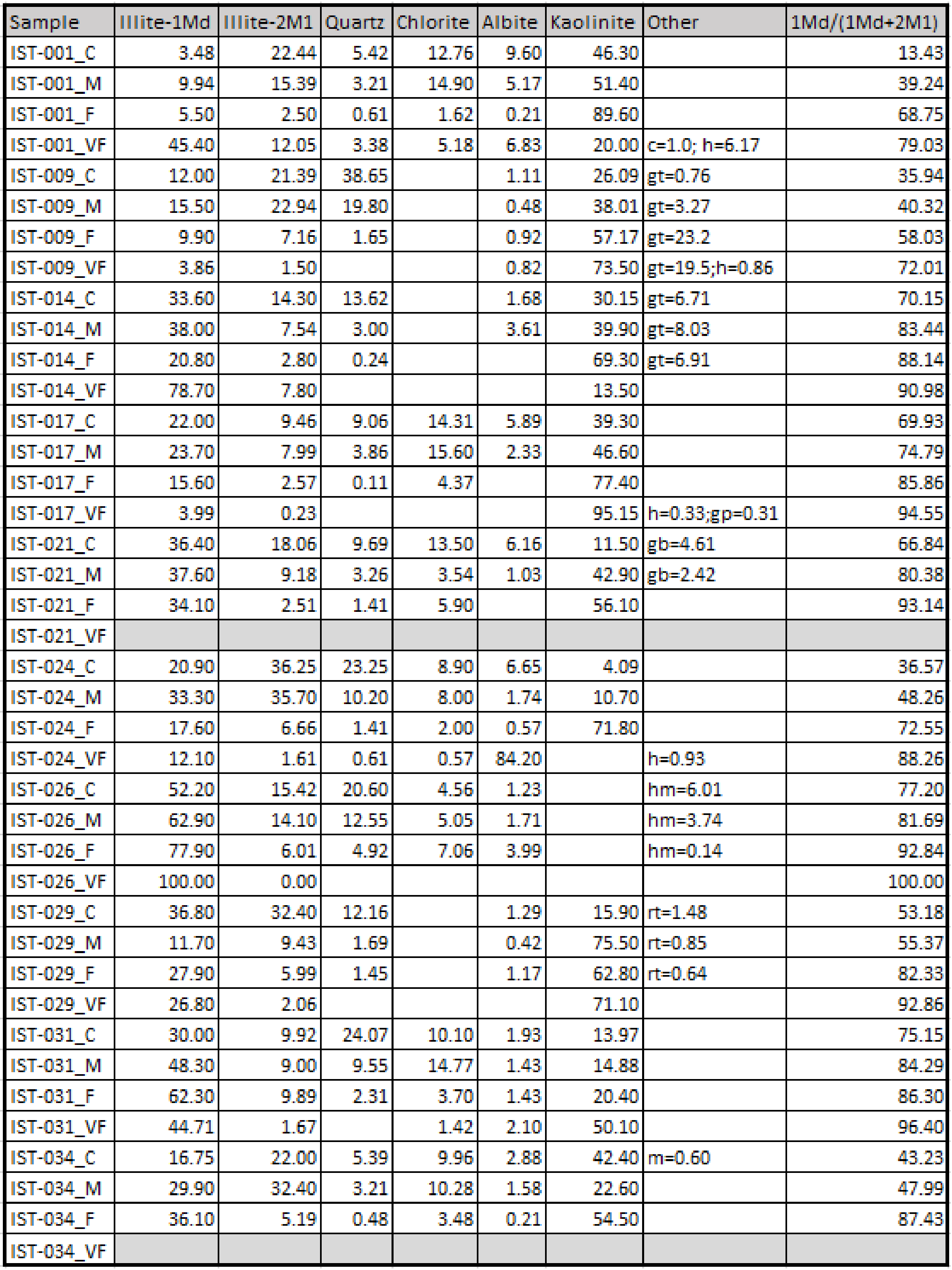

Sample	Illite-1Md	Illite-2M1	Quartz	Chlorite	Albite	Kaolinite	Other	1Md/(1Md+2M1)
IST-001_C	3.48	22.44	5.42	12.76	9.60	46.30		13.43
IST-001_M	9.94	15.39	3.21	14.90	5.17	51.40		39.24
IST-001_F	5.50	2.50	0.61	1.62	0.21	89.60		68.75
IST-001_VF	45.40	12.05	3.38	5.18	6.83	20.00	c=1.0; h=6.17	79.03
IST-009_C	12.00	21.39	38.65		1.11	26.09	gt=0.76	35.94
IST-009_M	15.50	22.94	19.80		0.48	38.01	gt=3.27	40.32
IST-009_F	9.90	7.16	1.65		0.92	57.17	gt=23.2	58.03
IST-009_VF	3.86	1.50			0.82	73.50	gt=19.5;h=0.86	72.01
IST-014_C	33.60	14.30	13.62		1.68	30.15	gt=6.71	70.15
IST-014_M	38.00	7.54	3.00		3.61	39.90	gt=8.03	83.44
IST-014_F	20.80	2.80	0.24			69.30	gt=6.91	88.14
IST-014_VF	78.70	7.80				13.50		90.98
IST-017_C	22.00	9.46	9.06	14.31	5.89	39.30		69.93
IST-017_M	23.70	7.99	3.86	15.60	2.33	46.60		74.79
IST-017_F	15.60	2.57	0.11	4.37		77.40		85.86
IST-017_VF	3.99	0.23				95.15	h=0.33;gp=0.31	94.55
IST-021_C	36.40	18.06	9.69	13.50	6.16	11.50	gb=4.61	66.84
IST-021_M	37.60	9.18	3.26	3.54	1.03	42.90	gb=2.42	80.38
IST-021_F	34.10	2.51	1.41	5.90		56.10		93.14
IST-021_VF								
IST-024_C	20.90	36.25	23.25	8.90	6.65	4.09		36.57
IST-024_M	33.30	35.70	10.20	8.00	1.74	10.70		48.26
IST-024_F	17.60	6.66	1.41	2.00	0.57	71.80		72.55
IST-024_VF	12.10	1.61	0.61	0.57	84.20		h=0.93	88.26
IST-026_C	52.20	15.42	20.60	4.56	1.23		hm=6.01	77.20
IST-026_M	62.90	14.10	12.55	5.05	1.71		hm=3.74	81.69
IST-026_F	77.90	6.01	4.92	7.06	3.99		hm=0.14	92.84
IST-026_VF	100.00	0.00						100.00
IST-029_C	36.80	32.40	12.16		1.29	15.90	rt=1.48	53.18
IST-029_M	11.70	9.43	1.69		0.42	75.50	rt=0.85	55.37
IST-029_F	27.90	5.99	1.45		1.17	62.80	rt=0.64	82.33
IST-029_VF	26.80	2.06				71.10		92.86
IST-031_C	30.00	9.92	24.07	10.10	1.93	13.97		75.15
IST-031_M	48.30	9.00	9.55	14.77	1.43	14.88		84.29
IST-031_F	62.30	9.89	2.31	3.70	1.43	20.40		86.30
IST-031_VF	44.71	1.67		1.42	2.10	50.10		96.40
IST-034_C	16.75	22.00	5.39	9.96	2.88	42.40	m=0.60	43.23
IST-034_M	29.90	32.40	3.21	10.28	1.58	22.60		47.99
IST-034_F	36.10	5.19	0.48	3.48	0.21	54.50		87.43
IST-034_VF								

Appendix II. Pseudotachylyte and Fault Gouge Dating of Mai’iu and Gwoira Faults Constrains the Late-Stage Exhumation Timing of the Dayman Gneiss Dome, Eastern Papua New Guinea

APPII.I. Abstract

Newly-discovered pseudotachylyte and clay-rich fault gouge in exhumed brittle structures of the Dayman Gneiss Dome, eastern Papua New Guinea, present unique opportunity to date mid-crustal and shallow crustal deformation processes at the tectonically active Australian-Pacific plate margin. Five pseudotachylyte samples were dated using $^{40}Ar/^{39}Ar$ geochronology, which identify an age span of coseismic deformation between ~2.2 Ma and ~3.0 Ma. Calculations that incorporate modern slip rate and fault dip result in estimated seismicity at depths of 8-10 km for their formation. Although initial X-ray characterization of clay-rich fault gouges of the Dayman Dome indicated the presence of illitic material, the application of the illite polytype analysis and quantitative X-ray powder diffraction using BGMN® show that illite is a minor constituent of these rocks. Due to the young expected ages of these fault gouges, their low initial K concentration, and high chlorite and feldspar content (which can cause recoil effects due to Cl and Ca), we do not believe Ar dating would yield interpretable results.

APPII.II. Introduction

The Dayman Dome is a domed landform of Late Cretaceous-Eocene age with a maximum elevation of 2850 m and aerial extent ~750 km^2 (Daczko et al., 2009), located in eastern Papua New Guinea (figure APPII.I). It is one of a series of gneiss domes along the obliquely convergent Australian-Pacific plate boundary zone first described by Ollier and Pain (1980). It preserves the youngest documented eclogite exposed at the Earth’s surface, with eclogite facies metamorphism dated by zircon U/Pb ion microprobe data as 4.3 Ma (Baldwin et al., 2004). The gneissic body’s exhumation from depths of ~75 km was rapid, and has been modeled as an adiabatic rise of a diapiric Rayleigh-Taylor instability (Little et al., 2011). Its final exhumation was by recent normal

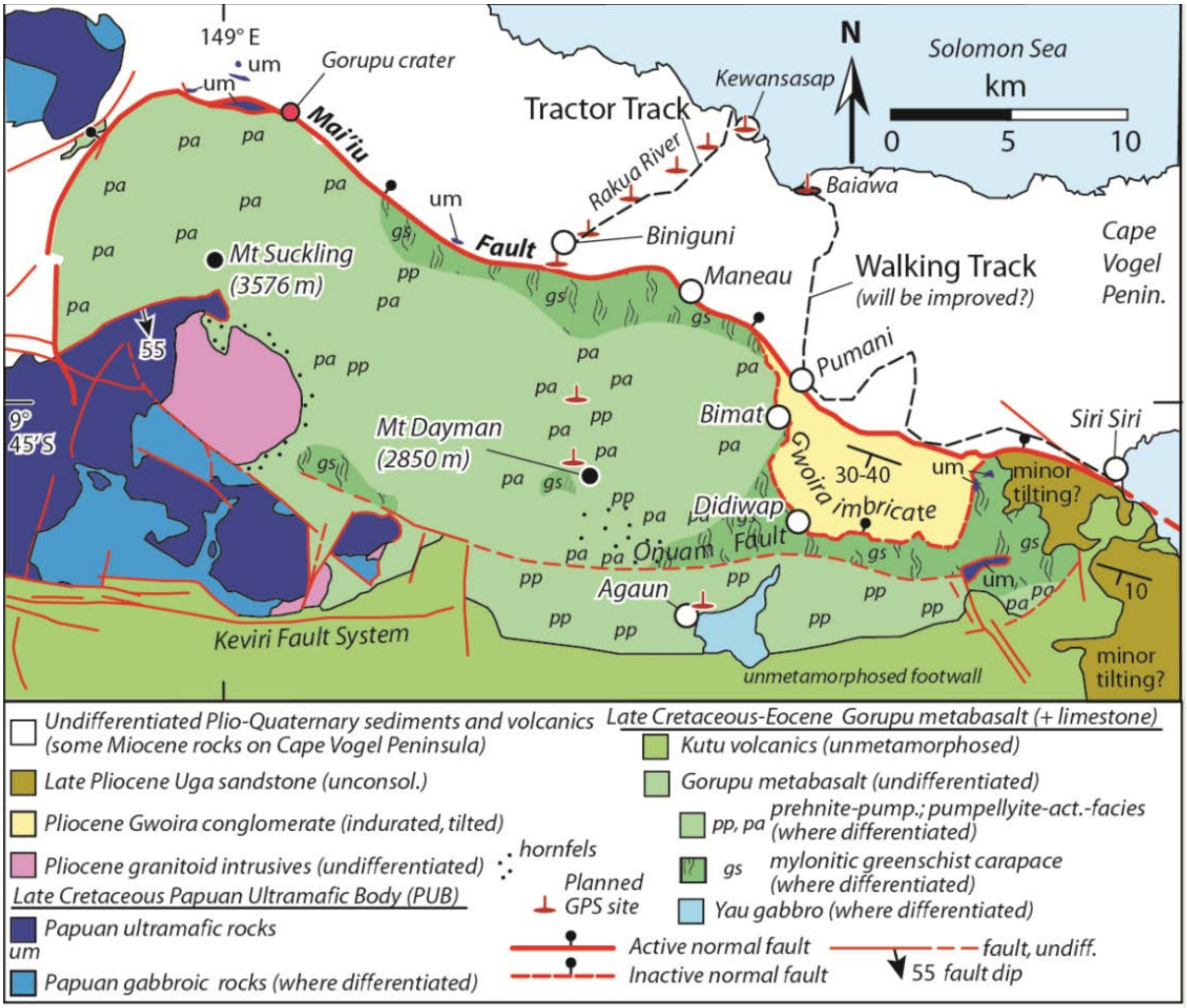

Figure APPII.I. Generalized geologic map of the Dayman dome area, Papua New Guinea (from Daczko et al., 2009)

faulting and minor erosion, dominated by a corrugated low-angle normal fault, the Mai'iu Fault, and its imbricate, the Gwoira Fault.

The <5 Ma upper-crustal exhumation timing of the Dayman Dome is not well constrained, but several observations of pseudotachylyte veins and clay-rich fault gouge along the main Dayman Dome bounding Mai'iu Fault and the inactive Gwoira Fault present a unique opportunity to directly date normal fault activity at shallow crustal levels. At the Gwoira Fault pseudotachylyte site, the footwall consists of finely laminated greenschist-facies basalt and pelagic-limestone-derived mylonite. The hanging wall consists of Pliocene-age gravels. A well-developed, foliated gouge hosts the sharp-margined pseudotachylyte, complete with obvious injection features (figure

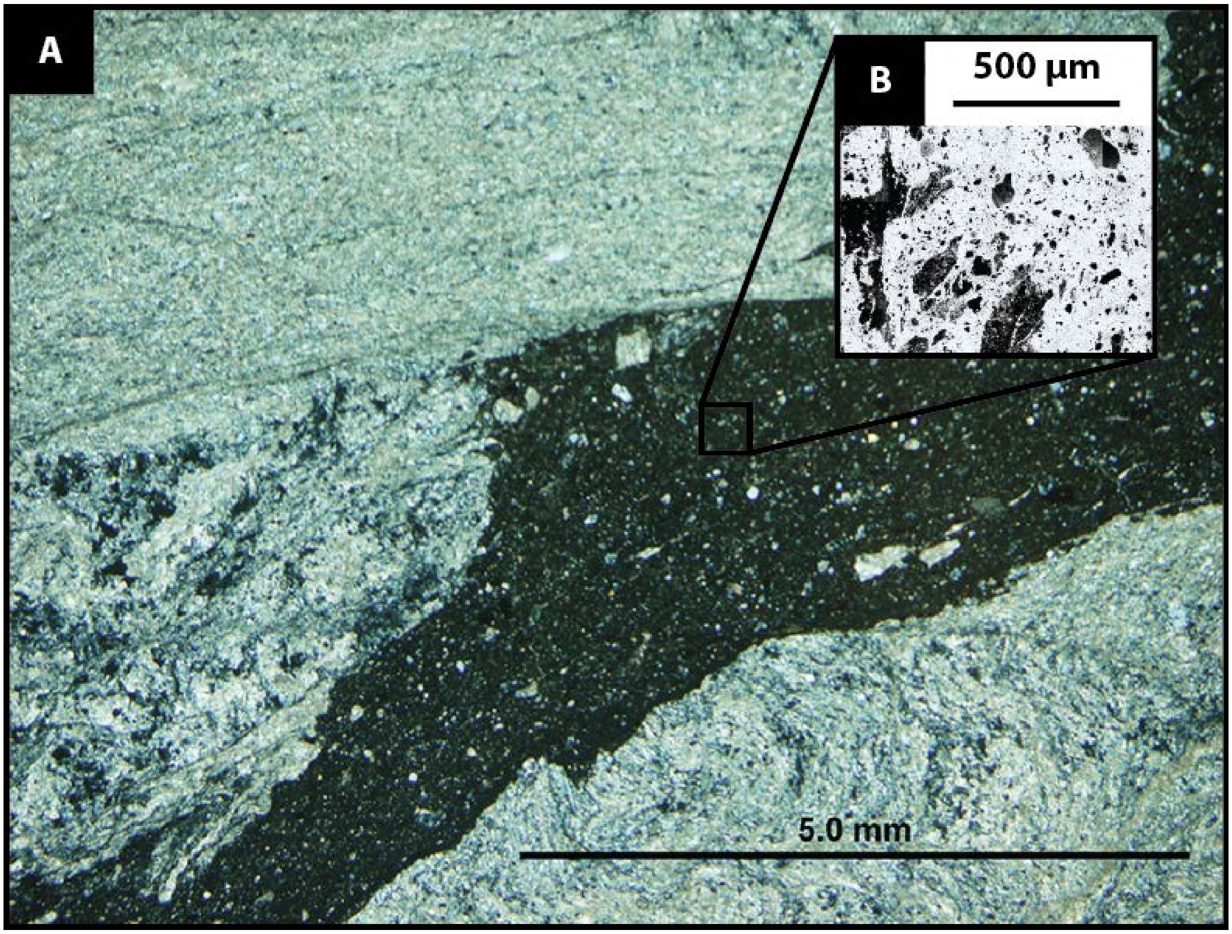

Figure APPII.II. A) Representative photomicrograph of PNG14-19C pseudotachylyte (cross-polarized light). Dark band is friction melt. B) High-contrast SEM image of PNG14-19C pseudotachylyte sample. Dark bodies represent host rock inclusions. Pixel analysis yielded >84% melt estimates for all tested samples.

APPII.IIA). We use advances in dating friction melts and in illite polytype analysis to constrain the late-stage exhumation history of this tectonically active plate margin.

APPII.III. Pseudotachylyte Dating

Five pseudotachylyte vein samples were selected for dating by $^{40}Ar/^{39}Ar$ geochronology; PNG14-19C, PNG16-151-E, PNG16-17.2-F1, PNG16-152-A, and PNG16-17x. PNG14-19C was characterized by high-contrast SEM pixel analysis to determine melt purity, and quantitative X-ray powder diffraction using BGMN® (Bergmann et al., 1998) to understand glass devitrification and bulk mineralogy. Sample PNG16-17x was investigated by SEM/EDS spectroscopy to determine elemental distribution within the friction melt and host rock. Five instances of sample PNG14-19C were dated (both with and without H_2O_2 treatment) to understand the influence of Cl-

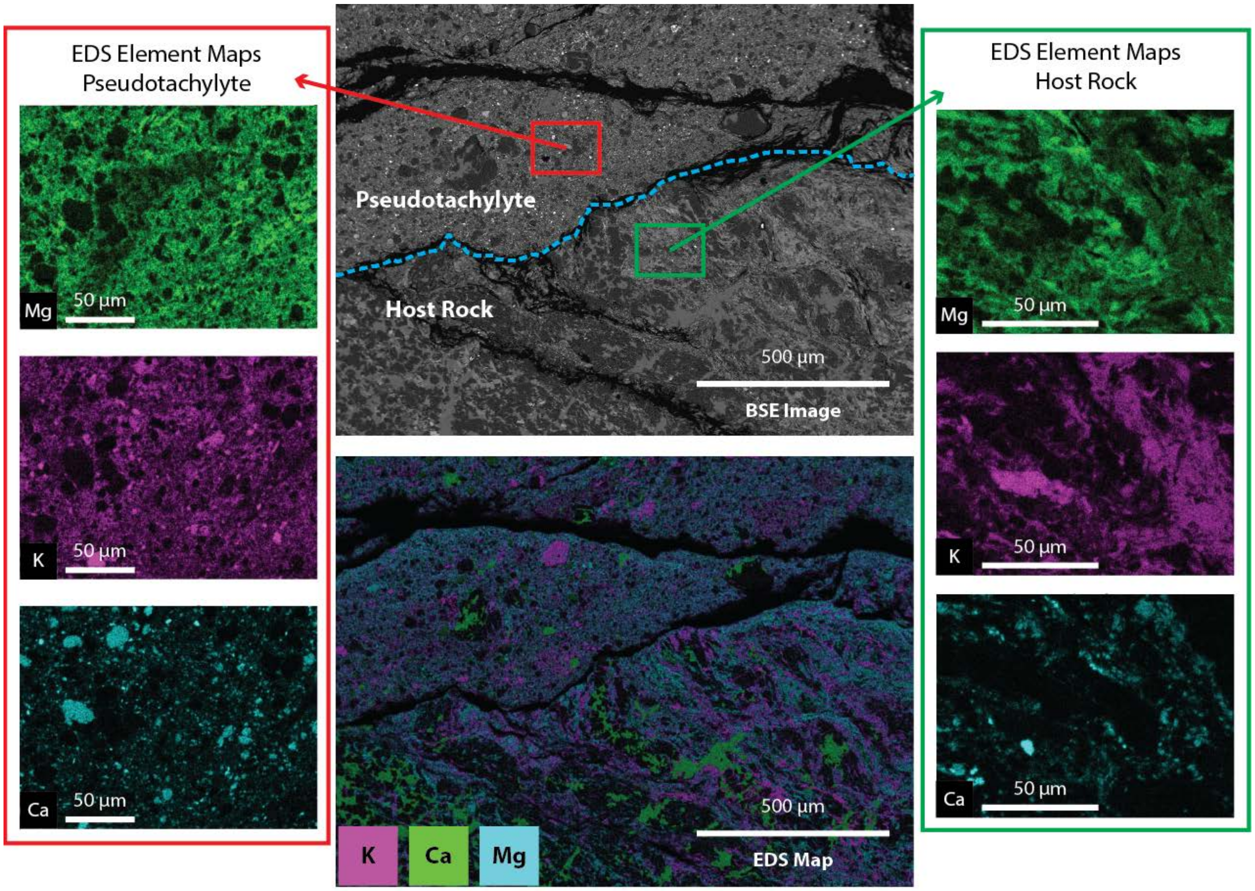

Figure APPII.III. Back-scatter electron images and Energy Dispersive Spectroscopy elemental maps of melt and host rock within sample PNG16-17x.

and Ca-bearing phases on the irradiation process and subsequent degassing spectra of these low K melts. Two instances of samples PNG16-151-E, PNG16-17.2-F1, PNG16-152-A, and PNG16-17x were each subsequently dated.

APPII.III.I. SEM Characterization

APPII.III.I.I. Energy Dispersive Spectroscopy (EDS) Elemental Mapping

Pseudotachylyte and host rock elemental distribution of sample PNG16-17x was investigated with a JEOL JSM-7800F field emission scanning electron microscope equipped with an energy dispersive spectroscopic (EDS) detector, located at the Electron Microbeam Analysis Laboratory at the University of Michigan (figure APPII.III). The host rock exhibits compositional banding and a larger grain size expected of a mylonite with a mafic protolith, and qualitative EDS analysis indicates average K concentrations ~2.8 wt. %. The friction melt is much finer grained, more homogeneous, and with a marginally higher qualitative EDS average K concentration of ~2.9 wt. %. Such an elemental distribution indicates that, depending upon the composition of host rock inclusions in a dated subsample of pseudotachylyte, Ca/K and Cl/K ratios could vary significantly due to low K concentration or recoil artifacts.

APPII.III.I.II. Quantitative Image Pixel Analysis

The process of coseismic injection of fluidized friction melt inherently entrains various amounts of unmelted and partially melted host material into a glassy matrix of pseudotachylyte. The use of scanning electron microscopy (SEM) and quantitative image pixel analysis techniques can characterize the ratio of host rock to melt for a given melt subsample (Warr et al., 2007; O'Brien and van der Pluijm, 2012). Two orthogonal faces of a ~1 mm melt cube of four subsamples of PNG14-19C were mapped using a Hitachi S-3200N scanning electron microscope at the Electron Microbeam Analysis Laboratory at the University of Michigan. The surface roughness contrasts between melt and host are quite significant, and these differences were accentuated by adding contrast during post-processing of the SEM images. Pixel counts of dark (host rock inclusions) to light material (friction melt) are used as ratios to quantify relative host and melt compositions (figure APPII.IIB). The ratios from the two orthogonal faces were averaged to give an estimate of bulk composition. The samples investigated all have high melt/host rock ratios, with melt representing >84% of the sample in all cases. Ratios are reported in table APPII.I.

Table APPII.I. Pseudotachylyte preparation and SEM pixel analysis results.

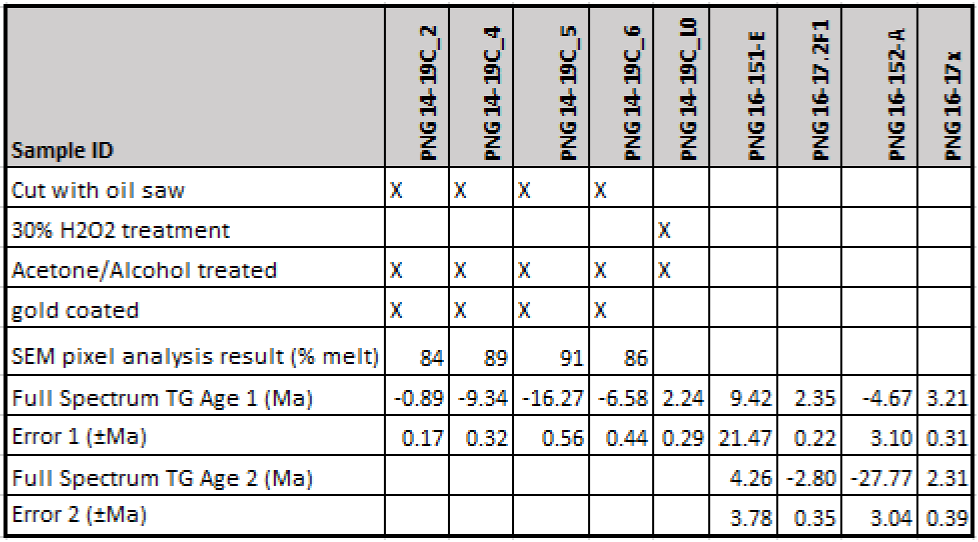

Sample ID	PNG 14-19C_2	PNG 14-19C_4	PNG 14-19C_5	PNG 14-19C_6	PNG 14-19C_10	PNG 16-151-E	PNG 16-17.2F1	PNG 16-152-A	PNG 16-17x
Cut with oil saw	X	X	X	X					
30% H2O2 treatment					X				
Acetone/Alcohol treated	X	X	X	X	X				
gold coated	X	X	X	X					
SEM pixel analysis result (% melt)	84	89	91	86					
Full Spectrum TG Age 1 (Ma)	-0.89	-9.34	-16.27	-6.58	2.24	9.42	2.35	-4.67	3.21
Error 1 (±Ma)	0.17	0.32	0.56	0.44	0.29	21.47	0.22	3.10	0.31
Full Spectrum TG Age 2 (Ma)						4.26	-2.80	-27.77	2.31
Error 2 (±Ma)						3.78	0.35	3.04	0.39

APPII.III.II. X-ray Analysis

Quantitative X-ray powder diffraction of hand-crushed samples of host rock and melt of sample PNG14-19C was conducted using the whole pattern matching Rietveld program BGMN® (figure

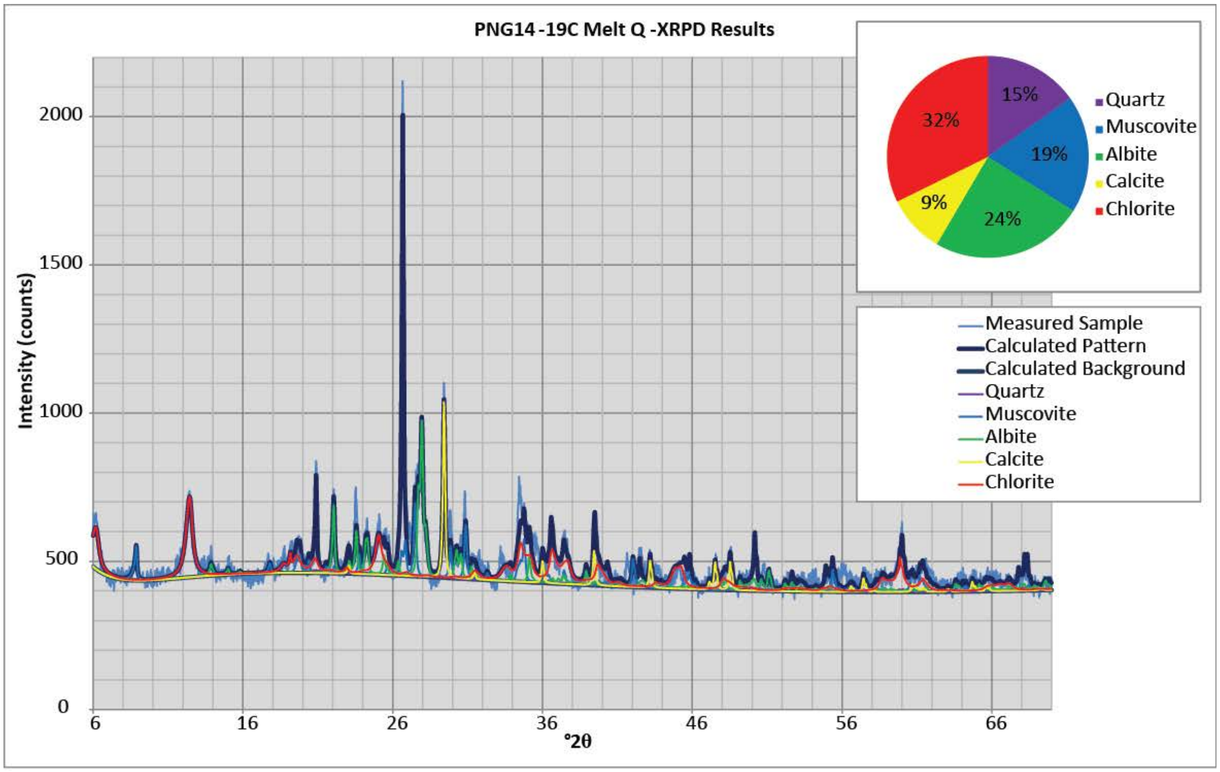

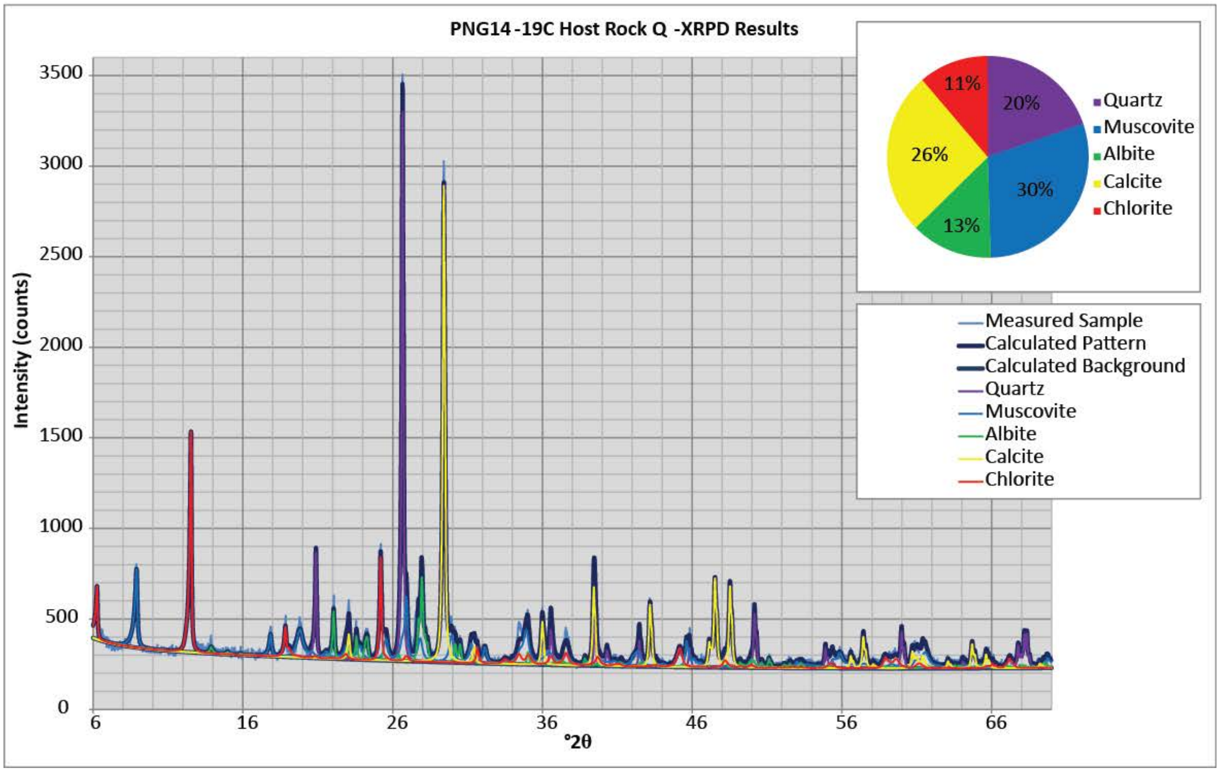

Figure APPII.IV. Quantitative X-ray powder diffraction results of host rock and melt samples from PNG14-19C. The background hump in the melt fraction characterizes a significant proportion of glassy material that is not devitrified, and identifies higher chlorite and albite proportions relative to the host rock.

APPII.IV). A background hump in the melt sample indicates that the pseudotachylyte is not completely devitrified, and amorphous (i.e. glassy) material remains a fairly significant proportion of the rock. In comparison with the host rock, the melt has a much higher proportion of both chlorite and albite as crystalline constituents. This is significant, as both Ca (in the feldspars) and Cl (adsorbed to clay surfaces) can create Ar isotopic products or cause unpredictable recoil effects during sample irradiation, as part of the dating procedure (Faure and Mensing, 2005). The increased proportion of these mineral constituents is likely due to the devitrification process. In this study, we mitigate these effects using the reduced integrated age method, whereby heating steps are correlated to likely degassing constituent phases using Ca/K and Cl/K ratios (Turner et al., 1978; Frey et al., 2007).

APPII.III.III. $^{40}Ar/^{39}Ar$ geochronology

Ar dating was conducted at the University of Michigan's Noble Gas Laboratory. The presence of a Cl-rich phase or phases that contributed to early (low-T) degassing, and a Ca-rich phase or phases that contributed to late (high-T) degassing likely do not represent pseudotachylyte melt, but the devitrification products chlorite and albite, or other host rock minerals (figure APPII.VA-B). The extremely high Ca/K (>4) and Cl/K (>0.005) ratios of several samples indicate a low K content of some pseudotachylyte subsamples, and therefore their unsuitability for dating. Workers investigating pseudotachylyte of the footwall of the Alpine Fault, New Zealand, attributed such variability in composition among genetically-related friction melts to host rock bulk chemistry variation, multiple pulses of melt generation during a single coseismic event, and fractional crystallization processes during cooling (Warr et al., 2003; Warr and van der Pluijm, 2005; Bossiere, 1991). The likely driver of the high variability in degassing spectra exhibited by our samples, therefore, is interpreted as variation in host rock composition, inclusion volume, and fractionation-driven melt composition.

We utilize the Ca/K and Cl/K ratios as discriminators between those heating steps that represent devitrification products and host rock minerals, and those heating steps that represent melt in a reduced integrated age approach (Turner et al., 1978; Frey et al., 2007). This type of integration allows for internal recoil distribution, instead of the use of a plateau age. The alternative approach, full spectrum integration that yields traditional retention ages, returns apparent negative ages when non-melt heating steps are included, which reflects very low $^{40}Ar/^{36}Ar$ ratios (below present-day value of 295.5), as indicated by the isochron plot in figure APPII.VC. The discrimination values

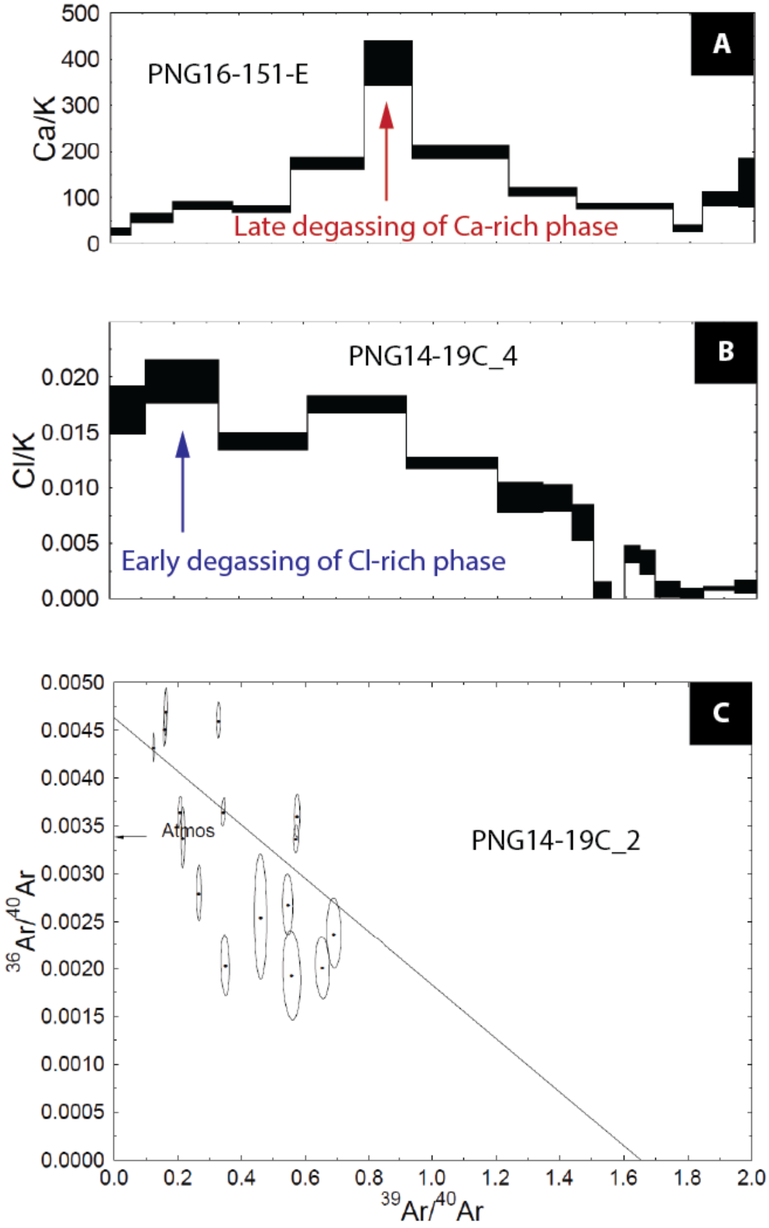

Figure APPII.V. A) Ca/K response during degassing of sample PNG16-151-E, showing overall high Ca/K ratios and indicating the presence of a high-Ca late-stage degassing constituent of a particularly Ca-rich phase (or K-poor). B) Cl/K response during degassing of sample PNG14-19C_4, indicating the presence of a high-Cl early-stage degassing constituent. C) PNG14-19C_4 isochron of traditional full spectrum integration approach, showing the correlation between 39/40 Ar ratio and 36/40 Ar ratio. Each heating step is indicated by a point, with an associated error ellipse. Predicted values above the atmospheric value (1/295.5) fall in negative age space, illustrating the ineffectiveness of a full spectrum integration approach with these fine-grained, partially devitrified pseudotachylytes samples.

(Cl/K>4 in early degassing and Ca/K>0.005 in late degassing) eliminate gas fractions that represent devitrification and isotope recoil artifacts to overcome this problem with full spectrum integration.

APPII.III.III.I. PNG14-19C

A total of 5 subsamples of PNG14-19C were dated. Subsamples 2, 4, 5 and 6 were analyzed by SEM pixel analysis before irradiation, and sample l0 was not (see table APPII.I for sample preparation steps). It was treated with 30% hydrogen peroxide to investigate the possibility of mass 39-hydrocarbon contamination from oil saw preparation. The effect of this possible contamination is likely negligible, as similar behavior for treated and untreated samples was observed. Figure APPII.VIB shows the degassing spectrum of sample PNG14-19C_l0, and gives a reduced integrated age of 2.24±0.29 Ma.

APPII.III.III.II. PNG16-151-E and PNG16-152-A

Two subsamples of PNG16-151-E and PNG16-152-A were dated, and all returned degassing spectra with Ca/K ratios >4 and Cl/K ratios >0.005 for all heating steps. These samples lacked sufficient K to return meaningful age data.

APPII.III.III.III. PNG16-17.2-F1

Two subsamples of PNG16-17.2-F1 were dated. One subsample returned an age of 2.27±0.37 Ma (figure APPII.VIA). The second subsample, however, had very high Cl concentrations and was unable to return meaningful age data.

APPII.III.III.IV. PNG16-17x

Both subsamples of PNG16-17x were dated successfully, and returned reduced integrated ages of 2.96±0.50 Ma and 3.00±0.43 Ma (figure APPII.VI C-D).

APPII.III.IV. Discussion

A window of large coseismic events is preserved by the four subsamples of successfully dated pseudotachylyte, between ~2.2 Ma and ~3.0 Ma. These dates represent maximum ages because the effect of incorporating 10-15 wt. % older host rock K would increase the age. Using a slip rate of ~1 cm/yr, based on GPS and ^{10}Be cosmogenic nuclide exposure scarp dating (Tim Little, personal communication) and a 30° fault dip, these Ar ages imply friction melt generating seismicity at ~8-10 km depths.

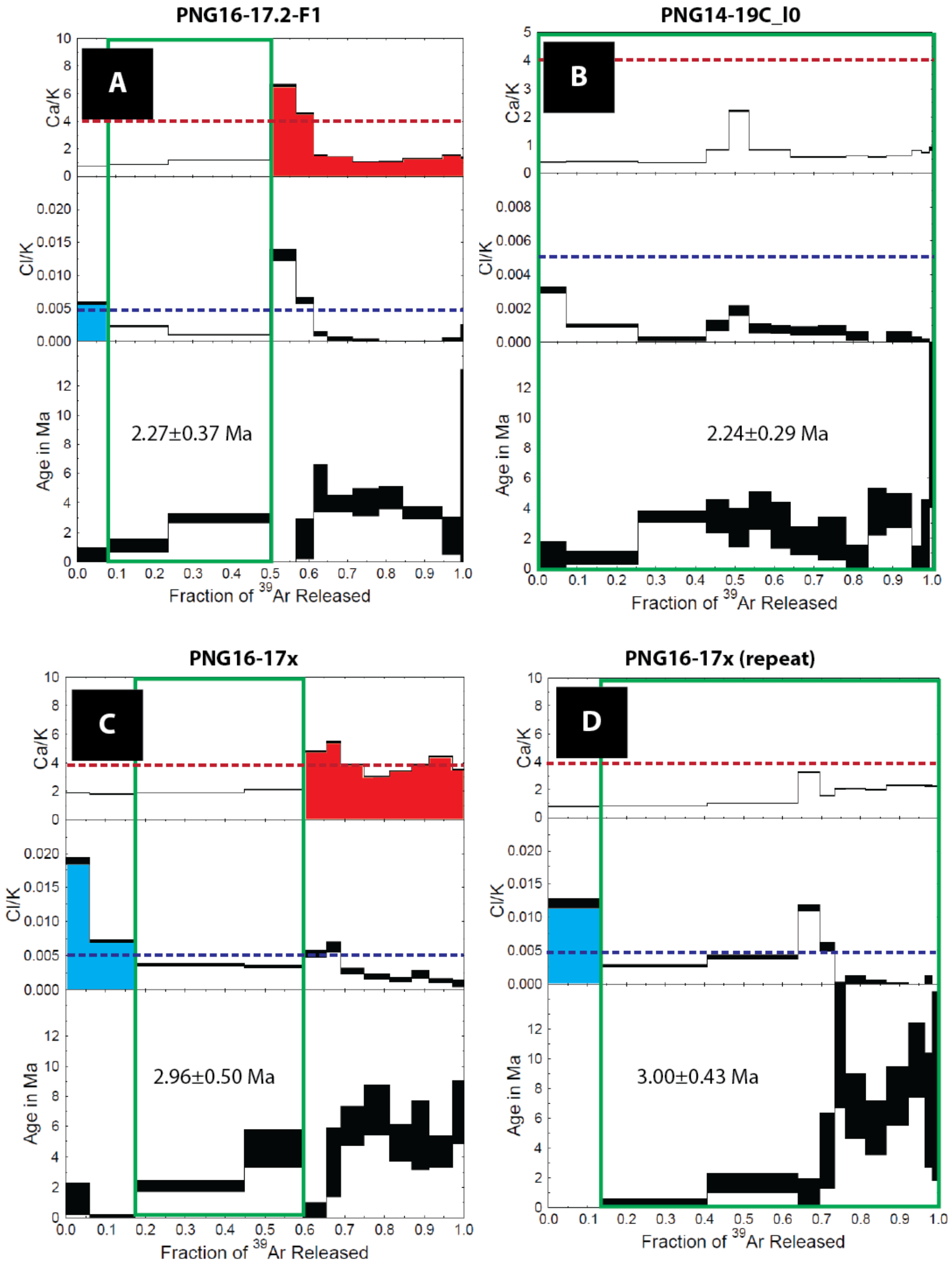

Figure APPII.VI. Degassing spectra of 4 successfully dated pseudotachylyte subsamples. Each value in these stepwise functions represents a heat step during the measurement process. The blue dashed line indicates the discriminatory Cl/K value of >0.005, used to differentiate high-Cl early-stage sample constituents. The red dashed line indicates the discriminatory Ca/K value of >4, used in differentiating high-Ca late-stage sample constituents. Corresponding blue and red heating steps were excluded from reduced integrated age calculations, leaving only those steps within the green box.

APPII.IV. Fault Gouge Dating

Four clay-rich fault gouges were selected as complementary candidates for brittle fault dating using the illite polytype analysis method (Haines and Van Der Pluijm, 2010; van der Pluijm and Hall, 2015); PNG14-32E, PNG16-30B, PNG15-50A-redux, and PNG16-17C. Each sample was separated into four, <2 µm size fractions and quantitative X-ray powder diffraction by BGMN® was conducted on each to quantify proportions of illite polytypes. See Boles et al. (2015) for further methodological details. The results of the X-ray investigation are listed in table APPII.II. Although illite is present in each of the four samples, the low proportions of the mineral indicate very low K concentrations. Additionally, high feldspar and chlorite content present difficulties in the Ar dating process, as they can lead to recoil artifacts due to high Cl/K and Ca/K ratios. Finally, the young

Table APPII.II. Q-XRPD results of PNG fault gouges

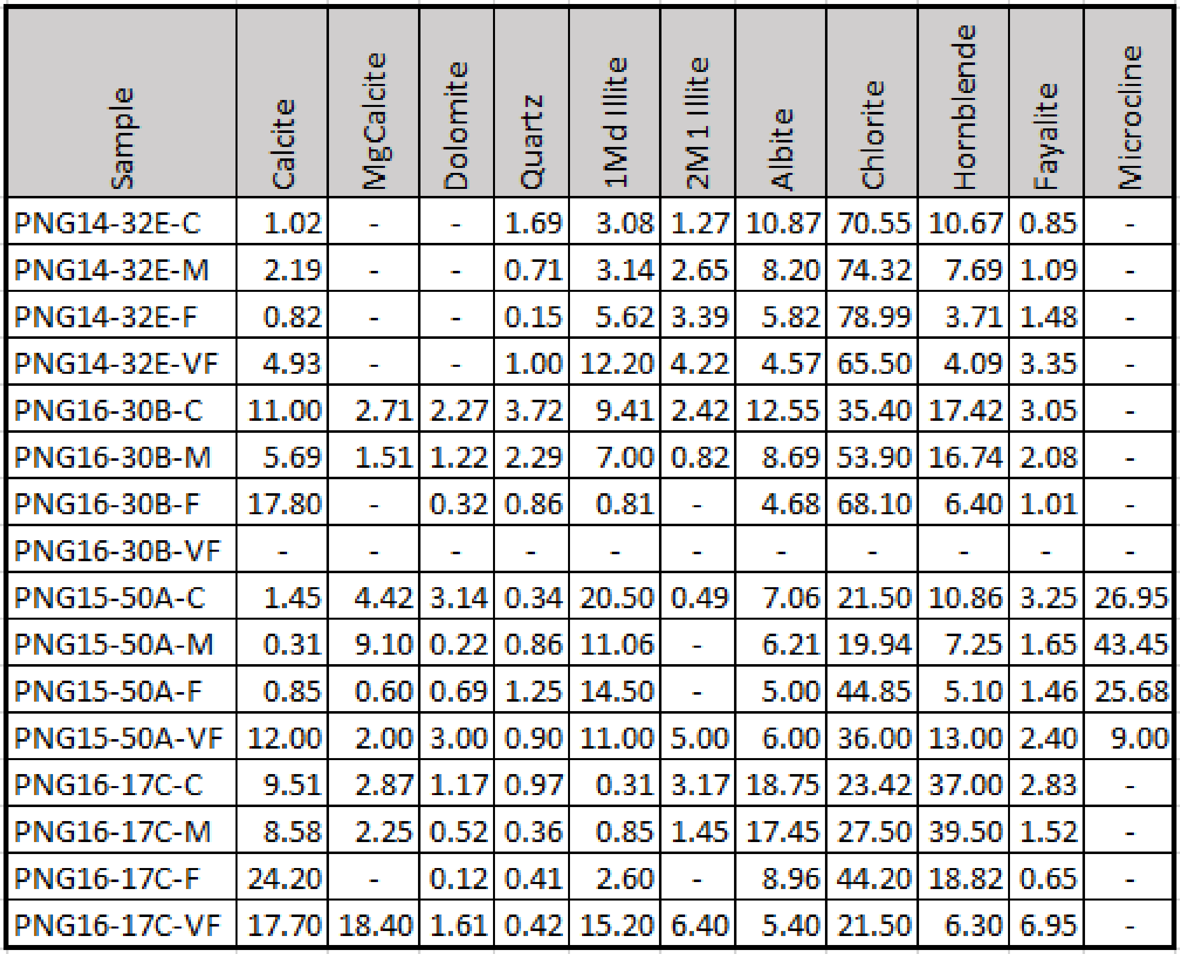

Sample	Calcite	MgCalcite	Dolomite	Quartz	1Md Illite	2M1 Illite	Albite	Chlorite	Hornblende	Fayalite	Microcline
PNG14-32E-C	1.02	-	-	1.69	3.08	1.27	10.87	70.55	10.67	0.85	-
PNG14-32E-M	2.19	-	-	0.71	3.14	2.65	8.20	74.32	7.69	1.09	-
PNG14-32E-F	0.82	-	-	0.15	5.62	3.39	5.82	78.99	3.71	1.48	-
PNG14-32E-VF	4.93	-	-	1.00	12.20	4.22	4.57	65.50	4.09	3.35	-
PNG16-30B-C	11.00	2.71	2.27	3.72	9.41	2.42	12.55	35.40	17.42	3.05	-
PNG16-30B-M	5.69	1.51	1.22	2.29	7.00	0.82	8.69	53.90	16.74	2.08	-
PNG16-30B-F	17.80	-	0.32	0.86	0.81	-	4.68	68.10	6.40	1.01	-
PNG16-30B-VF	-	-	-	-	-	-	-	-	-	-	-
PNG15-50A-C	1.45	4.42	3.14	0.34	20.50	0.49	7.06	21.50	10.86	3.25	26.95
PNG15-50A-M	0.31	9.10	0.22	0.86	11.06	-	6.21	19.94	7.25	1.65	43.45
PNG15-50A-F	0.85	0.60	0.69	1.25	14.50	-	5.00	44.85	5.10	1.46	25.68
PNG15-50A-VF	12.00	2.00	3.00	0.90	11.00	5.00	6.00	36.00	13.00	2.40	9.00
PNG16-17C-C	9.51	2.87	1.17	0.97	0.31	3.17	18.75	23.42	37.00	2.83	-
PNG16-17C-M	8.58	2.25	0.52	0.36	0.85	1.45	17.45	27.50	39.50	1.52	-
PNG16-17C-F	24.20	-	0.12	0.41	2.60	-	8.96	44.20	18.82	0.65	-
PNG16-17C-VF	17.70	18.40	1.61	0.42	15.20	6.40	5.40	21.50	6.30	6.95	-

expected ages would indicate that daughter product concentration would also be very low. We conclude that Ar dating of these fault gouges would likely return uninterpretable results.

APPII.V. Conclusions

Ar dating of several occurrences of pseudotachylyte identifies major coseismic events with maximum ages between ~2.2 and ~3.0 Ma that reflect rapid exhumation from mid-crustal seismicity levels of 8-10 km. Ca- and Cl-bearing phases that formed during devitrification of pseudotachylyte glass, and low initial K of the melt product, heightened the difficulty of analyzing these samples, but utilization of the reduced integrated age method mitigated these challenges. Illite, although present in all of the samples tested, is not in high enough concentrations to give confidence to full illite age analysis.

APPII.VI. Acknowledgments

This work was accomplished in collaboration with Tim Little of the University of Victoria, Wellington (New Zealand). Chris Hall provided expert support and interpretation of Ar degassing spectra. This research was supported by a Graduate Turner Award from the UM Department of Earth and Environmental Sciences.

Appendix III: Meteoric Fluid Cycling Recorded by Authigenic Illite in Clay-rich Zones of the San Andreas Fault Observatory at Depth (SAFOD) Borehole

APPIII.I. Abstract

This study presents a methodology to remove the non-illitic hydrous phase contribution to a stable isotopic measurement of a mixture of clays. The method results in isolation of the total illite isotopic signal for further use in the illite polytype analysis method. This technique is applied to clay-rich samples from the San Andreas Fault Observatory at Depth (SAFOD) borehole. They indicate that syn-deformational, authigenic illite has δD values of -90±3‰ and -85±7‰. Conversion to fluid values produces a range of -56 to -61‰, overlapping with the range of modern meteoric water in the area. We conclude that surficial fluid is a major constituent of San Andreas Fault geohydrology, that it circulates to depths >3 km, and that it contributes to the fault's unique mineralogy and mechanical behavior.

APPIII.II. Keywords

SAFOD, illite polytype analysis, H isotopes

APPIII.III. Introduction

One of the most striking results to emerge from Earthscope's San Andreas Fault Observatory at Depth (SAFOD) project, is the consensus building behind the theory that low-temperature, in-situ generation of nano-scale clay minerals—characterized by low coefficients of friction—has the potential to alter a lithospheric-scale fault's mechanical behavior in fundamental ways (Schleicher et al., 2006; Moore and Rymer, 2007; Collettini et al., 2009; Schleicher et al., 2010; Carpenter et al., 2011; Lockner et al., 2011; Schleicher et al., 2012). In addition to wall rock bulk chemistry and cataclastic processes incorporating wall rock into the damage zone of a fault system, the most important determinative factors in understanding secondary, fault-hosted clay mineralization are the transient properties associated with fault-related hydrologic architecture and geofluid heat and solute load (Carter et al., 1990; Bruhn et al., 1990; Knipe and McCaig, 1994). Fault-related fluid flow models (figure APPIII.I) and empirical observations often differ in fluid provenance and pathways in terms of direction, timing, and flux (McCaig, 1997; Sibson, 1990; Fricke et al., 1992; Mulch et al., 2004). Recent advances that utilize illite polytype analysis to elucidate the stable isotopic composition of synkinematic clay minerals provide critical constraints on the temperatures and composition of fluid reservoirs involved in deformation zones of the brittle crust (Boles et al., 2015). We employ these advances in this study in order to investigate the mineralizing fluid that was active in the San Andreas Fault system and responsible for synkinematic illite in clay-rich zones of the SAFOD borehole.

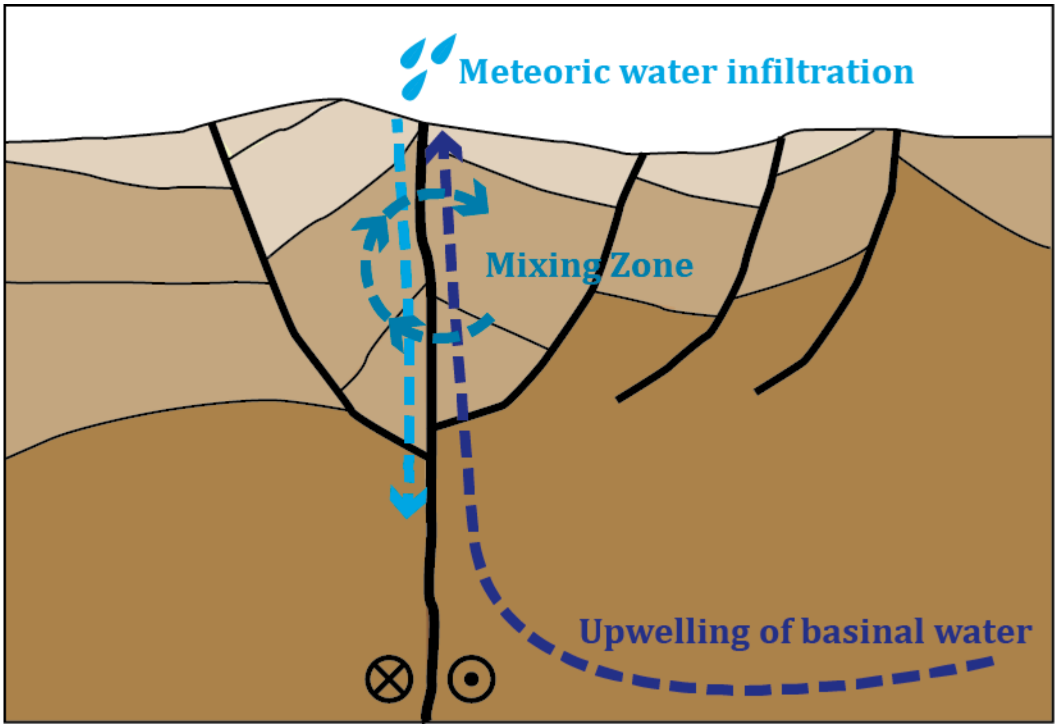

Figure APPIII.I. Various models of fluid flow in the San Andreas Fault.

APPIII.IV. Sample Description and Preparation

Four clay-rich samples from the SAFOD borehole were obtained: GR1S1, GR2S8, GR4S3, and GR6S5. The bulk, oriented clay fraction (<2 μm) of each sample was qualitatively characterized by X-ray diffraction in both air-dried and ethylene glycolated conditions (figure APPIII.II), using a Rigaku Ultima IV diffractometer located at the University of Michigan’s Electron Microbeam Analysis Laboratory.

Each sample was separated into four size fractions by centrifugation: coarse (1.0-2.0 μm), medium (0.2-1.0 μm), fine (0.05-.02 μm), and very fine (<0.05 μm). Random mounts of each size fraction of the two samples in which illite was identified were analyzed by quantitative X-ray powder diffraction using Rietveld program BGMN® (Bergmann et al., 1998). Proportions of chlorite and 1Md and 2M1 illite polytypes, as well as non-clay phases, were quantified for each grain size aliquot (results reported in table APPIII.II). An insufficient volume of sample GR1S1-VF precluded its use for quantitative analysis.

APPIII.IV.I. GR1S1

Sample GR1S1 is a foliated siltstone-shale cataclasite that was recovered from the middle of Core Run 2 section 4 (10,455.2 to 10,478.8 ft MD). Cataclasite foliation is defined by scaly fabric in the fine-grained portions, cm-thick color banding, and imbricate clasts of siltstone and sandstone wall rock. Qualitative X-ray analysis of the bulk clay portion of sample GR1S1 indicates the presence of illite and chlorite clay constituents (figure APPIII.II). Both illite and chlorite likely interstratify with small amounts of smectite. Quartz, calcite, and plagioclase feldspar were also identified.

APPIII.IV.II. GR2S8

Sample GR2S8 is a foliated gouge from a fault encountered at 10,480 ft MD, and appears in core near the top of Core Run 2 Section 7. The dark grayish-black, intensely sheared fault rock is extremely fine-grained and incohesive, with a wavy foliation defined by penetrative microscale shears. Wall rock porphyroclast volume is <5%, and lithology includes serpentinite, sandstone, and siltstone. The upper contact of the gouge with the cataclasite is inclined and sharp. Qualitative X-ray analysis (figure APPIII.II) indicates that the clay component is dominated by interlayered chlorite/smectite (corrensite, which is a 50% chlorite-50% smectite layered mineral). This is similar to other reports from gouge zones of SAFOD (Solum et al., 2006; Schleicher et al., 2009).

APPIII.IV.III. GR4S3

Sample GR4S3 is a foliated fault gouge recovered from depths 10,815.5 to 10,823.9 ft MD, and is associated with a fault encountered at 10,830 ft MD. It appears in Core Run 4 Section 2 and Core Run 4 Section 5. It is very macroscopically similar to the gouge encountered at 10,480 ft MD (GR2S8), with similar color, grain size, penetrative foliation, and wall rock porphyroclasts. Qualitative X-ray diffraction also yields similar results to sample GR2S8, with the clay fraction of the gouge dominated by chlorite/smectite (figure APPIII.II).

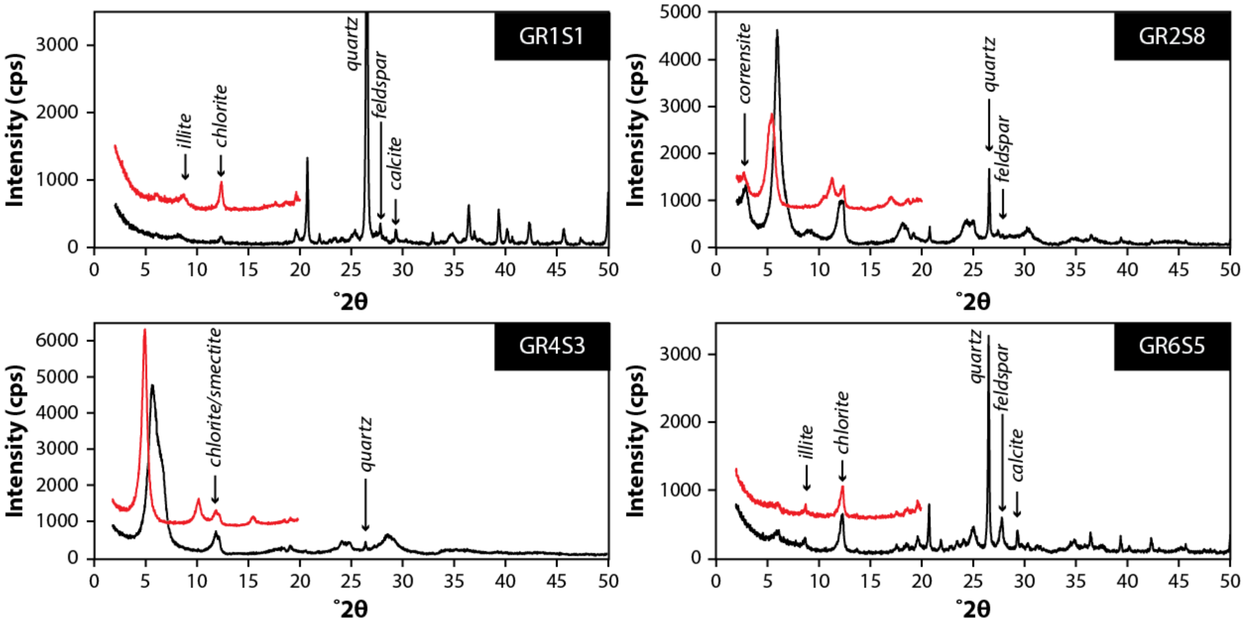

Figure APPIII.II. Qualitative X-ray analysis of SAFOD clay gouge samples.

APPIII.IV.IV. GR6S5

Sample GR6S5 is a sheared claystone and shale recovered in Core Run 6 Section 5. It comprises sheared, grayish-black claystone and shale within a brecciated and foliated sheared siltstone. Large, indurated clasts with prominent calcite veining are present in this unit; additionally, two fold hinges were identified in the central part of the unit. Qualitative X-ray analysis indicates a similar composition to sample GR1S1, with illite and chlorite comprising the clay fraction (with little, if any, interlayer smectite) and quartz, feldspar, and calcite also present (figure APPIII.II).

APPIII.V. Hydrogen Isotopic Analysis

δD values of each grain size of the four samples under investigation were measured at the Joint Goethe University – BiK-F Stable Isotope Facility Frankfurt using a ThermoFinnigan MAT 253 mass spectrometer in continuous flow mode coupled to a high temperature conversion elemental analyser (TC-EA). A sample weight of 1 mg was wrapped into Ag foil and dried overnight at 150°C in a stainless steel tray. Samples were rapidly transferred to a zero-blank autosampler in the stainless steel tray and the autosampler was immediately purged with helium gas to avoid re-hydration with ambient air moisture. This procedure ensures that only structural—not interlayer—water is measured. Standards were run in-line with unknowns and reproduced with an error below ±2 ‰. All δD values are reported relative to standard mean ocean water (VSMOW). Results are reported in table APPIII.I.

Table APPIII.I. H isotopic results

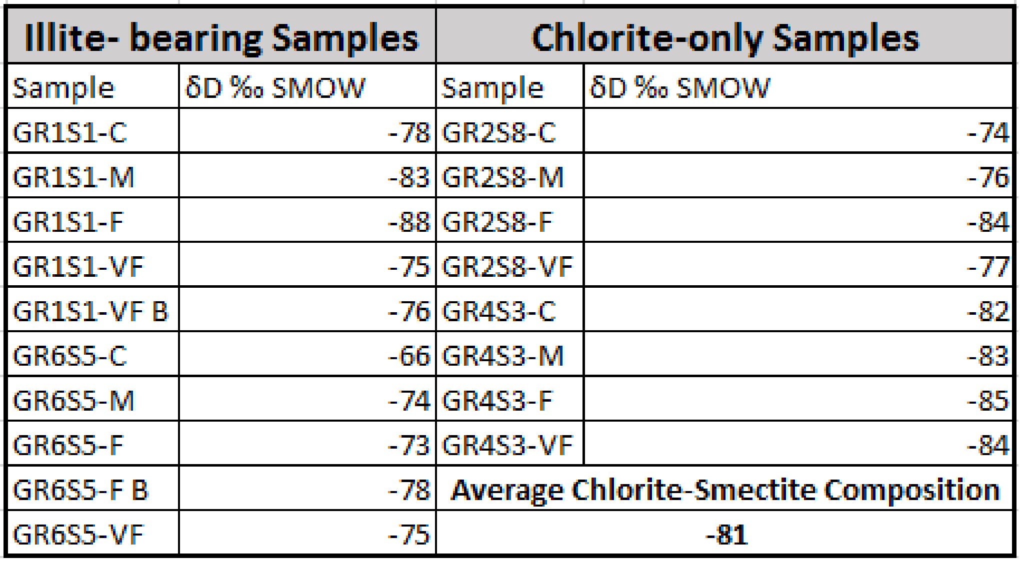

Illite- bearing Samples		Chlorite-only Samples	
Sample	δD ‰ SMOW	Sample	δD ‰ SMOW
GR1S1-C	-78	GR2S8-C	-74
GR1S1-M	-83	GR2S8-M	-76
GR1S1-F	-88	GR2S8-F	-84
GR1S1-VF	-75	GR2S8-VF	-77
GR1S1-VF B	-76	GR4S3-C	-82
GR6S5-C	-66	GR4S3-M	-83
GR6S5-M	-74	GR4S3-F	-85
GR6S5-F	-73	GR4S3-VF	-84
GR6S5-F B	-78	**Average Chlorite-Smectite Composition**	
GR6S5-VF	-75	**-81**	

APPIII.VI. Illite Polytype Analysis

The illite polytype analysis method was developed to isolate the isotopic signal of a single population of clay minerals in a mixture of phases. The δD values reported in table APPIII.I, combined with the Q-XRPD analysis results in table APPIII.II, indicate that the H value measured in some of these samples is, indeed, an aggregate signal of multiple hydrous phases. In samples GR2S8 and GR4S3, however, chlorite-smectite is the only hydrous phase, and for all size fractions of these samples the H isotopic compositions are similar. The arithmetic mean of these data is -81‰, which we use for our calculations as the end-member hydrogen composition of the chlorite-smectite in all of these samples. Samples GR1S1 and GR6S5, contain both 1Md and 2M1 illite, in addition to chlorite, that contribute to the aggregate H signal.

1Md illite is a low-temperature polytype of illite known to represent synkinematic, neoformed clays in fault zones (van der Pluijm et al., 2001). 2M1 illite is a higher-temperature polytype that represents the inherited detrital clay population. The plurality of grain size fractions, each with a different 1Md:2M1 ratio and isotopic composition facilitate the creation of a mixing line that can be extrapolated to end-member 1Md and 2M1 values. This, however, assumes only H isotopic contributions from these two phases. In the presence of a third phase, chlorite-smectite, we must first obtain a H isotopic composition of total illite before its constituent 1Md and 2M1 signals can be unmixed. Using the average chlorite-smectite H composition, the following methodology accounts for the various contributions of each of the three hydrous phases in order to find the total illite composition, which is then unmixed.

Illite contains 2 hydrogen molecules per crystallographic unit cell ($R_{0.89}Al_{1.85}Fe^{3+}_{0.05}Mg_{0.10}Si_{3.20}Al_{0.80}O_{10}(OH)_2$), as does smectite ($R_{0.33}^{+}(Al_{1.67}Mg_{0.33})Si_4O_{10}(OH)_2$. Interlayer H of swelling minerals is expelled before mass spectroscopic analysis by Ag foil packaging and heating. Chlorite, with an additional octahedral layer in its structure, contains 8 hydrogen molecules per crystallographic unit cell (2:1 sheet $[(R^{2+},R^{3+})_3(Si_{4-x}R^{3+}_x)O_{10}OH_2]^-$; octahedral sheet $[(R^{2+},R^{3+})_3(OH)_6]^+$). We assume an average chlorite/smectite ordering structure of 50:50, otherwise known as corrensite (Velde et al., 1986). We utilize the following equations to identify the contribution of total illite (i.e. 1Md+2M1) to the aggregate H signal of each size fraction by removing the H isotopic influence of the chlorite:

$$Eq.APPIII.I:$$

$$\alpha = \frac{\%\,chlorite}{\%chlorite + \%\,1Md\;illite + \%\,2M1\;illite}$$

$$Eq.APPIII.II:$$

$$\gamma = \frac{8\left(\frac{\alpha}{2}\right) + 2\left(\frac{\alpha}{2}\right)}{8\left(\frac{\alpha}{2}\right) + 2\left(\frac{\alpha}{2}\right) + 2(1-\alpha)} = \frac{5\alpha}{3\alpha + 2}$$

$$Eq.APPIII.III:$$

$$\varepsilon = \frac{\tau - \beta\gamma}{1 - \gamma}$$

$\alpha = weight\ percent\ chlorite\ normalized\ by\ total\ hydrous\ mineral\ weight\ percent$

$\gamma = percent\ of\ aggregate\ H\ signal\ contributed\ by\ chlorite$

$\tau = measured\ aggregate\ H\ composition$

$\beta = H\ composition\ of\ chlorite\ (= -81‰\ in\ this\ study)$

$\varepsilon = H\ composition\ of\ the\ total\ illite\ in\ the\ sample\ after\ the$
$chlorite\ contribution\ has\ been\ removed$

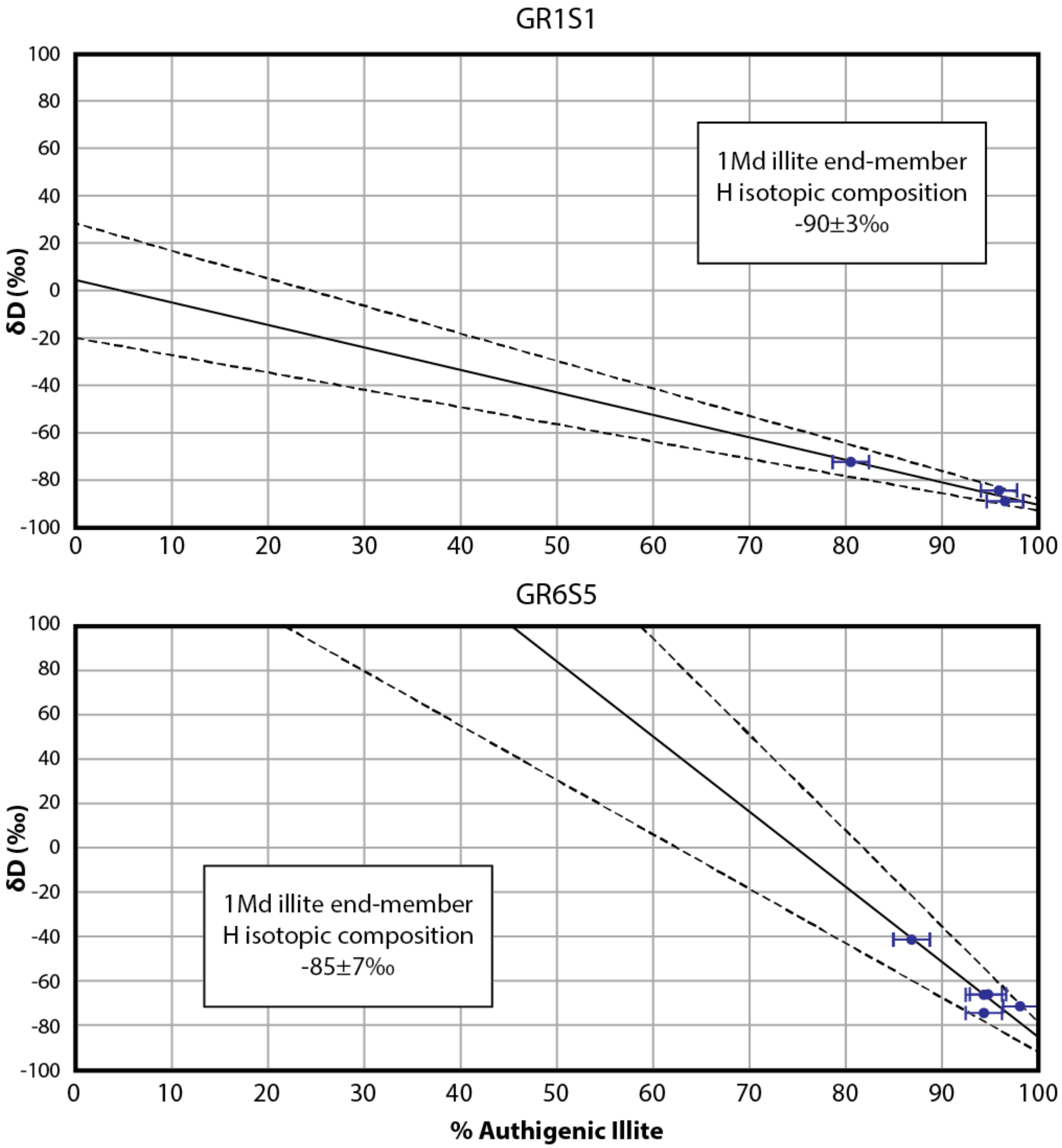

Figure APPIII.III. Illite polytype analysis H-isotopic mixing lines for samples GR1S1 and GR6S5.

Equation APPIII.I calculates the weight percent chlorite among total hydrous phases. Equation APPIII.II accounts for the varying H contributions of each type of mineral to the aggregate H signal and γ is the percent of the H molecules in the aggregate H signal that were contributed by chlorite-smectite. Using a corrensite end-member, half the chlorite weight percent calculated by Q-XRPD is chlorite (contributes 8 H) and half is smectite (contributes 2 H). The weight percent total illite, which is a composite of both 2M1 and 1Md, is 1-α and contributes 2 H per structural unit. Finally, Equation APPIII.III inputs the measured H and the known chlorite end-member composition to calculate a δD value for the total illite population. α and ε values calculated for each grain size fraction of the illite-bearing samples are reported in table APPIII.II. With a H composition calculated for total illite for each grain size fraction of the illite-bearing samples, we can now use ratios of 1Md:2M1 to unmix the authigenic population's end-member value by York linear regression of ε and %1Md (Mahon, 1996).

Table APPIII.II. Q-XRPD results for illite-bearing samples reported in weight percent, and calculated total illite H compositions (ε)

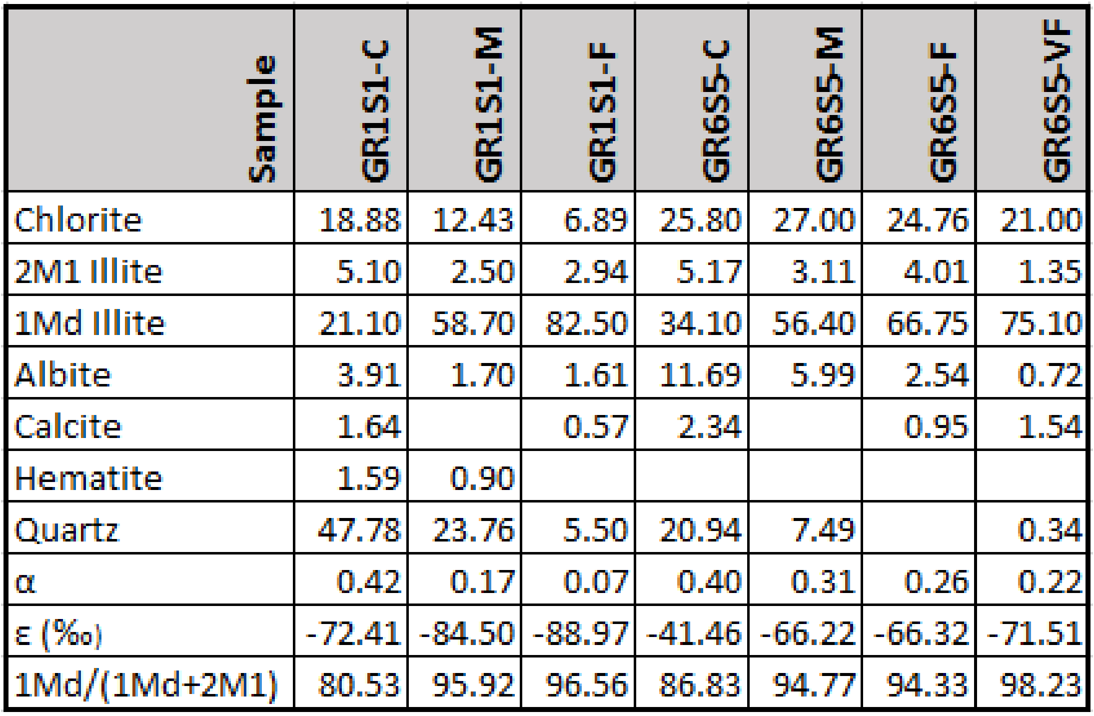

Sample	GR1S1-C	GR1S1-M	GR1S1-F	GR6S5-C	GR6S5-M	GR6S5-F	GR6S5-VF
Chlorite	18.88	12.43	6.89	25.80	27.00	24.76	21.00
2M1 Illite	5.10	2.50	2.94	5.17	3.11	4.01	1.35
1Md Illite	21.10	58.70	82.50	34.10	56.40	66.75	75.10
Albite	3.91	1.70	1.61	11.69	5.99	2.54	0.72
Calcite	1.64		0.57	2.34		0.95	1.54
Hematite	1.59	0.90					
Quartz	47.78	23.76	5.50	20.94	7.49		0.34
α	0.42	0.17	0.07	0.40	0.31	0.26	0.22
ε (‰)	-72.41	-84.50	-88.97	-41.46	-66.22	-66.32	-71.51
1Md/(1Md+2M1)	80.53	95.92	96.56	86.83	94.77	94.33	98.23

Figure APPIII.III shows the results of linear regression, and indicates that the 1Md populations of samples GR1S1 and GR6S5 have end-member compositions of -90±3‰ and -85±7‰, respectively. High proportions of the authigenic component of illite in both samples led to poorly-constrained detrital end-members. Whereas the 2M1 end-member H compositions have low accuracy, the 1Md end-member is robustly constrained for both samples.

We delimit the temperature of formation of the 1Md illite using the post-drilling equilibrated bottom-hole temperature of 93°C as a maximum temperature (Williams et al., 2004). Using this formation temperature in the fractionation equation of Capuano (1992), δD values for the fluid in equilibrium with the authigenic clay is in the range of -56 to -61‰. The modern-day meteoric fluid range for this area is -40 to -70‰ (Bowen and Revenaugh, 2003). Thus, we interpret the overlapping ranges to indicate that the fluid in equilibrium with synkinematic illite growth and San Andreas Fault creep is predominantly meteoric in nature, and therefore surface-derived fluids are circulating to depths >3 km along this part of the San Andreas Fault.

APPIII.VII. Conclusions

Qualitative and quantitative X-ray diffraction identify GR2S8 and GR4S3 as having only chlorite/smectite as its sole clay constituent, with an average H isotopic composition of -81‰, whereas samples GR1S1 and GR6S5 are comprised of mixtures of detrital and authigenic illite in addition to chlorite/smectite. A methodology is developed to remove the influence of the chlorite/smectite mineral phase from the aggregate H measurement of the illite-bearing samples. Illite polytype analysis allows the remaining H isotopic signal to be unmixed into 2M1 (detrital) and 1Md (authigenic) end-members, although the 2M1 end-member is poorly constrained due to the overwhelming proportions of authigenic material. End-member 1Md illite compositions are -90±3‰ for sample GR1S1 and -85±7‰ for sample GR6S5. These values correspond to fluid compositions in the range of -56 to -61‰, indicating a meteoric mineralizing fluid source. We conclude that the San Andreas Fault circulates surficial fluid to depths >3 km and that the heat and solute content of this meteoric fluid is the controlling factor for the origin of secondary minerals in fault rock of the SAFOD borehole.

References

Agosta, F., Mulch, A., Chamberlain, C.P., Aydin, A., 2008, Geochemical traces of CO2-rich fluid flow along normal faults in central Italy: Geophysical Journal International, v. 174, p. 758-770, doi: 10.1111/j.1365-246X.2008.03792.x.

Aja, S.U., Rosenberg, P.E., and Kittrick, J.A., 1991, Illite equilibria in solutions: I. Phase relationships in the system K2OAl2O3SiO2H2O between 25 and 250ºC: Geochimica et Cosmochimica Acta, v. 55, no. 5, p. 1353–1364, doi: 10.1016/0016-7037(91)90313-T.

Allis, R.G., and Shi, Y., 1995, New insights to temperature and pressure beneath the central Southern Alps, New Zealand: New Zealand Journal of Geology and Geophysics, v. 38, no. 4, p. 585–592, doi: 10.1080/00288306.1995.9514687.

Altaner, S., and Ylagan, R., 1997, Comparison of structural models of mixed-layer illite/smectite and reaction mechanisms of smectite illitization: Clays and Clay Minerals, v. 45, no. 4, p. 517–533.

Bachu, S., 1995, Synthesis and model of formation-water flow, Alberta Basin, Canada: American Association of Petroleum Geologists Bulletin, v. 79, no. 8, p. 1159–1178, doi: 10.1306/8D2B2209-171E-11D7-8645000102C1865D.

Bailey, S.W., 1980, Summary of recommendations of AIPEA nomenclature committee on clay minerals: American Mineralogist, v. 65, p. 1–7, doi: 10.1180/claymin.1980.015.1.07.

Baldwin, S.L., Monteleone, B.D., Webb, L.E., Fitzgerald, P.G., Grove, M., and Hill, E.J., 2004, Pliocene eclogite exhumation at plate tectonic rates in eastern Papua New Guinea.: Nature, v. 431, no. 7006, p. 263–267, doi: 10.1038/nature02846.

Beavan, J., Moore, M., Pearson, C., Henderson, M., Parsons, B., Bourne, S., England, P., Walcott, D., Blick, G., Darby, D., and Hodgkinson, K., 1999, Crustal deformation during 1994-1998 due to oblique continental collision in the central Southern Alps, New Zealand, and implications for seismic potential of the Alpine fault: Journal of Geophysical Research, v. 104, no. B11, p. 25,233-25,255.

Bense, F.A., Wemmer, K., Löbens, S., Siegesmund, S., 2014, Fault gouge analyses: K-Ar illite dating, clay mineralogy and tectonic significance—a study from the Sierras Pampeanas, Argentina: International Journal of Earth Sciences, v. 103, no. 1, p. 189-218, doi: 10.1007/s00531-013-0956-7.

Bérend, I., Cases, J.M., François, M., Uriot, J.P., Michot, L., Masion, A., and Thomas, F., 1995, Mechanism of adsorption and desorption of water vapor by homoionic montmorillonites: 2. The Li+, Na+, K+, Rb+ and Cs+ exchanged forms: Clays and Clay Minerals, v. 43, p. 324–336, doi: 10.1346 /CCMN .1995.0430307.

Berger, B.R., Tingley, J.V., Drew, L.J., 2003, Structural localization and origin of compartmentalized fluid flow, Comstock Lode, Virginia City, Nevada: Economic Geology, vol. 98, no. 2, p. 387-408, doi: 10.2113/gsecongeo.98.2.387.

Bergmann, J., 2005, Rietveld Analysis Program BGMN Manual: Dresden, Germany.

Bergmann, J., Friedel, P., and Kleeberg, R., 1998, BGMN—a new fundamental parameter based Rietveld program for laboratory X-ray sources, its use in quantitative analysis and structure investigations: Commission of Powder Diffraction, p. 5–8.

Bethke, C., 1986, Hydrologic constraints on the genesis of the Upper Mississippi Valley mineral district from Illinois basin brines: Economic Geology, v. 81. no. 2, p. 233-249.

Bethke, C., and Marshak, S., 1990, Brine migrations across North America-the plate tectonics of groundwater: Annual Review of Earth and Planetary Sciences, v. 18, p. 287–315.

Bish, D., 1993, Studies of clays and clay minerals using X-ray powder diffraction and the Rietveld method: CMS Short Course on Computer Applications in Clay Mineralogy, San Diego, CA.

Bish, D., and Reynolds, R., 1989, *Modern Powder Diffraction*: Mineralogical Society of America, Washington, D.C.

Bish, D., Reynolds, R., and Walker, J. (1993) Computer Applications to X-ray Powder Diffraction Analysis of Clay Minerals: CMS Workshop Series, Boulder, CO.

Bjorlykke, K., 1993, Fluid flow in sedimentary basins: Sedimentary Geology, v. 86, no. 1–2, p. 137–158, doi: 10.1016/0037-0738(93)90137-T.

Bjorlykke, K., 1994, Fluid-flow processes and diagenesis in sedimentary basins: Geological Society, London, Special Publications, v. 78, no. 1, p. 127–140, doi: 10.1144/GSL.SP.1994.078.01.11.

Blackmer, G.C., Omar, G.I., and Gold, D.P., 1994, Post-Alleghanian unroofing history of the Appalachian Basin, Pennsylvania, from fission track analysis and thermal models: Tectonics, v. 13, no. 5, p. 1259–1276.

Boese, C.M., Townend, J., Smith, E., and Stern, T., 2012, Microseismicity and stress in the vicinity of the Alpine Fault, central Southern Alps, New Zealand: Journal of Geophysical Research, v. 117, no. B2, p. B02302, doi: 10.1029/2011JB008460.

Boles, A., van der Pluijm, B.A., Mulch, A., Mutlu, H., Uysal, I.T., and Warr, L.N. (2015) Hydrogen and 40Ar/39Ar isotope evidence for multiple and protracted paleofluid flow events within the long-lived North Anatolian Keirogen (Turkey): Geochemistry, Geophysics, Geosystems, p. 1541–1576, doi: 10.1002/2014GC005684.

Boles, J., and Franks, S., 1979, Clay diagenesis in Wilcox sandstones of southwest Texas: implications of smectite diagenesis on sandstone cementation: Journal of Sedimentary Research, v. 49, no. 1, p. 55–70.

Boness, N.L., and Zoback, M.D., 2006, A multiscale study of the mechanisms controlling shear velocity anisotropy in the San Andreas Fault Observatory at Depth: Geophysics, v. 71, no. 5, p. F131, doi: 10.1190/1.2231107.

Bossiere, G., 1991, Petrology of pseudotachylytes from the Alpine Fault of New Zealand: Tectonophysics, v. 196, no. 1–2, p. 173–193, doi: 10.1016/0040-1951(91)90295-4.

Boulton, C., and Moore, D., 2014, Frictional properties of exhumed fault gouges in DFDP-1 cores, Alpine Fault, New Zealand: Geophysical Reseach Letters, v. 41, p. 1–7, doi: 10.1002/2013GL058236.

Boulton, C., Carpenter, B.M., Toy, V., and Marone, C., 2012, Physical properties of surface outcrop cataclastic fault rocks, Alpine Fault, New Zealand: Geochemistry, Geophysics, Geosystems, v. 13, no. 1, p. 3801-3820, doi: 10.1029/2011GC003872.

Boulton, C., Moore, D.E., Lockner, D.A., Toy, V.G., Townend, J., and Sutherland, R., 2014, Frictional properties of exhumed fault gouges in DFDP-1 cores, Alpine Fault, New Zealand: Geophysical Research Letters, p. 356–362, doi: 10.1002/2013GL058236.

Bourdelle, F., and Parra, T., 2013, Clay minerals as geo-thermometer: A comparative study based on high spatial resolution analyses of illite and chlorite in Gulf Coast sandstones (Texas, USA): American Mineralogist, v. 98, p. 914–926.

Bowen, G.J., and Revenaugh, J., 2003, Interpolating the isotopic composition of modern meteoric precipitation: Water Resources Research, v. 39, no. 10, doi: 10.1029/2003WR002086.

Bozkaya, Ö., Yalçin, H., and Göncüoğlu, M.C., 2012, Diagenetic and very low-grade metamorphic characteristics of the Paleozoic series of the Istanbul Terrane (NW Turkey): Swiss Journal of Geosciences, v. 105, no. 2, p. 183–201, doi: 10.1007/s00015-012-0108-2.

Bozkaya, Ö., Yalçin, H., Başibüyük, Z., and Bozkaya, G., 2007, Metamorphic-hosted pyrophyllite and dickite occurrences from the hydrous Al-silicate deposits of the Malatya-Pütürge region, central eastern Anatolia, Turkey: Clays and Clay Minerals, v. 55, no. 4, p. 423–442, doi: 10.1346/CCMN.2007.0550409.

Bozkurt, E., Mittwede, S.K., 2001, Introduction to the geology of Turkey—A synthesis: International Geology Review, vol. 43, no. 7, doi:10.1080/00206810109465034.

Brannon, J.C., Podosek, F.A., and Cole, S.C., 1997, Radiometric dating of Mississippi Valley-type ore deposits, *in* Sangster, D.F. ed., *Carbonate-Hosted Lead-Zinc Deposits*, Society of Economic Geologists, Special Publication No. 4, Littleton, CO, p. 536–545.

Brindley, G.W., and Brown, G. (Eds.), 1980, *Crystal Structure of Clay Minerals and their X-ray Identification*: Mineralogical Society, London.

Bruce, C.H., 1984, Smectite Dehydration-Its Relation to Structural Development and Hydrocarbon Accumulation in Northern Gulf of Mexico Basin: AAPG Bulletin, v. 68, no. 6, p. 673–683, doi: 10.1306/AD461363-16F7-11D7-8645000102C1865D.

Bruhn, R.L., Yonkee, W.A., and Parry, W.T., 1990, Structural and fluid-chemical properties of seismogenic normal faults: Tectonophysics, v. 175, p. 139–157, doi: 10.1016/0040 1951(90)90135-U.

Brune, J., Henyey, T., and Roy, R., 1969, Heat flow, stress, and rate of slip along the San Andreas fault, California: Journal of Geophysical Research, v. 74, no. 15. p. 3821-3827.

Bull, J.M., 1990, Structural style of intra-plate deformation, Central Indian Ocean Basin: evidence for the role of fracture zones: Tectonophysics, v. 184, no. 2, p. 213–228, doi: 10.1016/0040-1951(90)90054-C.

Burst, J.F.J., 1957, Postdiagenetic clay mineral environmental relationships in the Gulf Coast Eocene: Sixth National Conference on Clays and Clay Minerals, v. 155, p. 327–341, doi: 10.1346/CCMN.1957.0060124.

Buyce, M., and Friedman, G., 1975, Significance of authigenic K-feldspar in Cambrian-Ordovician carbonate rocks of the proto-Atlantic shelf in North America: Journal of Sedimentary Petrology, v. 45, no. 4, p. 808–821.

Byerlee, J., 1978, Friction of rocks: Pure and applied Geophysics, v. 116, p. 615-626.

Caine, J.S., Evans, J.P., and Forster, C.B., 1996, Fault zone architecture and permeability structure, Geology, v. 24, no. 11, p. 1025-1028, doi: 10.1130/0091-7613(1996)024<1025.

Campani, M., Mulch, A., Kempf, O., Schlunegger, F., Mancktelow, N., 2012, Miocene paleotopography of the Central Alps: Earth and Planetary Science Letters, vol. 337-338, p. 174-185, doi:10.1016/j.epsl.2012.05.017.

Canbaz, O., and Gökce, A., 2014, Microthermometric and stable isotopic (O and H) characteristics of fluid inclusions in the porphyry related Çöpler (İliç - Erzincan) gold deposit, central eastern Turkey: Central European Journal of Geosciences, v. 6, no. 2, p. 139–147, doi: 10.2478/s13533-012-0173-0.

Capuano, R., 1992, The temperature dependence of hydrogen isotope fractionation between clay minerals and water: Evidence from a geopressured system: Geochimica et Cosmochimica Acta, v. 56, p. 2547–2554.

Carlson, E.H., 1994, Geologic, Fluid Inclusion, and Isotopic Studies of the Findlay Arch District, Northwestern Ohio: Economic Geology, v. 89, p. 67–90.

Carpenter, B.M., Kitajima, H., Sutherland, R., Townend, J., Toy, V.G., and Saffer, D.M., 2014, Hydraulic and acoustic properties of the active Alpine Fault, New Zealand: Laboratory measurements on DFDP-1 drill core: Earth and Planetary Science Letters, v. 390, p. 45–51, doi: 10.1016/j.epsl.2013.12.023.

Carpenter, B.M., Marone, C., and Saffer, D.M., 2011, Weakness of the San Andreas Fault revealed by samples from the active fault zone: Nature Geoscience, v. 4, no. 4, p. 251–254, doi: 10.1038/ngeo1089.

Carpenter, B.M., Saffer, D.M., and Marone, C., 2012, Frictional properties and sliding stability of the San Andreas fault from deep drill core: Geology, v. 40, no. 8, p. 759–762, doi: 10.1130/G33007.1.

Carter, N.L., Kronenberg, A.K., Ross, J.V., and Wiltschko, D.V., 1990, Control of fluids on deformation of rocks: Geological Society, London, Special Publications, v. 54, no. 1, p. 1–13, doi: 10.1144/GSL.SP.1990.054.01.01.

Cathelineau, M., 1988, Cation site occupancy in chlorites and illites as function of temperature: Clay Minerals, v. 23, p. 471–485.

Cathles, L.M., and Smith, A.T., 1983, Thermal constraints on the formation of Mississippi Valley-type lead- zinc deposits and their implications for episodic basin dewatering and deposit genesis: Economic Geology, v. 78, no. 5, p. 983–1002, doi: 10.2113/gsecongeo.78.5.983.

Chen, F., Siebel, W., Satir, M., Terzioglu, M., and Saka, K., 2002, Geochronology of the Karadere basement (NW Turkey) and implications for the geological evolution of the Istanbul zone: International Journal of Earth Sciences, v. 91, no. 3, p. 469–481, doi: 10.1007/s00531-001-0239-6.

Chen, X., Madden, A.S., Bickmore, B.R., and Reches, Z., 2013, Dynamic weakening by nanoscale smoothing during fault slip: Geology, v. 41, p. 739–742, doi:10.1130/G34169.1.

Chester, F.M., et al., 2013, Structure and composition of the plate boundary slip zone for the 2011 Tohoku-Oki earthquake: Science, v. 342, p. 1208–1211, doi:10.1126/science.1243719.

Chester, F.M., Mori, J.J., Toczko, S., Eguchi, N., and the Expedition 343/343T Scientists, 2012, Japan Trench Fast Drilling Project (JFAST): Integrated Ocean Drilling Program Preliminary Report, Volume 343/343T: Tokyo, Integrated Ocean Drilling Program Management International, Inc., doi:10.2204/iodp.pr.343343T.2012.

Clauer, N., 2013, The K-Ar and 40Ar/39Ar methods revisited for dating fine-grained K-bearing clay minerals: Chemical Geology, v. 354, p. 163–185, doi: 10.1016/j.chemgeo.2013.05.030.

Clauer, N., Chaudhuri, S., Kralik, M., and Bonnot-Courtois, C., 1993, Effects of experimental leaching on RbSr and KAr isotopic systems and REE contents of diagenetic illite: Chemical Geology, v. 103, no. 1–4, p. 1–16, doi: 10.1016/0009-2541(93)90287-S.

Clauer, N., Fallick, A., and Eberl, D., 2013, K-Ar dating and δ18O-δD characterization of nanometric illite from Ordovician K-bentonites of the Appalachians: Illitization and the Acadian-Alleghenian tectonic activity: American Mineralogist, v. 98, p. 2144–2154.

Clauer, N., O'Neil, J., and Furlan, S., 1995, Clay minerals as records of temperature conditions and duration of thermal anomalies in the Paris Basin, France: Clay Minerals, v. 30, p. 1–13.

Clayton, J.L., and Swetland, P.J., 1980, Petroleum Generation and Migration in Denver Basin: AAPG Bulletin, v. 64, no. 10, p. 1613–1633, doi: 10.1306/C1EA57CE-16C9-11D7-8645000102C1865D.

Cleaves, E.T., Edwards, J.J., Glaser, J.D., and Weaver, K.N., 1968, Geologic Map of Maryland: Geologic Map, Maryland Geological Survey, 2 sheets.

Collettini, C., Niemeijer, A., Viti, C., and Marone, C., 2009, Fault zone fabric and fault weakness: Nature, v. 462, no. 7275, p. 907–910, doi: 10.1038/nature08585.

Collettini, C., Viti, C., Smith, S.A.F., and Holdsworth, R.E., 2009, Development of interconnected talc networks and weakening of continental low-angle normal faults: Geology, v. 37, no. 6, p. 567–570, doi: 10.1130/G25645A.1.

Colten-Bradley, A.A., 1987, Role of pressure in smectite dehydration: Effects on geopressures and smectite-to-illite transformation: American Association of Petroleum Geologists Bulletin, v. 71, p. 1414–1427.

Cooper, A.F., and Norris, R.J., 1994, Antatomy, structural evolution, and slip rate of a plate boundary thrust: The Alpine Fault at Gaunt Creek, Westland, New Zealand: Geological Society of America Bulletin, v. 106, no. May, p. 627--633, doi: 10.1130/0016-7606(1994)106<0627:ASEASR>2.3.CO;2.

Covey, M.C., Vrolijk, P.J., and Pevear, D.R., 1994, Direct dating of fault movement in the rocky mountain front range: Geological Society of America Annual Meeting, Seattle, WA, v. A-467.

Craddock, J., Jackson, M., van der Pluijm, B.A., and Versical, R., 1993, Regional shortening fabrics in eatern North America: far-field stress transmission from the Appalachian-Ouachita orogenic belt: Tectonics, v. 12, no. 1, p. 257–264.

Craw, D., and Campbell, J.R., 2004, Tectonic and structural setting for active mesothermal gold vein systems, Southern Alps, New Zealand: Journal of Structural Geology, v. 26, no. 6–7, p. 995–1005, doi: 10.1016/j.jsg.2003.11.012.

Craw, D., Upton, P., and Mackenzie, D.J., 2009, Hydrothermal alteration styles in ancient and modern orogenic gold deposits, New Zealand: New Zealand Journal of Geology and Geophysics, v. 52, no. 1, p. 11–26, doi: 10.1080/00288300909509874.

Criss, R.E., Taylor, H.P., 1986, Meteoric-hydrothermal systems, in Stable isotopes in high temperature geological processes, Reviews in Mineralogy and Geochemistry, vol. 16, p. 373-424,

Cuadros, J., 2006, Modeling of smectite illitization in burial diagenesis environments: Geochimica et Cosmochimica Acta, v. 70, no. 16, p. 4181–4195, doi: 10.1016/j.gca.2006.06.1372.

Daczko, N.R., Caffi, P., Halpin, J.A., and Mann, P., 2009, Exhumation of the Dayman dome metamorphic core complex, eastern Papua New Guinea: Journal of Metamorphic Geology, v. 27, no. 6, p. 405–422, doi: 10.1111/j.1525-1314.2009.00825.x.

Dalla Torre, M., Stern, W.B., and Frey, M., 1994, Determination of white K-mica polytype ratios: comparison of different XRD methods: Clay Minerals, v. 5, p. 717–726.

Day-Stirrat, R.J., Aplin, A.C., Środoń, J., and van der Pluijm, B.A., 2008, Diagenetic Reorientation of Phyllosilicate Minerals in Paleogene Mudstones of the Podhale Basin, Southern Poland: Clays and Clay Minerals, v. 56, no. 1, p. 100–111, doi: 10.1346/CCMN.2008.0560109.

Day-Stirrat, R.J., Dutton, S.P., Milliken, K.L., Loucks, R.G., Aplin, A.C., Hillier, S., and van der Pluijm, B.A., 2010, Fabric anisotropy induced by primary depositional variations in the silt: clay ratio in two fine-grained slope fan complexes: Texas Gulf Coast and northern North Sea: Sedimentary Geology, v. 226, no. 1–4, p. 42–53, doi: 10.1016/j.sedgeo.2010.02.007.

Day-Stirrat, R.J., Flemings, P.B., You, Y., Aplin, A.C., and van der Pluijm, B.A., 2012, The fabric consolidation in Gulf of Mexico mudstones: Marine Geology, v. 295-298, p. 77-85, doi: 10.1016/j.margeo.2011.12.003.

Day-Stirrat, R.J., Flemings, P.B., You, Y., and van der Pluijm, B.A., 2013, Modification of mudstone fabric and pore structure as a result of slope failure: Ursa Basin, Gulf of Mexico: Marine Geology, v. 341, p. 58–67, doi: 10.1016/j.margeo.2013.05.003.

Day-Stirrat, R.J., Loucks, R.G., Milliken, K.L., Hillier, S., and van der Pluijm, B.A., 2008, Phyllosilicate orientation demonstrates early timing of compactional stabilization in calcite-cemented concretions in the Barnett Shale (Late Mississippian), Fort Worth Basin, Texas (U.S.A): Sedimentary Geology, v. 208, no. 1–2, p. 27–35, doi: 10.1016/j.sedgeo.2008.04.007.

Day-Stirrat, R.J., Schleicher, A.M., Schneider, J., Flemings, P.B., Germaine, J.T., and van der Pluijm, B.A., 2011, Preferred orientation of phyllosilicates: Effects of composition and stress on resedimented mudstone microfabrics: Journal of Structural Geology, v. 33, no. 9, p. 1347–1358, doi: 10.1016/j.jsg.2011.06.007.

de Caritat, P., Hutcheon, I., and Walshe, J.L., 1993, Chlorite geothermometry: A review: Clays and Clay Minerals, v. 41, no. 2, p. 219–239, doi: 10.1346/CCMN.1993.0410210.

De Pascale, G.P., and Langridge, R.M., 2012, New on-fault evidence for a great earthquake in A.D. 1717, central Alpine fault, New Zealand: Geology, v. 40, no. 9, p. 791–794, doi: 10.1130/G33363.1.

Delgado, A., and Reyes, E., 1996, Oxygen and hydrogen isotope compositions in clay minerals: A potential single-mineral geothermometer: Geochimica et Cosmochimica Acta, v. 60, no. 21, p. 4285–4289.

DeMets, C., Gordon, R.G., and Argus, D.F., 2010, Geologically current plate motions: Geophysical Journal International, v. 181, no. 1, p. 1–80, doi: 10.1111/j.1365-246X.2009.04491.x.

Deming, D., and Nunn, J.A., 1991, Numerical simulations of brine migration by topographically driven recharge: Journal of Geophysical Research, v. 96, no. B2, p. 2485–2499.

Deming, D., Nunn, J.A., and Evans, D.G., 1990, Thermal effects of compaction-driven groundwater flow from overthrust belts: Journal of Geophysical Research, v. 95, no. b5, p. 6669, doi: 10.1029/JB095iB05p06669.

Derkowski, A., Drits, V.A., and McCarty, D.K., 2012, Rehydration of dehydrated-dehydroxylated smectite in a low water vapor environment: American Mineralogist, v. 97, no. 1, p. 110–127, doi: 10.2138/am.2012.3872.

Dietel, J., 2015, Mineralogical and chemical properties of thermally treated and ground illitic clays as precursor materials for geopolymer binders: University of Greifswald Dissertation.

Dong, H., Hall, C., Peacor, D., Halliday, A., 1995, Mechanisms of argon retention in clays revealed by laser 40Ar-39Ar dating: Science, v. 267, no. 5196, p. 355-359, DOI: 10.1126/science.267.5196.355

Dong, H., Hall, C.M., Peacor, D.R., Halliday, A.N., and Pevear, D.R., 2000, Thermal 40Ar/39Ar separation of diagenetic from detrital illitic clays in Gulf Coast shales: Earth and Planetary Science Letters, v. 175, p. 309–325, doi: 10.1016/S0012-821X(99)00294-0.

Douglas, R.G., and Woodruff, F., 1981, Deep sea benthic foraminifera, in Emiliani ed., *The Sea vol. 7,* p. 1233–1327, Wiley-Interscience, New York.

Dudek, T., Środoón, J., Eberl, D.D., Elsass, F., and Uhlik, P., 2002, Thickness distribution of illite crystals in shales. I: X-ray diffraction vs. high-resolution transmission electron microscopy measurements: Clays and Clay Minerals, v. 50, no. 5, p. 562–577, doi:

10.1346/000986002320679305.

Elliott, W.C., and Aronson, J.L., 1987, Alleghanian episode of K-bentonite illitization in the southern Appalachian Basin: Geology, v. 15, p. 735-739, doi: 10.1130/0091-7613(1987)15<735.

Engelder, T., 1985, Loading paths to joint propagation during a tectonic cycle: an example from the Appalachian Plateau, U.S.A.: Journal of Structural Geology, v. 7, no. 3–4, p. 459–476, doi: 10.1016/0191-8141(85)90049-5.

Engelder, T., and Lacazette, A., 1990, Natural Hydraulic Fracturing: in Barton, N., and Stephansson, O., eds., *Rock Joints*, A.A. Balkema, Rotterdam, p. 35–44.

Engelder, T., Lash, G.G., and Uzcátegui, R.S., 2009, Joint sets that enhance production from Middle and Upper Devonian gas shales of the Appalachian Basin: AAPG Bulletin, v. 93, no. 7, p. 857–889, doi: 10.1306/03230908032.

Eslinger, E.V., Savin, S.M., 1973, Mineralogy and oxygen isotope geochemistry of the hydrothermally altered rock of the Ohaki Broadlands, New Zealand geothermal area: American Journal of Science, v. 273, p. 240-267.

Eslinger, E.V., Savin, S.M., and Yeh, H.W., 1979, Oxygen isotope geothermometry of diagenetically altered shales: SEPM Special Publications, v. 26, p. 113–124.

Faulkner, D.R., Jackson, C.L., Lunn, R.J., Schlische, R.W., Shipton, Z.K., Wibberley, C.J., and Withjack, M.O., 2010, A review of recent developments concerning the structure, mechanics and fluid flow properties of fault zones: Journal of Structural Geology, v. 32, no. 11, p. 1557–1575, doi: 10.1016/j.jsg.2010.06.009.

Faure, G., and Mensing, T.M., 2005, *Isotopes: principles and applications*: John Wiley & Sons, Inc., Hoboken, New Jersey.

Fichtner, A., Saygin, E., Taymaz, T., Cupillard, P., Capdeville, Y., Trampert, J., 2013, The deep structure of the North Anatolian Fault Zone: Earth and Planetary Science Letters, v. 373, p. 109-117, doi:10.1016/j.epsl.2013.04.027.

Fitz-Diaz, E., and van der Pluijm, B., 2013, Fold dating: A new Ar/Ar illite dating application to constrain the age of deformation in shallow crustal rocks: Journal of Structural Geology, v. 54, p. 174–179, doi: 10.1016/j.jsg.2013.05.011.

Fitz-Díaz, E., Camprubí, A., Cienfuegos-Alvarado, E., Morales-Puente, P., Schleicher, A.M., and van der Pluijm, B.A., 2014, Newly-formed illite preserves fluid sources during folding of shale and limestone rocks; an example from the Mexican Fold-Thrust Belt: Earth and Planetary Science Letters, v. 391, p. 263–273, doi: 10.1016/j.epsl.2013.12.025.

Fitz-Díaz, E., Hall, C., and van der Pluijm, B.A., 2016, XRD-based 40Ar/39Ar age correction for fine-grained illite, with application to folded carbonates in the Monterrey Salient (northern Mexico): Geochimica et Cosmochimica Acta, doi: 10.1016/j.gca.2016.02.004.

Fitz-Diaz, E., Hudleston, P., Siebenaller, L., Kirschner, D., Camprubí, A., Tolson, G., and Puig, T.P., 2011, Insights into fluid flow and water-rock interaction during deformation of carbonate sequences in the Mexican fold-thrust belt: Journal of Structural Geology, v. 33, no. 8, p. 1237–1253, doi: 10.1016/j.jsg.2011.05.009.

Freed, R.L., and Peacor, D.R., 1989, Variability in temperature of the smectite/illite reaction in Gulf Coast sediments: Clay Minerals, v. 24, p. 171– 180, doi:10.1180/claymin.1989.024.2.05.

Frey, H.M., Lange, R.A., Hall, C.M., Delgado-Granados, H., and Carmichael, I.S.E., 2007, A pliocene ignimbrite flare-up along the Tepic-Zacoalco rift: Evidence for the initial stages of rifting between the Jalisco block (Mexico) and North America: Geological Society of America Bulletin, v. 119, no. 1–2, p. 49–64, doi: 10.1130/B25950.1.

Frey, M., 1987, Very low-grade metamorphism of clastic sedimentary rocks, in Frey, M. ed., *Low Temperature Metamorphism*, p. 9–58, Chapman & Hall, New York.

Fricke, H.C., Wickham, S.M., and O'Neil, J.R., 1992, Oxygen and hydrogen isotope evidence for meteoric water infiltration during mylonitization and uplift in the Ruby Mountains-East Humboldt Range core complex, Nevada: Contributions to Mineralogy and Petrology, v. 111, no. 2, p. 203–221, doi: 10.1007/BF00348952.

Friedman, G.M., and Sanders, J.E., 1982, of Devonian anthracite implies former great (~6.5 km) depth of burial of Catskill Mountains , New York: Geology, v. 10, p. 93-96.

Fujita, T., Yoshimi, I., Shibayama, A., Miyazaki, T., Abe, K., Sato, M., Yen, W., and Svoboda, J., 2001, Crushing and Liberation of Materials by Electrical Disintegration: The European Journal of Mineral Processing and Environmental Protection, v. 1, no. 2, p. 113–122.

Fulton, P.M., et al., 2013, Low coseismic friction on the Tohoku-Oki fault determined from temperature measurements: Science, v. 342, p. 1214– 1217, doi:10.1126/science.1243641.

Galfetti, T., Bucher, H., Brayard, A., Hochuli, P.A., Weissert, H., Guodun, K., Atudorei, V., and Guex, J., 2007, Late Early Triassic climate change: Insights from carbonate carbon isotopes, sedimentary evolution and ammonoid paleobiogeography: Palaeogeography, Palaeoclimatology, Palaeoecology, v. 243, no. 3–4, p. 394–411, doi: 10.1016/j.palaeo.2006.08.014.

Garven, G., 1995, Continental-scale groundwater flow and geologic processes: Annual Review of Earth and Planetary Sciences, v. 23, p. 89–117.

Gébelin, A., Mulch, A., Teyssier, C., Chamberlain, C.P., Heizler, M., 2012, Coupled basin detachment systems as paleoaltimetry archives of the western North American Cordillera:

Earth and Planetary Science Letters, vol. 335-336, p. 36-47, doi:10.1016/j.epsl.2012.04.029.

Gorur, N., Monod, O., Okay, A.I., Şengör, A.M.C., Tuysuz, O., Yigitbas, E., Sakinc, M., and Akkok, R., 1997, Palaeogeographic and tectonic position of the Carboniferous rocks of the western Pontides (Turkey) in the frame of the Variscan belt: Bulletin De La Societe Geologique De France, v. 168, no. 2, p. 197–205.

Graham, C.M., 1981, Experimental hydrogen isotope studies III: Diffusion of hydrogen in hydrous minerals, and stable isotope exchange in metamorphic rocks: Contributions to Mineralogy and Petrology, v. 76, no. 2, p. 216–228, doi: 10.1007/BF00371961.

Graham, C.M., Viglino, J.A, and Harmon, R.S., 1987, Experimental study of hydrogen-isotope exchange between aluminous chlorite and water and of hydrogen diffusion in chlorite: American Mineralogist, v. 72, p. 566–579.

Grathoff, G., and Moore, D., 1996, Illite Polytype Quantification Using WILDFIRE Calculated X-ray Diffraction Patterns: Clays and Clay Minerals, v. 44, no. 6, p. 835-842.

Grathoff, G.H., Moore, D.M., Hay, R.L., and Wemmer, K., 2001, Origin of illite in the lower Paleozoic of the Illinois basin: Evidence for brine migrations: Geological Society of America Bulletin, v. 113, no. 8, p. 1092–1104, doi: 10.1130/0016-7606(2001)113<1092:OOIITL>2.0.CO;2.

Gülyüz, E., Kaymakci, N., Meijers, M.J.M., van Hinsbergen, D.J.J., Lefebvre, C., Vissers, R.L.M., Hendriks, B.W.H., and Peynircioğlu, A.A., 2013, Late Eocene evolution of the Çiçekdağı Basin (central Turkey): Syn-sedimentary compression during microcontinent continent collision in central Anatolia: Tectonophysics, v. 602, p. 286–299, doi: 10.1016/j.tecto.2012.07.003.

Haines, S., Lynch, E., Mulch, A., Valley, J.W., and van der Pluijm, B.A., 2016 Meteoric fluid infiltration in crustal-scale normal fault systems as indicated by δ^{18}O and δ^{2}H geochemistry and ^{40}Ar/^{39}Ar dating of neoformed clays in brittle fault rocks: Lithosphere, v. 4, p. L483.1, doi: 10.1130/L483.1.

Haines, S.H., and van der Pluijm, B.A., 2008, Clay quantification and Ar–Ar dating of synthetic and natural gouge: Application to the Miocene Sierra Mazatán detachment fault, Sonora, Mexico: Journal of Structural Geology, v. 30, no. 4, p. 525–538, doi: 10.1016/j.jsg.2007.11.012.

Haines, S.H., and van der Pluijm, B.A., 2012, Patterns of mineral transformations in clay gouge, with examples from low-angle normal fault rocks in the western USA: Journal of Structural Geology, v. 43, p. 2–32, doi: 10.1016/j.jsg.2012.05.004.

Haines, S.H., and van der Pluijm, B.A., 2010, Dating the detachment fault system of the Ruby Mountains, Nevada: Significance for the kinematics of low-angle normal faults: Tectonics,

v. 29, no. 4, p. 1–20, doi: 10.1029/2009TC002552.

Haines, S.H., Kaproth, B., Marone, C., Saffer, D., and van der Pluijm, B.A., 2013, Shear zones in clay-rich fault gouge: A laboratory study of fabric development and evolution: Journal of Structural Geology, v. 51, p. 206-225, doi: 10.1016/j.jsg.2013.01.002.

Hall, C.M., 2013, Direct measurement of recoil effects on 40Ar/39Ar standards, *in* Jourdan, F., Mark, D.F., and Verati, C. eds., *Advances in 40Ar/39Ar Dating: from Archaeology to Planetary Sciences*, Geological Society, London, Special Publications, v. 378.

Hamilton, P.J., 2003, A review of radiometric dating techniques for clay mineral cements in sandstonces: International Association of Sedimentology Special Publications, v. 34, p. 253-287.

Harder, H., 1974, Illite mineral synthesis at surface temperatures: Chemical Geology, 14, no. 4, p. 241–253, doi: 10.1016/0009-2541(74)90062-X.

Harris, A.G., 1979, Conodont color alteration, an organo-mineral metamorphic index and its application to Appalachian Basin geology: SEPM Special Publication No. 26, p. 3–16.

Hatcher, R.D., Thomas, W.A., Viele, G.W., 1989, The Appalachian-Ouachita Orogen in the United States: Geological Society of America Monograph, 767 pages, doi:10.1130/DNAG-GNA-F2.

Hatcher, R., 2010, The Appalachian orogen: A brief summary: Geological Society of America Memoir, v. 206, no. 1, p. 1–19, doi: 10.1130/2010.1206(01).

Hay, R.L., Lee, M., Kolata, D.R., Matthews, J.C., and Morton, J.P., 1988, Episodic potassic diagenesis of Ordovician tuffs in the Mississippi Valley area: Geology, v. 16, no. 8, p. 743, doi: 10.1130/0091-7613(1988)016<0743:EPDOOT>2.3.CO;2.

Hearn, P., Sutter, J., and Belkin, H., 1987, Evidence for Late-Paleozoic brine migration in Cambrian carbonate rocks of the central and southern Appalachians: Implications for Mississippi Valley-type sulfide mineralization: Geochimica et Cosmochimica Acta, v. 51, p. 1323–1334.

Hetzel, R., Zwingmann, H., Mulch, A., Gessner, K., Akal, C., Hampel, A., Güngör, T., Petschick, R., Mikes, T., and Wedin, F., 2013, Spatiotemporal evolution of brittle normal faulting and fluid infiltration in detachment fault systems: A case study from the Menderes Massif, western Turkey: Tectonics, v. 32, no. 3, p. 364–376, doi: 10.1002/tect.20031.

Hickman, S., and Zoback, M., 2004, Stress orientations and magnitudes in the SAFOD pilot hole: Geophysical Research Letters, v. 31, no. 15, doi: 10.1029/2004GL020043.

Hickman, S., Sibson, R., and Bruhn, R., 1995, Introduction to special section : Mechanical involvement of fluids in faulting, Journal of Geophysical Research, v. 100, no. B7, p. 12831-12840, doi: 10.1029/95JB01121.

Hillier, S., 1999, Use of an Air Brush to Spray Dry Samples for X-ray Powder Diffraction: Clay Minerals, v. 34, no. 1, p. 127–135, doi: 10.1180/claymin.1999.034.1.14.

Hillier, S., 2000, Accurate quantitative analysis of clay and other minerals in sandstones by XRD: comparison of a Rietveld and a reference intensity ratio (RIR) method and the importance of sample preparation: Clay Minerals, v. 35, no. 1, p. 291–291, doi: 10.1180/000985500546666.

Hillier, S., 2003, Quantitative analysis of clay and other minerals in sandstones by X-ray powder diffraction (XRPD): International Association of Sedimentology Special Publications, v. 34, p. 213–251.

Hirono, T., Fujimoto, K., Yokoyama, T., Hamada, Y., Tanikawa, W., Tadai, O., Mishima, T., Tanimizu, M., Lin, W., Soh, W., and Song, S.R., 2008, Clay mineral reactions caused by frictional heating during an earthquake: An example from the Taiwan Chelungpu fault: Geophysical Research Letters, v. 35, no. 16, p. 1–6, doi: 10.1029/2008GL034476.

Hnat, J.S., and van der Pluijm, B.A., 2014, Fault gouge dating in the Southern Appalachians, USA: Geological Society of America Bulletin, v. 126, no. 5-6, p. 639-651, doi: 10.1130/B30905.1.

Ho, N.C., Peacor, D.R., and van der Pluijm, B.A., 1995, Reorientation mechanisms of phyllosilicates in the mudstone-to-slate transition at Lehigh Gap, Pennsylvania: Journal of Structural Geology, v. 17, no. 3, p. 345–356, doi: 10.1016/0191-8141(94)00065-8.

Ho, N.C., Peacor, D.R., and Van Der Pluijm, B.A., 1999, Preferred orientation of phyllosilicates in Gulf Coast mudstones and relation to the smectite-illite transition: Clays and Clay Minerals, v. 47, no. 4, p. 495–504, doi: 10.1346/CCMN.1999.0470412.

Ho, N.C., van der Pluijm, B.A., and Peacor, D.R., 2001, Static recrystallization and preferred orientation of phyllosilicates: Michigamme Formation, Northern Michigan, USA: Journal of Structural Geology, v. 23, no. 6–7, p. 887–893, doi: 10.1016/S0191-8141(00)00162-0.

Hoffman, J., Hower, J., and Aronson, J.L., 1976, Radiometric dating of time of thrusting in the disturbed belt of Montana: Geology, v. 4, no. 1, p. 16–20, doi: 10.1130/0091-7613(1976)4<16:RDOTOT>2.0.CO;2.

Holdsworth, R., 2004, Weak Faults — Rotten Cores: Science, v. 303, no. January, p. 181–182, doi: 10.1126/science.1092491.

Howell, P.D., and van der Pluijm, B.A., 1999, Structural sequences and styles of subsidence in the Michigan Basin: Geological Society of America Bulletin, v. 111, p. 974-991.

Hower, J., and Mowatt, T.C., 1966, The mineralogy of illites and mixed-layer illite/montmorillonites: American Mineralogist, v.51, p.825-854.

Hower, J., Eslinger, E.V., Hower, M.E., and Perry, E., 1976, Mechanism of burial metamorphism of argillaceous sediment: 1. Mineralogical and chemical evidence, Geological Society of America Bulletin, v. 87, p. 725–737, doi: 10.1130/00167606(1976)87<725.

Hower, J., Hurley, P.M., Pinson, W.H., and Fairbairn, H.W., 1963, The dependence of K-Ar age on the mineralogy of various particle size ranges in a shale: Geochimica et Cosmochimica Acta, 27, no. 38, p. 405–410, doi: 10.1016/0016-7037(63)90080-2.

Huang, W., Bassett, W.A., and Wu, T., 1994, Dehydration and hydration of montmorillonite at elevated temperatures and pressures monitored using synchrotron radiation: American Mineralogist, v. 79, p. 683–691.

Huang, W., Longo, J., and Pevear, D., 1993, An experimentally derived kinetic model for smectite-to-illite conversion and its use as a geothermometer: Clays and Clay Minerals, v. 41, no. 2, p. 162–177.

Ikari, M.J., Carpenter, B.M., Kopf, A.J., and Marone, C., 2014, Frictional strength, rate-dependence, and healing in DFDP-1 borehole samples from the Alpine Fault, New Zealand: Tectonophysics, p. 1–8, doi: 10.1016/j.tecto.2014.05.005.

Ikari, M.J., Saffer, D.M., and Marone, C., 2009, Frictional and hydrologic properties of clay-rich fault gouge: Journal of Geophysical Research: Solid Earth, v. 114, no. 5, p. 1–18, doi: 10.1029/2008JB006089.

Inoue, A., Meunier, A., Patrier-Mas, P., Rigault, C., Beaufort, D., and Vieillard, P., 2009, Application of chemical geothermometry to low-temperature trioctahedral chlorites: Clays and Clay Minerals, v. 57, no. 3, p. 371–382, doi: 10.1346/CCMN.2009.0570309.

Jacob, G., Kisch, H.J., and Van Der Pluijm, B.A., 2000, The relationship of phyllosilicate orientation, X-ray diffraction intensity ratios, and c/b fissility ratios in metasedimentary rocks of the Helvetic zone of the Swiss Alps and the Caledonides of Jamtland, central western Sweden: Journal of Structural Geology, v. 22, no. 2, p. 245–258, doi: 10.1016/S0191-8141(99)00149-2.

Jenkins, R., and Snyder, R. (1996) *Introduction to X-ray Powder Diffraction*: Wiley, New York.

Kameda, J., Shimizu, M., Ujiie, K., Hirose, T., Ikari, M., Mori, J., Oohashi, K., and Kimura, G., 2015, Pelagic smectite as an important factor in tsunamigenic slip along the Japan Trench: Geology, v. 43, p. 155–158, doi:10.1130/G35948.1.

Kamp, P.J.J., 1986, Late Cretaceous-Cenozoic tectonic development of the southwest pacific region: Tectonophysics, v. 121, no. 2–4, p. 225–251, doi: 10.1016/0040-1951(86)90045-4.

Kaufhold, S., Hein, M., Dohrmann, R., and Ufer, K., 2012, Quantification of the mineralogical composition of clays using FTIR spectroscopy: Vibrational Spectroscopy, v. 59, p. 29–39, doi: 10.1016/j.vibspec.2011.12.012.

Kim, J., Peacor, D., Tessier, D., and Elsass, F., 1995, A technique for maintaining texture and permanent expansion of smectite interlayers for TEM observations: Clays and Clay Minerals, v. 43, no. 1, p. 51-57.

Kirkpatrick, J.D., et al., 2015, Structure and lithology of the Japan Trench subduction plate boundary fault: Tectonics, v. 34, p. 53–69, doi: 10.1002/2014TC003695.

Kleeberg, R., 2009, State-of-the-art and trends in quantitative phase analysis of geological and raw materials: European Powder Diffraction Conference, EPDIC 11, doi: 10.1524/zksu.2009.0007.

Knipe, R.J., and McCaig, A.M., 1994, Microstructural and microchemical consequences of fluid flow in deforming rocks: Geological Society, London, Special Publications, v. 78, no. 1, p. 99–111, doi: 10.1144/GSL.SP.1994.078.01.09.

Koons, P., Norris, R., Craw, D., and Cooper, A., 2003, Influence of exhumation on the structural evolution of transpressional plate boundaries: An example from the Southern Alps, New Zealand: Geology, v. 31, no. 1, p. 3–6, doi: 10.1130/0091-7613(2003)031<0003.

Kuo, L.W., Song, S.R., Yeh, E.C., Chen, H.F., 2009, Clay mineral anomalies in the fault zone of the Chelungpu Fault, Taiwan, and their implications: Geophysical Research Letters, v. 36, no. 18, p. 2-7, doi:10.1029/2009GL039269.

Kuo, L.W., Song, S.R., Huang, L., Yeh, E.C., and Chen, H.F., 2011, Temperature estimates of coseismic heating in clay-rich fault gouges, the Chelungpu fault zones, Taiwan: Tectonophysics, v. 502, no. 3–4, p. 315–327, doi: 10.1016/j.tecto.2011.02.001.

Kyser, T.K., Kerrich, R., 1991, Retrograde exchange of hydrogen isotopes between hydrous minerals and water at low temperatures: *in* Taylor, Jr., H.P., O'Neil, J.R., and Kaplan, I.R., (eds.), Stable Isotope Geochemistry: A Tribute to Samuel Epstein, Geochemical Society Special Publication No. 3.

Lacroix, B., Charpentier, D., Buatier, M., Vennemann, T., Labaume, P., Adatte, T., Travé, A., and Dubois, M., 2012, Formation of chlorite during thrust fault reactivation. Record of fluid origin and P–T conditions in the Monte Perdido thrust fault (southern Pyrenees): Contributions to Mineralogy and Petrology, v. 163, no. 6, p. 1083–1102, doi: 10.1007/s00410-011-0718-0.

Laubach, S.E., Eichhubl, P., Hilgers, C., and Lander, R.H., 2010, Structural diagenesis: Journal of Structural Geology, v. 32, no. 12, p. 1866–1872, doi: 10.1016/j.jsg.2010.10.001.

Lawrence, J.R., and Taylor, H.P.J., 1972, Hydrogen and oxygen isotope systematics in weathering profiles: Geochimica et Cosmochimica Acta, v. 36, no. 12, p. 1377–1393, doi: 10.1016/0016-

7037(72)90068-3.

Lay, T., Fujii, Y., Geist, E., Koketsu, K., Rubinstein, J., Sagiya, T., and Simons, M., 2013, Introduction to the special issue on the 2011 Tohoku earthquake and tsunami: Seismological Society of America Bulletin, v. 103, p. 1165–1170, doi: 10.1785 /0120130001.

Leach, D.L., Bradley, D., Lewchuk, M.T., Symons, D.T.A., De Marsily, G., and Brannon, J., 2001, Mississippi Valley-type lead-zinc deposits through geological time: Implications from recent age-dating research: Mineralium Deposita, v. 36, no. 8, p. 711–740, doi: 10.1007/s001260100208.

Leitner, B., Eberhart-Phillips, D., Anderson, H., and Nabelek, J., 2001, A focused look at the Alpine fault, New Zealand: Seismicity, focal mechanisms, and stress observations: Journal of Geophysical Research, v. 106, no. B2, p. 2193–2220.

Leveille, G.P., Knipe, R., More, C., 1997, Compartmentalization of Rotliegendes gas reservoirs by sealing faults, Jupiter Fields area, southern North Sea. In: Ziegler, K., Turner, P. & Daines S.R (eds) *Petroleum Geology of the Southern North Sea; Future Potential,* Geological Society, London, Special Publications, vol. 123, p. 87–104, doi: 10.1144/GSL.SP.1997.123.01.06.

Liewig, N., Clauer, N., and Sommer, F., 1987, Rb-Sr and K-Ar Dating of Clay Diagenesis in Jurassic Sandstone Oil Reservoir, North Sea: American Association of Petroleum Geologists Bulletin, v. 71, no. 12, p. 1467–1474.

Little, T.A., Hacker, B.R., Gordon, S.M., Baldwin, S.L., Fitzgerald, P.G., Ellis, S., and Korchinski, M., 2011, Diapiric exhumation of Earth's youngest (UHP) eclogites in the gneiss domes of the D'Entrecasteaux Islands, Papua New Guinea: Tectonophysics, v. 510, no. 1–2, p. 39–68, doi: 10.1016/j.tecto.2011.06.006.

Lockner, D.A., Morrow, C., Moore, D., and Hickman, S., 2011, Low strength of deep San Andreas fault gouge from SAFOD core: Nature, v. 472, no. 7341, p. 82–85, doi: 10.1038/nature09927.

López, D., and Smith, L., 1995, Fluid flow in fault zones: analysis of the interplay of convective circulation and topographically driven groundwater flow: Water Resources Research, v. 31, no. 6, p. 1489–1503.

Lu, G., Mccabe, C., Hanor, J.S., and Ferrell, R.E., 1991, A genetic link between remagnetization and potassic metasomatism in the Devonian Onondaga Formation, Northern Appalachian Basin: Geophysical Research Letters, v. 18, no. 11, p. 2047–2050.

Lüdecke, T., Mikes, T., Rojay, B., Cosca, M., Mulch, A., 2013, Oligo-Miocene paleoenvironment and paleohydrology of Central Anatolian lake basins, Turkish Journal of Earth Sciences, vol. 22, p. 793-819, doi:10.3906/yer-1207-11.

Lund-Snee, J.E., Toy, V.G., and Gessner, K., 2014, Significance of brittle deformation in the footwall of the Alpine Fault, New Zealand: Smithy Creek Fault zone: Journal of Structural Geology, v. 64, p. 79–98, doi: 10.1016/j.jsg.2013.06.002.

Maden, N., Aydin, A., Kadirov, F., 2014, Determination of the crustal and thermal structure of the Erzurum-Horasan-Pasinler Basins (Eastern Türkiye) using gravity and magnetic data: Pure and Applied Geophysics, doi:10.1007/s00024-014-1001-x.

Mahon, K., 1996, The New "York" regression: Application of an improved statistical method to geochemistry: International Geology Review, v. 38, p. 293–303.

Mancktelow, N., Zwingmann, H., Campani, M., Fügenschuh, B., Mulch, A., 2015, Timing and conditions of brittle faulting on the Silltal-Brenner Fault Zone, Eastern Alps (Austria): Swiss Journal of Geosciences, v. 108, p. 305-326, doi: 10.1007/s00015-015-0179-y.

Mann, U., and Mueller, G., 1980, Composition of sediments of the Japan Trench Transect, Legs 56 and 57, Deep Sea Drilling Project: in Scientific Party, Initial reports of the Deep Sea Drilling Project, Volume 56, 57: Washington, D.C., U.S. Government Printing Office, p. 939–977, doi: 10.2973/dsdp.proc.5657.133.1980.

Manning, E.B., and Elmore, R.D., 2012, Rock magnetism and identification of remanence components in the Marcellus Shale, Pennsylvania: Geological Society, London, Special Publications, v. 371, no. 1, p. 271–282, doi: 10.1144/SP371.9.

Marshak, S., Karlstom, K., and Timmons, J.M., 2000, Inversion of proterozoic extensional faults: An explanation for the pattern of Laramide and Ancestral rockies intracratonic deformation, United States: Geology, v. 28, no. 8, p. 735–738, doi: 10.1130/0091-7613(2000)28<735:IOPEFA>2.0.CO;2.

Matenaar, I.F., 2002, Compaction and microfabric rearrangement of fine-grained siliciclastic sediments: PhD Thesis, University of Newcastle-Upon-Tyne, UK, p. 253 pp.

Mathews, W.H., 1975, Cenozoic erosion and erosion surfaces of eastern North America: American Journal of Science, v. 275, p. 818–824, doi: 10.2475/ajs.275.7.818.

Maxwell, D.T., and Hower, J., 1967, High-grade diagenesis and low-grade metamor-phism of illite in the precambrian belt series: The American Mineralogist, v.52, no. 1955, p. 843–857.

Mazzini, I., Hudackova, N., Joniak, P., Kovacova, M., Mikes, T., Mulch, A., Rojay, B., Lucifora, S., Esu, D., Soulie-Märsche, I., 2013, Palaeoenvironmental And Chronological Constraints On The Tuğlu Formation (Çankırı Basin, Central Anatolia, Turkey): Turkish Journal of Earth Sciences, vol. 22, p. 747-777, DOI: 10.3906/yer-1207-10.

McCabe, C., Jackson, M., and Saffer, B., 1989, Regional Patterns of Magnetite Authigenesis in the Appalachian Basin: Implications for the Mechanism of Late Paleozoic Remagnetization: Journal of Geophysical Research, v. 94, no. B8, p. 429–443.

McCaig, A., 1997, The geochemistry of volatile fluid flow in shear zones, *in* Holness, M.B. ed., Deformation-Enhanced Fluid Transport in the Earth's Crust and Mantle, Mineral. Soc. Ser. vol. 8, Chapman & Hall, London, p. 227–266.

Meunier, A., and Velde, B., 2004, Thermodynamic Stability of Illite, *in Illite: Origins, Evolution and Metamorphism*, Springer-Verlag, Berlin Heidelberg, p. 40–48.

Middleton, G. V., 1973, Johannes Walther's Law of the Correlation of Facies: Bulletin of the Geological Society of America, v. 84, no. 3, p. 979–988, doi: 10.1130/0016-7606(1973)84<979:JWLOTC>2.0.CO;2.

Miller, J.D., and Kent, D.V., 1988, Regional trends in the timing of Alleghenian remagnetization in the Appalachians: Geology, v. 16, p. 588–591.

Mitra, S., 1987, Regional variations in deformation mechanisms and structural styles in the central Appalachian orogenic belt: Geological Society of America Bulletin, v. 98, no. 5, p. 569–590, doi: 10.1130/0016-7606(1987)98<569:rvidma>2.0.co;2.

Molnar, P., 1988, Continental tectonics in the aftermath of plate tectonics: Nature, v. 335, no. 6186, p. 131–137, doi: 10.1038/335131a0.

Momper, J.A., 1978, Oil Migration Limitations Suggested by Geological and Geochemical Considerations: AAPG Short Courses, v. 34, p. T.1-60.

Moore, D.E., and Rymer, M.J., 2007, Talc-bearing serpentinite and the creeping section of the San Andreas fault.: Nature, v. 448, no. 7155, p. 795–797, doi: 10.1038/nature06064.

Moore, D.M., and Reynolds, R.C., Jr., 1997, *X-ray diffraction and the identification and analysis of clay minerals* (second edition): New York, Oxford University Press, 378 p.

Moore, J.C., and Saffer, D., 2001, Updip limit of the seismogenic zone beneath the accretionary prism of Southwest Japan: An effect of diagenetic to low-grade metamorphic processes and increasing effective stress: Geology, v. 29, no. 2, p. 183–186, doi: 10.1130/0091-7613(2001)029<0183:ULOTSZ>2.0.CO;2.

Morad, S., Worden, R., and Ketzer, J., 2003, Oxygen and hydrogen isotopic composition of diagenetic clay minerals in sandstones: a review of the data and controls: International Association of Sedimentology Special Publications, v. 34, p. 63–91, doi: 10.1002/9781444304336.ch3.

Morgan, W.J., 1968, Rises, Trenches, Great Faults and Crustal Blocks: Tectonophysics, v. 73, no. 6, p. 1959–1982, doi: 10.1016/0040-1951(91)90408-K.

Mori, J., Chester, F.M., Eguchi, N., and Toczko, S., 2012, Integrated Ocean Drilling Program Expedition 343 Scientific Prospectus: Japan Trench Fast Earthquake Drilling Project

(JFAST): Integrated Ocean Drilling Program Management International, Inc., doi:10.2204/iodp.sp.343.2012.

Morrow, C.A., Shi, L.Q., and Byerlee, J.D., 1982, Strain hardening and strength of clay-rich fault gouges: Journal of Geophysical Research, v. 87, no. B8, p. 6771, doi: 10.1029/JB087iB08p06771.

Muir-Wood, R., 1994, Earthquakes, strain-cycling and the mobilization of fluids, in Parnell, J. (ed.) Geofluids: Origin, Migration and Evolution of Fluids in Sedimentary Basins, Geological Society Special Publication No. 78, p. 85–98.

Mulch, A., and Chamberlain, C.P., 2007, Stable Isotope Paleoaltimetry in Orogenic Belts The Silicate Record in Surface and Crustal Geological Archives: Reviews in Mineralogy and Geochemistry, v. 66, no. 1, p. 89–118, doi: 10.2138/rmg.2007.66.4.

Mulch, A., Teyssier, C., Cosca, M.A., Vennemann, T.W., 2006, Thermomechanical analysis of strain localization in a ductile detachment zone: Journal of Geophysical Research: Solid Earth, v. 111, B12405, doi:10.1029/2005jb004032.

Mulch, A., Teyssier, C., Cosca, M.A., Vanderhaeghe, O., and Vennemann, T.W., 2004, Reconstructing paleoelevation in eroded orogens: Geology, v. 32, no. 6, p. 525, doi: 10.1130/G20394.1.

Mutlu, H., Uysal, T.I., Altunel, E., Karabacak, V., Feng, Y., Zhao, J., and Atalay, O., 2010, Rb–Sr systematics of fault gouges from the North Anatolian Fault Zone (Turkey): Journal of Structural Geology, v. 32, no. 2, p. 216–221, doi: 10.1016/j.jsg.2009.11.006.

Neprochnov, Y.P., Levchenko, O. V., Merklin, L.R., and Sedov, V.V., 1988, The structure and tectonics of the intraplate deformation area in the Indian Ocean: Tectonophysics, v. 156, no. 1–2, doi: 10.1016/0040-1951(88)90285-5.

Nickelsen, R.P., and Hough, V.N., 1967, Jointing in the Appalachian Plateau of Pennsylvania: Geological Society of America Bulletin, v. 78, p. 609–630.

Norris, R.J., and Cooper, A.F., 1997, Erosional control on the structural evolution of a transpressional thrust complex on the Alpine fault, New Zealand: Journal of Structural Geology, v. 19, no. 10, p. 1323–1342, doi: 10.1016/S0191-8141(97)00036-9.

Norris, R.J., and Cooper, A.F., 2000, Late Quaternary slip rates and slip partitioning on the Alpine Fault, New Zealand: Journal of Structural Geology, v. 23, no. 2–3, p. 507–520, doi: 10.1016/S0191-8141(00)00122-X.

Norris, R.J., and Cooper, A.F., 2007, The Alpine Fault, New Zealand: Surface Geology and Field Relationships: A Continental Plate Boundary: Tectonics at South Island, New Zealand, p. 157–175, doi: 10.1029/175GM09.

Nunn, A., Deming, D., 1991, Thermal constraints on basin-scale flow systems: Geophysical Research Letters, v. 18, no. 5, p. 967–970.

O'Brien, T.M., van der Pluijm, B.A., 2012, Timing of Iapetus Ocean rifting from Ar geochronology of pseudotachylytes in the St. Lawrence rift system of southern Quebec: Geology, v. 40, no. 5, p. 443–446, doi: 10.1130/G32691.1.

Okay, A., 1989, Tectonic Units and Sutures in the Pontides, Northern Turkey in Şengör, A.M.C. (ed.) *Tectonic Evolution of the Tethyan Region,* p. 109-116, Kluwer Academic Publishers.

Okay, A.I., Şengör, A.M.C., Gorur, N., 1994, Kinematic history of the opening of the Black Sea and its effect on the surrounding regions: Geology v. 22, p. 267-270.

Oliver, J., 1986, Fluids expelled tectonically from orogenic belts: Their role in hydrocarbon migration and other geologic phenomena, Geology, v. 14, no. 2, p. 99–102, doi: 10.1130/0091-7613(1986)14<99:FETFOB>2.0.CO;2.

Ollier, C.D., and Pain, C.F., 1980, Actively rising surficial gneiss domes in Papua New Guinea: Journal of the Geological Society of Australia, v. 27, no. 1–2, p. 33–44, doi: 10.1080/00167618008729116.

Olsen, P.E., 1997, Stratigraphic Record of the Early Mesozoic Breakup of Pangea in the Laurasia-Gondwana Rift System: Annual Review of Earth and Planetary Sciences, v. 25, no. 1, p. 337–401, doi: 10.1146/annurev.earth.25.1.337.

Omotoso, O., McCarty, D.K., Hillier, S., and Kleeberg, R., 2006, Some successful approaches to quantitative mineral analysis as revealed by the 3rd reynolds cup contest: Clays and Clay Minerals, v. 54, no. 6, p. 748–760, doi: 10.1346/CCMN.2006.0540609.

Pană, D.I., and van der Pluijm, B.A., 2014, Orogenic pulses in the Alberta Rocky Mountains: Radiometric dating of major faults and comparison with the regional tectono-stratigraphic record: Bulletin of the Geological Society of America, v. 127, no. 3–4, p. 480–502, doi: 10.1130/B31069.1.

Passchier, C.W., and Trouw, R.A.J., 2005, *Microtectonics*: Springer, New York.

Peacor, D.R., Bauluz, B., Dong, H., Tillick, D., and Yan, Y., 2002, Transmission and analytical electron microscopy evidence for high Mg contents of 1M illite: Absence of 1M polytypism in normal prograde diagenetic sequences of pelitic rocks: Clays and Clay Minerals,v. 50, no. 6, p. 757–765, doi: 10.1346/000986002762090281.

Perry, E.A., and Hower, J., 1970, Burial diagenesis in Gulf Coast politic sediments: Clays and Clay Minerals, v. 18, p. 165–177, doi:10.1346 /CCMN .1970 .0180306.

Person, M., Mulch, A., Teyssier, C., and Gao, Y., 2007, Isotope transport and exchange within metamorphic core complexes: American Journal of Science, v. 307, no. 3, p. 555-589, doi:10.2475/03.2007.01.

Person, M., and Baumgartner, L., 1995, New evidence for long-distance fluid migration within the Earth's crust: Reviews of Geophysics, v. 33, no. 2S, p. 1083–1091, doi: 10.1029/95RG00254.

Pevear, D.R., 1992, Illite age analysis, a new tool for basin thermal history analysis, *in* Kharaka, Y. and Maest, A. eds., *Water-Rock Interaction*, A.A. Balkema, Rotterdam, p. 1251–1254.

Pevear, D.R., 1999, Illite and hydrocarbon exploration: Proceedings of the National Academy of Sciences of the United States of America, v. 96, no. 7, p. 3440–6, doi: 10.1073/pnas.96.7.3440.

Peyser, C.E., and Poulsen, C.J., 2008, Controls on Permo-Carboniferous precipitation over tropical Pangaea: A GCM sensitivity study: Palaeogeography, Palaeoclimatology, Palaeoecology, v. 268, no. 3–4, p. 181–192, doi: 10.1016/j.palaeo.2008.03.048.

Pollastro, R.M., 1985, Mineralogical and Morphological Evidence for the Formation of Illite at the Expense of Illite/Smectite: Clays and Clay Minerals, v. 33, no. 4, p. 265–274, doi: 10.1346/CCMN.1985.0330401.

Pollastro, R.M., 1993, Considerations and applications of the illite/smectite geothermometer in hydrocarbon-bearing rocks of Miocene to Mississippian age: Clays and Clay Minerals, v. 41, no. 2, p. 119–133.

Poppe, L., Paskevich, V., Hathaway, J., and Blackwood, D., 2001, A Laboratory Manual for X-ray Powder Diffraction: U.S. Geological Survey Open File Report 01-041.

Poulsen, C.J., Pollard, D., Montañez, I.P., and Rowley, D., 2007, Late Paleozoic tropical climate response to Gondwanan deglaciation: Geology, v. 35, no. 9, p. 771–774, doi: 10.1130/G23841A.1.

Preto, N., Kustatscher, E., and Wignall, P.B., 2010, Triassic climates - State of the art and perspectives: Palaeogeography, Palaeoclimatology, Palaeoecology, v. 290, no. 1–4, p. 1–10, doi: 10.1016/j.palaeo.2010.03.015.

Quinlan, G.M., and Beaumont, C., 1984, Appalachian thrusting, lithospheric flexure, and the Paleozoic stratigraphy of the Eastern Interior of North America: Canadian Journal of Earth Sciences, v. 21, no. 9, p. 973–996, doi: 10.1139/e84-103.

Rayleigh, Lord, 1896, Theoretical considerations respecting the separation of gases by diffusion and similar processes: The London, Edinburgh, and Dublin Philosophical Magazine and Journal of Science, v. 42, no. 259, p. 493–498, doi: 10.1080/14786449608620944.

Reed, J.S., Spotila, J.A., Eriksson, K.A., and Bodnar, R.J., 2005, Burial and exhumation history of

Pennsylvanian strata, central Appalachian basin: An integrated study: Basin Research, v. 17, no. 2, p. 259–268, doi: 10.1111/j.1365-2117.2005.00265.x.

Reynolds, R.C., and Thomson, C.H. (1993) Illite from the potsdam sandstone of New York: A probable noncentrosymmetric mica structure: Clays and Clay Minerals, v. 41, no. 1, p. 66–72, doi: 10.1346/CCMN.1993.0410107.

Reynolds, R.C.J., 1993, WILDFIRE- A computer program for the calculation of three-dimensional powder X-ray diffraction patters for mica polytypes and their disordered variations.

Rice, J.R., 2006, Heating and weakening of faults during earthquake slip: Journal of Geophysical Research, v. 111, B05311, doi: 10.1029 /2005JB004006.

Rietveld, H.M., 1967, Line profiles of neutron powder-diffraction peaks for structure refinement: Acta Crystallographica, v. 22, no. 1, p. 151–152, doi: 10.1107/S0365110X67000234.

Rietveld, H.M., 1969, A profile refinement method for nuclear and magnetic structures: Journal of Applied Crystallography, v. 2, no. 2, p. 65–71, doi: 10.1107/S0021889869006558.

Roaldset, E., Wei, H., and Grimstad, S., 1998, Smectite to illite conversion by hydrous pyrolysis: Clay Minerals, v. 33, no. 1, p. 147–158, doi: 10.1180/000985598545336.

Rogers, K.M., Wassenaar, L.I., Soto, D.X., and Bartle, J.A., 2012, A feather-precipitation hydrogen isoscape model for New Zealand: implications for eco-forensics: Ecosphere, v. 3, no. 7, p. 1-13, doi: 10.1890/ES11-00343.1.

Rozanski, K., Araguás-Araguás, L., and Gonfiantini, R., 1993, Isotopic Patterns in Modern Global Precipitation: *in* Climate Change in Continental Isotopic Records, American Geophysical Union Monographs, v. 78, , p. 1–36, doi: 10.1029/GM078p0001.

Ryder, R.T., Crangle, R.D., Trippi, M.H., Swezey, C.S., Lentz, E.E., Rowan, E.L., and Hope, R.S., 2009, Geologic cross section D–D’ through the Appalachian basin from the Findlay arch, Sandusky County, Ohio, to the Valley and Ridge province, Hardy County, West Virginia: U.S. Geological Survey Scientific Investigations Map 3067, 2 sheets, no. 52– pamphlet.

Sacks, J.S., Suyehiro, K., and Acton, G.D., 2000, Proceedings of the Ocean Drilling Program, Initial reports, Volume 186: College Station, Texas, Ocean Drilling Program, doi:10.2973/odp.proc.ir .186.2000.

Saffer, D.M., and Marone, C., 2003, Comparison of smectite- and illite-rich gouge frictional properties: application to the updip limit of the seismogenic zone along subduction megathrusts: Earth and Planetary Science Letters, v. 215, no. 1–2, p. 219–235, doi: 10.1016/S0012-821X(03)00424-2.

Saffer, D.M., Frye, K.M., Marone, C., and Mair, K., 2001, Laboratory results indicating complex and potentially unstable frictional behavior of smectite clay: Geophysical Research Letters,

v. 28, no. 12, p. 2297–2300, doi: 10.1029/2001GL012869.

Samson, S.D., and Alexander, E.C., 1987, Calibration of the interlaboratory 40Ar39Ar dating standard, MMhb-1: Chemical Geology: Isotope Geoscience Section, v. 66, no. 1–2, p. 27–34, doi: 10.1016/0168-9622(87)90025-X.

Satir, M., and Taubald, H., 2001, Hydrogen and oxygen isotope evidence for fluid-rock interactions in the Menderes massif, western Turkey, International Journal of Earth Sciences, v. 89, no. 4, p. 812–821, doi: 10.1007/s005310000135.

Savin, S., Epstein, S., 1970, The oxygen and hydrogen isotope geochemistry of clay minerals: Geochimica et Cosmochimica Acta, v. 34, no. 1540.

Schedl, A., 1992, Non-Darcian fluid flow during the Alleghenian Orogeny: Earth and Planetary Science Letters, v. 113, p. 511–519.

Schedl, A., McCabe, C., Montanez, I., Fullagar, P.D., and Valley, J.W., 1993, Alleghenian regional diagenesis: A response to the migration of modified metamorphic fluids derived from beneath the Blue Ridge-Piedmont thrust sheet: The Journal of Geology, v. 100, no. 3, p. 339–352.

Schemmel, F., Mikes, T., Rojay, B., and Mulch, a., 2013, The impact of topography on isotopes in precipitation across the Central Anatolian Plateau (Turkey): American Journal of Science, v. 313, no. 2, p. 61–80, doi: 10.2475/02.2013.01.

Schleicher, A.M., Boles, A., and van der Pluijm, B.A., 2015a, Response of natural smectite to seismogenic heating and potential implications for the 2011 Tohoku earthquake in the Japan Trench: Geology, v. 43, no. 9, p. G36846.1, doi: 10.1130/G36846.1.

Schleicher, A.M., van der Pluijm, B.A., Solum, J.G., Warr, L.N., 2006, Origin and significance of clay-coated fractures in mucrock fragments of the SAFOD borehole (Parkfield, California): Geophysical Research Letters, v. 33, no. 16, p. L16313, doi:10.1029/2006GL026505.

Schleicher, A.M., van der Pluijm, B.A., and Warr, L.N., 2010, Nanocoatings of clay and creep of the San Andreas fault at Parkfield, California: Geology, v. 38, no. 7, p. 667–670, doi: 10.1130/G31091.1.

Schleicher, A.M., van der Pluijm, B.A., and Warr, L.N., 2012, Chlorite-smectite clay minerals and fault behavior: New evidence from the San Andreas Fault Observatory at Depth (SAFOD) core: Lithosphere, v. 4, no. 3, p. 209–220, doi: 10.1130/L158.1.

Schleicher, A.M., Warr, L.N., and van der Pluijm, B.A., 2008, On the origin of mixed-layered clay minerals from the San Andreas Fault at 2.5–3 km vertical depth (SAFOD drillhole at Parkfield, California): Contributions to Mineralogy and Petrology, v. 157, no. 2, p. 173–187, doi: 10.1007/s00410-008-0328-7.

Schleicher, A.M., Sutherland, R., Townend, J., Toy, V.G., and van der Pluijm, B.A., 2015b, Clay mineral formation and fabric development in the DFDP-1B borehole, central Alpine Fault, New Zealand: New Zealand Journal of Geology and Geophysics, v. 58, no. 1, p. 13–21, doi: 10.1080/00288306.2014.979841.

Schleicher, A.M., Tourscher, S.N., van der Pluijm, B.A., and Warr, L.N., 2009, Constraints on mineralization, fluid-rock interaction, and mass transfer during faulting at 2–3 km depth from the SAFOD drill hole: Journal of Geophysical Research, v. 114, no. B4, p. 1–12, doi: 10.1029/2008JB006092.

Scholz, C., 1987, Wear and gouge formation in brittle faulting: Geology, v. 15, p. 493-495, doi: 10.1130/0091-7613(1987)15<493.

Scotese, C.R., Van der Voo, R., McCabe, C., 1982, Paleomagnetism of the Upper Silurian and Lower Devonian carbonates of New York State: evidence for secondary magnetizations residing in magnetite: Physics of the Earth and Planetary Interiors, v. 30, no. 4, p. 385–395, doi: 10.1016/0031-9201(82)90048-6.

Şengör, A.M.C., Yilmaz, Y., and Sungurlu, O., 1984, Tectonics of the Mediterranean Cimmerides: nature and evolution of the western termination of Palaeo-Tethys: Geological Society, London, Special Publications, v. 17, no. 1, p. 77–112, doi: 10.1144/GSL.SP.1984.017.01.04.

Şengör, A.M.C., 1985, Strike-slip faulting and related basin formation in zones of tectonic escape: Turkey as a case study: SEPM Special Publications, no. 37, p. 227–264.

Şengör, A.M.C., Yilmaz, Y., 1981, Tethyan evolution of Turkey: a plate tectonic approach: Tectonophysics, v. 75, doi: 10.1016/0040-1951(81)90275-4.

Şengör, A.M.C., Grall, C., İmren C., Le Pichon, X., Görür, N., Henry, P., Karabulut, H., Siyako, M., 2014, The geometry of the North Anatolian transform fault in the Sea of Marmara and its temporal evolution: implications for the development of intracontinental transform faults: Canadian Journal of Earth Sciences, v. 51, p. 222-242, doi: 10.1139/cjes-2013-0160.

Şengör, A.M.C., Natal'in, B.A., 1996, Palaeotectonics of Asia: Fragments of a synthesis: in Yin, A., Harrison, M., (eds.) *The Tectonic Evolution of Asia*, Rubey Colloquium, pp. 486 640, Cambridge: Cambridge Univ. Press.

Şengör, A.M.C., Tüysüz, O., İmren, C., Sakınç, M., Eyidoğan, H., Görür, N., Le Pinchon, X., Rangin, C., 2005, The North Anatolian Fault: A New Look, Annual Review of the Earth and Planetary Sciences, vol. 33, p. 37-112, doi: 10.1146/annurev.earth.32.101802.120415.

Sheppard, S., and Gilg, H., 1996, Stable isotope geochemistry of clay minerals: Clay Minerals, v. 31, p. 1–24.

Sheppard, S., Nielsen, R., and Taylor, H., 1969, Oxygen and hydrogen isotope ratios of clay minerals from porphyry copper deposits: Economic Geology, v. 64, p. 755–777.

Sheppard, S.M.F., 1986, Characterization and isotopic variations in natural waters: Review in Mineralogy, v. 16, p. 165–184.

Sheppard, Simon M.F., 1986, Characterization and isotopic variations in natural waters, Reviews in Mineralogy and Geochemistry, vol. 16, p. 165-183.

Shi, Y., Allis, R., and Davey, F., 1996, Thermal modeling of the Southern Alps, New Zealand: Pure and Applied Geophysics, v. 146, no. 3–4, p. 469–501, doi: 10.1007/BF00874730.

Si, J., Li, H., Kuo, L., Pei, J., Song, S., and Wang, H., 2014, Clay mineral anomalies in the Yingxiu-Beichuan fault zone from the WFSD-1 drilling core and its implication for the faulting mechanism during the 2008 Wenchuan earthquake (Mw 7.9): Tectonophysics, v. 619–620, p. 171–178, doi: 10.1016/j.tecto.2013.09.022.

Sibson, R., 1977, Fault rocks and fault mechanisms: Journal of the Geological Society, v. 133, p. 191–213, doi: 10.1144/gsjgs.133.3.0191.

Sibson, R.H., 1990, Conditions for fault-valve behaviour: Geological Society, London, Special Publications, v. 54, no. 1, p. 15–28, doi: 10.1144/GSL.SP.1990.054.01.02.

Sibson, R.H., 1992, Implications of fault-valve behaviour for rupture nucleation and recurrence, Tectonophysics, v. 211, no. 1-4, p. 283–293, doi:10.1016/0040-1951(92)90065-E.

Sibson, R.H., 2005, Hinge-parallel fluid flow in fold-thrust belts: how widespread? Proceedings of the Geologists' Association, v. 116, no. 3–4, p. 301–309, doi: 10.1016/S0016-7878(05)80048-3.

Sibson, R.H., and Toy, V.G., 2006, The Habitat of Fault-Generated Pseudotachylyte : Presence vs Absence of Friction-Melt: in Earthquakes: Radiated Energy and the Physics of Faulting: American Geophysical Union Monograph Series, v. 170, p.153-166.

Sibson, R.H., White, S.H., and Atkinson, B.K., 1981, Structure and distribution of fault rocks in the Alpine Fault Zone, New Zealand: Geological Society, London, Special Publications, v. 9, no. 1, p. 197–210, doi: 10.1144/GSL.SP.1981.009.01.18.

Simpson, C., Wintsch, R.P., 1989, Evidence for deformation-induced K-feldspar replacement by myrmekite: Journal of Metamorphic Geology, vol. 7, p. 261-275, doi:10.1111/j.1525 1314.1989.tb00588.x.

Singh, S.C., Hananto, N., Qin, Y., Leclerc, F., Avianto, P., Tapponnier, P.E., Carton, H., Wei, S., Nugroho, A.B., Gemilang, W.A., Sieh, K., and Barbot, S., 2017, The discovery of a conjugate system of faults in the Wharton Basin intraplate deformation zone: Science Advances, v. 3, no. 1, p. e1601689, doi: 10.1126/sciadv.1601689.

Slingerland, R., and Furlong, K.P., 1989, Geodynamic and Geomorphic Evolution of the Permo-

Triassic Appalachian Mountains: Geomorphology, v. 2, p. 23–37.

Solum, J.G., 2003, Influence of phyllosilicate mineral assemblages, fabrics, and fluids on the behavior of the Punchbowl fault, southern California: Journal of Geophysical Research, v. 108, no. B5, p. 1–12, doi: 10.1029/2002JB001858.

Solum, J.G., Hickman, S.H., Lockner, D.A., Moore, D.E., van der Pluijm, B.A., Schleicher, A.M., and Evans, J.P., 2006, Mineralogical characterization of protolith and fault rocks from the SAFOD Main Hole: Geophysical Research Letters, v. 33, no. 21, p. 1–5, doi: 10.1029/2006GL027285.

Solum, J.G., van der Pluijm, B.A., and Peacor, D.R. (2005) Neocrystallization, fabrics and age of clay minerals from an exposure of the Moab Fault, Utah: Journal of Structural Geology, v. 27, no. 9, p. 1563–1576, doi: 10.1016/j.jsg.2005.05.002.

Środoń, J., 2002, Quantitative mineralogy of sedimentary rocks with emphasis on clays and with applications to K-Ar dating: Mineralogical Magazine, v. 66, no. 5, p. 677–687, doi:10.1180/0026461026650055.

Środoń, J., Drits, V., McCarty, D., Hsieh, J., and Eberl, D., 2001, Quantitative x-ray diffraction analysis of clay-bearing rocks from random preparations: Clays and Clay Minerals, v. 49, no. 6, p. 514–528.

Staisch, L.M., 2014, The Tectonic Evolution of the Hoh Xil Basin and Kunlun Shan : Implications for the Uplift History of the Northern Tibetan Plateau: University of Michigan Dissertation.

Stamatakos, J., Hirt, A.M., and Lowrie, W., 1996, The age and timing of folding in the central Appalachians from paleomagnetic results: Geological Society of America Bulletin, v. 108, no. 7, p. 815–829, doi: 10.1130/0016-7606(1996)108<0815:TAATOF>2.3.CO;2.

Sutherland, R., Berryman, K., and Norris, R., 2006, Quaternary slip rate and geomorphology of the Alpine fault: Implications for kinematics and seismic hazard in southwest New Zealand: Bulletin of the Geological Society of America, v. 118, no. 3–4, p. 464–474, doi: 10.1130/B25627.1.

Sutherland, R., Davey, F., and Beavan, J., 2000, Plate boundary deformation in South Island, New Zealand, is related to inherited lithospheric structure: Earth and Planetary Science Letters, v. 177, no. 3–4, p. 141–151, doi: 10.1016/S0012-821X(00)00043-1.

Sutherland, R., Eberhart-Phillips, D., Harris, R.N., Stern, T., Beavan, J., Ellis, S., Henrys, S., Cox, S.C., Norris, R.J., Berryman, K.R., Townend, J., Bannister, S., Pettinga, J., Leitner, B., et al., 2007, Do great earthquakes occur on the Alpine fault in central South Island, New Zealand? A Continental Plate Boundary: Tectonics at South Island, New Zealand, v. 175, p. 235–251, doi: 10.1029/175gm12.

Sutherland, R., Townend, J., Toy, V., Allen, M., Baratin, L., Barth, N., Beacroft, B.L., Boese, C., Boles, A., Boulton, C., Capova, L., Carpenter, B., Celerier, B., Chamberlain, C., et al., 2015, Deep Fault Driling Project (DFDP), Alpine Fault Boreholes DFDP-2A and DFDP-2B Technical Completion Report: GNS Science Report, v. 50, no. October, p. 269.

Sutherland, R., Toy, V.G., Townend, J., Cox, S.C., Eccles, J.D., Faulkner, D.R., Prior, D.J., Norris, R.J., Mariani, E., Boulton, C., Carpenter, B.M., Menzies, C.D., Little, T. a., Hasting, M., et al., 2012, Drilling reveals fluid control on architecture and rupture of the Alpine fault, New Zealand: Geology, v. 40, no. 12, p. 1143–1146, doi: 10.1130/G33614.1.

Suzuoki, T., Epstein, S., 1976, Hydrogen isotope fractionation between OH-bearing minerals and water: Geochimica et Cosmochimica Acta, v. 40, no. 10, p. 1229–1240, doi: 10.1016/0016-7037(76)90158-7.

Sverjensky, D.A., 1986, Genesis of Mississippi Valley-type lead-zinc deposits: Annual Review of the Earth Planetary Sciences, v. 147, no. 1, p. 7–99, doi: 10.1146/annurev.earth.14.1.177.

Tapponnier, P., Peltzer, G., and Dain, A.L., 1982, Propagating extrusion tectonics in Asia: New insights from simple experiments with plasticine, Geology, v. 10, p. 611–616, doi: 10.1130/0091-7613(1982)10<611.

Tettenhorst, R.T., and Corbató, C.E., 1993, Quantitative analysis of mixtures of 1M and 2M1 dioctahedral micas by X-ray diffraction: Clays and Clay Minerals, v. 41, no. 1, p. 45–55, doi: 10.1346/CCMN.1993.0410105.

Toby, B.H., 2006, R factors in Rietveld analysis : How good is good enough ? Powder Diffraction, v. 21, p. 67–70, doi: 10.1154/1.2179804.

Torsvik, T.H., Carlos, D., Mosar, J., Cocks, L.R.M., and Malme, T.N., 2002, Global reconstructions and North Atlantic paleogeography 440 Ma to recent: BATLAS—Mid Norway plate reconstruction atlas with global and Atlantic perspectives, p. 18–39.

Torsvik, T.H., Van der Voo, R., Preeden, U., Niocaill, C.M., Steinberger, B., Doubrovine, P. V., van Hinsbergen, D.J.J., Domeier, M., Gaina, C., Tohver, E., Meert, J.G., McCausland, P.J.A., and Cocks, L.R.M., 2012, Phanerozoic polar wander, palaeogeography and dynamics: Earth-Science Reviews, v. 114, no. 3–4, p. 325–368, doi: 10.1016/j.earscirev.2012.06.002.

Toulkeridis, T., Clauer, N., Chaudhuri, S., and Goldstein, S.L., 1998, Multimethod (K – Ar , Rb – Sr , Sm – Nd) dating of bentonite minerals from the eastern United States: Basin Research, v. 10, p. 261–270.

Toulkeridis, T., Goldstein, S.L., Clauer, N., Kroner, A., and Lowe, D.R., 1994, Sm-Nd dating of Fig Tree clay minerals of the Barberton Greenstone Belt, South Africa: Geology, v. 22, no. 3, p. 199–202, doi: 10.1130/0091-7613(1994)022<0199:SNDOFT>2.3.CO;2.

Townend, J., and Zoback, M., 2000, How faulting keeps the crust strong: Geology, v. 28, p. 399-402, doi: 10.1130/0091-7613(2000)28<399.

Townend, J., Sutherland, R., and Toy, V., 2009, Deep Fault Drilling Project—Alpine Fault, New Zealand: Scientific Drilling, no. 8, Sept 2009, p. 75–82, doi: 10.2204/iodp.sd.8.12.2009.

Townend, J., Sutherland, R., Toy, V.G., Eccles, J.D., Boulton, C., Cox, S.C., and McNamara, D., 2013, Late-interseismic state of a continental plate-bounding fault: Petrophysical results from DFDP-1 wireline logging and core analysis, Alpine Fault, New Zealand: Geochemistry, Geophysics, Geosystems, v. 14, no. 9, p. 3801–3820, doi: 10.1002/ggge.20236.

Toy, V.G., Boulton, C.J., Sutherland, R., Townend, J., Norris, R.J., Little, T.A., Prior, D.J., Mariani, E., Faulkner, D., Menzies, C.D., Scott, H., and Carpenter, B.M., 2015, Fault rock lithologies and architecture of the central Alpine fault, New Zealand, revealed by DFDP-1 drilling: Lithosphere, v. 7, no. 2, p. 155–173, doi: 10.1130/L395.1.

Toy, V.G., Ritchie, S., and Sibson, R.H., 2011, Diverse habitats of pseudotachylytes in the Alpine Fault Zone and relationships to current seismicity: Geological Society, London, Special Publications, v. 359, no. 1, p. 115–133, doi: 10.1144/SP359.7.

Turner, G., Enright, M.C., and Cadogan, P.H., 1978, The early history of chondrite parent bodies inferred from 40Ar-39Ar ages, *in* Proceedings of the Lunar and Planetary Science Conference, p. 989–1025.

Ufer, K., Stanjek, H., Roth, G., Dohrmann, R., Kleeberg, R., and Kaufhold, S., 2008, Quantitative phase analysis of bentonites by the rietveld method: Clays and Clay Minerals, v. 56, no. 2, p. 272–282, doi: 10.1346/CCMN.2008.0560210.

Uhlík, P., Šucha, V., Elsass, F., and Čaplovičová, M., 2000, High-resolution transmission electron microscopy of mixed-layer clays dispersed in PVP-10: a new technique to distinguish detrital and authigenic illitic material: Clay Minerals, v. 35, p. 781–789, doi: 10.1180/000985500547232.

Ujiie, K., et al., 2013, Low coseismic shear stress on the Tohoku-Oki megathrust determined from laboratory experiments: Science, v. 342, p. 1211– 1214, doi:10.1126/science.1243485.

Ustaömer, T., Robertson, A.H.F., 1993, A Late Palaeozoic-Early Mesozoic marginal basin along the active southern continental margin of Eurasia: evidence from the Central Pontides (Turkey) and adjacent regions: Geological Journal, v. 28, p. 219–238.

Uysal, I., Mutlu, H., Altunel, E., Karabacak, V., and Golding, S., 2006, Clay mineralogical and isotopic (K–Ar, δ18O, δD) constraints on the evolution of the North Anatolian Fault Zone, Turkey: Earth and Planetary Science Letters, v. 243, no. 1-2, p. 181–194, doi: 10.1016/j.epsl.2005.12.025.

van der Pluijm, B.A., Craddock, J., Graham, B., and Harris, J., 1997, Paleostress in cratonic North America: Implications for deformation of continental interiors: Science, v. 277, no. August, p. 794–796.

van der Pluijm, B.A., and Hall, C., 2015, Brittle Fault Dating, in *Encyclopedia of Scientific Dating Methods*, Springer, New York.

van der Pluijm, B.A., Hall, C.M., Vrolijk, P.J., Pevear, D.R., and Covey, M.C., 2001, The dating of shallow faults in the Earth's crust: Nature, v. 412, no. 6843, p. 172–5, doi: 10.1038/35084053.

van der Pluijm, B.A., Ho, N., and Peacor, D., 1994, High-resolution X-ray texture goniometry: Journal of Structural Geology, v. 16, no. 7, p. 1029–1032.

Van der Voo, R., 1988, Paleozoic paleogeography of North America, Gondwana, and intervening displaced terranes: Comparisons of paleomagnetism with paleoclimatology and biogeographical patterns: Bulletin of the Geological Society of America, v. 100, no. 3, p. 311–324, doi: 10.1130/0016-7606(1988)100<0311:PPONAG>2.3.CO;2.

Van der Voo, R., 1993, *Paleomagnetism of the Atlantic, Tethys, and Iapetus Oceans*: Cambridge University Press, New York.

Van der Voo, R., and Torsvik, T.H., 2012, The history of remagnetization of sedimentary rocks: deceptions, developments and discoveries: Geological Society, London, Special Publications, v. 371, no. 1, p. 23–53, doi: 10.1144/SP371.2.

van Hinsbergen, D., Kaymakci, N., Spakman, W., Torsvik, T., 2010, Reconciling the geological history of western Turkey with plate circuits and mantle tomography: Earth and Planetary Science Letters, v. 297, p. 674-686, doi:10.1016/j.epsl.2010.07.024.

Velde, B., and Hower, J., 1963, Petrological significance of illite polymorphism in Paleozoic sedimentary rocks: American Mineralogist, v. 48, no. 1959.

Velde, B., Suzuki, T., and Nicot, E., 1986, Pressure-Temperature-Composition of Illite/Smectite Mixed-Layer Minerals: Niger Delta Mudstones and Other Examples.: Clays and Clay Minerals, v. 34, no. 4, p. 435–441, doi: 10.1346/CCMN.1986.0340410.

Verdel, C., van der Pluijm, B.A., and Niemi, N., 2012, Variation of illite/muscovite 40Ar/39Ar age spectra during progressive low-grade metamorphism: An example from the US Cordillera: Contributions to Mineralogy and Petrology, v. 164, no. 3, p. 521–536, doi: 10.1007/s00410-012-0751-7.

Vidal, O., De Andrade, V., Lewin, E., Munoz, M., Parra, T., and Pascarelli, S., 2006, P-T-deformation-Fe3+/Fe2+ mapping at the thin section scale and comparison with XANES mapping: Application to a garnet-bearing metapelite from the Sambagawa metamorphic belt (Japan): Journal of Metamorphic Geology, v. 24, no. 7, p. 669–683, doi: 10.1111/j.1525-1314.2006.00661.x.

Vidal, O., Parra, T., and Trotet, F., 2001, A thermodynamic model for Fe-Mg aluminous chlorite using data from phase equilibrium experiments and natural pelitic assemblages in the 100 degrees to 600 degrees C, 1 to 25 kb range: American Journal of Science, v. 301, no. 6, p. 557–592, doi: 10.2475/ajs.301.6.557.

Vidal, O., Parra, T., and Vieillard, P., 2005, Thermodynamic properties of the Tschermak solid solution in Fe-chlorite: Application to natural examples and possible role of oxidation: American Mineralogist, v. 90, no. 2–3, p. 347–358, doi: 10.2138/am.2005.1554.

Vrolijk, P., 1990, On the mechanical role of smectite in subduction zones: Geology, v. 18, no. 8, p. 703–707, doi: 10.1130/0091-7613(1990)018<0703:OTMROS>2.3.CO.

Vrolijk, P., van der Pluijm, B.A., 1999, Clay gouge: Journal of Structural Geology, v. 21, no. 8–9, p. 1039–1048, doi: 10.1016/S0191-8141(99)00103-0.

Warr, L.N., Cox, S., 2001, Clay mineral transformations and weakening mechanisms along the Alpine Fault, New Zealand: Geological Society, London, Special Publications, v. 186, no. 1, p. 85–101, doi: 10.1144/GSL.SP.2001.186.01.06.

Warr, L.N., van der Pluijm, B.A., 2005, Crystal fractionation in the friction melts of seismic faults (Alpine Fault, New Zealand): Tectonophysics, v. 402, no. 1–4 SPEC. ISS, p. 111–124, doi: 10.1016/j.tecto.2004.12.034.

Warr, L.N., Hofmann, H., and van der Pluijm, B.A., 2016, Constraining the alteration history of a Late Cretaceous Patagonian volcaniclastic bentonite–ash–mudstone sequence using K–Ar and 40Ar/39Ar isotopes: International Journal of Earth Sciences, doi: 10.1007/s00531-016-1315-2.

Warr, L.N., van der Pluijm, B.A., and Tourscher, S., 2007, The age and depth of exhumed friction melts along the Alpine fault, New Zealand: Geology, v. 35, no. 7, p. 603, doi: 10.1130/G23541A.1.

Warr, L.N., van der Pluijm, B.A., Peacor, D.R., and Hall, C.M., 2003, Frictional melt pulses during a ~1.1 Ma earthquake along the Alpine Fault, New Zealand: Earth and Planetary Science Letters, v. 209, no. 1–2, p. 39–52, doi: 10.1016/S0012-821X(03)00070-0.

Warr., L.N., Wojatschke, J., Carpenter, B.M., Marone, C., Schleicher, A.M., van der Pluijm, B.A., 2014, A “slice-and-view” (FIB–SEM) study of clay gouge from the SAFOD creeping section of the San Andreas Fault at ∼2.7 km depth, Journal of Structural Geology, vol. 69, p. 234-244, doi:10.1016/j.jsg.2014.10.006.

Wenner, D.B., and Taylor, H.P., 1971, Temperatures of serpentinization of ultramafic rocks based on O18/O16 fractionation between coexisting serpentine and magnetite: Contributions to Mineralogy and Petrology, v. 32, no. 3, p. 165–185, doi: 10.1007/BF00643332.

Wijbrans, J.R., and McDougall, I., 1986, 40Ar/39Ar dating of white micas from an Alpine high-pressure metamorphic belt on Naxos (Greece): the resetting of the argon isotopic system:

Contributions to Mineralogy and Petrology, v. 93, no. 2, p. 187–194, doi: 10.1007/BF00371320.

Williams, C.F., Grubb, F. V., and Galanis, S.P., 2004, Heat flow in the SAFOD pilot hole and implications for the strength of the San Andreas Fault: Geophysical Research Letters, v. 31, no. 15, p. 22–25, doi: 10.1029/2003GL019352.

Williams, J.N., Toy, V.G., Massiot, C., McNamara, D.D., and Wang, T., 2016, Damaged beyond repair? Characterising the damage zone of a fault late in its interseismic cycle, the Alpine Fault, New Zealand: Journal of Structural Geology, v. 90, p. 76–94, doi: 10.1016/j.jsg.2016.07.006.

Williams, L.B., Turner, A., Hervig, R.L., 2007, Intracrystalline boron isotope partitioning in illite-smectite: Testing the geothermometer: American Mineralogist, v. 92, no. 11–12, p. 1958–1965, doi: 10.2138/am.2007.2531.

Wintsch, R., 1995, Fluid-rock reaction weakening of fault zones: Journal of Geophysical Research, v. 100, p. 13021-13032, DOI: 10.1029/94JB02622.

Wirth, R., 2009, Focused Ion Beam (FIB) combined with SEM and TEM : Advanced analytical tools for studies of chemical composition, microstructure and crystal structure in geomaterials on a nanometre scale: Chemical Geology, v. 261, no. 3–4, p. 217–229, doi: 10.1016/j.chemgeo.2008.05.019.

Wolters, F., Emmerich, K., 2007, Thermal reactions of smectites-relation of dehydroxylation temperature to octahedral structure: Thermochimica Acta, v. 462, no. 1–2, p. 80–88, doi: 10.1016/j.tca.2007.06.002.

Yamaguchi, A., et al., 2011, Progressive illitization in fault gouge caused by seismic slip propagation along a megasplay fault in the Nankai Trough: Geology, v. 39, p. 995–998, doi:10.1130 /G32038.1.

Yamasaki, T., Wright, T.J., and Houseman, G.A., 2014, Weak ductile shear zone beneath a major strike-slip fault: Inferences from earthquake cycle model constrained by geodetic observations of the western North Anatolian Fault Zone, Journal of Geophysical Research, v. 119, p. 3678-3699, doi: 10.1002/2013JB010347.

Yates, D.M., Rosenberg, P.E., 1997, Formation and stability of endmember illite: II. Solid equilibration experiments at 100 to 250°C and Pv soln: Geochimica et Cosmochimica Acta, v. 61, no. 15, p. 3135–3144, doi: 10.1016/S0016-7037(97)00156-7.

Yeh, H., 1980, D/H Ratios late-stage dehydration of shales during burial: Geochimica et Cosmochimica Acta, v. 44, p. 341–352.

Yeh, H.W., Savin, S.M., 1977, Mechanism of burial metamorphism of argillaceous sediment: 3. O-isotope evidence: Geological Society of America Bulletin, v. 88, p. 1321–1330.

Ylagan, R.F., Kim, C.S., Pevear, D.R., Vrolijk, P.J., 2002, Illite polytype quantification for accurate K-Ar age determination: American Mineralogist, v. 87, no. 11–12, p. 1536–1545.

Zachos, J.C., Dickens, G.R., Zeebe, R.E., 2008, An early Cenozoic perspective on greenhouse warming and carbon-cycle dynamics: Nature, v. 451, p. 279-283, doi:10.1038/nature06588.

Zattin, M., Cavazza, W., Okay, A.I., Federici, I., Fellin, M.G., Pignalosa, A., Reiners, P., 2010, A precursor of the North Anatolian Fault in the Marmara Sea region: Journal of Asian Earth Sciences, v. 39, 97-108, doi:10.1016/j.jseaes.2010.02.014.

Zhang, L., Liu, Y., Guo, L., Yang, D., Fang, Z., Chen, T., Ren, H., and Yu, B., 2014, Isotope geochemistry of mercury and its relation to earthquake in the Wenchuan Earthquake Fault Scientific Drilling Project Hole-1 (WFSD-1): Tectonophysics, v. 619–620, p. 79–85, doi: 10.1016/j.tecto.2013.08.025.

Zharkov, M.A., and Chumakov, N.M., 2001, Paleogeography and Sedimentation Settings during Permian – Triassic Reorganizations in Biosphere: Stratigraphy and Geological Correlation, v. 9, no. 4, p. 340–363.

Ziegler, A.M., Scotese, C.R., and Barrett, S.F., 1983, Mesozoic and Cenozoic Paleogeographic Maps, *in* Brosche and Sundermann (eds.) *Tidal Friction and the Earth's Rotation II*, Springer-Verlag, Berlin Heidelberg, p. 240–252.

Zoback, M.D., and Townend, J., 2001, Implications of hydrostatic pore pressures and high crustal strength for the deformation of intraplate lithosphere: Tectonophysics, v. 336, no. 1–4, p. 19–30, doi: 10.1016/S0040-1951(01)00091-9.

Zwingmann, H., Mancktelow, N., Antognini, M., Lucchini, R., 2010, Dating of shallow faults: New constraints from the AlpTransit tunnel site (Switzerland): Geology, v. 38, no. 6, p. 487-490, doi: 10.1130/G30785.1.